THE UNIVERSITY *of* EDINBURGH

DEM modelling and quantitative validation of flow characteristics and blending of pellets in a planar silo

by

Veera Pratap Reddy Kasina

A dissertation submitted in partial fulfilment
for the degree of
Doctor of Philosophy

in the
Institute for Infrastructure and Environment
School of Engineering
UNIVERSITY OF EDINBURGH

2016

Declaration of authorship

This thesis entitled, "*DEM modelling and quantitative validation of flow characteristics and blending of pellets in a planar silo*" is submitted to the University of Edinburgh for the degree of Doctor of Philosophy. The research work described and reported in this thesis has been completed solely by *Veera Pratap Reddy Kasin*a under the supervision of *Prof. Jin Y. Ooi, Prof. Jian-Fei Chen and Mr. Hans Schneider*.

Where other sources are quoted full references are given.

Publications based on this thesis:

Kasina, V.P.R., Chen, J.F., Schneider, H., Ooi, J.Y. Quantitative validation of DEM predictions of flow of cylindrical pellets in a flat bottom silo. *To be submitted for review*.

Kasina, V.P.R., Chen, J.F., Schneider, H., Ooi, J.Y., 2014. DEM validation and investigation of boundary effects on flow patterns in model planar silos. *Infrastructure and Environment Scotland 2nd Postgraduate conference*, September 2014, Edinburgh.

Mathews, J., Kasina, V.P.R., Combarros, M., Chen, J.F., Ooi, J.Y., Kwade, A.R., Schneider, H., Wu, W., 2013. Experimental investigation of flow and segregation behaviour of bulk solids in silos under high gravity conditions. *Particles 2013*, September 2013, Germany.

Kasina, V.P.R., Chen, J.F., Ooi, J.Y., Wilms, H., Schneider, H., 2012. DEM modelling and experiments on granular flow in silos with internals. *7th International Conference for Conveying and Handling of Particulate Solids*, September 2012, Germany.

Veera Pratap Reddy Kasina
September 2016

Abstract

Blending processes in a silo minimise the fluctuations in the property of bulk solids with the blending performance being strongly influenced by the flow pattern and operating mode among other process parameters such as batch size and type of input fluctuations. An accurate prediction of flow characteristics such as flow channel boundary and velocity profiles is important for understanding and quantifying the blending performance, thereby increasing the scope for new design by minimising the number of expensive pilot scale experiments required. In this thesis, the Discrete Element Method (DEM) is deployed to predict and understand the flow characteristics and blending of cylindrical plastic pellets in a planar flat bottom silo and a multi-flow blender (a silo with an insert and a blending tube). The predictions are validated against high-resolution velocity measurements analysed using Particle Image Velocimetry (PIV) technique.

A planar model silo was built to measure the flow of pellets using PIV technique. The existing GeoPIV Matlab module was customised to extract the velocity fields in the Eulerian frame of reference and its accuracy has been verified. The developed tool was then applied to quantitatively investigate the mechanism of evolution of flow in a flat bottom silo and the dependency of the state of developed flow on the depth of the planar silo. It was shown that the development of flow during discharge can be divided into two stages: a rapid upward propagation of plug flow followed by a widening of the flow channel with increasing shearing boundaries. The size of the flow channel was found to be increasing with the depth of the silo. For the 100 mm deep silo, the flow is three dimensional with significant retardation in velocity at the frontal walls, whilst a negligible retardation was found for the 20 and 40 mm deep model silos. The thickness and frontal wall friction in planar silos thus play an important role in the development of flow patterns in model silos.

In this thesis, DEM model calibration relating the macro-scale bulk friction and micro- scale particle friction at different rolling friction values was developed from DEM simulations of Jenike direct shear box. During the direct shear simulation, a constant normal force was achieved with the use of a shear lid geometry made with glued spheres thereby eliminating the use of a traditional servo control function. The influence of particle rotations and rolling friction on the limiting bulk friction for

different particle sliding friction coefficients was explored. The accuracy of the calibration data was assessed by simulating the flow in a flat bottom silo and comparing the model predictions of flow rate, velocity profiles and flow channel boundary with the experiments. A good quantitative agreement was found between the experiment and simulations. The DEM model predictions were also compared with the kinematic model. Following the validation of the model, it was shown that the frontal friction and rolling friction are the influential parameters in simulating the flow patterns such as semi-mass and internal flow. It was further shown that flow transits from semi-mass flow to internal flow with the increase of frontal wall friction. The drastic influence of frontal wall friction on stress, flow patterns and force chains were analysed highlighting its implications on interpretations in 2D test silos.

Finally, the developed DEM and PIV tools are employed to investigate blending in a flat bottom and multi-flow blender silo for different flow patterns. The analysis showed that the blending is more effective with the internal flow when compared to semi-mass flow in a flat bottom silo, in both continuous and discontinuous modes for a variety of process conditions such as batch size, the number of recirculation and frequency of input fluctuations. An algorithm was developed to evaluate the blending performance from the spatially averaged Eulerian velocity fields.

The flow in a relatively large-scale multi-flow blender comprising nearly 606,000 particles, thereby fully replicating the test silo, was simulated and the challenges in reproducing the test conditions of continuous and discontinuous modes of operation were discussed. The flow patterns and blending were first analysed from the experiments in different configurations of the insert. Using the same input parameters for the model, it was shown that the model predictions of the velocity profiles along the height of the silo are in good agreement with the experiments. Internal flow, mixed flow and mass flow were predicted for the diverging, straight and converging insert configurations respectively and the blending performance for each of these configurations suggests an optimal configuration of the blender thereby demonstrating the potential of PIV and DEM in design optimisation. The possibility of conducting the DEM simulations under increased gravity in order to reduce the computational time has also been explored.

Acknowledgements

I would like to sincerely thank my supervisor Prof. Jin Y Ooi for his constant encouragement and excellent supervision during the course of this research because of whom I evolved as an independent researcher. I am also grateful to my second supervisor Prof. Jian-Fei Chen for his careful and critical comments on the work.

I am very thankful to Hans Schneider for sharing his industrial experience on silo blending and also for being my mentor during my stay in Germany.

I would also like to acknowledge the financial support by EU under Marie Curie Actions ITN (Project No. ITN 238577).

I would to like express my deep gratitude to all the technical staff at Zeppelin Technology centre, Friedrichshafen in Germany, particularly Hermann Baier for fabricating the experimental set-up and Barbara Bucher for the help in material characterisation tests.

I would also like to acknowledge the help of Derek Jardine in installing the experiment set-up in the laboratory and I also extend my thanks to IT staff for helping me in data storage and other related issues.

I am very thankful to Prof. Abdel Sanad, John Morrissey, Alvaro Janda, Carlos Labra and Prashant Gupta for many useful discussions. I would also like to thank all my colleagues and friends at the University for their wonder company and the support in Edinburgh.

Finally, special thanks to my parents and relatives who sacrificed everything, without them nothing would have been possible.

CONTENTS

List of figures

List of tables

In dedication to my parents for making me be who I am

Chapter 1

1. Introduction

1.1 Background

Silos are used for storage of bulk solids and large scale process operations such as blending and degassing. The blending of bulk solids is an important process operation in industries ranging from pharmaceutical to mining where the capacities to be handled ranges from pill size batches to tonnes of ore (Johanson, 1970). The blending process minimises the fluctuations in the product quality arising from different batch processes and also from the variation in the quality of different raw materials. While small batch sizes are blended using mechanically agitated mixers, it can be economical to blend intermediate size batches while they are stored in a bin, by recirculating them in order to achieve a uniform property of interest such as chemical composition, melt index or colour of pellets (Johanson, 1970; Wilms, 1986). Blending in silos is achieved by controlling the flow pattern of the bulk solids using a variety of methods including the installation of inserts and blending pipes. The homogenisation of polymer powders and pellets at reduced blending time is a major area of interest for industry (Wilms, 1992).

Johanson (1970) first introduced the concept of in-bin blending in a mass-flow hopper. He proposed two essential conditions in order to have a successful blending. The first one is that the bin should be designed to achieve mass flow so as to avoid the formation of stagnant zones and the second condition is that the particles entering the bin should have a sufficient difference in residence times at different horizontal positions. He stated that "the success of in-bin blending depends on matching the bin configuration with the properties of the solid so that the flow patterns in the bin produces the required blending action". Several designs of industrial silo blenders are built on this concept, either (a) by imposing secondary flow patterns in a mass flow silo through the installation of inserts as well as tubes, or (b) by extracting the material simultaneously from different zones of the silo via the installation of long vertical pipes with multiple intake openings at different levels. Some of the existing

industrial blenders are introduced below to further explain the principle of blending (Manjunath et al., 1992; Wilms, 1992).

Figure 1.1 (a) - (d) shows the schematic of various silo blenders such as multi-pipe, multi-channel, centro and multi-flow blender. The first three blenders shown in this figure works on the principle of simultaneously extracting the material from different locations. In the multi-pipe and multi-channel blender, this is achieved by installing numerous vertical pipes with multiple intake openings at different levels of the silo. Each pipe is sub-divided into three compartments using vertical baffles. Therefore, an arrangement of 6 vertical pipes and 3 intake openings at different levels can sample material from 18 different locations and thus achieving a widespread in the residence times of the material. The material sampled from each of these vertical pipes combines with the material from the core of a silo and eventually mixes in the blending chamber below the hopper, as indicated by the red arrows in Figure 1.1 (a) and 1.1 (b). The only difference in the multi-channel and multi-pipe blender is the way the vertical pipes are supported in the silo. In the case of the former, vertical pipes are supported using the external supporting elements while in the later, the rear wall of the pipe is welded to the walls of the silo thereby achieving a high structural rigidity. Figure 1.1 (c) shows the centro-blender which is mainly used for sticky pellets and cohesive powders. Because of the poor flowability of these solids, a larger pipe diameter is required to avoid arching in the multi-pipe blenders. However, the pipe diameter can only be increased to a limited size due to economical reasons. The blending process in this silo also works on the same principle as described for the multi-pipe and multi-channel blender, by having a large central pipe with multiple small hopper elements at different levels.

Based on the idea of Bi-insert® developed by Johanson (1982), other classes of silo blenders have been developed which work on the principle of imposing a secondary velocity profile on top of a uniform velocity profile in the vertical section of a mass-flow silo. One of such blender is shown in Figure 1.1 (d): a multi-flow blender. A secondary velocity profile is imposed by installing a cone-in-cone insert and a small vertical tube in the vicinity of the hopper. As can be seen in this figure, these internal elements create a differential vertical velocity for material flowing in the annuli

between the hopper, the cone-in-cone insert and the blending tube, thereby a creating a spread in the residence time distribution. The ability of the internals to impose a secondary velocity profile only extends to a limited height in the cylindrical section of the silo above which the velocity profiles are uniform. These blenders are thus more efficient with squat configuration with an aspect ratio less than 1.75. Because of its simplicity in its structure, the existing storage silos can be easily retrofitted with these internals to convert into a blending silos (Wilms, 1992).

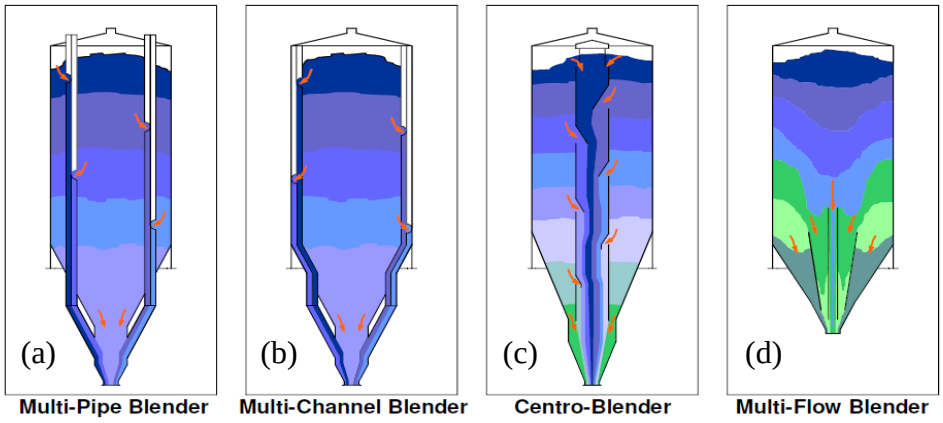

Figure 1.1 Schematic of different gravity silo blenders demonstrating the principle of blending process.

1.2 Motivation

The flow patterns developed in a silo play a major role in determining the performance of a blending silo. For example, Figure 1.2 shows the experimental demonstration of the development of flow channel around a blending pipe in a flat-bottom silo. The blending efficiency, in this case, depends on the size and shape of the flow channel developed around the intake opening of the pipe – in this example, the steeper this flow channel, the higher would be the efficiency. The prediction and the quantification of these flow characteristics can therefore be useful in optimising the blending performance. Another such example is shown in Figure 1.3, the flow patterns are visualised with the aid of blue and yellow coloured layers of pellets in

the centro- and multi-flow blenders. Although the flow patterns have been visualised, there are no quantitative results on the flow characteristics (such as size and shape of the flow channel, velocity profiles within the flow channel) across the silo height.

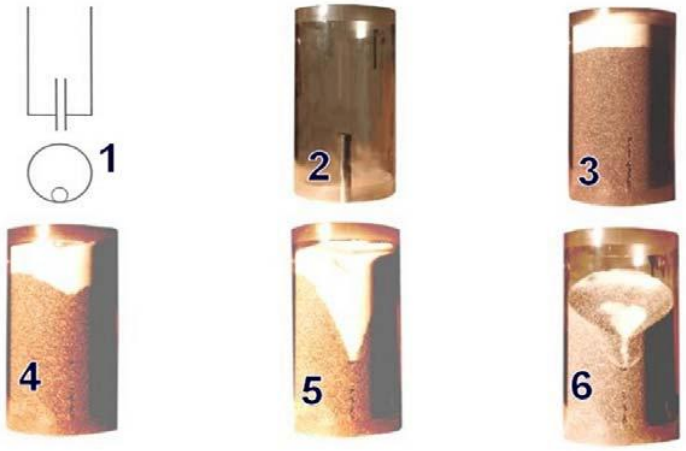

Figure 1.2 Visualisation experiments demonstrating the development of flow channel around a blending pipe in a flat bottom silo.

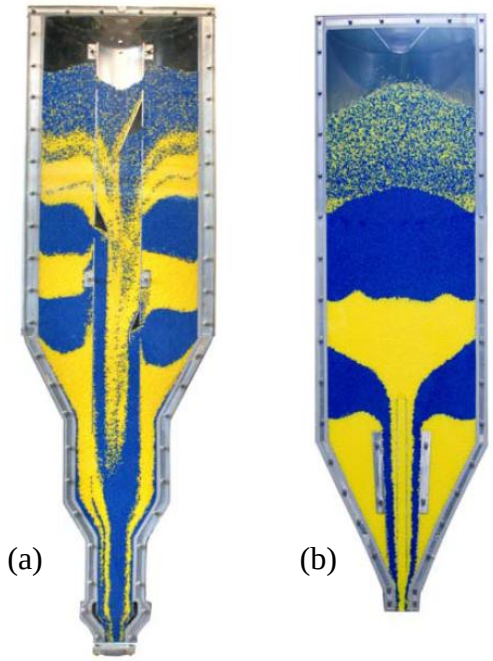

Figure 1.3 Visualisation of flow zones (a) Centro-blender (b) Multi-flow blender.

Experiments to investigate blending efficiency are expensive and time consuming and often provide very limited information about the flow. Whilst, a few theories have been successfully developed for the design of relatively simple silo configurations for mass flow and funnel flow (Craig, 1996; Jenike and Shield, 1959; Johanson, 1964, 2006), a reliable prediction of flow profiles around internals such as inserts and blending pipes remains a considerable challenge (Härtl, 2008) therefore one has to rely on expensive and exhaustive experiments to analyse the blending in complex geometries.

Discrete element method (DEM) is increasingly used to simulate the complex granular flows in industrial systems and it has a great potential to study the flow patterns and blending in a silo. However, it is important to validate a DEM model for simple silo configurations (such as a flat bottom silo) before simulating any industrial system. "Validation is the process of determining the degree to which a model is an accurate representation of the real world from the perspective of the intended use of the model" (Ooi, 2013). Thus, the validation process involves assessing the model accuracy by comparing the pertinent measured quantities, which include wall pressures, flow rate and velocity fields in the case of a silo flow investigation, with the corresponding model predictions. The predictions can be validated against high-resolution velocity measurements analysed using Particle Image Velocimetry (PIV) technique.

1.3 Objectives and structure of thesis

The aim of this research is to gain the scientific understanding of flow and blending of granules from a lab scale planar silo and further to compare the flow behaviour with the predictions of Discrete Element Method (DEM). The main objectives of the work are listed below in the increasing order of chapters from 3 to 7:

i. To understand the evolution of flow of granules in a flat-bottom silo using the Particle Image Velocimetry (PIV) technique (presented in chapter 3),
ii. To study the relationship between the bulk and particle scale friction using DEM simulations of Jenike direct shear box (presented in chapter 4),

iii. To quantitatively validate the DEM model and further to investigate the effect of front and back wall friction on velocity and stress fields in 2D test silos (presented in chapter 5),

iv. To understand the blending in an internal and a semi-mass flow from DEM simulations in a flat-bottom silo and further to test accuracy of traditional impulse-stimulus approach (presented in chapter 6),

v. To understand the development of flow patterns and blending for different configurations of the insert in a multi-flow blender using the developed PIV and DEM tools (presented in chapter 7).

The work in this thesis is organised into eight chapters as follows:

a. **Chapter 1** gives the background of blending in silos followed by motivation, aim and objectives of the work.

b. **Chapter 2** presents the literature review concerning experimental and numerical studies of blending and flow patterns in silos. The theory of PIV and DEM followed the respective studies in the silo are also presented.

c. **Chapter 3** presents the studies of the accuracy of PIV technique which is then followed by the description of various features of a newly built experimental setup for planar silo and then the chapter ends with an experimental study to quantify the evolution of flow of granules in a flat-bottom silo during the batch discharge.

d. **Chapter 4** presents DEM model representation of test pellets followed by the simulations of Jenike direct shear box in order to obtain the relationship between the bulk friction and particle scale friction.

e. **Chapter 5** presents the quantitative validation of DEM predictions of flow in a flat-bottom silo and investigates the influential parameters that affect the flow patterns.

f. **Chapter 6** presents the DEM study of blending in a flat-bottom silo and discusses the various methods of analysis of blending in continuous and discontinuous modes. This chapter ends with the development of an algorithm to evaluate blending from the Eulerian velocity fields.

g. **Chapter 7** presents the experimental and DEM studies of flow and blending in a multi-flow blender for different angles of the cone-in-cone insert using the developed PIV and DEM tools.
h. **Chapter 8** presents the conclusions and recommendation for future work.

Chapter 2

2. Literature review

2.1 Introduction

Following the brief introduction of silo blending and its relation to flow patterns in the previous chapter, this chapter covers the literature concerning the modelling and the experimentation of flow and blending in a silo focussing mainly on the topics related to the current work. The literature studies covered in this chapter can be broadly classified into three categories: the studies of blending in a silo followed by the theory of Particle Image Velocimetry (PIV) and its application to silo flow and finally the theory of Discrete Element Method (DEM) and the literature concerning the various aspects related to the DEM modelling of flow in silos.

2.2 Blending in silos

Blending in a silo is a process operation in which various batches of the bulk solids are homogenised to increase the uniformity of the final product. Beaudry (1948) defined the blender efficiency (also called variance reduction ratio, VRR) as the ratio of the variance of fluctuations (of a property of interest) in the incoming stream to the variance of fluctuations in the outgoing stream. The fluctuations in a particular property can exist between the solids of the same batch and of different batches (Beaudry, 1948; Wilms, 1986). The performance analysis of a silo blender, therefore, requires the data of input and output time variation of a target property of the bulk solid, for example, the melt flow index of polymers or the colour of pellets (Wilms, 1986).

In a lab scale or a pilot scale experimental studies of in-bin blending, it is common to choose the colour as a representative property as it is easy to recognise and to measure the colour concentration in the outflow of a blender, provided all the coloured pellets have the same flow properties. One can ask the following questions before conducting such experiments with the coloured particles:

- How to replicate the inlet fluctuations of a given property (such as melt index of pellets) using a colour?
- How many number of colours should be used?
- What percentage of each colour material should be used?
- How to collect the samples at the outlet during operation and at what time intervals?
- How to separate the colours at the end of each experiment to start a fresh experiment?
- What operating modes (continuous mode or discontinuous mode) should the experiment be conducted?

The answers to the above questions depends on the specific objective of the experiment which could be: to compare the performance of different blenders under the same operating conditions, to obtain the residence time distribution (RTD) function of a blender, to test the performance of a new design in continuous and discontinuous modes of operation.

In experiments it is not always possible to replicate the random input property fluctuations that could exist in real scenario and therefore, often experiments are conducted for idealised situations, for example inlet fluctuations can be represented as a step signal by loading the bin with alternative layers of colored material (refer to Figure 1.3) usually two colours with 50 % to 50 % ratio (Wilms, 1988). Samples of a certain size are then collected at regular intervals during the discharge. The fraction of each colour is then measured from the collected samples in order to obtain the time variation of fluctuations of colour concentration in the outflow. However, the main challenge in conducting these type of experiments is that fresh batches of unmixed material are required for each new experiment, as it time-consuming and difficult to separate large quantities of the mixed coloured pellets at the end of the discharge. This problem can be avoided to some extent by assuming the blender as a linear time- invariant system (Craig et al., 1994; Eichler, Dau and Ebert, 1997a; Roberts, 1991a). With this assumption, the blender can be characterised entirely by a single function called impulse response or RTD function. The performance analysis of the blender reduces simply to the measurement of RTD function. The time

variation of outlet concentration can then be evaluated by computing the convolution integral of any arbitrary input concentration variation and the RTD function.

In the following subsections, first the fundamental concept of RTD is described followed by the discussion of various studies to predict the blending in a silo using RTD function and linear system theory.

2.2.1 Residence time distribution (RTD) function

A blender is characterised by the residence time distribution (RTD) or the exit age distribution function. The concept of RTD was first introduced by Danckwerts (1953). The model and the equations described here were taken from his work. Consider a vessel of volume V occupied by a fluid flowing continuously with a steady flow rate Q. Imagine that any property of the fluid at the inlet changes suddenly, for example if the colour of the fluid changes from white to red. Assume that the red colour tracer of quantity V_{tr} is virtually injected into the inlet stream for a very short period of time, as a pulse signal. Let us say, the fraction of material having the residence times between t and $t+dt$ is $E(t)dt$, where $E(t)$ is the residence time or exit age distribution function, $F(t)$ and $C(t)$ be the fraction and concentration of the red material in the outflow at any time t. The dimensionless form of time t can be written as,

$$\theta = \frac{Vt}{Q} \qquad (2.1)$$

where V is the volume of the vessel and Q is the volumetric flow rate.

The response of the tracer in the outflow (called as F-diagrams) for various idealised flow scenarios is shown in Figure 2.1 (a) – (d). Figure 2.1 (a) shows the response of a tracer if the flow is uniform or piston type, in which all the fluid elements of the tracer stream exits at the same time. It is obvious that due to the lack of velocity gradients, all the tracer material leaves the vessel at the same time, resulting in no mixing. Due to the presence of viscous effects in the fluid flow, a departure from the ideal inviscid flow can be seen in Figure 2.1 (b) where there is always some longitudinal mixing due to the presence of velocity gradients. Figure 2.1 (c) depicts the perfect mixing scenario, in which the tracer material present at all times in the

flow. Figure 2.1 (d) shows the response when there are dead regions in the flow in which considerable fraction of tracer spend time larger than the average residence time. Figure 2.2 (a) - (d) shows the corresponding concentration variation of tracer (called as C – diagrams) for each scenario. The relationship between C_o *(t), F (t)* and *E (t)* is given by (2.2). The derivation for this equation can be found in Danckwerts (1953).

$$\mathbf{C_o(t) = \frac{V_{tr}}{Q}\frac{dF(t)}{dt} = \frac{V_{tr}}{Q}E(t)} \qquad \textbf{(2.2)}$$

If the concentration distribution of the tracer material in the outflow is known, then the RTD function *E (t)* can be evaluated using (2.2).

The RTD function has the following three important properties:

a) The mean residence (t_m) of the material leaving the vessel can be calculated from the first moment of *E (t)* given by (2.3).

$$\mathbf{t_m = \int_0^\infty t\,E(t)\,d\theta} \qquad \textbf{(2.3)}$$

b) The second moment gives the degree of dispersion (σ^2) around the mean which is given by (2.4).

$$\mathbf{\sigma^2 = \int_0^\infty (t - t_m)E(t)d\theta} \qquad \textbf{(2.4)}$$

c) The area of the curve *E (t) vs. t* indicates the summation of the fraction of the tracer material that left the vessel, which is equal to 1 when there are no dead zones.

The dimensionless form of RTD function *E (θ)* can be written as,

$$\mathbf{E(\theta) = t_m\,E(t)} \qquad \textbf{(2.5)}$$

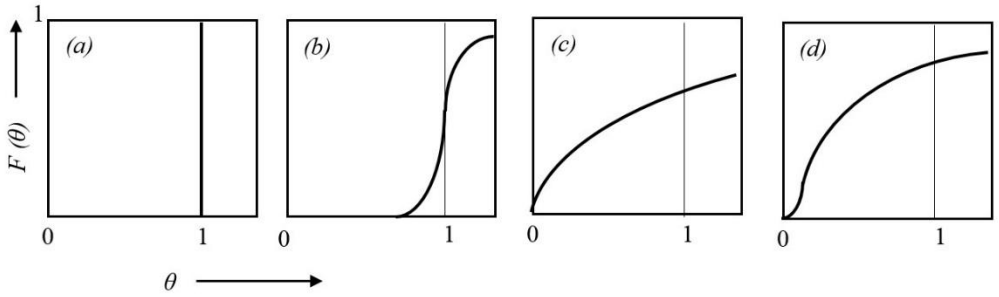

Figure 2.1 Fraction of tracer material that left the vessel (a) Piston flow (b) Piston flow with longitudinal mixing (c) complete mixing (d) dead water (reproduced from Danckwerts (1953)).

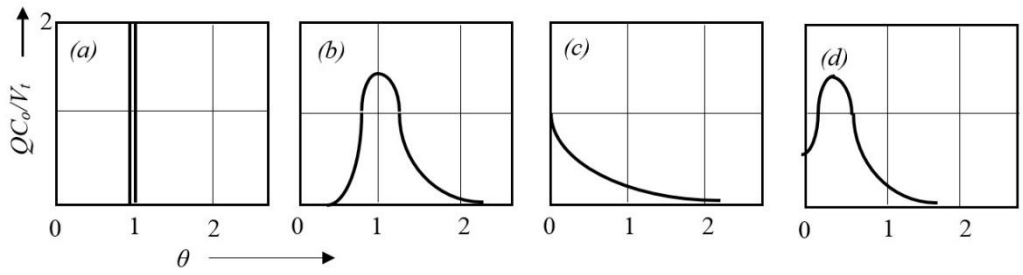

Figure 2.2 Concentration of tracer material in the outflow of the vessel (a) Piston flow (b) Piston flow with longitudinal mixing (c) complete mixing (d) dead water (reproduced from Danckwerts (1953)).

2.2.2 Prediction of In-bin blending

Numerous studies of blending in silo have been published over the years (Bagster, 1973; Bartholomew, 1992; Boss and Dabrowska, 1985; Boss, 1986; Brown and Nielsen, 1998; Carson and Royal, 1991, 1992; Cassidy, Scrivens and Michaelides, 1992; Craig et al., 1994; Dau and Ebert, 1996; Dau, Ebert and Haehner, 1994; Eichler, Dau and Ebert, 1996, 1997a, 1997b; Gericke, 1993; Goins, 1984; Johanson, 1970, 1982b, 2006; Kiesgen and Wilms, 1991; Manjunath, de Silva and Roberts, 1992; Peshcl, 1986; Roberts, 1991b; Roth, 1982; Schulze, 1995; Scrivens, Michaelides and Thomson, 1991; Standish, Liu and McLean, 1988; Stein, 1990;

Weiler et al., 2012; Wilms, 1986, 1988, 1992; Young, 1982). In this subsection, the key literature is discussed highlighting the significant work regarding the methods to determine RTD and to predict the blending performance in a silo.

The concept of in-bin blending was first introduced by Johanson (1970). He stated that the "The success of in-bin blending depends on matching the bin configuration with the properties of the solid so the flow patterns in the bin produces the required blending action". For an efficient blending he proposed the following two essential conditions:

a) There should be no stagnant zones in the bin i.e. the bin should be designed for mass flow.
b) There should be a sufficient difference between the residence times of solids in different horizontal positions in the bin.

In addition to the above two conditions, a third condition was specified by Johanson (2006), which states that the velocity profiles in the blender must produce mixing at a scale smaller than the size of the final product sample.

Johanson (1970) developed a theory to predict the blending in a hopper operating in a discontinuous mode. A thin layer of marker particles is placed initially on the top hopper and constantly recycled several times by depositing them again on the top. The schematic of the initial condition of the hopper is shown in Figure 2.3. In this scenario, he assumed that the RTD function of the hopper is of triangular distribution (in the other words the markers discharge during the first pass into a triangular distribution), which is defined by two parameters as shown in Figure 2.4. The two parameters which include: V_1, the volume of the solids discharged before the first appearance of the marker particles at the outlet and P, the volume of silo contents discharged during which all the marker particles left the silo.

The total number of marker particles (N) can be calculated from the area of the concentration curve given by (2.6).

$$\mathbf{N = \frac{1}{2} C_m P} \qquad \textbf{(2.6)}$$

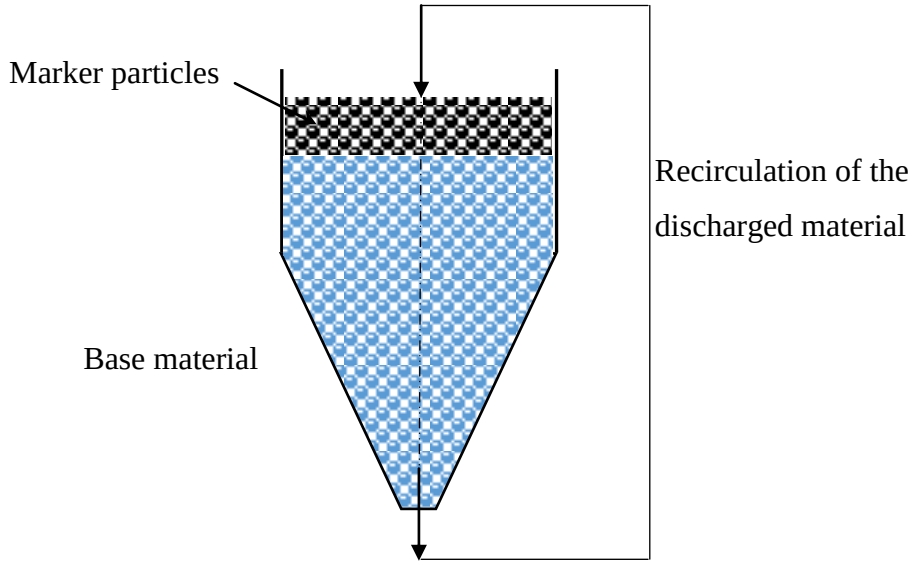

Figure 2.3 Schematic illustration of in-bin blending in a hopper.

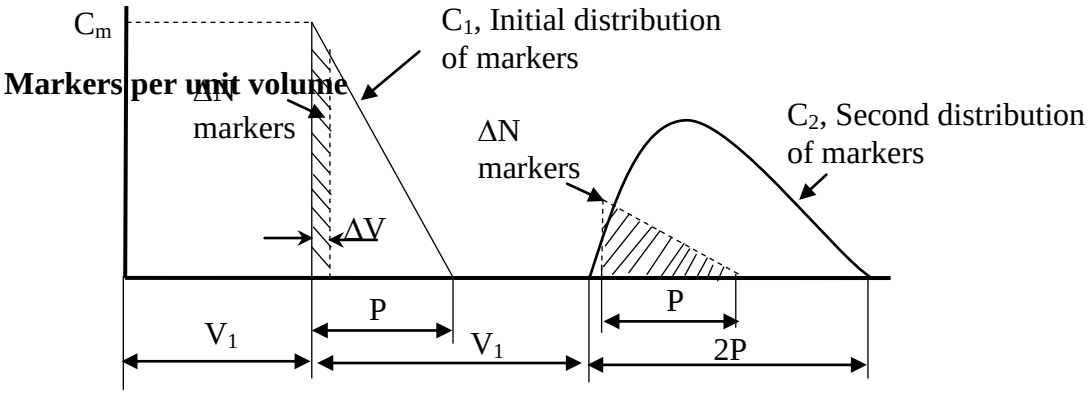

Figure 2.4 Theoretical mixing of a single layer of markers (reproduced from Johanson (1970)).

The volume of the silo contents is given by (2.7),

$$\mathbf{V_t = V_1 + \frac{P}{3}} \qquad \textbf{(2.7)}$$

The shape of the marker concentration distribution during the successive passes is then calculated by noting that each incremental volume ΔV from the first pass discharges into the same triangular distribution when deposited at the top of the silo. The number of particles ΔN containing ΔV can be given by (2.8).

$$\mathbf{\Delta N(v) = C_1(v)\ x\ \Delta V} \qquad \textbf{(2.8)}$$

The summation of all these elemental triangular distributions gives the marker concentration during the second pass and so on. He derived the generalised equation for the marker concentration during the N^{th} pass which is given by (2.9) - (2.11).

$$\mathbf{C_N(V) = \int_{\emptyset=0}^{V} 2\,\frac{C_{N-1}(\emptyset)}{P}\left(\frac{P+\emptyset-V}{P}\right)\,d\emptyset} \quad , \qquad \textbf{(2.9)}$$

$$0 \le V \le P$$

$$\mathbf{C_N\,(V) = \int_{\emptyset=V-nP}^{V} 2\,\frac{C_{N-1}(\emptyset)}{P}\left(\frac{P+\emptyset-V}{P}\right)d\emptyset\ ,} \qquad \textbf{(2.10)}$$

$$nP \le V \le (n+1)\,P$$

$$n = 1, 2, 3 \ldots N\text{-}2$$

$$\mathbf{C_N\,(V) = \int_{\emptyset=V-nP}^{V} 2\,\frac{C_{N-1}((N-1)P-\emptyset)}{P}\left(\frac{NP-V-\emptyset}{P}\right)d\emptyset,} \qquad \textbf{(2.11)}$$

$$(N - 1)\,P \le V \le N\,P$$

The marker concentration at the outlet from the second pass to any *N* number of passes was calculated analytically for different ratios of V_1/P. It was found that the value of V_1/P significantly affects the performance of the blending and concluded that the objective to design an efficient blender is to minimise the quantity V_1/P. It should be noted that the low value of V_1/P implies that there exists an overlap between the concentration distribution of successive passes and larger this overlap, the better the blending in the silo. This ratio is directly related to the flow patterns or velocity profiles which in turn is a function of the configuration of the bin and the flow properties of the bulk solids.

It should be noted that V_1/P for a given bin configuration can only be obtained by conducting experiments in a small scale model silo as there is no unique solution available for the velocity profiles in a hopper except in the case of a mass flow silo. The theoretical model of Johanson (1970) is limited only to the hopper and it is applicable for a hopper operating in discontinuous mode.

Roberts (1991) generalised the in-bin blending theory of Johanson (1970). As presented in Craig (1996), he used the concept of the impulse response of a linear system. He showed that when the silo is subjected to any arbitrary input signal *u (V)*, the output signal or the marker concentration *y (V)* at any time can be calculated using the convolution integral given by (2.12), as illustrated in Figure 2.5, by assuming the silo as a linear system.

$$\mathbf{y(V)} = \int_{\mathbf{0}}^{\mathbf{V}} \mathbf{u(V-\xi)h(V)\,dV} \qquad \textbf{(2.12)}$$

where ξ is a dummy variable, *h (V)* is the impulse response or weighing function or RTD function.

The generalised expression of the linear impulse response of markers *h (V)* in a hopper as assumed by Johanson (1970) can be given by (2.13) and (2.14).

$$\mathbf{h(V) = 0} \qquad \text{for} \quad 0 < V < V_1 \qquad \textbf{(2.13)}$$

$$\mathbf{h(V)} = \frac{\mathbf{2}}{\mathbf{V_p}}\left[\mathbf{1} - \frac{\mathbf{V}}{\mathbf{V_p}}\right] \quad \text{for} \quad V_1 < V < V_1 + V_p \qquad \textbf{(2.14)}$$

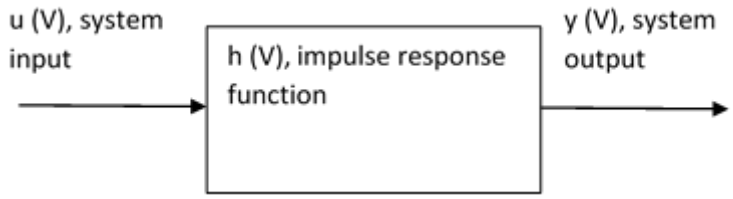

Figure 2.5 Linear system model of silo system (Roberts, 1991).

Carson and Royal (1992) employed experiments to determine the impulse response of a thin layer of marker particles placed on the top of the base material in a hopper. He developed an algorithm to calculate the marker concentration in the outflow for any number of passes using the data of, the variation of marker concentration during the first pass. Samples of equal volume were collected in the outflow of the hopper to measure the concentration of marker particles in each sample during the first pass. The percentage of marker concentration in each sample is plotted against the sample number as shown in Figure 2.6. It should be noted that the sample number in this plot represents the increasing time with the discharge. It can be seen in this figure that the marker concentration of 100 % at the inlet of the hopper, discharges in varying concentrations of 5 %, 30 %, 29 %, 21 %, 10 % and 5 % in each sample number of 4, 5, 6, 7, 8 and 9 respectively.

Carson and Royal (1992) computed the marker concentration in the subsequent passes using the response from the first pass described as follows: It is assumed that any X % of markers deposited at the inlet of hopper, discharges in a similar fashion to that of 100 % markers during the first pass and also in the same proportion and the same time sequence. For example, as shown in, the sample 4 with 5 % marker concentration during the first pass when placed again on the top, discharges again from the hopper starting from sample number 8 on time axis with following distribution: 0.25 % in sample 8, 1.5 % in sample 9, 1.45 % in sample 10, 1.05 % in sample 11, 0.5 % in sample 12 and 0.25 in sample 13. Similarly, the samples 5 to 9

during the first pass discharges in appropriate proportions. The final computational result of these calculations after two bin volumes recycled is shown in Figure 2.7. The overlap between the concentrations from different samples that are discharged at the same time are then summed up to get the total maker concentration. The overlap between the marker concentrations can be seen in the sample number starting from 8 as shown in Figure 2.7.

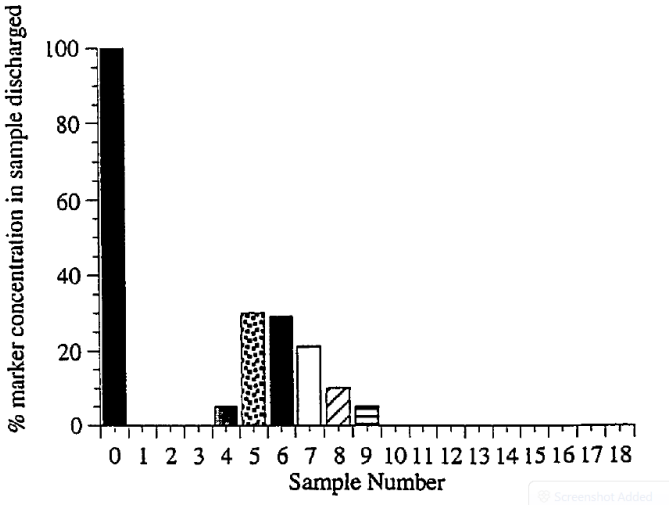

Figure 2.6 Test result of Carson and Royal (1992) showing the marker concentration during the first pass (taken from Craig (1996)).

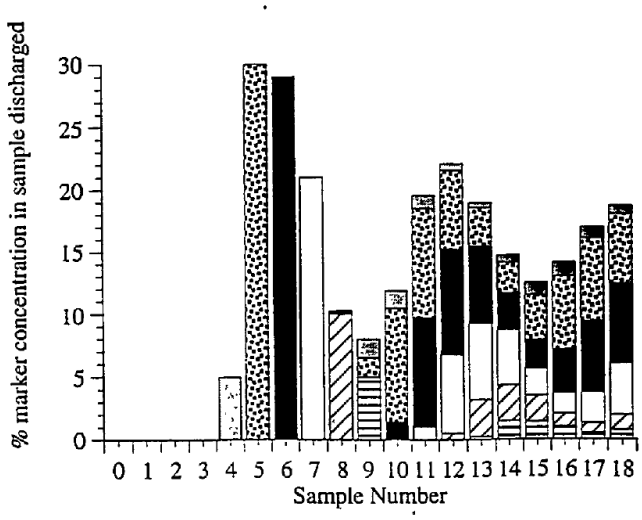

Figure 2.7 Computational result of Carson and Royal (1992) marker concentration after two bin volumes recycled (taken from Craig (1996)).

The marker concentration during the first pass that was obtained in the experiments of Carson and Royal (1992) is similar to the assumed triangular distribution by Johanson (1970) and Roberts (1991). However, the assumed triangular distribution is only limited to the hoppers and is not valid or gives erroneous results in the hopper with insert, whereas the experimental procedure shown by Carson and Royal (1992) can be obviously employed to the silo of various configurations.

Craig (1996) computed the blending performance in a mass flow hopper using only the bulk material properties. He used the analytical solution of radial velocity field by Jenike (1961) to compute the RTD response function and the blending performance using the procedure developed by Roberts (1991). Dau et al. (1994) developed an optoelectronic measuring system to measure the concentration of discharged tracer particles in the mixture. The tracer particles are introduced as a direct pulse when the blender is operating with the base material in a steady state mode. The concentration distribution is then measured at the outlet. The dimensionless RTD E(θ) is then calculated using (2.15).

$$\mathbf{E(\theta)} = \boldsymbol{\tau}\frac{\mathbf{C_{out}(t)}}{\int_0^\infty \mathbf{C_{out}(t)\,dt}} \tag{2.15}$$

$$\boldsymbol{\tau} = \frac{\mathbf{V_b}}{\mathbf{Q_b}} \tag{2.16}$$

where C_{out} is the measured concentration distribution at the outlet, τ is the mean residence time, V_b is the volume of the blender, Q_b is the volumetric flow rate through the blender.

The convolution integral given by (2.17) is then used to compute the outlet concentration in both continuous and discontinuous modes of operation.

$$\mathbf{C_{out}(\theta)} = \int_{\boldsymbol{\tau=0}}^{\boldsymbol{\tau=\theta}} \mathbf{C_{in}(\theta)E(\theta-\tau)d\tau} \tag{2.17}$$

Similar to the work of Craig (1996), Johanson (2006) presented a methodology to compute the RTD function using the material properties. He computed the RTD function from the analytical solution of velocity fields in a cone-in-cone blender. The blending performance is then evaluated using the linear system theory for different operation conditions such as different frequencies of input fluctuations and different wall frictions.

It was found that majority of the published studies rely on the experimental data to get the RTD function except for simple geometries like the mass flow in a hopper, mass flow in a Binsert or cone-in-cone blender in which analytical solution of Jenike theory has been used to predict the blending. However, if the flow in a hopper is not a mass flow, the theory is not applicable to calculate the velocity fields and therefore the blending performance cannot be predicted. Due to the lack of reliable constitutive models, industry purely rely on the experiments to quantify the blending and no attempt has been made to understand the blending from the flow patterns (such as size and shape of flow channel boundary, velocity distributions within the flow channel) developed around the internals (such as inserts and blending tube) in the silo.

Discrete Element Method (DEM) first developed by Cundall and Strack (1979) is increasingly used in recent years to investigate the behaviour of granular solids in industrial systems such as silos, mixers and milling. A growing interest in DEM is seen with the advent of high performance computing machines, as well as the ability of DEM to model phenomena at particle scale without phenomenal assumptions that exists in the constitutive models (Ooi and She, 1997; Ooi et al., 1996; Rotter et al., 1998; Vidyapati and Subramaniam, 2013). However, it is very much essential to quantitatively validate DEM model by solving a simple silo configuration such as flat bottom silo prior to its application in simulating industrial scale blenders (Ooi, 2013). In this thesis, Particle Image velocimetry (PIV) technique has been used to collect the validation data for the DEM model and also to understand the flow behaviour from the measured velocity profiles. In the following section, the theory of

PIV is presented followed by various studies investigating the flow in silo using this technique.

2.3 Particle image velocimetry and its application to silo flow

Particle Image Velocimetry (PIV) is a digital imaging technique commonly used to measure the velocity fields in a fluid flow and it has also been applied in granular flows (Lueptow et al., 2000; Medina et al., 1998). It uses the principle of digital image correlation to find the displacement of tracers in the flow. For the case of fluids, the flow has to be seeded with tracer particles that closely follow the fluid however for geo materials like sand the unique surface texture, different coloured grains and the voids between the grains can act as a tracer (White et al., 2003). Recognising these inherent features of geomaterials, a modified PIV approach was developed by White et al. (2003) to measure the strain fields. It was demonstrated in their work that the precision, accuracy and the resolution of the modified technique was an order of magnitude greater than the previous image based methods (Butterfield & Andrawes, 1973). They developed a MATLAB module by implementing PIV and named it "GeoPIV" as it is particularly developed to suit geotechnical applications. The theory, the sources of error, the advantages and disadvantages of measurements in Eulerian and Lagrangian frames of reference are described below.

2.3.1 Theory

The theory developed by White et al. (2003) is described here. A digital image can be expressed mathematically as a matrix of pixels with *m* rows and *n* columns, where *m* and *n* represent the number of pixels along the width and the height of the image, respectively. Each element of the matrix takes the value of brightness either in grayscale or RGB scale with 8-bit or 16-bit colour depth.

Let us first consider digital image 1 at time $t = t_1$ as shown in Figure 2.8 (a). Suppose divide this image into small squares and each square region is called as a patch. Let

us assume that each patch contains a unique distribution of pixel colour intensity in comparison to its surrounding patches. Now consider the second image at time $t = t_1+dt$ produced after the displacement of patches in image 1. Consequently, there can exist a correlation between the two images provided that the identity (distribution of brightness values) of each patch is fully or partly preserved during the deformation in a time interval *dt*. A search patch, greater than the size of the test patch, for each corresponding test patch, can be created in image 2 as shown in Figure 2.8 (b). The displacement vector of the test patch (shown in Figure 2.8 (c)) can be determined using a correlation algorithm that calculates the correlation coefficients between the colour intensities of test patch and the search patch. The typical results of the correlation algorithm are shown in Figure 2.9 (a) - (c). Figure 2.9 (a) shows the correlation coefficients in the domain of the search zone of size (s_u x s_v) pixels. Each value represents the correlation coefficient of the test patch at each location in the search patch and it can be clearly seen that there exists a peak correlation. The position of the peak correlation coefficient in the search patch gives the displaced position of the test patch. The displacement vector can then be calculated from the two position vectors of the test patch in images 1 and 2. The correlation coefficients are efficiently evaluated in the frequency domain by applying fast Fourier transform (FFT) to each patch (White et al., 2003).

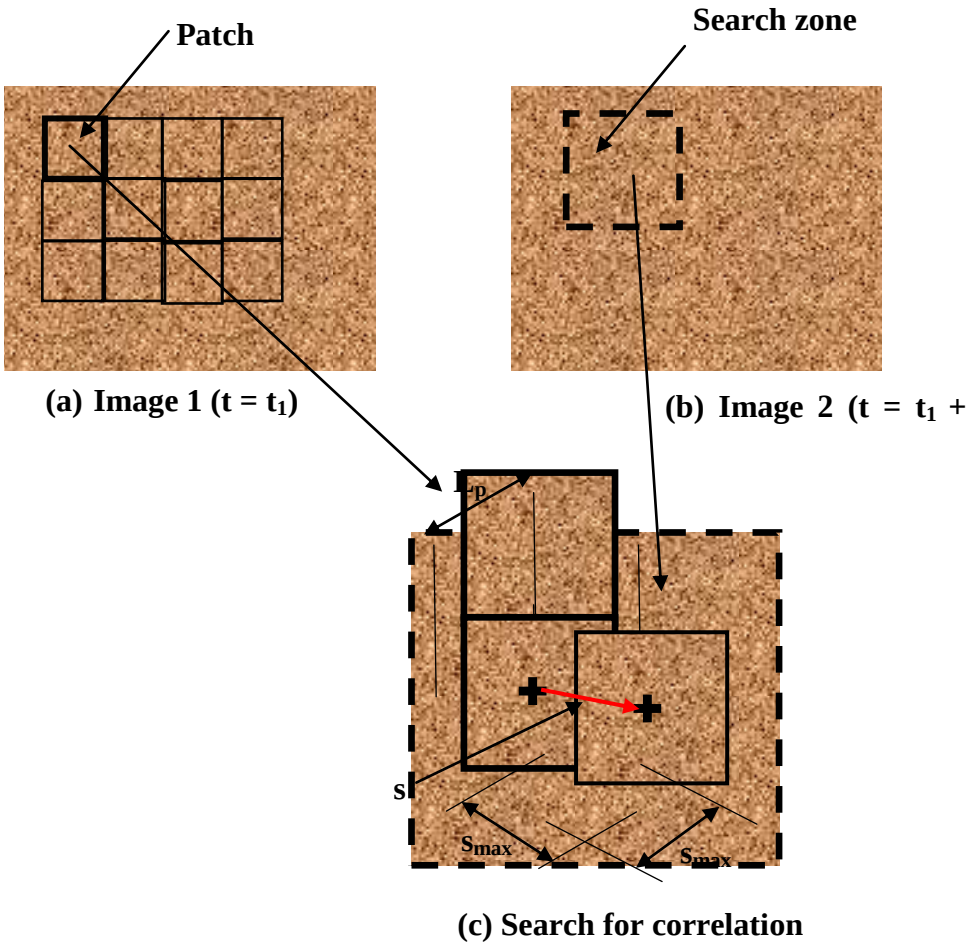

Figure 2.8 Principle of PIV analysis (adapted from White et al. (2003)**).**

The highest peak shown in Figure 2.9 (a) indicates the location of the correlation peak with a resolution of ± 1 pixel. A close-up view of this peak is shown in Figure 2.9 (b). To improve the resolution of the peak location, a bicubic polynomial is fitted in the region close to the peak in order to obtain a sub-pixel resolution. The correlation values around the peak after interpolation are shown in Figure 2.9 (c). The bicubic polynomial is evaluated at 1/200th pixel interval, i.e., giving a measurement resolution of 0.005 pixels.

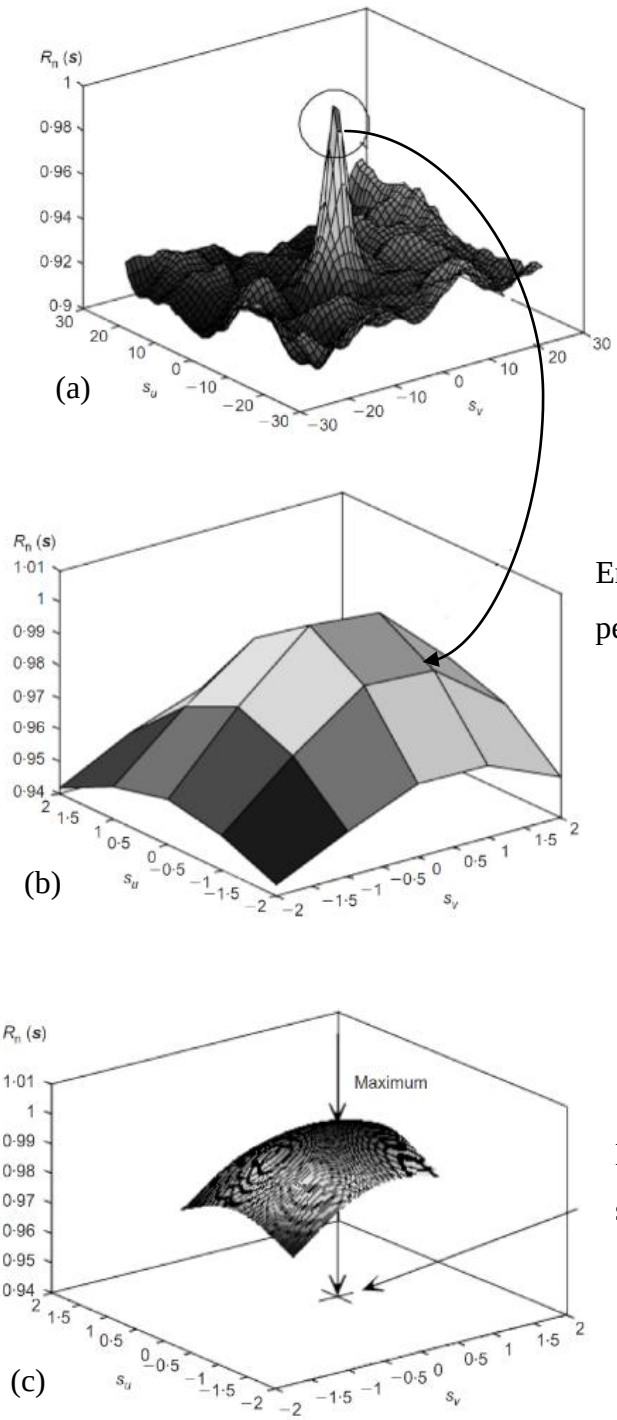

Figure 2.9 Evaluation of displacement vector from correlation plane R(s): (a) correlation function R_n (s); (b) highest correlation peak (integer pixel); (c) sub-pixel interpolation using cubic fit over ±1 pixel of integer correlation (taken from White et al. (2003)**).**

The procedure is repeated for the rest of the test patches in image 1 and also repeated for the subsequent image pairs. The flow chart of the analysis is shown in Figure 2.10.

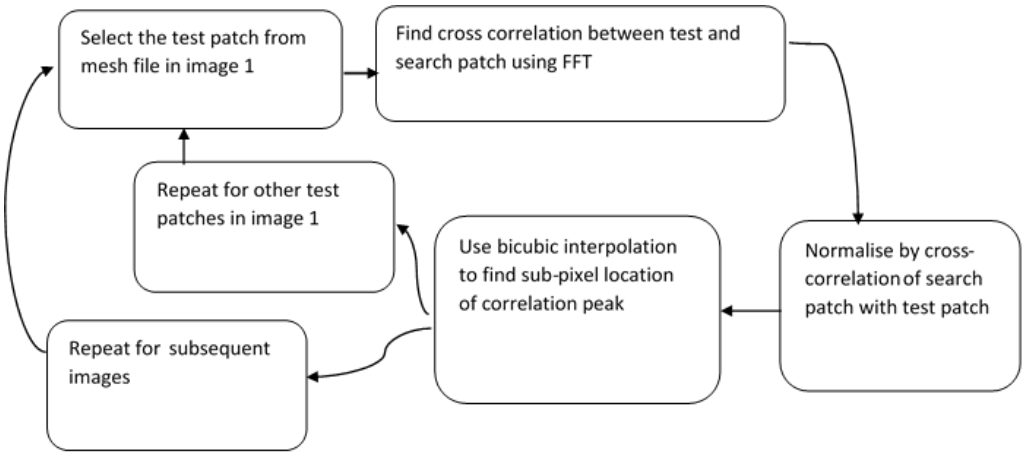

Figure 2.10 Flow chart of GeoPIV (taken from White et al. (2003)**).**

2.3.2 Deformation of patch and associated errors

The deformation of the patch is related to the changes in the spatial distribution and magnitude of colour intensities during a time interval *dt*. Haung et al. (1993) discussed the major sources of deformation of the patch and the associated errors that one needs to consider while applying the PIV technique to fluid flows. Although they discussed the sources of errors with reference to the measurements in fluid flows, they are equally applicable to granular flows. He highlighted that in reality the test patch rarely matches (that means a correlation coefficient of less than one) fully with the search patch due to the deformation of the patch. They have listed the following factors that cause the deformation of a patch:

- Noise: Noise is a random disturbance of local intensity in time and space which can occur due to slight changes in the light from one image to another or noise of the CCD sensor.

- Systems error: It is the error caused due to the misalignment of sequential video frames. These may be caused by vibration of the camera or the test set-up.
- Turbulent flow motions: The random motion of particles can cause the differences between the patches at *t* and *t+dt*.
- Out-of-pattern/plane motions: Due to the three-dimensional nature of the flow, the particles in the image plane may move out of the foreground or in the case of two-dimensional flow, a particle may move out of the search patch.
- Velocity gradients: If there exists a local gradient of velocity within the test patch, the shape of the patch can be considerably distorted if the time interval is large and it would lead to a low value of correlation coefficient.

The equations to estimate the errors due to out-of-pattern motions and velocity gradients are presented in Haung et al. (1993). All of these errors would lead to a cross-correlation coefficient (R) of less than one. The deformation rate (D) of the patch is defined as D =1 - R. A minimum correlation coefficient (R_o) was defined to set the limit on deformation of the patch (D_o = 1-R_o). A R_o value greater than 0.5 is recommended. If the deformation rate is greater than D_o, the velocity measurement is rejected.

2.3.3 Lagrangian and Eulerian description

In a Lagrangian frame of reference, the position of a particle is tracked through time. In GeoPIV, that means the position of a patch is tracked through a series of images from the start to the end. Calculations in a Lagrangian frame of reference using GeoPIV can lead to erroneous results (particularly for dense granular flows) mainly because of two reasons. Firstly, the individual particle tracking requires the patch size to be same as the particle size which in turn means the traced particle colour should be highly distinguishable from the neighbouring particles in order to get a good correlation or the particle should be in a very lean flow (e.g., dilute phase pneumatic conveying of particles). Secondly, the errors in the displacement measurement can accumulate over time mainly due to any random changes in the lighting. Another disadvantage of using the Lagrangian method is that only the information about the particle paths and velocities along these paths is obtained;

information such as temporal velocity distribution at any given location cannot be recovered.

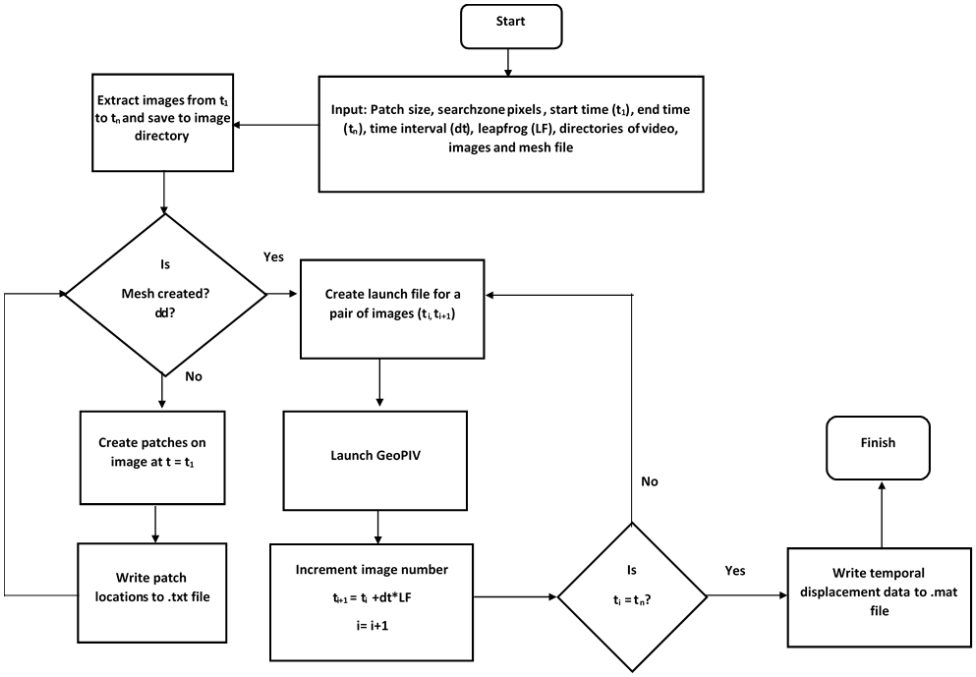

Figure 2.11 Flow chart developed to evaluate Eulerian displacement fields using GeoPIV.

In the Eulerian frame of reference, the focus is on the calculation of the displacement for every instant at a fixed location. In GeoPIV, that means the position of a patch remains the same in all the image pairs. For a continuous large deformation of material (e.g., the flow in a silo), the calculations in this frame can give reliable results provided that a small time interval is chosen. The Eulerian approach also produces displacement fields as a function of both position and time, thus giving a huge amount of information about the flow. Therefore, measurements in this frame of reference make it possible to fully study the unsteady flow phenomena. The GeoPIV software was originally developed to measure the displacements in the Lagrangian frame of reference and in this work without changing the original GeoPIV source code, additional functions have been developed in MatLab to calculate the displacements in the Eulerian frame of reference. The flow chart of analysis of displacement fields in this frame of reference in illustrated in Figure 2.11.

2.3.4 **Flow patterns in silo and application of PIV**

The review of flow of granular materials in silos can be found in (Nedderman et al., 1982; Tuzun et al., 1982). Jenike (1964) in his pioneering work coined the terms mass flow and funnel flow to categorise the flow patterns in a silo. In a mass flow, the material during the discharge is in motion at all the locations in the silo whereas in a funnel flow, the material near the side walls remain stationary during the discharge. The schematic of both these flow patterns is depicted in Figure 2.12.

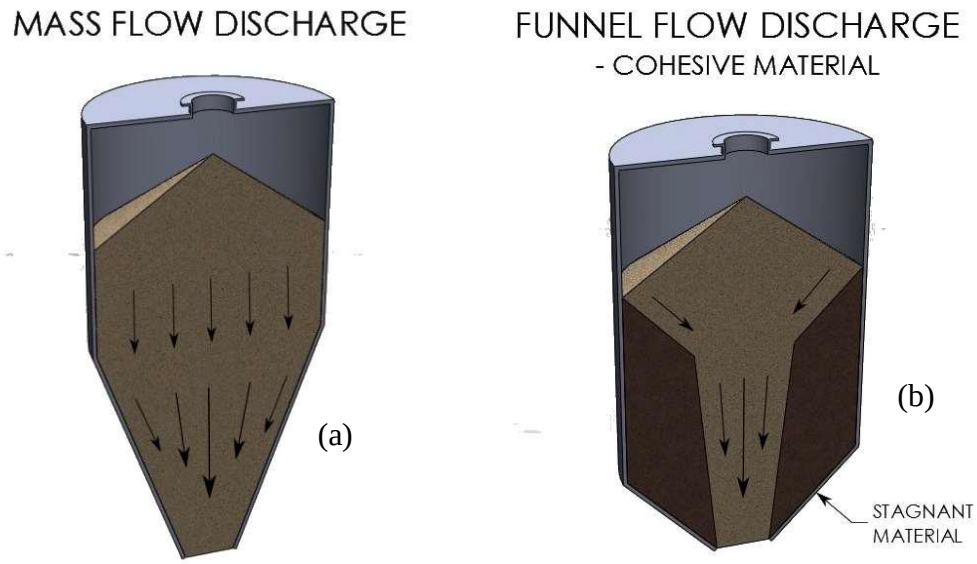

Figure 2.12 Flow patterns in the silo (a) Mass flow (b) funnel flow (Morrissey, 2013)**.**

Tuzun et al. (1982) reviewed the models to obtain velocity distributions of slow flow of granular material in hoppers. The plasticity and kinematic models to describe the flow patterns in a silo have been discussed. Jenike (1964) assumed the granular material as incompressible, rigid-plastic and considered that the stress is independent of strain rate. He then obtained the exact solution of stress and velocity fields for three specific set of variables including hopper half angle, hopper wall friction and

angle of internal friction. If the solution for any set of variables does not exist, the flow is considered as a funnel flow otherwise a mass flow. Based on this criteria, he developed a chart that defines the boundary between the mass flow and funnel flow in a plane strain silo and a symmetric silo for a given set of these three variables.

Nedderman and Tüzün (1979) developed a kinematic model to predict the velocity fields using only one empirical constant or a kinematic constant B. This model does not consider the stress distribution in the material but assumes the particle simply fall into the free spaces created by the particles beneath it by its own weight ignoring the stress gradients. As illustrated in Figure 2.13, consider two particles P and Q in the lower layer that moves with different vertical velocities (v) and as per the assumption, the horizontal velocity (u) of the particle R is a function of vertical velocity gradient given by (2.18).

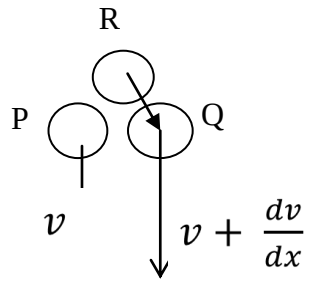

Figure 2.13 Illustration of the kinematic model (Nedderman and Tüzün,1979).

$$u = -B\,\frac{\partial v}{\partial x} \qquad \textbf{(2.18)}$$

where B is the kinematic constant.

Combining the (2.18) with continuity equation (2.19) gives the equation (2.10),

$$\frac{\partial v}{\partial y} = B\,\frac{\partial^2 v}{\partial x^2} \qquad \textbf{(2.19)}$$

The solution to the equation (2.19) is given by,

$$v = v_0 \exp\left(-\frac{x^2}{4By}\right) \quad v = v_0 \exp\left(-\frac{x^2}{4By}\right) \quad v = v_0 \exp\left(-\frac{x^2}{4By}\right) \quad v = v_0 \exp\left(\qquad \textbf{(2.20)}$$

where v_o is the centreline velocity, y is the vertical distance from the outlet of the silo and x is the horizontal coordinate.

Watson and Rotter (1996) generalised the kinematic model of Nedderman and Tüzün (1979) using finite element method in order to apply to it to a wide range of geometries, boundary conditions and material properties. They analysed the steady-state velocity fields during the discharge of cohesion less solids from a planar flat bottom silo. Zhang and Ooi (1998) have also used the kinematic model to predict the funnel flow in a silo during the batch discharge.

Numerous experimental investigations of flow patterns of granular material in planar silos have been reported in the literature (Babout et al., 2013a; Buick et al., 2004; Choi, Kudrolli and Bazant, 2005a; Michalowski, 1984; Ostendorf and Schwedes, 2005; Sielamowicz, Czech and Kowalewski, 2011a; Slominski, Niedostatkiewicz and Tejchman, 2007; Tüzun and Nedderman, 1982; Ulissi, Ippolito and Calvo, 2009; Watson and Rotter, 1996; Zhang and Ooi, 1998). Majority of these studies were aimed at measuring the flow characteristics behind the transparent front wall of the silo in order to either validate the mathematical models of the flow (Johanson, 1964; Tüzün and Nedderman, 1979; Zhang and Ooi, 1998) or to understand a physical phenomenon (Babout et al., 2013b; Choi, Kudrolli and Bazant, 2005a). In particular, the flat bottom silo configuration was widely used as it is possible to observe all the flow regimes (stagnant, quasi-static and fast flowing regimes) of a granular material (Zhang and Ooi, 1998). The flow patterns in a flat bottom silo depend on several factors including bulk friction, wall friction, size and shape of the material, method of filling and size of the outlet. The studies on the dependence of flow rate on properties of material and size of the orifice are well established in the literature (Beverloo, Leniger and Velde, 1961; Fowler and Glastonrury, 1959; Harmens, 1963;

Johanson, 1965). The empirical relationship developed by Beverloo (1961) is commonly used to calculate the flow rate through the orifice. Tüzun and Nedderman (1982) conducted an extensive parametric investigation in a flat bottom silo to understand the flow patterns of glass ballotini. They studied the influence of width of the silo, the size of the orifice, wall friction and particle size on the observed flow fields. More recently the effect of side wall friction and density of packing on size of the stagnant zone in funnel flow hopper were investigated using X-Ray tomography (Babout et al., 2013a).

PIV technique has been used by many researchers to measure the dynamic velocity fields of granular material during the discharge from a silo. The measured data has been used to quantify the flow characteristics (such as size and shape of the flow channel boundary, the velocity distributions and the diffusion characteristics) and also to validate mathematical models of the granular flow (Albaraki and Antony, 2014; Buick et al., 2004; Medina et al., 1998, 2000; Ostendorf and Schwedes, 2005; Sielamowicz, Blonski and Kowalewski, 2005; Sielamowicz, Czech and Kowalewski, 2010, 2011b, 2011a; Steingart and Evans, 2005; Ulissi, Ippolito and Calvo, 2009; Zhao et al., 2008). In this work, Particle Image Velocimetry (PIV) is deployed to measure the velocity fields in a flat bottom silo and in a silo with inserts of different configurations to understand the flow evolution and to characterise the steady state velocity fields.

2.4 Discrete element method and its application to silo flow

In this section the characteristics of a granular material, the governing equations of motion, calculation of tangential and normal overlap, and the contact force and torque models are described. The others aspects of DEM such as contact detection algorithm, time step and the calculation sequence, the equations for non-spherical particles can be found in several PhD theses (Chung, 2006; Hartl, 2008; Morrissey, 2013).

2.4.1 Granular materials

Granular material is an assembly of solid particles of different sizes and shapes which can resist shear stresses unlike fluids. It can take the shape of a heap at rest

and flow like a liquid when subjected to external forces. Granular material can be categorised into different groups based on the size range of individual particles as ultra-fine power (0.1 μm – 1.0 μm), super fine powder (1 μm – 10 μm), granular powder (10 μm – 100 μm), granular solids (100 μm – 3 mm) and broken solids (3 mm – 1.0 mm) and the corresponding individual constituents can be referred as ultrafine particle, superfine particle, granular particle, granule and grain respectively (Nedderman, 1992). They are also classified as wet granular materials and dry cohesionless granular materials. No general constitutive laws are available to date to describe the diverse behaviour of these materials. The difficulty arises due to the fundamental characteristics of granular materials such as negligible thermal fluctuations, highly dissipative interactions, and lack of separation between the microscopic grain scale and the macroscopic scale of the flow (Forterre and Pouliquen, 2008). In these scenarios particle based methods like Monte Carlo simulations, Molecular dynamics simulations and the discrete element method (DEM) seems to be viable alternatives. These methods give dynamic information about the trajectories of particles and the force between the particles which otherwise difficult to get through the physical experiments (Zhu et al., 2007).

2.4.2 Governing equations

The DEM is a particle-based method which solves the motion of each individual particle in a granular assembly. Two types of DEM approaches are commonly seen: soft particle and hard particle approaches (Zhu et al., 2007). The hard particle approach is an event-driven method mainly suited for the dilute granular system (Ketterhagen, Curtis and Wassgren, 2005). The soft particle approach developed by Cundall and Strack (1979) is a time-driven method which is applicable for dense granular systems. The soft-particle DEM approach was followed in this work as explained below.

A dense granular system is characterised by a long enduring frictional contacts between the particles. With the particle-particle interactions being dominant, the motion of each particle is governed by the contact forces between the particles. The calculation of contact force is thus one of the key aspects of DEM. In a soft particle DEM, the deformation of a contact pair is modelled by allowing the particles to

overlap by a small extent and the deformations are then used to calculate the contact forces. The calculations of DEM thus alternates between the application of Newton's second law and a force displacement law at the contact (Cundall and Strack, 1979). The main advantage of soft particle DEM lies in its ability to handle multiple contacts at a time. This is possible by choosing a very small time step during which the disturbance does not propagate farther than its immediate neighbours.

The translation and rotation of each particle in a cohesionless assembly is governed by the Newton's second law of motion as given by (2.21) and (2.22) respectively.

$$\mathbf{m_i}\frac{\mathbf{d\overrightarrow{v_i}}}{\mathbf{dt}} = \sum_{\mathbf{j}} \vec{\mathbf{F}}_{\mathbf{ij}}^{\mathbf{c}} + \vec{\mathbf{F}}_{\mathbf{i}}^{\mathbf{g}} + \vec{\mathbf{F}}_{\mathbf{i}}^{\mathbf{ext}} \qquad \textbf{(2.21)}$$

$$\mathbf{I_i}\frac{\mathbf{d\omega_i}}{\mathbf{dt}} = \sum_{\mathbf{j}}\left(\mathbf{T}_{\mathbf{ij}}^{\mathbf{f}} + \mathbf{T}_{\mathbf{ij}}^{\mathbf{r}}\right) \qquad \textbf{(2.22)}$$

where m_i and I_i are the mass and moment of inertia of particle i respectively, $\vec{F}_{ij}^{c}$ is the contact force between the particles i and j, $\vec{F}_{i}^{g}$ is the gravitational force, $\vec{\mathrm{F}}_{\mathrm{i}}^{\mathrm{ext}}$ is the external body force, T_{ij}^{f} is the frictional torque and T_{ij}^{r} is the rolling resistance torque.

The schematic of the forces acting on a particle are illustrated in Figure 2.14 (a). The various forces acting on the particle includes gravitational force, contact forces and other external forces that can exist in the presence of fluid (such as lift and drag forces). In the case of wet granular materials non-contact forces like cohesive forces can also exist. The torque acting on the particle can be resulted from two sources: frictional torque, the friction at the contact surface generates a torque and the rolling resisting torque.

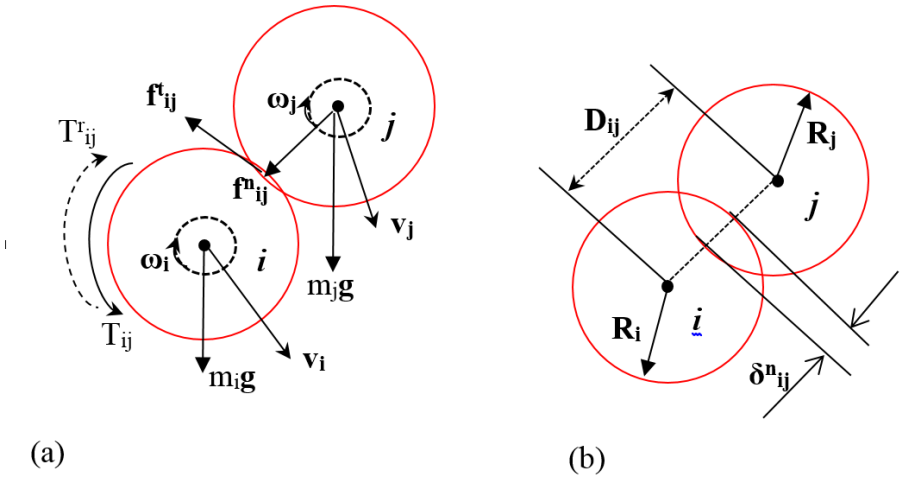

Figure 2.14 (a) Schematic of forces acting on a particle (Zhu et al., 2007) **(b) Representation of normal overlap.**

2.4.3 Normal and tangential overlap

Two particles *i* and *j* are said be in contact if $D_{ij} < (R_i + R_j)$, where D_{ij} is the distance between the particle centres and R_i, R_j are the radius of particles *i* and *j* respectively as shown in Figure 2.14 (b). The overlap creates due to the relative velocities of the particles in contact. It is decomposed into normal and tangential overlap given by (2.23) and (2.24) (Luding, 2008).

$$\boldsymbol{\delta_n = \int v_n \, dt} \tag{2.23}$$

$$\boldsymbol{\delta_t = \int v_t \, dt} \tag{2.24}$$

$$\boldsymbol{v_t = v_{ij} - n(n.v_{ij})} \tag{2.25}$$

$$\boldsymbol{v_{ij} = v_i - v_j + a_i' n \times \omega_i + a_j' n \times \omega_j} \tag{2.26}$$

where δ_n and δ_t are the normal and tangential overlaps respectively, v_n and v_t are the normal and tangential velocities at the contact, n is the unit normal vector at the contact and v_{ij}, ω_i and ω_j, v_i and v_j are the relative velocity vector, the angular velocity of particles, and the linear velocity of the particles i and j respectively, a' is the corrected or deformed radius given by $a' = R - \delta_n/2$, where R is the equivalent radius.

2.4.4 Contact force models

Most of the contact force models are developed based on the analogy of a spring deformation as shown in Figure 2.15.The total contact force is decomposed into total normal force (F_n) and total tangential force (F_t). The total normal force contains two parts: spring contact normal force (f^n) and normal damping force (f^n_d) as highlighted in Figure 2.15 and similarly for the total tangential force.

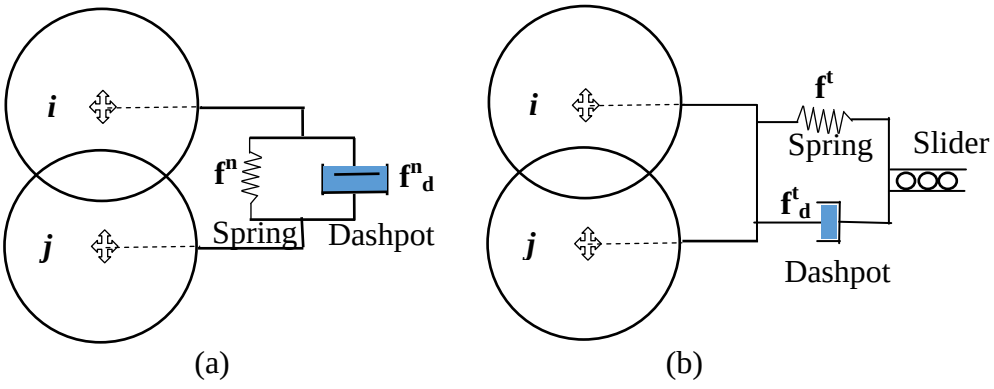

Figure 2.15 Spring and damper analogy of a contact deformation (a) Normal contact (b) Tangential contact.

The normal force models are categorised into continuous potential models, linear viscoelastic models, non-linear viscoelastic models and hysteresis models (Kruggel-Emden et al., 2007). Continuous potential models are based on the excluded volume effect and the dissipation of kinetic energy. More details on this model can be found in (Aoki and Akiyama, 1995; Langston et al., 1993). Viscoelastic models are

commonly used which are based on the principles of elasticity. The linear and non-linear viscoelastic models are discussed below.

2.4.4.1 Linear-force model with damping

Of all the models, the linear model is the simplest in which the spring behaves according to the Hooke's law *i.e.* the contact force is linearly proportional to the overlap. The equations for the total normal contact force and tangential force are given by (2.27) & (2.28).

$$\boldsymbol{F_n = \mathbf{k_n}\delta_n + \mathbf{c_n}v_n} \tag{2.27}$$

$$\mathbf{F_t = \min(k_t\delta_t + c_t v_t, \mu_s f^n)} \tag{2.28}$$

where k_n and k_t are the normal and tangential spring stiffness respectively, c_n and c_t are the normal and tangential damping coefficients respectively and μ_s is the sliding friction coefficient.

2.4.4.2 Non-linear force model with damping

Hertz (1882) developed a theory to describe the normal contact between the two spheres with a non-linear relationship between the normal force and normal displacement (Zhu et al., 2007). Simplified versions of force models are developed by several researchers based on the work of Hertz (Langston, 1995; Langston, Tüzün and Heyes, 1995; Zhou et al., 1999). The simplified normal force is given by 2.29.

$$\mathbf{f^n = \frac{4}{3} E^* \sqrt{R^*} \delta_n^{3/2}} \tag{2.29}$$

The normal damping force model proposed by Tsuji et al. (1992) is presented here. This model gives a constant coefficient of restitution and a collision time dependent on the initial velocity (Kruggel-Emden et al., 2007). The equation for the normal damping force is given by (2.30).

$$\mathbf{f_d^n = -2\sqrt{\frac{5}{6}}\beta\sqrt{k_n m^*}\,\overrightarrow{v_{rel}^n}} \quad \textbf{(2.30)}$$

$$\boldsymbol{\beta = \frac{\ln e}{\sqrt{\ln^2 e + \pi^2}}} \quad \textbf{(2.31)}$$

$$\mathbf{k_n = 2E^*\sqrt{R^*\delta_n}} \quad \textbf{(2.32)}$$

where E^* is the equivalent Young's modulus and R^* is equivalent radius, m* is the equivalent mass, k_n is the normal stiffness, e is the coefficient of restitution and v^n_{rel} is the relative normal velocity.

$$\mathbf{\frac{1}{E^*} = \frac{(1-\vartheta_i^2)}{E_i} + \frac{(1-\vartheta_j^2)}{E_j}} \quad \textbf{(2.33)}$$

$$\mathbf{\frac{1}{R^*} = \frac{1}{R_i} + \frac{1}{R_j}} \quad \textbf{(2.34)}$$

where E, v, R and m are the Young's modulus, the Poisson's ratio, the radius and mass of the particle i and j respectively.

Mindlin and Deresiewica (1953) developed a tangential force model that considers the whole loading history and instantaneous change of normal and tangential displacement. The equations of no-slip Hertz-Mindlin model are presented here. The contact tangential force is given by (2.35) and the corresponding damping force is given by (5.16). The full description of the model can be found in Di Renzo and Di Maio (2004). A detailed studies investigating the behaviour of different contact force models during elastic collisions have been conducted by Thornton et al. (2011). He demonstrated the limitations of non-linear integral equations of tangential contact force models.

$$\mathbf{f^t = -8G^*\sqrt{R^*\delta_n}\,\delta_t} \tag{2.35}$$

$$\mathbf{f_d^t = -2\sqrt{\frac{5}{6}}\beta\sqrt{k_t m^*}\,\overrightarrow{v_{rel}^t}} \tag{2.36}$$

$$\mathbf{k_t = 8G^*\sqrt{R^*\delta_n}} \tag{2.37}$$

$$\mathbf{\frac{1}{G^*} = \frac{(2-\vartheta_i)}{G_i} + \frac{(2-\vartheta_j)}{G_j}} \tag{2.38}$$

where G^* is the equivalent shear modulus, G_i and G_j are the shear modulus of particles i and j respectively, and v^t_{rel} is the relative tangential velocity.

In both linear and non-linear force models the total tangential force is limited by the Coulomb friction law. When the tangential force at the contact reaches its limiting frictional force, the particle is allowed to slide and there is no viscous dissipation of energy in tangential direction during sliding.

2.4.5 Torque models

The torque that acts on the particle arises mainly from two sources: first, the friction between the particles generates a frictional torque simply given by the product of tangential force and the radius of the particle and the second is the rolling resistance torque, which arises due to the asymmetric distribution of normal force in the contact area of non-spherical particles. The rotation due to the twisting of the particles can be negligible in case of planar silo flow mainly due to the lack of velocity gradients along perpendicular direction of the plane and hence the twisting resistance to the particles can be ignored.

There are various models available to account for the rolling friction torque as reviewed by Ai et al. (2011). A novel three dimensional model was developed by Jiang et al. (2015) that incorporates both rolling and twisting resistance. A simple contact independent directional constant torque model is used in this work (Sakaguchi and Ozaki, 1993; Zhou et al., 2002, 1999). The rolling friction torque applied on the particle is given by (5.19).

$$\boldsymbol{\tau_i = -\mu_r f_n R_i \vec{\omega}_i} \quad \textbf{(2.39)}$$

where μ_r is the coefficient of rolling friction, f_n is the contact normal force, R_i *is* the distance from the contact point to the centre of mass and $\vec{\omega}_i$ is the unit angular velocity.

2.4.6 **Application of DEM to silo flow**

2.4.6.1 Identification of input parameters

The most important elements in simulating an industrial particulate system using DEM are to model the shape of the real particles and to obtain the material parameters at particle scale. It is a common practice in industries to measure the bulk friction (both with wall and particle-particle) to design the industrial equipment such as silos. However, in DEM, particle scale friction values are required which are different from bulk scale/ continuum values. During the early studies of validation of DEM for silo flow (Negi, Lu and Jofriet, 1997; Yang, 2001), the particle scale properties were assumed to be the same as the corresponding continuum property of the bulk solids. However, recent studies showed that the particle scale material properties are different from the corresponding bulk values (Chung and Ooi, 2006; Härtl and Ooi, 2011; Ketterhagen et al., 2009a). Recently, two approaches are mainly followed by several researchers to obtain the input parameters of the DEM model. The first approach involves directly measuring the properties at particle scale (Balevičius et al., 2011; Mack et al., 2011). In addition to difficulties in measuring the particle scale properties, it is apparent that this approach works only if the shape and size of the particles are modelled exactly as the real particles. However, the majority of the particle shapes in industries are rather complex and modelling the complex particle shapes in DEM is still an active area of research (Höhner, Wirtz and Scherer, 2013; Liu et al., 2014; Williams et al., 2014).

The second approach known as calibration involves measuring the bulk properties of the granular material using standard element tests followed by the corresponding DEM simulations with different sets of input parameters, with the task to identify the parameters that gives the measured bulk properties (Coetzee and Els, 2009). This

approach has been proven to be successful because of its simplicity and also the fact that the bulk property data can be readily available or measured for most of the granular materials in industries. This approach also allows the complex particle shape to be simplified with basic shapes like spheres or combination of spheres (Favier et al., 2001).

2.4.6.2 Model validation

"Validation is the process of determining the degree to which a model is an accurate representation of the real world from the perspective of the intended use of the model" (Ooi, 2013). Thus, the validation process involves assessing the model accuracy by comparing a measured quantity (includes wall pressures, flow rate and velocity fields in case of a silo flow investigation) with the corresponding model prediction. Moreover, it is important to identify a relevant quantity for comparison with the experiment: for example, to assess the accuracy of DEM in predicting the mixing efficiency in silos, the accuracy of quantities that are directly related to mixing, such as velocity fields and colour concentration, need to be assessed; a mere comparison of wall pressure or flow rate is not sufficient.

The following highlight some of the validation studies of DEM models to simulate the flow in silos (Balevičius et al., 2011; Coetzee and Els, 2009; González-Montellano et al., 2011; Höhner, Wirtz and Scherer, 2013; Ketterhagen et al., 2009a; Liu et al., 2014; Mack et al., 2011; Negi, Lu and Jofriet, 1997).

Coetzee and Els (2009) presented the DEM modelling of discharge of corn grains in a flat bottom silo for two opening widths of 45 mm and 80 mm. The corn grains were approximated with a simple shape of two clumped spheres. The particle-particle friction and stiffness were calibrated from the simulations of direct shear and compression tests. The predicted flow patterns were compared qualitatively with the recorded images. The outflow rate with outlet widths of 45 mm and 80 mm was found to be over predicted by 31.4 % and 7.1 % respectively, however, the reasons for the discrepancy were not discussed in detail.

González-Montellano et al. (2011) developed a DEM model to predict the flow behaviour of glass beads and maize grains in a model silo. The shape of the maize

grains was approximated using multi-sphere particles with the value of particle-particle friction for glass beads adopted from Chung et al. (2004) and for maize grains from Coetzee and Els (2009). They found a reasonable agreement in discharge time for spherical glass beads whereas a calibration was required for maize grains which were non-spherical in shape. Their calibration of properties for maize grains involved varying the values of frictional properties until acceptable predictions were obtained. The accuracy of flow patterns was assessed qualitatively.

Liu et al. (2014) investigated the flow characteristics and discharge rate of ellipsoids in a flat bottom silo using DEM. The DEM model was validated by qualitatively comparing the flow patterns with the recorded images. The effect of particle shape was then studied by changing the aspect ratio of the ellipsoid.

Majority of the DEM validation studies of silo discharge were qualitative in nature while assessing the accuracy of flow patterns. More recently, Weiler et al. (2012) conducted DEM simulations of a Binsert blender to determine the RTD function of a tablet-shaped polyvinyl chloride (PVC) and polyethylene (PE) granules. They have quantitatively compared the predictions of RTD function against the experimental measurements. They have made several simplifications such as scaling down the size of the silo by a factor of 2, scaling up the radius of the particle by a factor of 2 and modelling the tablet shaped granules using spheres. With all these simplifications, surprisingly they have reported a good quantitative agreement. The proper justification about the choice of frictional parameters of the model has not been discussed. In this work, without making major simplifications to the particle size and the silo geometry, validation studies of DEM have been conducted after carefully choosing the friction parameters of the model.

2.4.6.3 Averaging of micro scale results of DEM

While DEM calculates the velocities at grain scale and stresses at contact scale, it is often useful to evaluate these quantities over a representative volume in order to produce the continuum fields. The derived continuum quantities are used to compare against the corresponding experimental measurements and also used to extract quantities of engineering relevance (Ooi, 2013). Several averaging techniques have

been developed to convert microscopic quantities to the macroscopic scale. A review of these techniques is presented in Zhu et al. (2007). The averaging techniques are classified into volume, time volume and weighted time volume averaging methods. The volume averaging technique was mainly developed for quasi static systems ignoring the inertia of the system. The time averaging method was found to be suitable for rapid granular flow. However it was highlighted in the review of Zhu et al. (2007) that continuum quantities obtained by volume and time volume methods may not satisfy the conversation equations of mass and momentum. A weighted time-volume averaging method was developed to overcome this problem (Babic, 1997; Zhu and Yu, 2002). In this method, the average value of a representative volume is calculated by applying a weighted function *h(r)* to all the particles in the volume as shown in Figure 2.16. For example, the average mass density and the velocity are calculated from (2.40) & (2.41) respectively. The equations for the weighing function and for the other variables such as angular velocity, stress and couple stress can be seen in (Goldhirsch, 2010; Labra et al., 2013; Weinhart et al., 2012; Zhu and Yu, 2002; Zhu et al., 2007). The weighing function can be defined using the Gaussian or Heaviside functions.

$$\boldsymbol{\rho = \int_{T1}^{T2} \sum_i h_i m_i ds} \qquad \textbf{(2.40)}$$

$$\boldsymbol{\vec{u} = \frac{1}{\rho} \int_{T1}^{T2} \sum_i h_i m_i \vec{v_i} ds} \qquad \textbf{(2.41)}$$

where ρ is the bulk density, $\vec{u}$ is the coarse grained velocity, m_i and $\vec{v_i}$ are the mass and velocity of the particle i in the averaging volume respectively, h_i is the value of the weighing function for particle i.

A post processing tool box (P4 software) has been developed at the University of Edinburgh to analyse particle scale DEM results within GiD visualisation software. The software is very robust in analysing the granular flows in complex industrial equipment such as silos, mixers, ball mills and fluidised beds (Labra et al., 2013).

This software has been used in this work for averaging velocities and stresses during discharge in silo flow.

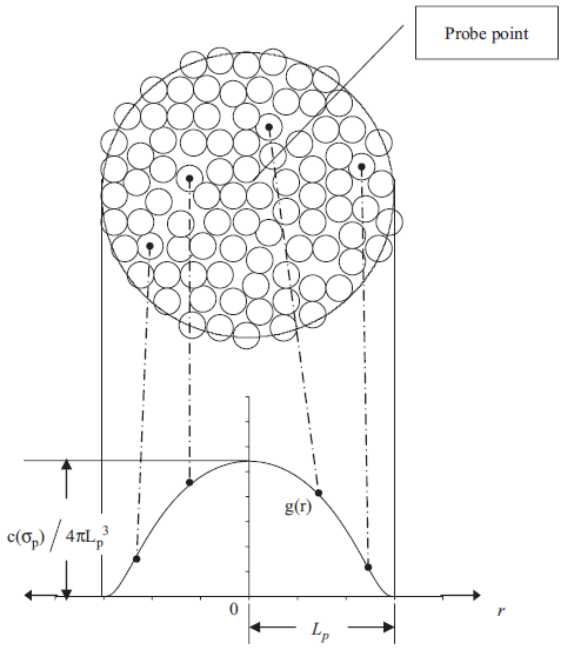

Figure 2.16 Concept of weighting for spatial averaging (taken from (Zhu et al., 2007) **).**

2.5 Summary

The literature concerning the prediction of in-bin blending has been discussed. While there exist analytical studies of blending in simple geometries like mass flow hopper and mass flow in a cone-in-cone blender, one has to rely on expensive and exhaustive experiments to analyse the blending in complex geometries due to the lack of reliable constitutive models that can fully describe the complex flow patterns developed in a silo.

Discrete element method (DEM) is increasingly used to simulate the complex granular flows in industrial systems and it has a great potential to study the flow patterns and blending in the silo. However, it is important to validate the DEM model before simulating any industrial system. It is found that much of the literature is

focussed on qualitative analysis while assessing the accuracy of the DEM model, studies that address the quantitative analysis of the accuracy of predicted flow patterns in a silo are not available. Particle image velocimetry technique (PIV) will be used to collect the required validation data of flow patterns in a planar silo and also to understand the flow characteristics of pellets from the measurement velocities.

Chapter 3

3. Flow measurement using Particle Image Velocimetry and application to silo flow

3.1 Introduction

The performance of GeoPIV was assessed by White et al. (2003) by conducting a simple experiment using a translation tray in which the sand is uniformly translated in the horizontal direction by 1 pixel using a micrometre (refer to the section 2.4 for the theory of PIV and algorithm for GeoPIV). The pair of images recorded before and after the translation was then used to measure the displacement. The mean value of displacement of several patches created over the area of the sand was reported to be 1.0017 pixels with a standard deviation of 0.01 pixel, which amounts to a small discrepancy. Whereas in the case of a silo flow, the deformations could be large in magnitude and also gradients can exist in both the horizontal and vertical directions, unlike in the case of a translation box. As it is known that the presence of velocity or deformation gradients is one of the major sources of error in the PIV technique (Haung et al., 1993), it is, therefore, important to assess its accuracy in the case of silo flow. The only challenge for this task is to obtain the images of flow in a silo with already known true values of velocities but thanks to DEM which can simulate and generate artificial images of flow of particles in a silo.

The objectives of the work presented in this chapter are to firstly assess the accuracy of the PIV technique using artificially- or computer- generated images from the DEM simulations of a flat bottom silo. The second objective is to apply this technique to measure and investigate the evolution of flow of granules during the discharge from a flat bottom silo for three different depths of the silo (gap between the front and back wall of the silo) of 20 mm, 40 mm and 100 mm.

3.2 Artificial images of flow in silo

The artificial images were generated from the DEM simulations of a steady state discharge of non-spherical particles from a 2D flat bottom silo. A steady-state flow of particles from the silo was achieved by maintaining a constant head level during the discharge. The height and width of the silo are 300 mm and 150 mm respectively and the depth of the silo is 3 mm. Since the sole purpose of this simulation is to generate the artificial images of the flow, the modelling details are not presented here. The DEM modelling of the silo discharge is discussed in greater detail in chapter 5.

The simulated flow patterns for the velocity measurement are illustrated in Figure 3.1 (a) - (f). Snapshots of the flow during the discharge are shown at time intervals of 0.1 sec. The steady state flow patterns were visualised by creating alternative horizontal layers of blue and yellow particles at a reference time (t = 0 s) as shown in Figure 3.1 (a). The marked layers deform as the discharge progresses. It can be seen that close to the outlet, the particles at the centre flow faster than the particles close to the side walls whereas far from the outlet the particles move at the same velocity. In the other words, the flow close to the outlet is characterised by strong velocity gradients and there exist negligible gradients far from the outlet. It is of interest in this study to assess the accuracy of measurement of velocity distribution (both horizontal and vertical) close to the outlet and also far from the outlet of the silo.

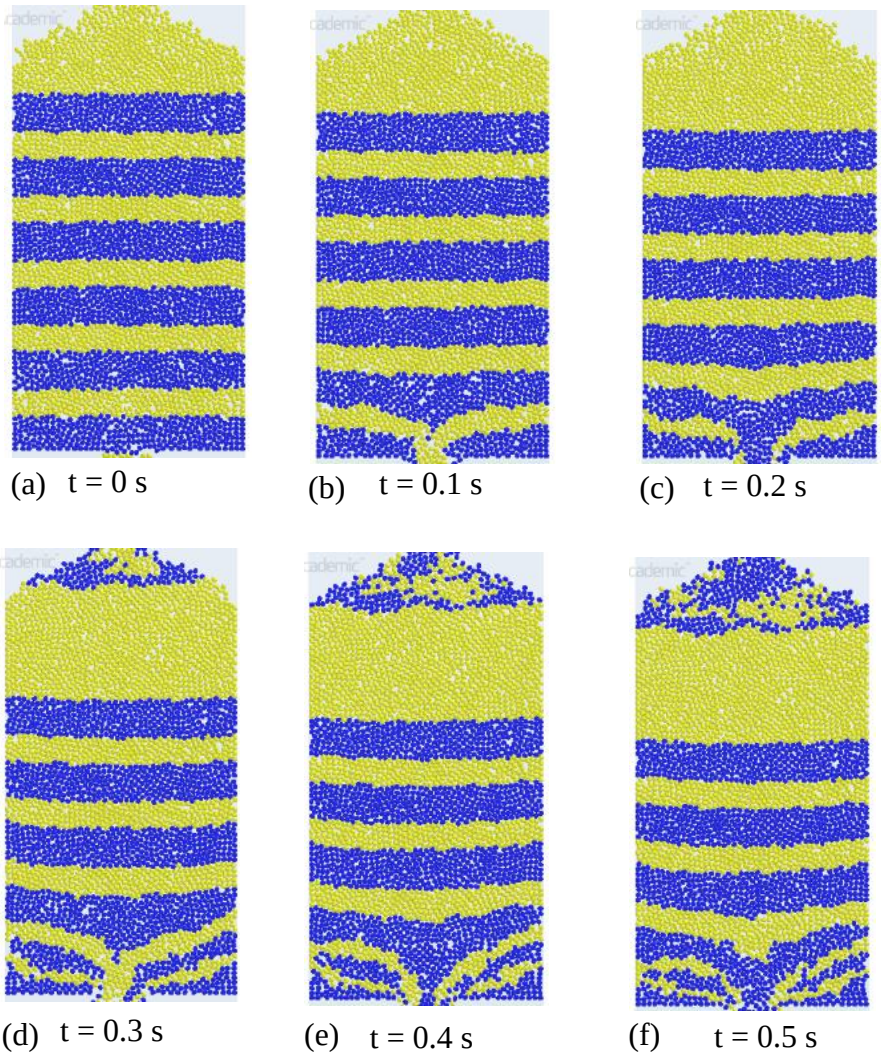

Figure 3.1 Deformation of coloured layers at different instants during silo discharge depicting the flow patterns.

3.3 PIV analysis procedure

The PIV analysis mainly consists of four main steps:

i. Determination of input parameters: Estimating the input parameters such as patch size, maximum displacement and time interval between the images,

ii. Generation of patches: Generating patch locations on the image at t = 0 sec,

iii. Measurement of displacement of each patch: Measuring the displacement fields in pixel coordinates from the series of images from $t = t_o$ to $t = t_n$ using GeoPIV,

iv. Post-processing the displacement fields: Converting the displacement fields in pixels to velocity fields in mm/s, removing the data outliers (if any) and calculating the relevant quantities of the flow such as flow rate, shape and size of flow channel boundary. A post-processing tool has been developed in MATLAB for this purpose.

A total of 100 images were extracted using the post-processing tool supplied with the EDEM 2.7 software. The colour of all the particles was set to be yellow and the voids between the particles are of a grey colour. It is also possible to set a colour distribution within the particle and between the particles but one single colour for all the particles was specified so that a bimodal colour distribution (between particles and voids) could be achieved. The unique bimodal distribution of colour intensity of both particle and voids serves as a tracer.

The patches shown in Figure 3.2 are created to extract the local average horizontal and vertical velocities from DEM and the same patches are used to measure the velocities using PIV. It should be noted that the velocities measured in PIV are pixel based while in DEM they are based on the individual particle velocity. In the other words, in PIV the average velocities of all the pixels in a given patch are considered while the average velocities of all the particle centres are calculated in DEM. A patch size of 10 mm x 10 mm was created, both in PIV and DEM. For patch generation in PIV, MATLAB program was developed to create the patch coordinates from the input of four corner coordinates and the interval size in horizontal and vertical directions.

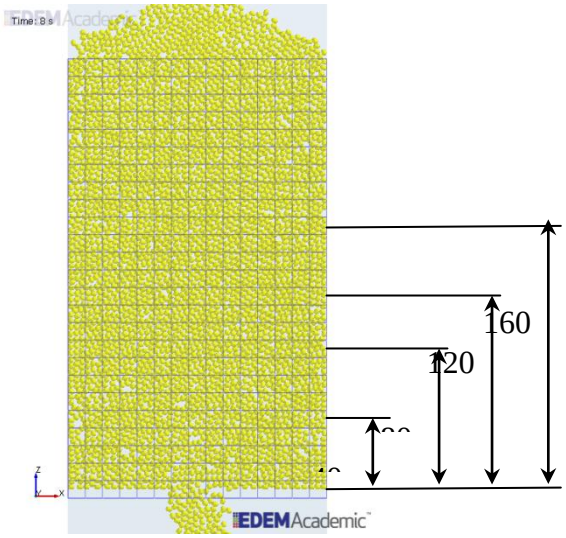

Figure 3.2 Binning to get local average velocity with DEM and PIV.

The minimum time interval between the pair of images for the PIV analysis can be estimated from the maximum particle velocity in the system and the limiting displacement of the patch. In the case of a silo discharge, the maximum particle velocity in the silo, which usually occurs near the outlet, can be estimated from volumetric flow rate using the experimental data or an empirical correlation. The limiting displacement is the displacement of a patch between a pair of images which is large enough so that the identity of the patch is preserved without any deformation. For example, if the time interval is high, the displacement can also be high so that it can deform due to the gradient of velocities within the patch. A rough estimate of limiting displacement in a given time interval was obtained by visual inspection of local displacement in a pair of images using image processing software such as ImageJ. A time interval of 0.005 s between the consecutive images was used in this study.

The measurements of temporal variation of vertical velocity at different heights along the centreline of the silo, the time-averaged local horizontal and vertical velocity distributions at these heights were compared with the corresponding velocities extracted from the DEM.

3.4 Accuracy of PIV measurements

For a given patch size, the output of a PIV measurement depends on the factors such as image resolution, the accuracy of the scale factor, time interval between the image pair and the external factors including the changes in lighting, alignment of camera with respect to the silo, and vibration of the camera and the test set-up. As the images for this study were artificially generated, the influence of external factors was nullified. A time interval of 0.005 sec was found to be sufficient to estimate the displacement.

Images were exported at various spatial resolutions of 250 x 350, 500 x 700, 1000 x 1400 and 2000 x 2800 to study its effect on the measurement. The images at different resolutions are shown in Figure 3.3 (a) – (d). As it can be seen from these images, the resolution of the voids increases with an increase of the image resolution. The scale factor (M) of these images was calculated from the known horizontal distance between the side walls of the silo and the corresponding number of pixels between them with an accuracy of ± 2 pixels using the ImageJ software. The value of M was found to be 1.13 ± 0.013, 2.27 ± 0.013, 4.54 ± 0.013 and 9.1 ± 0.013 pixels/mm for the image resolutions of 250 x 350, 500 x 700, 1000 x 1400 and 2000 x 2800 respectively.

After converting the displacements from image space to object space system using the scale factor, the velocity at each point was then calculated from the displacement and the time interval between the two consecutive images. The temporal velocity data of each patch was scanned for data outliers using the Hampel filter (Fore et al., 2005; Pearson, 2005).

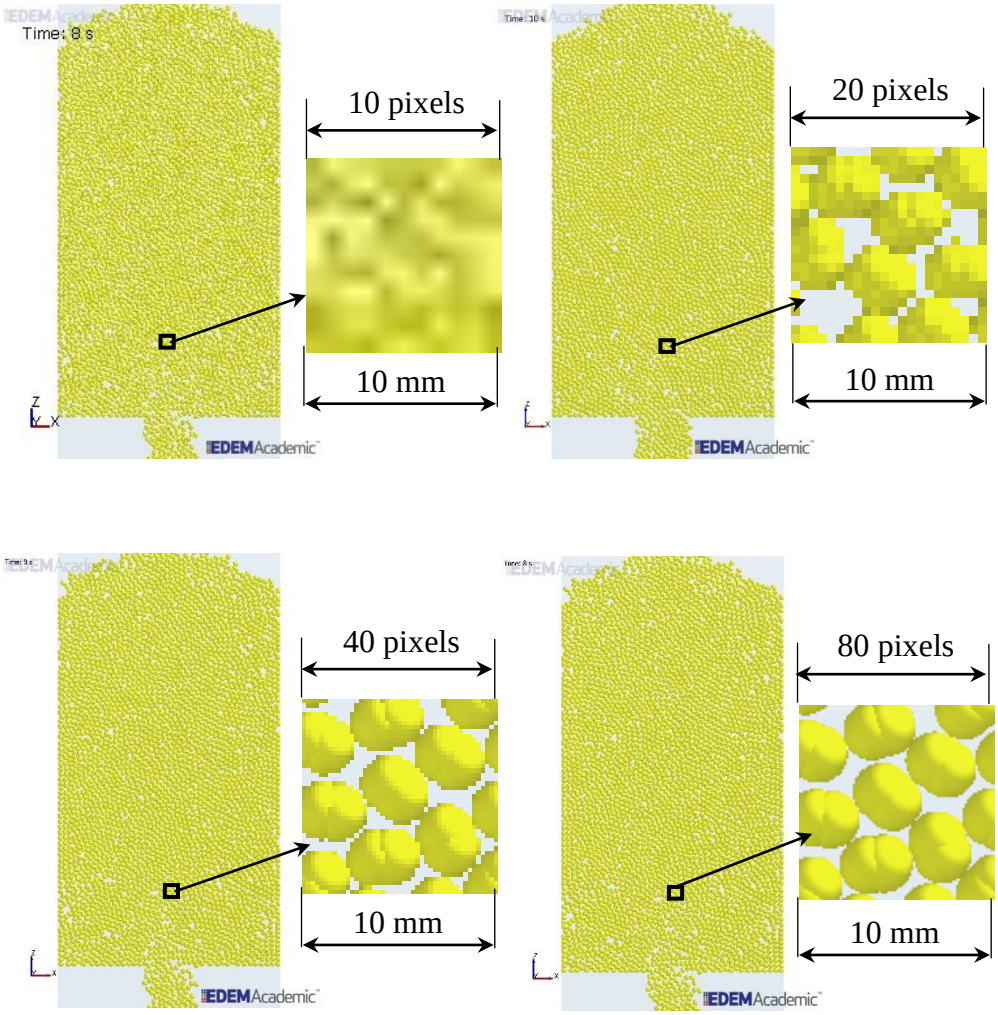

Figure 3.3 Images of silo and zoomed view of patches at different image resolutions (a) 250 x 350 (b) 500 x 700 (c) 1000 x 1400 (d) 2000 x 2800.

3.5 Comparison of centreline velocity

Figure 3.4 shows the comparison of measured centreline vertical velocities with the corresponding DEM values at a distance of Z = 160 mm above the outlet for four image resolutions of 250 x 350, 500 x 700, 1000 x 1400, 2000 x 2800. As expected it can be seen that with an image resolution of 250 x 500, the local velocity measurements of the patch bear no correlation with the corresponding DEM values mainly because of lack of sufficient pixel intensity in the patch: the size of each pixel is greater than the size of the void between the particles. As the resolution is further

increased to 500 x 700, the PIV measurements correlate with the DEM values as shown in Figure 3.4 (b). It can also be seen from this figure that the measured velocities are smaller and the majority of them lie around the mean of the corresponding DEM values. At this resolution, the errors in the mean and the standard deviation of measured and calculated values over a period of 1 sec were found to be -5.08 % and -16.8 % respectively. As shown in Figure 3.4 (c), with a further increase in image resolution to 1000 x 1400, the error in the mean velocity was reduced from -5.08 % to -0.37 % and while the error in the standard deviation was reduced from -16.8% to -5%. No further noticeable reduction in discrepancy was found with the increase in image resolution to 2000 x 2800. Figure 3.5 shows the comparison of measurements of vertical velocity at three other heights along the centreline of the silo for an image resolution of 1000 x 1400. The discrepancy in mean velocities at Z = 40 mm and Z = 160 mm were found to be 2.9 % and 0.37% respectively. Except close to the outlet, it is evident that the measurements of the velocity fluctuations even with a moderate image resolution of 1000 x 1400 are of good accuracy. The correlation between the time series of measured velocity data can also be better estimated using standard mathematical correlation functions.

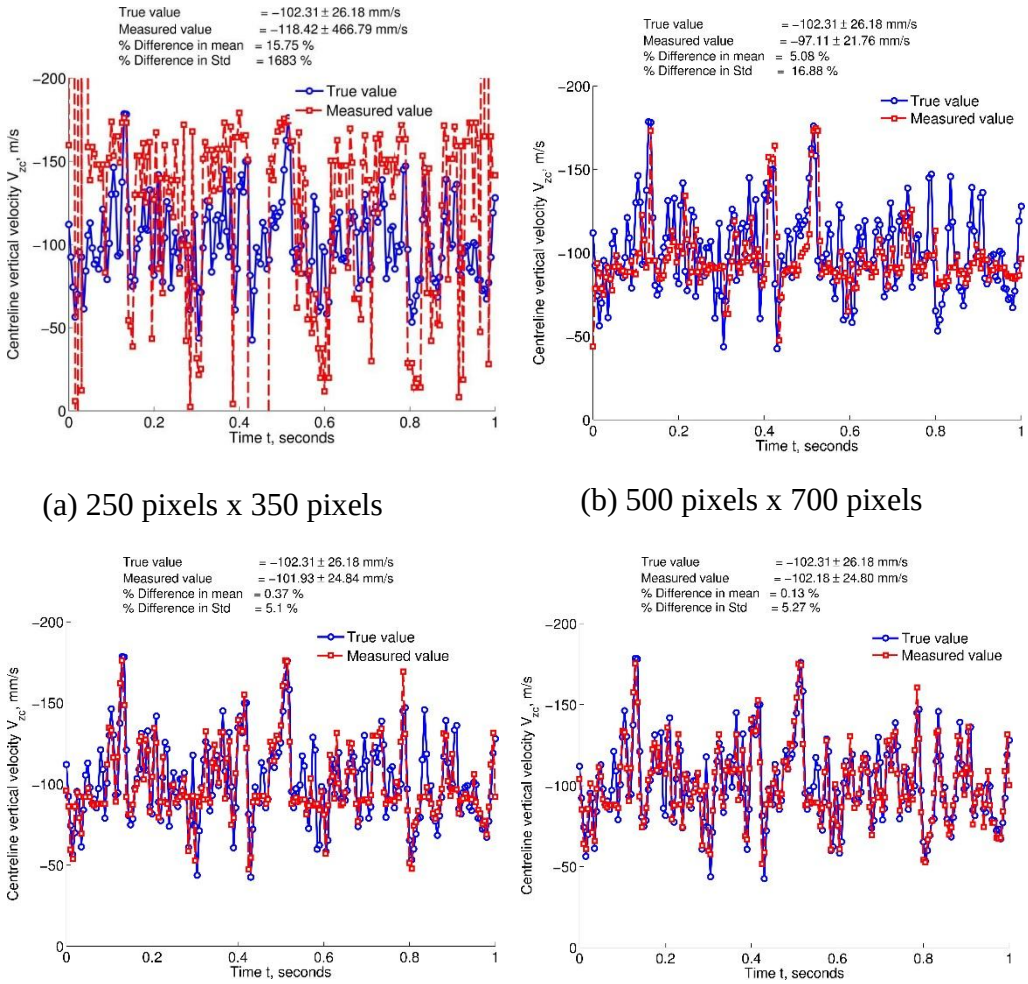

Figure 3.4 Comparison of temporal variation of centreline vertical velocities measured by PIV against the locally averaged DEM velocities (Patch size = 40 and Z = 160 mm).

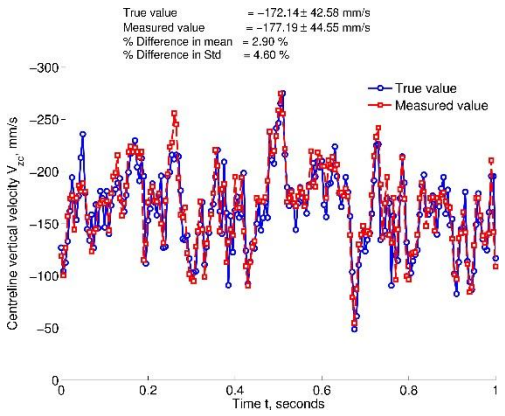

(a) Z = 40 mm

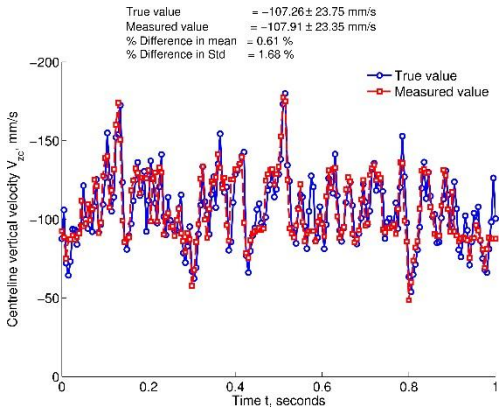

(b) Z = 80 mm

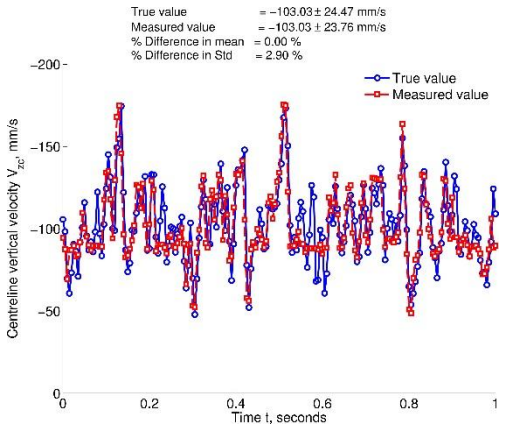

(c) Z = 120 mm

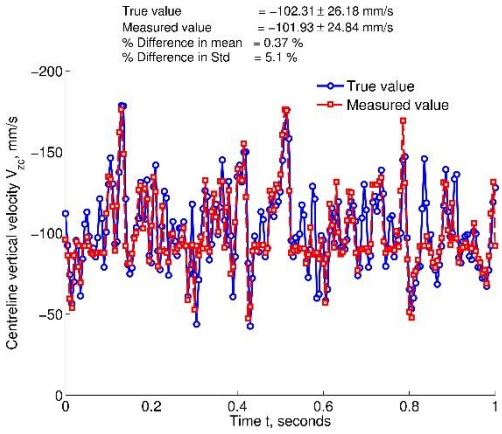

(c) Z = 160 mm

Figure 3.5 Comparison of temporal variation of centreline vertical velocities measured by PIV against the locally averaged DEM velocities (Patch size = 40 and resolution=1000x1400).

3.5.1 Velocity profiles at different heights

The flow in a silo is often characterised by the velocity profiles across the width at different heights. It is, therefore, important to check the accuracy of the measurements of vertical and horizontal velocity distributions. The instantaneous velocities for each patch are averaged over a duration of 1 sec and these time-averaged vertical velocity profiles at various distances above the outlet (Z = 40 mm,

80 mm, 120 mm and 160 mm) are compared against the corresponding actual or true DEM values, as shown in Figure 3.6. As shown earlier, the velocity measurements for an image resolution of 250 x 350 are completely random and have no correlation with DEM values (as can be seen in Figure 3.4 (a)) and, therefore, their data is not shown here. At all heights, a discrepancy in cross-sectional mean velocity of 4 – 5 % was found with an image resolution of 500 x 700 and it was found to reduce drastically to 0.1 - 0.3 % with an increase of resolution to 1000 x 1400. Furthermore, it can also be seen that no improvement was found with the increase in resolution to 2000 x 2800. A similar trend can also be seen in the measurement of horizontal velocities at various heights as shown in Figure 3.7.

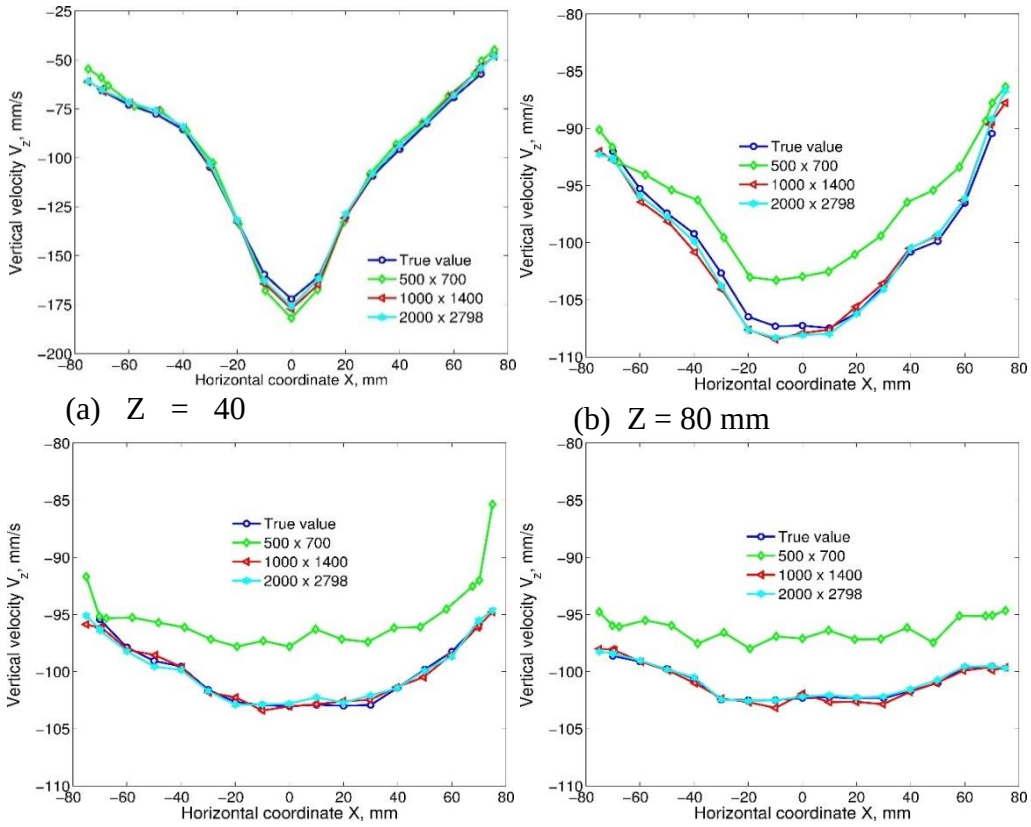

(a) Z = 40 (b) Z = 80 mm

(c) Z = 120 (d) Z = 160

Figure 3.6 Comparison of time-averaged vertical velocity profiles measured by PIV against the DEM local averaged velocity at different heights (Patch size = 40 and resolution= 1000x1400).

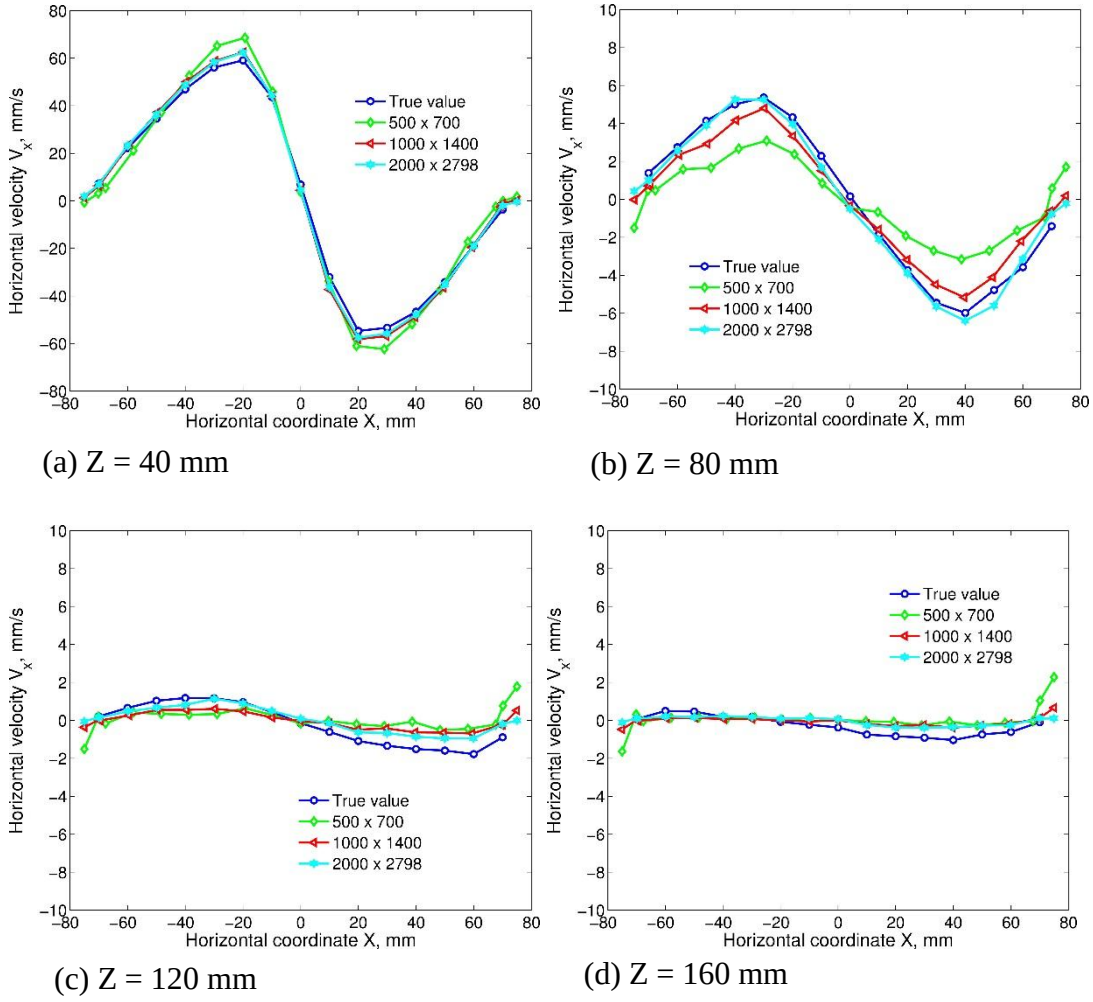

(a) Z = 40 mm (b) Z = 80 mm

(c) Z = 120 mm (d) Z = 160 mm

Figure 3.7 Comparison of time-averaged horizontal velocity profiles measured by against the DEM local averaged velocity for the different resolution of images.

3.5.2 Concluding remarks about the accuracy

It should be noted that the PIV works on the basic principle of autocorrelation between the pixel colour intensities of a test patch (at $t = t_1$) and a search patch (at $t = t_1+dt$) and if the test patch contains a unique pattern/distribution of colour intensities compared to its neighbouring pixels, a distinct peak in correlation value can be detected in the search patch. Conversely, if the test patch contains only fewer pixels and with intensity values more identical to that of neighbouring pixels, a

distinct correlation peak cannot be located leading to an inaccurate measurement. Therefore, a unique colour intensity pattern or distribution is highly desirable and it can be achieved by any of the following methods:

i. The presence of natural colour texture in the test material, e.g., fine grains of sand.

ii. Random mixing of two or three differently coloured particles with the same flow properties.

iii. The voids (between the particles) can be of a different colour from that of particles thereby naturally leading to a combination of voids and particles that produce a unique distribution of colour intensity.

In the assessment study conducted here, all the particles are of the same colour and, therefore, the pixel representation of voids between the particles becomes highly important. As the size of the voids between the particles is usually smaller relative to the size of particles particularly in dense flows like silo flow, a sufficient image resolution is required to properly represent the void in order to make an accurate measurement.

Having assessed the accuracy of PIV for silo flow (as discussed in sections 3.2 and 3.4), the developed PIV tool was used to investigate the evolution of flow of granules in a flat bottom silo. The accuracy of PIV has been assessed for an idealised scenario in which the errors due to the external sources such as changes in lighting and vibration of the experimental are eliminated. In the real case scenarios, the errors due to these sources needs to be estimated and care must be taken to avoid these errors during experimentation.

In the following sections, the brief details of the silo experimental set-up and the test procedure are presented followed by the measurement procedure of velocity fields during the discharge from the flat bottom configuration of the test silo. Finally, the evolution of flow patterns is described from the measured velocity fields and the dependency of the depth of the silo on the flow patterns is discussed.

3.6 Test set-up with flat bottom silo configuration

The description of the silo test facility is given in Appendix A. Here only the summary of the appendix is given: A planar rectangular silo of 2.5 m height and 0.45 m wide has been built by Zeppelin Systems GmbH, Germany. The set-up has been designed to quantitatively measure the flow patterns of granules using Particle Image Velocimetry (PIV). The design features and the components of the model silo have been discussed. The width (range: 100 mm to 450 mm), outlet size (range: 0 to 450 mm), hopper angle (range: 0 to 90^{o}) can be changed to any desired value within the limits. The silo can also be configured to three different depths of 20 mm, 40 mm and 100 mm.

The schematic view of the test silo with a flat bottom configuration is shown in Figure 3.8 (a). The width of the silo (W) and filling height level (H) were set to 450 mm and 1125 mm respectively which gives an aspect ratio (H/W) of 2.5. The size of the outlet was set to 40 mm. Each experiment involves digitally recording the flow behind the transparent front wall using a high-speed camera, measuring the mass flow rate and also the bulk density at the end of filling. The silo was filled with pellets using a pneumatic conveying system. The filling pipe was placed in the centre of the silo from which the pellets discharge in the form of a jet with a conical shape. Once the fill level reached the desired height, the discharge of pellets was then allowed by manually opening the thin plate attached to the outlet.

The front surface of the silo was illuminated with an incandescent light source. To ensure the formation of dark voids between the pellets, the light was projected parallel to the front wall. A Photron FASTCAM SA6 camera was used to record the flow. The camera was mounted on a stand with its axis perpendicular to the central axis of the silo. Images were recorded at a frame rate of 60 fps with a resolution of 1940 pixels x 1440 pixels. The maximum possible recording time at this frame rate was 32 sec which is also approximately equal to the total discharge time from the silo. The maximum recording time depends on the selected frame rate: the higher the frame rate, the lower the recording time. For example, if the frame rate were increased from 60 fps to 600 fps, the maximum recording time would be reduced from 32 sec to 3.2 sec.

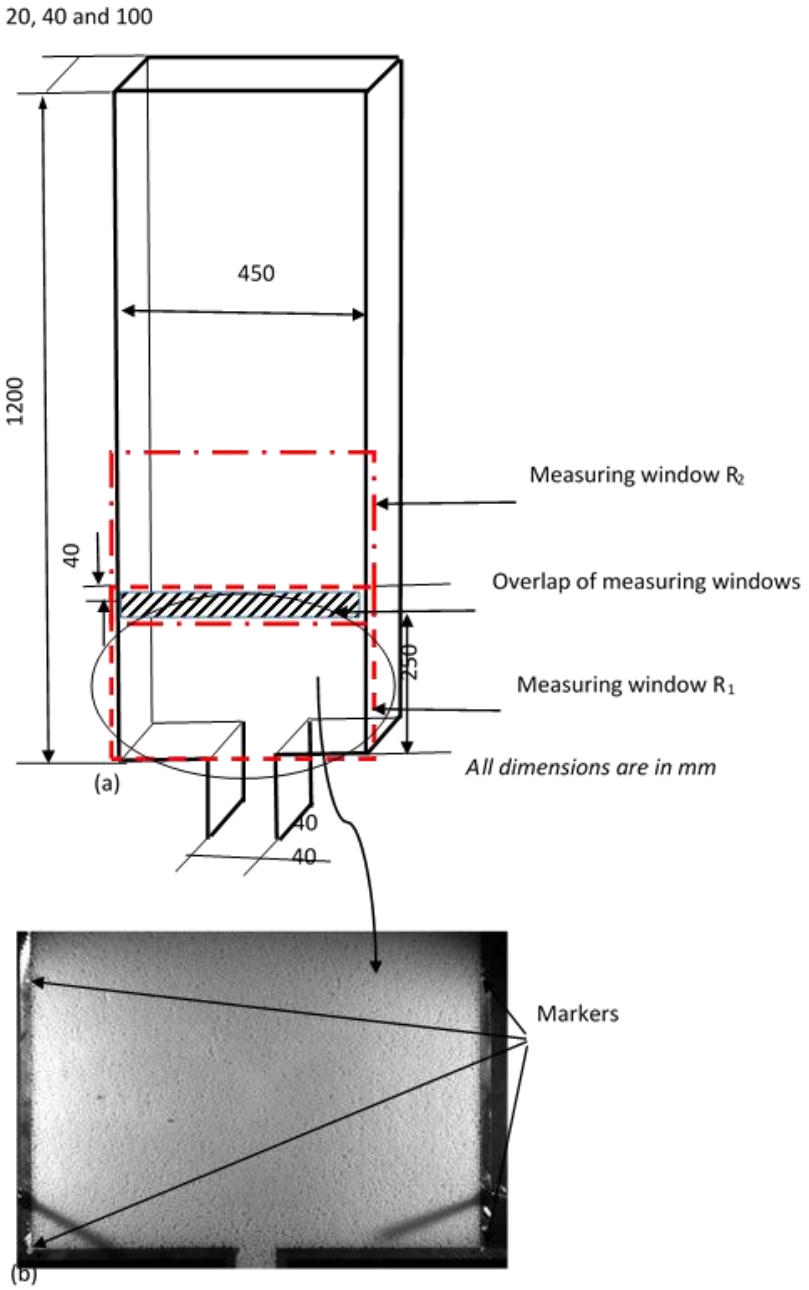

Figure 3.8 (a) Schematic of dimensions of the test silo indicating measuring windows (b) Snapshot of recorded image indicating the markers.

3.7 **Properties of the test pellets**

The selection of bulk solid for the experiments is a critical task and it should be selected by considering the various aspects of the flow measurement, DEM modelling and its use in industry. Considering all the aspects, the following requirements were defined:

- It should be a freely flowing bulk solid;
- It should have minimal wall friction at the front and back walls for less retardation of flow at the boundaries;
- The mean size of the granules should be computationally manageable without scaling up;
- The surface of solid should be opaque to avoid reflection of light with the illumination of the front wall.

High-density polyethylene (HDPE) of yellow colour pellets found to satisfy these requirements and is also widely produced polymer in industries. The size, shape and flow characteristics of the pellets were measured using the facilities at Zeppelin technology centre. The size and shape characteristics of the pellets were measured using the particle size analyser CAMSIZER®. The pellets were of cylindrical shape with rounded edges. The picture of the pellets is shown in Figure 3.9. The equivalent diameter and sphericity were found to be 3.8 mm and 0.85 respectively. The uniformity coefficient was found to be 1.34. It is not possible to get the axial dimensions (diameter and height) of the pellets using CAMSIZER®, hence, a Vernier callipers was used for this purpose. The measurements of 50 random pellets were taken with an accuracy of ±0.01 mm. The diameter and height of the pellets were found to be 3.96 ± 0.13 mm and 3.12 ± 0.28 mm.

The solids density provided by the supplier is in the range of 940-970 kg/m^3. The effective angle of internal friction and wall friction were measured using the direct shear tester. The angle of the internal friction is 30 ± 1 deg. The wall friction of the pellets with aluminium wall and with perspex wall was found to be 9.5 ± 1 deg and 11 ± 1 deg respectively.

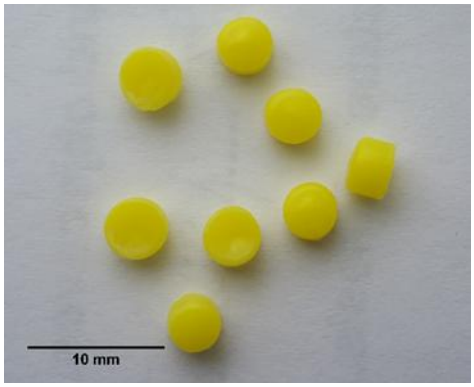

Figure 3.9 HDPE pellets.

3.8 Flow measurement using PIV

The various aspects of the PIV measurement such as the selection of the optimum size of the measuring window, generation of patches, determination of scale factor, the precision of the measurement, effect of the patch size and the repeatability of the measurements are discussed in this section.

3.8.1 Size of the measuring window

The spatial extent (width and height of the silo) over which the images are to be recorded for PIV analysis can be referred to as a measuring window. One has to decide the size of the measuring window before recording the flow. The main criterion is that the measuring window should have enough pixel density (pixels/mm^2) in order to permit an accurate measurement. For a given image resolution, the larger the size of this window, the smaller the pixel density. As discussed in section 3.5.2, the pixels that comprise the voids should be distinguishable from the pixels of the particles in order to facilitate an accurate measurement.

The maximum resolution of the Photron FASTCAM SA6 camera is 1940 x 1440. Since the width of the silo is 450 mm, the maximum pixel density along the width would be 4.3 pixels/mm. The maximum utilisation of the camera resolution along the silo width would then limit the maximum height of the window to 333 mm. However, it should be noted that the fill height level in the silo is 1125 mm, so in

order to make the measurements of the flow along the full height, one has to consider the multiple measuring windows with a certain amount of overlap between each window as shown in Figure 3.8 (a). A measuring window of size 470 mm x 250 mm with an overlap of around 40 mm between the windows was selected. A photograph of the experimental set-up with test pellets in the first measuring window R_1 is shown in Figure 3.8 (b).

A pixel intensity of 4.3 pixels/mm converts to an approximately 16 pixels x 16 pixels per particle (considering the equivalent diameter of the particle to be 3.8 mm). This also means the voids as small as $1/16^{th}$ fraction of the particle size can be captured in the image which is good enough to make an accurate measurement.

3.8.2 Patch generation and scale factor

Four markers were placed on the side walls of the silo in each measuring window as indicated in Figure 3.8 (b). There are three purposes of these markers: first is to use them as reference points to generate the patches and second is to calculate the scale factor and third is to use them as intersection points when merging the results from all the measuring windows. Figure 3.10 shows the centres of the patch locations generated over the image in a rectangular pattern. An interval of the size of $1/8^{th}$ of the outlet width was selected in this study which is small enough to measure all the spatial variations.

The scale factor *M* can be calculated from the known horizontal distance (in mm) between the side walls in the image and the number of pixels between them. The accuracy of calculation of *M* directly affects the accuracy of the velocity measurements as shown in (3.1).

$$v = \frac{ds}{M * dt} \tag{3.1}$$

where *v* is the velocity in mm/s, *ds* is the measured displacement in pixels, *dt* is the time interval in sec and *M* is the magnification factor in pixels/mm.

It is often possible that the conversion factor *M* is not constant across the image and it varies depending on the amount of distortion in the image. Many researchers assumed a constant scale factor and it was pointed out by White et al. (2003) that this assumption is valid only if the camera behaves according to the pin-hole model, i.e., if the object plane is exactly parallel to the CCD plane and the pixels are square. White et al. (2003) identified several sources of image distortion such as non-coplanarity of the CCD and object planes, lens distortion, refraction through viewing window and the pixel non-squaredness. They presented the theory of photogrammetry to model the spatial variations of the scale factor. This theory is not necessary for the current analysis because, in each experiment care was taken to ensure that the CCD plane of the camera is parallel to the front wall of the silo. To estimate the variations in M across the image, it was calculated from both the bottom and top markers and found that it only varies by a slight amount: 4.08 pixels/mm at the bottom and 4.09 pixels/mm at the top. To consider these slight variations in the value of M, it was assumed that *M* varies linearly along the height of the measuring window.

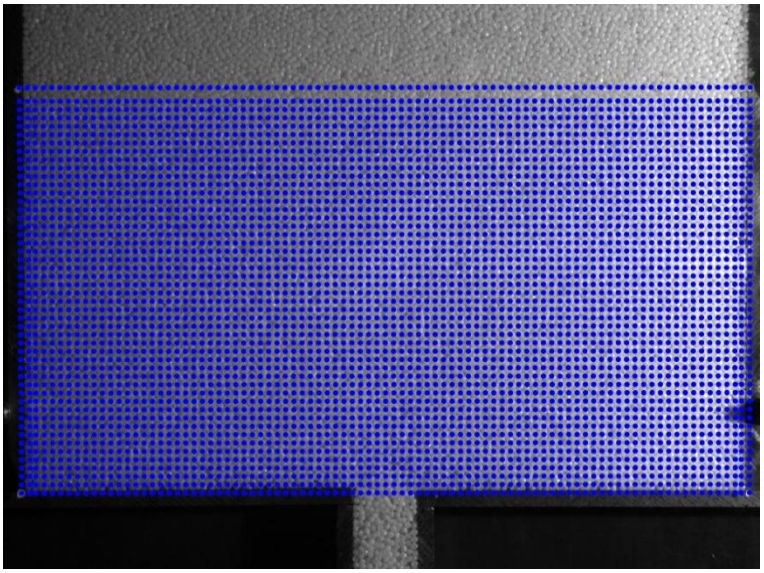

Figure 3.10 Coordinates of patches created in the recorded image.

3.8.2.1 Precision

Precision is defined as the standard deviation of the repeated measurements of the same value. It was shown by White et al. (2003) that the precision of the displacement measurement increases with the increase of patch size. The precision errors are attributed to the numerical errors that can occur due to the subpixel interpolation around the asymmetric correlation peak and also due to slight changes in light between the images. To establish the precision of the measurements in the current experiments, images were taken when the material was held stationary in the silo. Any deviations measured from the zero velocity value can then be regarded as the precision.

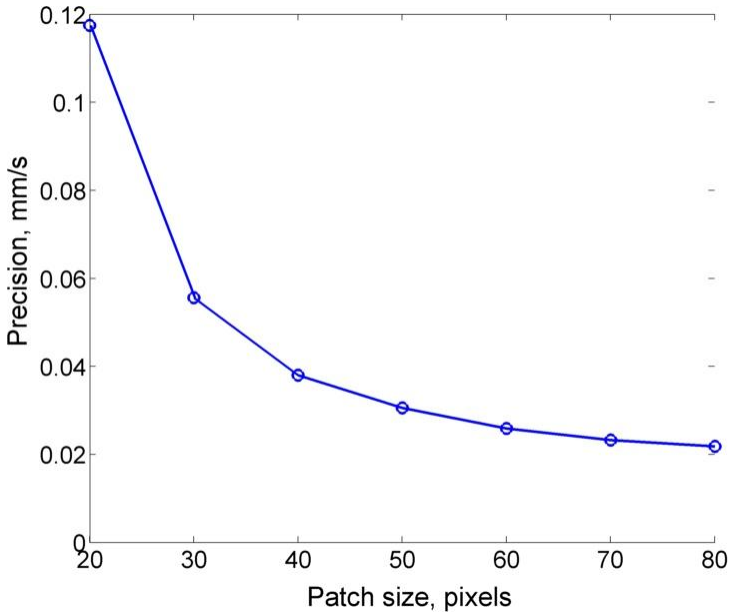

Figure 3.11 Effect of patch size on the precision of the velocity measurement.

Figure 3.11 shows the precision of the velocity measurement and its variation with the patch size. It can be seen that the precision of the measurement increases with the increase of patch size. The standard deviation in the measurement was found to be ± 0.12 mm/s and ± 0.025 mm/s for a patch size of 20 pixels x 20 pixels and 80 pixels x 80 pixels respectively. These errors are very small in magnitude when compared to velocities in the silo which are the order of 100 mm/s.

3.8.2.2 Effect of patch size

It is known that one of the major sources of error in PIV is the presence of velocity gradients within the patch. In the shear flow region of a silo, the presence of high velocity gradients can deform the image pattern within the patch if its size is large. It is, therefore, important to check the dependency of patch size on the measurements. Four different patch sizes (20 x 20, 40 x 40, 60 x 60 and 80 x 80) were considered for this study. Figure 3.12 (a) and (b) shows the temporal variation of measured instantaneous centreline velocity from the start of discharge at distances of Z = 40 mm and Z = 160 mm above the outlet for four different patch sizes. It can be seen that the measurements for all considered patch sizes at both the heights are similar except for a patch size of 20 pixels x 20 pixels at Z = 40 mm.

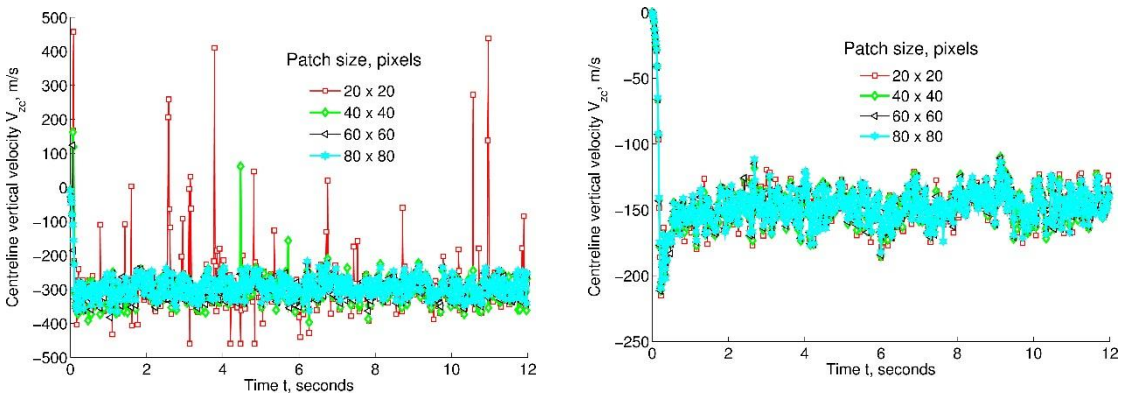

(a) Z = 40 mm (b) Z = 120 mm

Figure 3.12 Effect of patch size on the centreline velocity at different heights.

Figure 3.13 shows the comparison of time-averaged horizontal and vertical velocity profiles illustrating the negligible influence of patch size on the averaged values. The velocities are averaged during 4 sec to 6 sec from the start of discharge. The negligible influence of patch size indicates that the image pattern in the patch does not deform significantly. The reason could be that the images are recorded at a frame speed of 60 fps, i.e., at a time interval of 0.0167 sec during which the shear formation may be smaller. It should be also noted that the larger the patch size the greater the

time required to compute the correlation coefficient matrix. A patch size of 40 pixels x 40 pixels was selected for the study which is approximately 2.5 particle diameters.

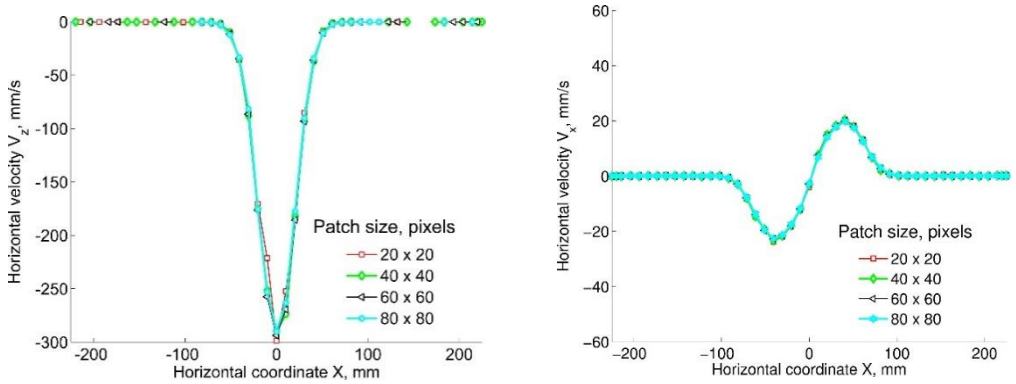

(a) Z = 40 mm

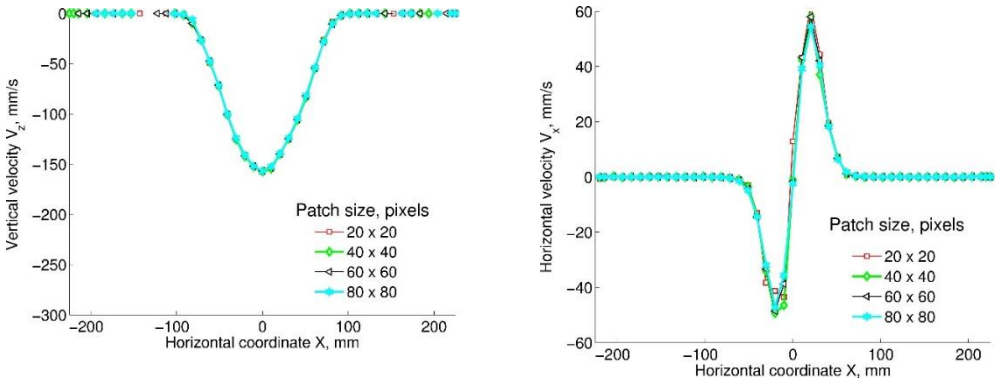

(b) Z = 120 mm

Figure 3.13 Effect of patch size on the time averaged vertical and horizontal velocity profiles (averaged during t = 4 to 6 sec).

3.8.2.3 Repeatability

Experiments in each measuring window were repeated at-least three times to ensure that the observed flow behaviour is repeatable. The same filling conditions were maintained for each experiment to minimise the effect of filling on the flow behaviour. The measurement of centreline velocities at different heights from the outlet was compared for each repeated experiment as shown in Figure 3.14 (a) – (b) for three depths of the silo. A good repeatability was found. The coefficient variance

of fluctuations (percentage ratio of standard deviation to the mean) in velocity was found to be 9.7 %, 6.9 % and 5.5 % for 20 mm, 40 mm and 100 mm silo depths respectively.

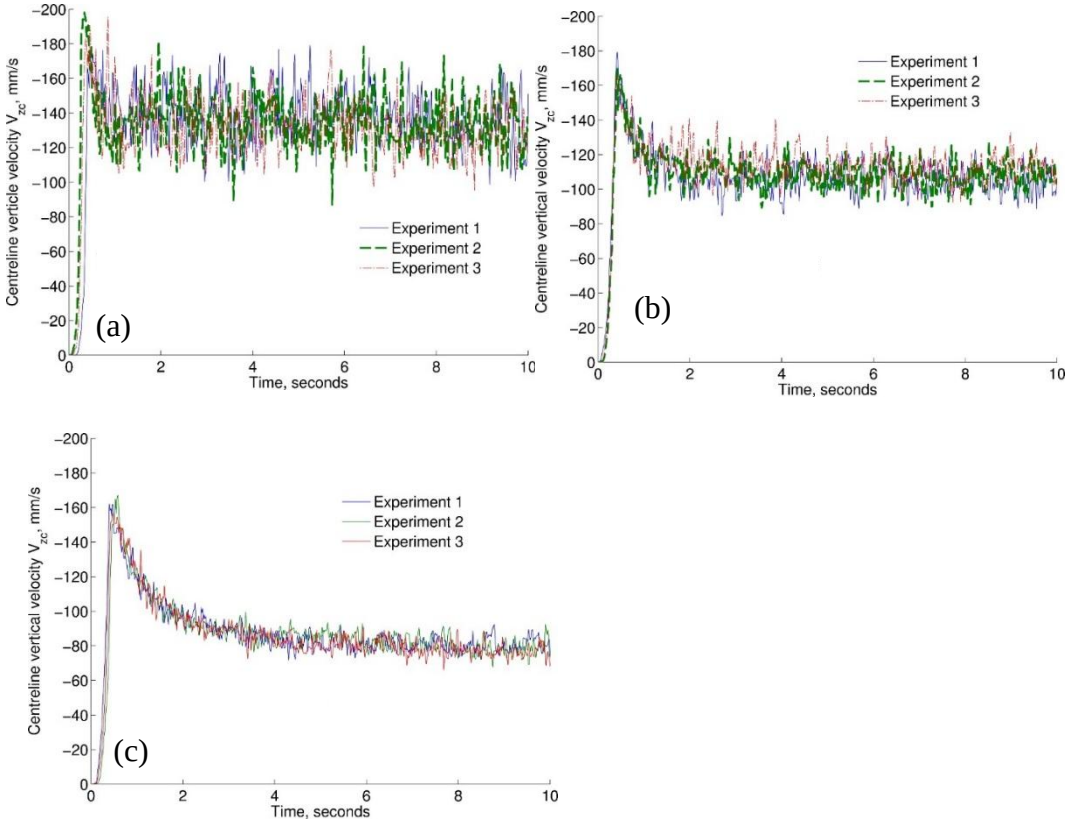

Figure 3.14 Temporal variation of centreline velocity at Z = 200 mm (a) Depth = 20 mm (b) Depth = 40 mm (c) Depth = 100 mm.

3.9 Evolution of flow patterns in a flat bottom silo

The availability of a large amount of velocity measurements at each point in the silo offers the possibility of accurately quantifying the flow from the start of discharge to the point of its development to a steady state. For example, in each measuring window, a total of 4600 patches were created and the velocity was measured at each location for a time duration of 25 sec, i.e., 1500 time instants. Therefore, a total of 6.9 million data points exists in each measuring window. Flow characteristics such as velocity profiles/distributions and flow channel boundary (FCB) at different instants

can be extracted from the measured data. These flow characteristics give insights into the mechanism of flow evolution, the size and shape of the stagnant zones and whether or not existing models can describe the flow.

3.9.1 Observations of void evolution

Figure 3.15 (a)-(h) shows the recorded images at different instants (t = 0, 0.1, 0.3, 0.5, 1, 2, 3 and 4 sec) during the discharge. Upon opening the outlet, the material starts to dilate, creating a distinct density gradient between the flowing and stagnant regions. This can be seen from the visible difference in void ratio between these regions in this series of images; for example, at t = 0 sec there is no noticeable difference in void ratio across the silo whereas at t = 0.1 s after the start of discharge, an increase in void ratio can be seen close to the outlet. As the discharge progresses, the voids propagate upwards in both the vertical and horizontal directions which can be considered as a propagation of a density/dilation wave. The speed of wave propagation depends on the magnitude of the density difference between the flowing and stagnant zones (Nedderman, 1995). The shape and size of the boundary of the density wave and the velocity profiles within the flow zone were extracted from the velocity measurement as discussed below.

(a) t = 0 sec

(b) t = 0.1 sec

(c) t = 0.3 sec

(d) t = 0.5 sec

(e) t = 1 sec

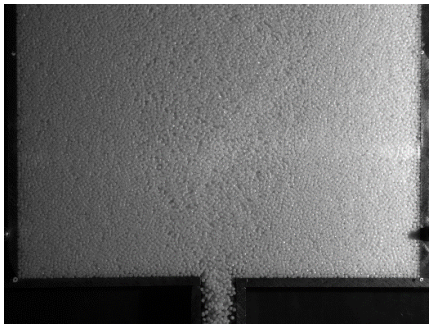

(f) t = 2 sec

(g) t = 3 sec

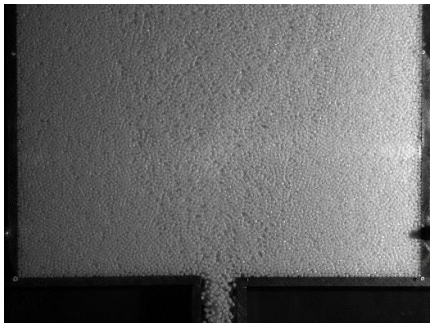

(h) t = 4 sec

Figure 3.15 Extracts of recorded images during the gravity discharge from a flat bottom silo.

3.9.2 **Representation of flow**

It is more convenient and easy to understand if the velocity profiles and the flow channel boundary plots are combined and superimposed on the schematic of the silo. For example, a snapshot of the flow shown in Figure 3.16 (a) can be represented using the plots shown in Figure 3.16 (b) and (c). All the velocities shown on this plot are equally scaled such that the distance from the horizontal axis at any height gives the magnitude. The red curve shown in this plot indicates the flow channel boundary (FCB). The definition of FCB is discussed later in the sub section 3.9.4. Similar plots will be used in the following sections and the rest of the thesis to represent the flow.

It should also be noted that as the flow is measured separately in each measuring window, the measurements from each window should be combined to get the full picture of the flow. Figure 3.17 (a) shows the snapshots of the discharge in measuring windows R_1 (bottom) and R_2 (top) at the same instant from the start of discharge. The two images are extracted from videos of two independent experiments. Since the experiments are carefully controlled to achieve good repeatability, the results from these two regions can be combined to represent the flow over a large height as shown in Figure 3.17 (b). The difference between the velocities in the overlap region of consecutive windows is found to be within the variability of each experiment.

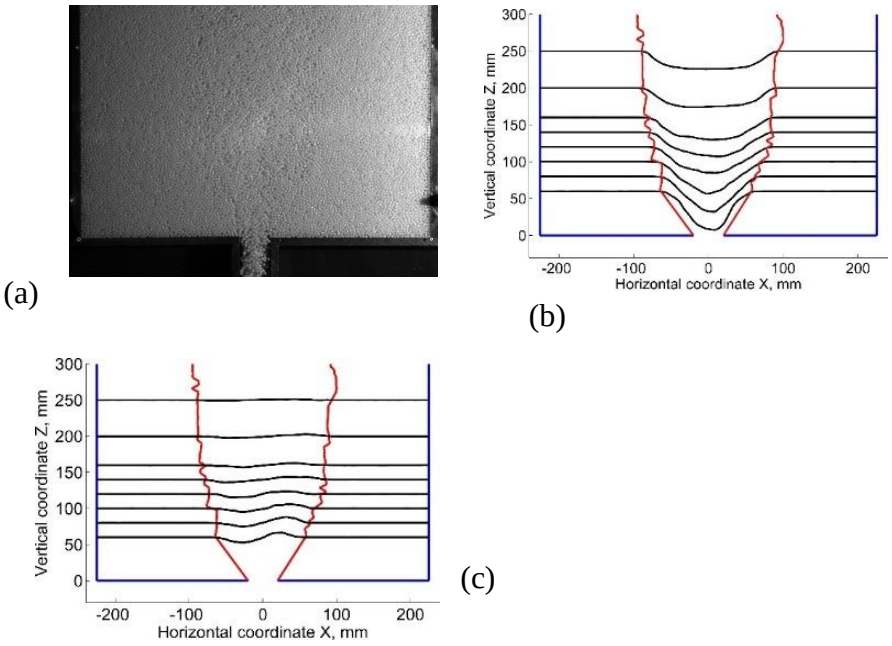

Figure 3.16 Visualisation of flow at t =1 sec (a) snapshot of image (b) line profiles of vertical velocity* (c) line profiles of horizontal velocity* (d) contour plot of vertical velocity. (*Red curves represent flow channel boundaries defined as 1% of centreline velocity)

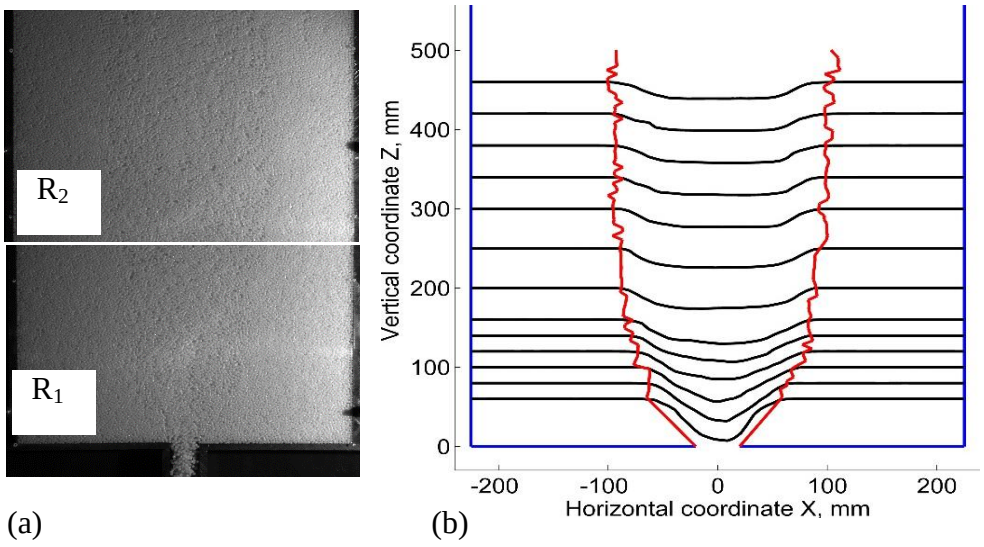

Figure 3.17 (a) Snapshot of images in measuring windows R_1 and R_2 (b) Merging the measurements of two measuring windows.

3.9.3 **Centreline velocity**

The evolution of flow channel can be partly studied from the temporal variation of centreline vertical velocity at different heights (Z = 40, 80, 120, 160 and 220 mm) as shown in Figure 3.18. It can be seen that at all heights the centreline velocity increases to a maximum value in a very short period of time and thereafter decreases before reaching a steady state value (irrespective of decreasing head level in the silo). The rapid increase in the centreline velocity occurs due to the upward propagation of the flow and thereafter a gradual decrease in magnitude was evident which is due to the sideward propagation of the flow channel as illustrated in the following section.

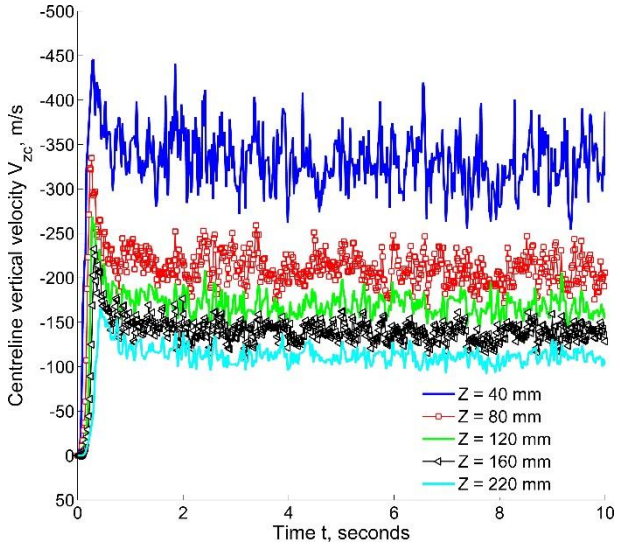

Figure 3.18 Temporal variation of centreline velocity at different heights in a 40 mm deep silo.

3.9.4 **Flow channel boundary and velocity profiles**

Figure 3.19 (a) – (f) shows the evolution of vertical velocity distribution and flow channel boundary during the very initial stages of the discharge. This set of figures illustrates the major events of the development of the flow during the discharge from 0.1 sec to 0.6 sec, for a silo of 40 mm deep. Blue lines represent the silo walls, the black lines represent the measured vertical velocity at a given height (amount of displacement from horizontal line represents the magnitude of the velocity) and two

red curves represent the FCB which is defined as the locus of points of minimum vertical velocity at all heights. The minimum velocity at any height can be defined in terms of percentage of centreline velocity as proposed by Watson and Rotter (1996). A criterion of 1 % of the centreline velocity at a given height is used to define the location of the minimum velocity.

The development of the flow can be divided into two stages: first stage, rapid upwards propagation of plug flow and the second stage, widening of the flow channel by shearing. During the first stage, the particles close to the outlet, discharge by free fall upon opening the outlet, thereby creating an empty space in the shape of an arch and the flow in the silo then initiates with the collapse of this arch due to a high stress gradient. The flow propagates quickly in the upward direction until it reaches the surface. This mechanism is illustrated in Figure 3.19 (a) – (f) from changes in vertical velocity distribution through space and time. By the end of the first stage, the flow was found to be fully developed along the height of silo in the form of a narrow plug-like flow as shown in Figure 3.20 (a) at t = 1 sec. At this stage, the flow channel is constrained around the centreline of the silo and its shape is vertical at distances far from the outlet and curved close to the outlet. The FCB then starts to expand sideways until it reaches a steady state condition as depicted in Figure 3.20 (a) – (f).

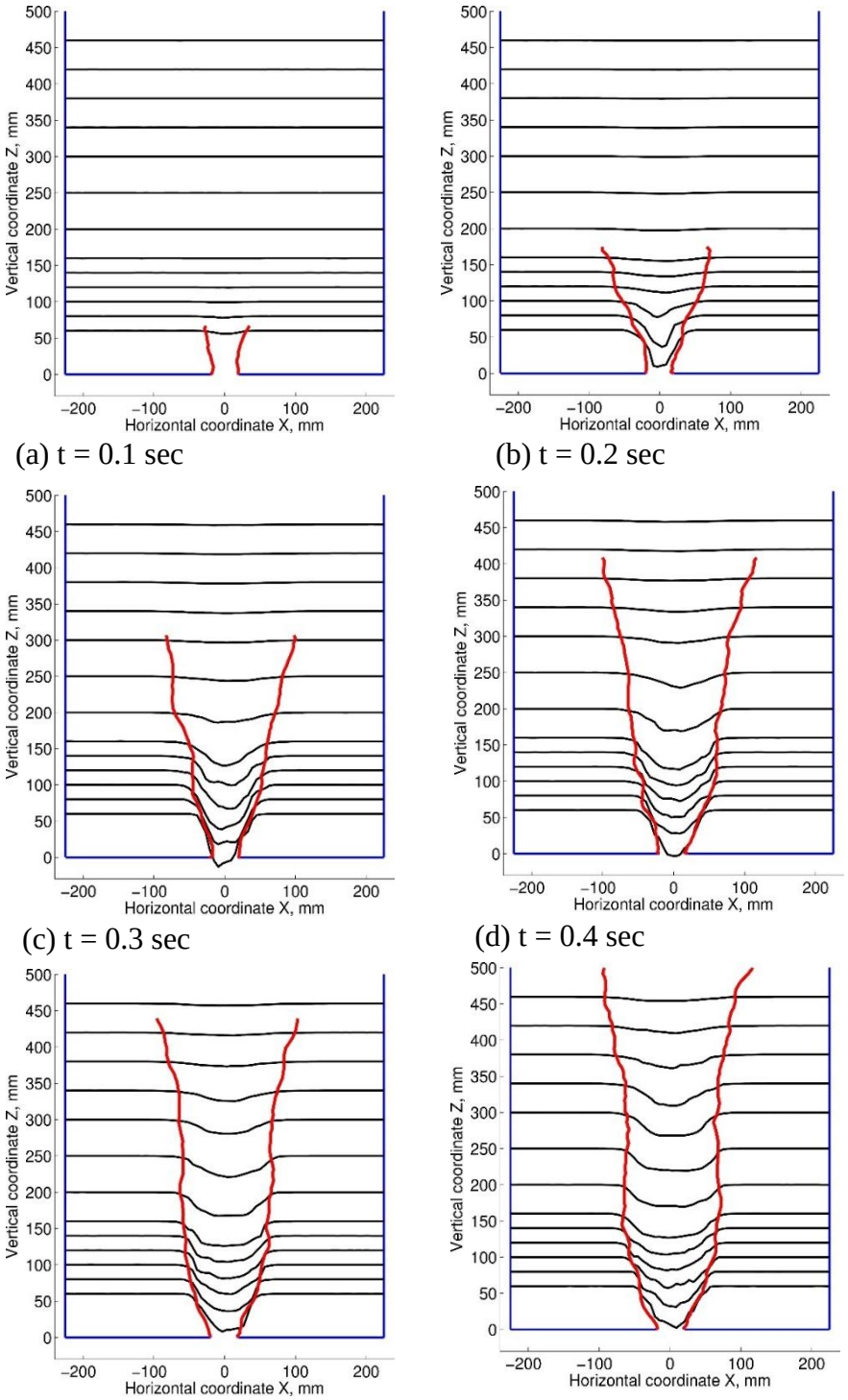

Figure 3.19 Evolution of flow channel boundary and velocity profiles during initial stages of flow.

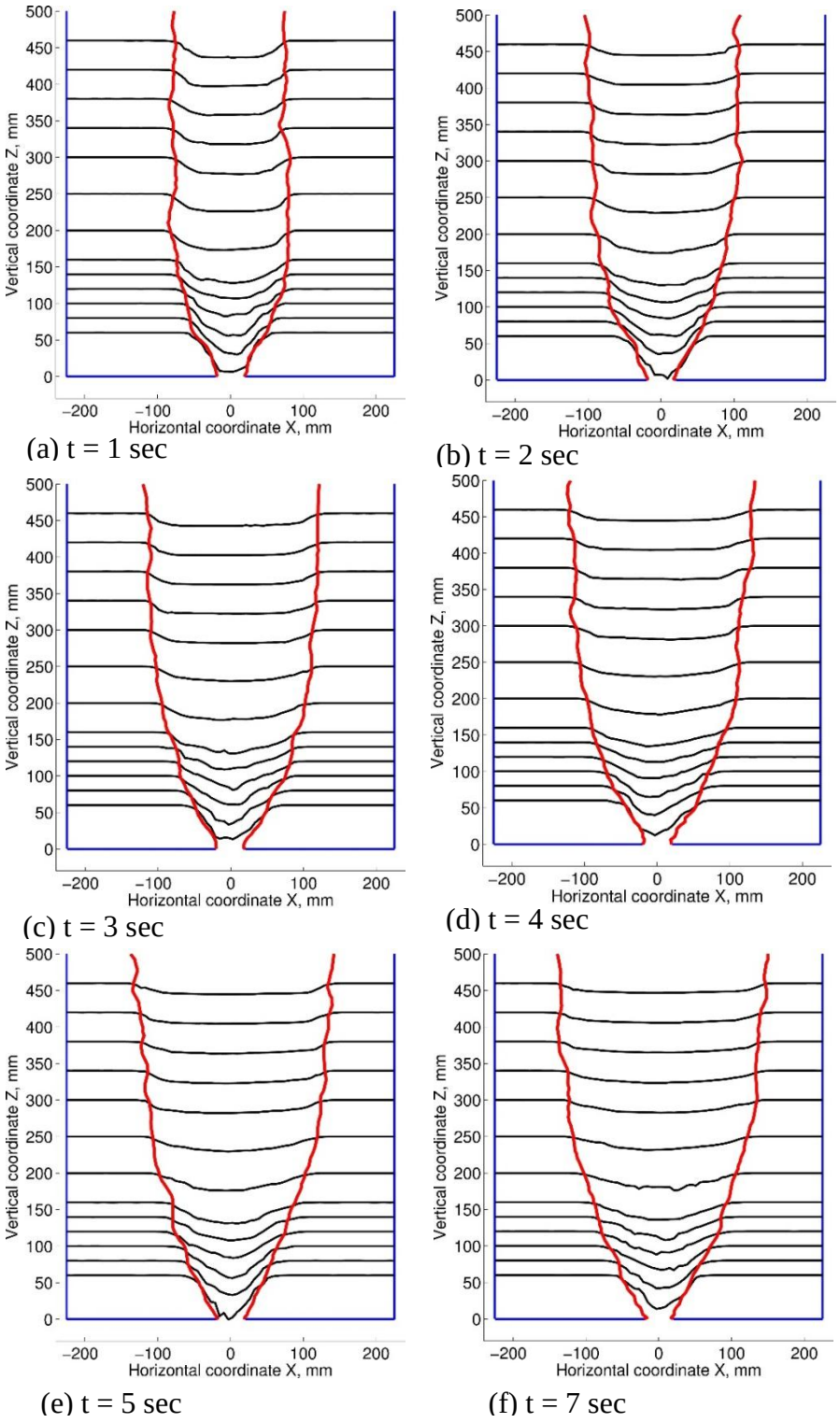

Figure 3.20 Widening of flow channel boundary and velocity profiles during the discharge in a flat bottom silo.

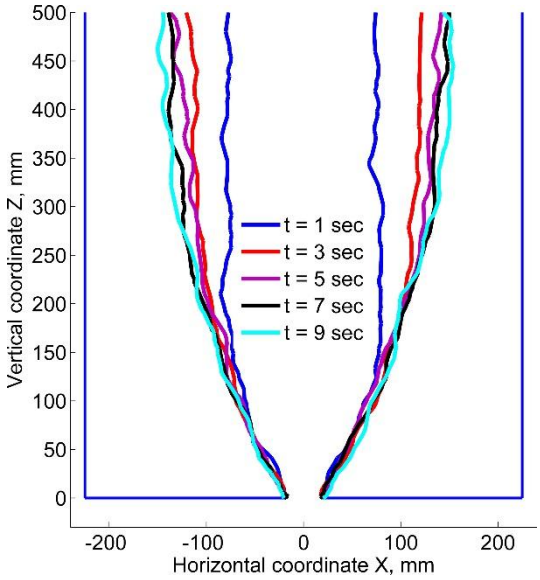

Figure 3.21 Sidewards propagation of flow channel during the discharge in a flat bottom silo.

Figure 3.21 shows the sideways development of the FCB. It should be noted that the curved shape of the FCB remains steady whereas the vertical part of the FCB widens towards the side wall before reaching a steady state. In the steady state regime, the shape of the velocity profile at any height depends only on the velocity profile beneath it or in the other words the information of the velocity propagates upwards, which is also the physical basis of the kinematic model developed by Nedderman and Tüzün (1979). The flow channel close to the outlet develops into a curved or funnel shape up to a certain 'transition' distance from the outlet and thereafter forms a vertical flow channel. In the funnel flow zone, the velocity is a maximum at the centre and gradually decreases towards the wall and in the vertical flow zone, the velocity is uniform across the width of the flow channel except near the boundary where a thin shear band is developed.

Nedderman (1995) highlighted that the original kinematic model of Nedderman and Tüzün (1979) has fallen out of favour for unsteady flow in bins as it doesn't consider the dilation of the material during the initiation of the flow and cannot predict the transition from the funnel to a plug flow. Therefore, he proposed a modified

kinematic model that incorporates the dilation. This modified model calculates the size and shape of the FCB at different instants during the discharge. The FCB was considered as a density wave that propagates upwards.

By applying the mass conversation equation across the FCB, Nedderman (1995) derived that the normal velocity of the wave (W) is equal to the $\Delta\rho/\rho$ times the velocity of flow (V) where $\Delta\rho$ is the difference between the densities of the stagnant zone and the flow zone, ρ is the flowing bulk density. The vertical velocity of the flow (V) in this equation is described by the kinematic model. It was assumed that the stagnant and the flowing zones have constant densities of ρ_o and ρ respectively. He then compared the predictions with the batch discharge experiments of Watson and Rotter (1996) in a flat bottom silo. It can be seen that the only input parameters of this model are the density ratio (ratio of densities between the flowing and non-flowing zones) and the kinematic constant B. He assumed the arbitrary values of kinematic constant that gives the good predictions with the experiments and $\Delta\rho/\rho$ taken as 10%. Furthermore, this model does not predict the existence of a steady state after the initial period of flow development and it also assumes that the kinematic constant B does not change with time which may not necessarily hold true. Despite all of these assumptions, good predictions of the experimental results were achieved by adjusting B.

Waters and Drescher (2000) also developed a model to describe the evolution of plug flow in both planar and axisymmetric hoppers. This model was developed purely on the experimental observations of flow development. They categorised the flow development into five phases and in each phase the growth in the size of the flow channel was calculated from the global mass conservation and local mass conservation across the boundary. The initial shape of the FCB was approximated with simplified straight lines (inclined close to the outlet and vertical away from the outlet) and velocities within the FCB were approximated by assuming a radial velocity field close to the outlet and vertical velocity fields away from the outlet. This model qualitatively explains the observations made in the current experiments.

A generalised model that quantitatively describes the evolution of flow channel and the velocity profiles within the flow channel does not exist mainly because of its

dependency on several factors such as the height of the material in the bin, type of filling, particle size and its angularity, wall friction and geometry of silo (Waters and Drescher, 2000). Particle-based methods such as DEM can be deployed to study the flow evolution of granules in a silo.

3.10 Effect of depth of the silo on flow patterns

In general, industrial silos are of circular or rectangular cross-sectional shape; these produce three-dimensional flow patterns which pose difficulties for experimental investigation, particularly using PIV. However, the complexity of the problem can be greatly reduced with the assumption of axisymmetric flow in the case of a cylindrical bunker or a planar flow in the case of rectangular or wedge hoppers. This effectively reduces a 3D problem to a 2D problem (Tuzun et al., 1982). This scenario can be easily replicated in simulations by using a periodic boundary condition or a frictionless wall condition in the direction of depth of the silo. Due to the presence of finite-wall friction at the front and back walls of the silo, a perfect plane strain flow scenario may not be possible to achieve in the experiments. In addition to this, the presence of physical front and back walls in a laboratory-scale test silo poses a challenge in representing the 3D flow, mainly for two reasons: firstly, the presence of wall friction which can retard the flow at the front and back walls and secondly the amount space between the front and back walls of silo, the smaller the space the greater the tendency of arching the flow. The effect of depth of the silo on the developed flow patterns is analysed in this section.

3.10.1 Flow channel boundary

The mechanism of evolution of flow patterns described in section 3.9 was also observed in 20 mm and 100 mm deep silos. It is obvious that by increasing the depth of the silo the particles have a greater freedom of movement. Therefore, the velocity of density wave/FCB propagation was found to increase with increasing thickness and consequently a wider flow channel was observed for 100 mm deep silo as shown in Figure 3.22. The angle of discharge (the angle that the FCB makes with the horizontal axis) was found to be approximately 39^o, 36^o and 29^o for silos of depths 20, 40 and 100 mm, respectively.

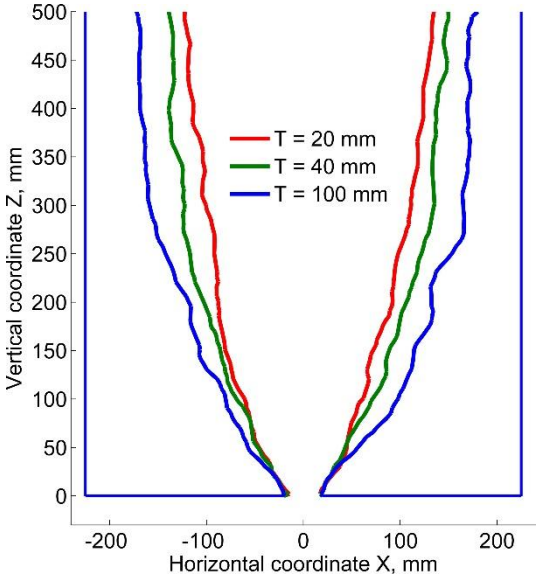

Figure 3.22 Shape and size of flow channel boundary at t = 6 s from the start of discharge for different depths of the silo.

3.10.2 **Mass flow rate**

The average mass flow rate can be calculated from the time-averaged velocity profiles using the (3.2).

$$m_{PIV} = \rho_b \left[\int_0^W \overline{V_z}(x).dx \right] T \qquad \textbf{(3.2)}$$

where ρ_b is the flowing bulk density in kg/m^3, $\overline{V_z}$ is the time averaged vertical velocity in m/s, W is the width of the silo in m, T is the thickness of the silo in m.

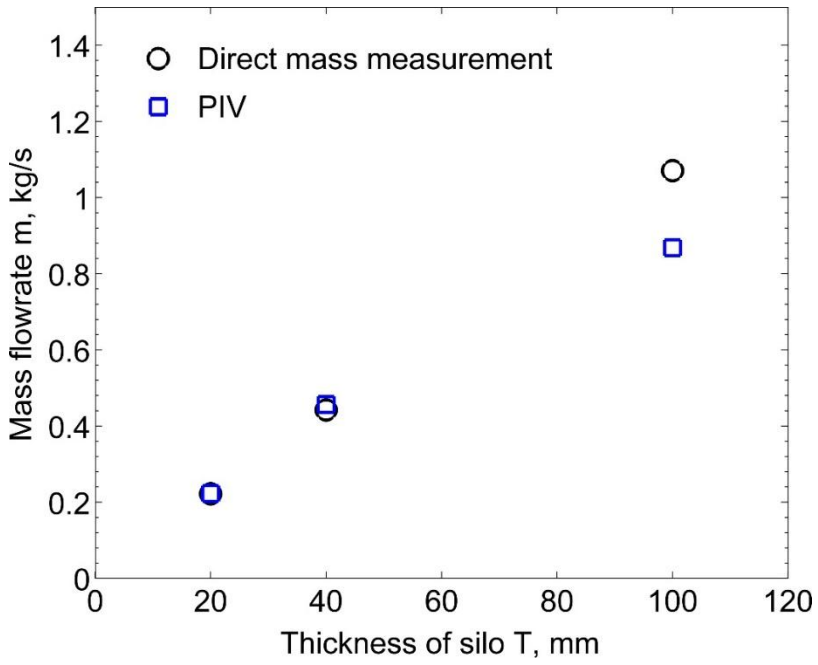

Figure 3.23 Comparison of PIV-evaluated mass flow rate with direct scale measurements.

Due to the lack of data of flowing bulk density of the material, the bulk densities at the end of filling were used in the calculations of the mass flow rate and they found to be 663.58 ± 12.82, 666.71 ± 5 and 589.53 ± 2.27 kg/m3 for 20, 40 and 100 mm deep silos respectively. It can be noticed that the bulk density achieved in the case of 100 mm thick silo is lower by nearly 12 %. The existence of lower bulk density at larger thickness could be associated due to the reduction in filling velocity of the pellets because of increased gap between the filling pipe and the frontal walls in a 100 mm thick silo. Figure 3.23 shows the comparisons of the calculated mass flow rates with the direct mass flow rate measurements in 20, 40 and 100 mm deep silos. It was found that there is a difference of -18 % between PIV evaluated and direct mass measurements for the 100 mm deep silo while only a difference of -0.46 % and -3.26 % exists for the 20 mm and 40 mm deep silos respectively. The main reason for these differences is attributed to the assumption of constant velocity along the depth of the silo, as the flow is only measured at the front wall of the silo. Thus, any amount of difference implies that the velocity at the front wall differs from the mean velocity (along the depth). Therefore, the difference of -18 % for 100 mm deep silo suggests that the flow is 3D with a significant retardation of flow (relative to the bulk

flow across the cross-section of the silo) at the front and back walls and a planar 2D motion exists for 20 mm and 40 mm deep silos. Although the retardation is negligible for a silo of small depths, the flow patterns could be mainly governed by the wall friction at the front and back wall because of the arching. The effect of front and back wall friction on the flow patterns can be studied using DEM simulations as presented in Chapter 5.

3.11 **Summary**

In this chapter, the accuracy of PIV technique has been assessed using the computer generated images of the silo flow followed by the application of PIV to the experiments in a flat bottom silo in order to understand the evolution of flow of pellets from the start of discharge to a steady state and further to analyse the depth of the silo on the steady state flow patterns.

The PIV measurements of patch velocities from artificial DEM images were compared with the corresponding locally averaged particle velocities in order to assess the accuracy of the PIV technique. The accuracy of velocity measurements as a function of image resolution has been discussed. It was found that the number of pixels representing the voids within a patch is an important factor that affects the accuracy of the measurement. It was also found that a moderate image resolution of 1000 pixels x 1400 pixels is adequate to make an accurate measurement of mean velocity within ± 0.5 %.

The evolution of flow during the discharge from a flat bottom silo has been studied from the spatial and temporal changes of the flow channel boundary and velocity profiles within the flow channel. It was shown that the flow propagates upwards very quickly to the surface during the initial stages of the discharge followed by the sideward expansion of the flow. It was found that with the increase in the depth of the silo, the size of the steady state flow channel increases and the angle of discharge decreases. The analysis of the mass flow rate from the velocity profiles revealed that there exists a significant retardation of flow at the frontal wall of the silo for a 100 mm depth and a negligible retardation for 40 mm and 20 mm deep silo.

Chapter 4

4. Calibration of a DEM model for simulating the flow of granules in silos

4.1 Introduction

Discrete Element Method (DEM) is increasingly used in recent years to investigate the behaviour of granular solids in industrial systems such as silos, mixers and milling. A growing interest in DEM is seen with the advent of high-performance computing machines, as well as the ability of DEM to model phenomena at particle scale without phenomenal assumptions that exists in the constitutive models (Ooi and She, 1997; Ooi et al., 1996; Rotter et al., 1998; Vidyapati and Subramaniam, 2013). However, it is very much essential to quantitatively validate DEM model by solving a simple silo configuration such as flat bottom silo prior to its application in simulating industrial scale blenders (Ooi, 2013).

The simulation work in this thesis is divided into four chapters (Chapters 4 to 7). In the current chapter, the calibration of the DEM model is presented followed by the next chapter where the quantitative validation of predictions of flow in a flat bottom silo and a parametric study are presented. The validated model is then used to investigate the extent of blending in a small scale flat bottom silo (Chapter 6) followed by the studies in a relatively large scale multi-flow blender silo (Chapter 7).

The theory of the DEM is presented in section 2.5. In this chapter, the modelling of size and shape of the test granules is first presented followed by the description of the methodology of Jenike direct shear simulations. The rest of the chapter explores the relationship between the bulk friction and the particle scale friction at different rolling frictions and the influence of particle rotations on the mobilised particle scale is also analysed.

4.2 Modelling size and shape of test pellets

The DEM model was developed for high density polyethylene (HDPE) pellets shown in Figure 4.1. The properties of the pellets are presented in section 3.6. The diameter and height of the pellets are 3.96 ± 0.13 mm and 3.12 ± 0.28 mm respectively. The angle of internal friction of the pellets is 30 ± 1 deg. The wall friction with aluminium and perspex were $9.5^{o} \pm 1^{o}$ and $11^{o} \pm 1^{o}$ respectively.

A multi-sphere approach was used to represent the test pellets in which case the contact models based on the spherical contact are equally applicable (Favier, Abbaspour-Fard and Kremmer, 2001). The cylindrical test pellet was approximated with three different shapes: a single sphere, two and four clumped spheres as shown in Figure 4.2. The diameter of the single sphere particle was taken as the equivalent diameter of the pellet. In the case of clumped spheres, the diameter of each sphere was taken as 3 mm with a centre-to-centre distance of 0.75 mm thereby giving an aspect ratio of 1.25. The main difference between the two and four clumped particle shape is that the later has no preferential axis of rolling while the former can roll about the axis that connects the sphere. It should also be noted the combination of two or four spheres does not accurately represent the shape of the pellets shown in the Figure 4.1. As the focus of the study is to reproduce bulk behaviour of the pellets, the local anisotropies in the shape were ignored. The changes in the bulk behaviour due to this approximation were accounted with the application of appropriate rolling resistance. The effect of combination of shape and the rolling resistance on bulk behaviour of granules is still an active area of research.

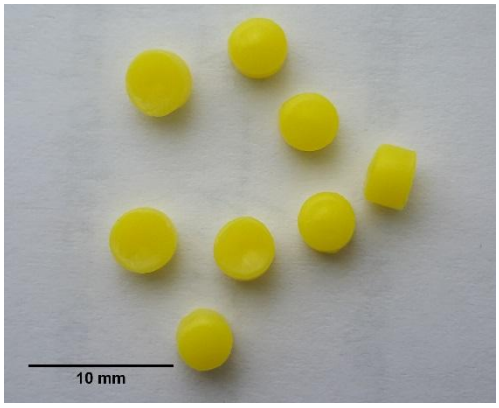

Figure 4.1 HDPE pellets.

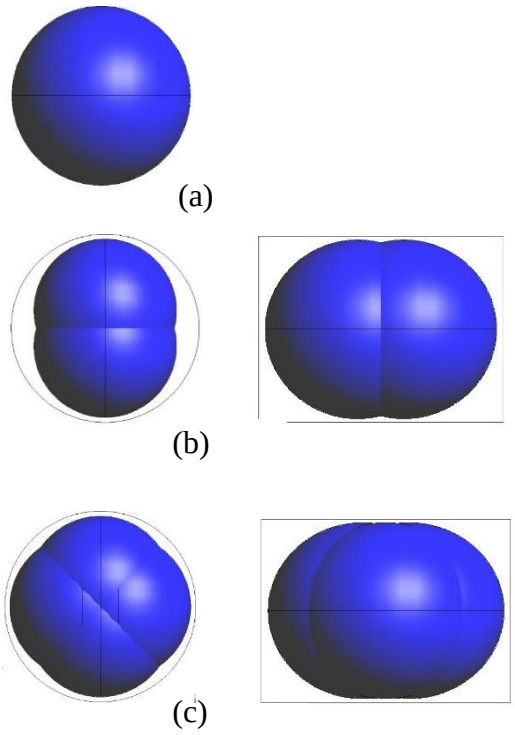

Figure 4.2 Particle shapes (a) sphere (b) 2 sphere (b) 4 sphere.

4.3 Jenike direct shear simulations

Jenike direct shear set-up is used as a calibration experiment to determine the particle scale parameters from the measured bulk friction. It is widely used to measure the internal friction and wall friction of the bulk solids (ranging from fine powders to granules) at different levels of normal stress. The complete details of the test set-up for the measurement of internal friction and wall friction can be found in ASTM (2000). Here only the basic details of the set-up that are required for the modelling are discussed. It consists of a bottom ring and a shear ring of equal diameter and a shear lid. The rings are initially arranged such that the inner edge of the shear ring touches the outer edge of the bottom ring giving an eccentricity of 3 mm. In this arrangement, both the rings are completely filled with the particles and the top surface is scrapped to form a flat horizontal surface. A normal stress is then applied to the shear lid. Under the constant normal load, the shear ring and lid are translated horizontally at a constant strain rate for a total distance of 6 mm. The resisting shear

force is recorded during the shearing. The shear force reaches a steady value after translating to a fraction of the total shear distance. The steady state shear force and the corresponding normal stress is then used to calculate the internal friction. For the wall friction measurement, the same procedure is followed except that the bottom ring is replaced by the wall material.

Chung and Ooi (2011) conducted benchmark tests involving the impact of two spheres and a sphere with rigid plane to verify the commercial DEM codes: PFC3D and EDEM. DEM simulations were conducted using EDEM 2.7 commercial software in this work.

4.3.1 **Simulation set-up**

4.3.1.1 Geometric model

A standard cell/ring size of diameter 95 mm was used. The wall thickness of each ring is 3 mm. The height of the bottom ring and the shear ring are 13 mm and 16 mm respectively. The geometry of the shear ring and the bottom ring were created using the pre-processor of EDEM software. The numerical models of the Jenike internal and wall friction set-ups are shown in Figure 4.3 and Figure 4.4 respectively. The shear lid is modelled as a particle wall (as indicated in Figure 4.3) instead of a flat geometric surface and the uses of this approach are discussed in section 4.3.2.

4.3.1.2 Mechanical and interaction properties

The input parameters of the model and the corresponding values are listed in Table 4.1. The mechanical properties which includes the solid density (ρ_s), Young's modulus (E) and Poisson ratio (v). The solids density provided by the supplier is in the range of 940 - 970 kg/m^3. A solids density of 950 kg/m^3 was adapted in the simulations. The Young's modulus and Poisson ratio were chosen close to the real values 1E+08 Pa and 0.4 respectively. It is also a common practice to choose a low value of E in order to save the computational time (Lommen, Schott and Lodewijks, 2014).

The interaction properties which includes the coefficient of restitution, particle-particle friction, particle-wall friction and the rolling friction. As the values of

particle scale friction are not known beforehand, a low particle friction of 0.1 and a zero rolling friction was used during the particle generation in the shear cell. A low value of coefficient of restitution of 1E-04 was used by assuming that the CoR has a negligible effect on the bulk friction. This has also been confirmed for by considering different values of CoR as discussed in section 4.4.1. Particle-particle and particle-wall sliding friction values ranging from 0 to 1 at an interval of 0.1 and the rolling values of 0, 0.05, 0.1, 0.2 and 0.5 were considered. The sliding friction between the particles and the shear lid was taken as 1 to replicate the fully rough wall condition.

Table 4.1 DEM input parameters of Jenike simulations.

Property name	DEM Particles
Diameter, d_p (mm)	3
Aspect ratio for two and four clumped spheres	1.25
Density, ρ_s (kg/m^3)	950
Poisson ratio, ν	0.4
Shear modulus, G (Pa)	$1x10^8$
Particle coefficient of restitution, e	$1x10^{-4}$, 0.1 and 1
Particle-Particle sliding friction, $\mu_{s\text{-}pp}$	0 to 1 interval of 0.1
Particle-Particle rolling friction, $\mu_{r\text{-}pp}$	0, 0.05, 0.1,0.2 and 0.5
Particle-wall ring friction	0
Particle-shear lid friction	1

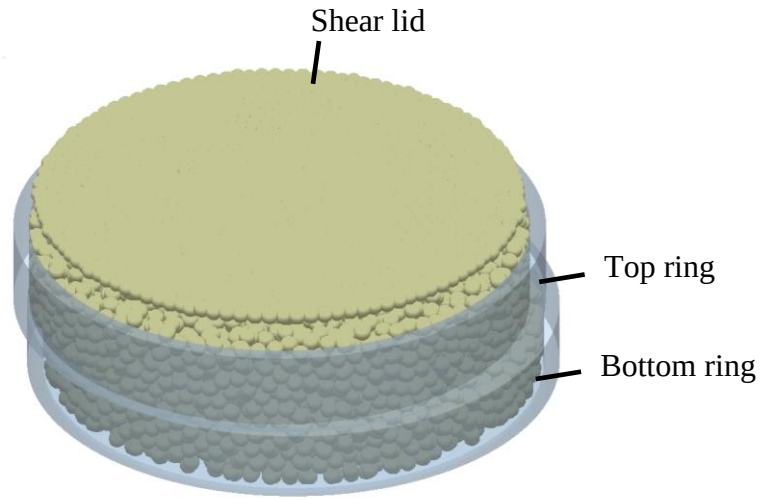

Figure 4.3 Jenike direct shear setup for measuring the internal angle of friction.

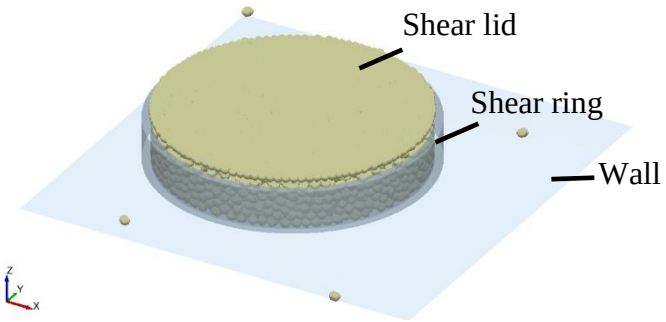

Figure 4.4 Jenike direct shear setup to measure wall friction angle.

4.3.1.3 Simulation parameters and procedure

Hertz-Mindlin contact model with viscous damping was used. A simple contact independent directional constant torque model is used in this work (Sakaguchi and Ozaki, 1993; Zhou et al., 2002, 1999). The rolling friction torque applied to the particle is given by (4.1).

$$\boldsymbol{\tau_i = -\mu_r f_n R_i \vec{\omega}_i} \qquad \textbf{(4.1)}$$

The Rayleigh time step was found to be 1.5421 x 10^{-5} sec. A calculation time step of 10 % of Rayleigh time was used. The data was saved at a time interval of 0.005 sec.

Particles were randomly generated using a dynamic factory function in EDEM 2.7 and the total number of particles at the end of filling for the sphere, two spheres and four spheres were found to be 4085, 6589 and 5513 respectively. At the end of filling, the assembly was then consolidated by applying a constant normal stress of 4 kPa for 0.2 sec. The methodology to apply the constant normal stress is discussed in section 4.3.2. The consolidated particle assembly was then sheared by translating the shear ring at 3 mm/s for a total distance of 6 mm giving a total shearing time of 2 seconds.

4.3.2 Application of constant normal stress

It is obvious that the normal stress in the shear plane should be held constant during the shearing. One method to achieve this is to use a servo-control function to control the vertical velocity of the shear lid geometry (Cui and O'Sullivan, 2006; Härtl and Ooi, 2008, 2011). Härtl and Ooi (2008) used the servo-control function (available in PFC software (Itasca Consulting Group Inc, 2006) in which the vertical velocity of the shear lid is controlled by the difference between the target stress and the wall contact stress via a stability function as shown in (4.2) and (4.3). They concluded that the coefficient of variance (CoV) of fluctuations in normal force acting on the lid during shearing is less than 0.4 %.

$$\dot{\mathbf{u}} = \mathbf{F}\left(\boldsymbol{\sigma}_{\mathbf{w}} - \boldsymbol{\sigma}_{\mathbf{t}}\right) \tag{4.2}$$

$$\mathbf{F} = \frac{\boldsymbol{\alpha}\mathbf{A}}{\mathbf{K_n}\Delta\mathbf{t}} \tag{4.3}$$

where σ_w is the current wall stress, σ_t is the target wall stress, F is the gain function, α is the relaxation factor, K_n is the sum of contact stiffness of all contacts with the wall, A is contact area of the shear lid and Δt is the computational time step.

The disadvantage of this approach is that only the translation of the shear lid is controlled ignoring the rotation of the lid. This also means that even if the contact force between the lid and the particle assembly is non-uniform (which produces a moment about the centroid of the lid), the lid is not allowed to rotate. This may lead to an increased resistance of the particle assembly against shearing, giving rise to an artificial increase in bulk friction. This has been confirmed in section 4.4 by comparing the current results with the results of Härtl and Ooi (2008). To overcome this problem, an alternative approach was developed that allows the lid to rotate and also maintains the constant normal force value described as follows.

In the DEM, since the motion of the geometry is not resolved: it is either fixed in the simulation or set in a motion based on the pre-defined kinematic conditions. Therefore, the force can only be applied to a geometry through a kinematic boundary condition, as used in the servo-control function. To overcome this problem, the flat geometric surface of the shear lid was replaced by a particle plate created with a number of spheres. The individual spheres that constitute the lid are allowed to overlap to any extent to form a solid circular particle plate as indicated in Figure 4.3. This new shear lid can be treated as a single rigid particle and all the equations are equally applicable to this particle plate like any other particles in the simulation domain. This conversion of a flat geometric surface to a single particle surface makes it possible to apply directly a constant external body force using EDEM API functionality.

An external vertical force given by (4.4) was applied to the particle shear lid. The first term in this equation nullifies the gravity for this particle and the second term applies a pre-defined normal force (F_N). Since both the shear ring and the shear lid should move simultaneously at a constant horizontal velocity (V_s) from the start of the shearing, a horizontal force given by (4.5) is applied. The first term in the equation 4.4 nullifies the current horizontal velocity (V_x) at any time and assigns a predefined shearing velocity (V_s). The second term cancels the total contact horizontal force applied by the particles on the lid. It should be also noted that these two equations are only applied to particle shear lid excluding the actual particles in the simulation.

$$\mathbf{F_{ext,z} = -mg - F_N} \quad \textbf{(4.4)}$$

$$\mathbf{F_{ext,x} = -\frac{m}{dt}(V_x + V_s) - F_{c,x}} \quad \textbf{(4.5)}$$

where m is the total mass of the particle shear lid and F_N is the required normal force, dt is the computational time step, $F_{c,x}$ is the total calculated contact force in horizontal direction between the particle shear lid and particles in the assembly, V_s is the required shear speed, V_x is the horizontal velocity of the particle wall at any instant and F_N is the total normal force to be applied on the shear lid.

4.3.3 Calculation of bulk friction from geometry forces

The total shear force (F_t) acting along the shear plane can be deduced from the force equilibrium of the shear ring or the bottom ring as shown in Figure 4.5. It is the sum of the total horizontal force acting on the shear lid (F_{t1}) and the shear ring (F_{t2}). The bulk friction angle ($\emptyset$) is then calculated using (4.6).

$$\emptyset = \mathbf{tan^{-1}} \frac{F_{t,avg}}{F_n + W_{solids}} \quad \textbf{(4.6)}$$

where $F_{t,\,avg}$ is the time averaged shear force during the steady state and W_{solids} of the solids above the shear plane.

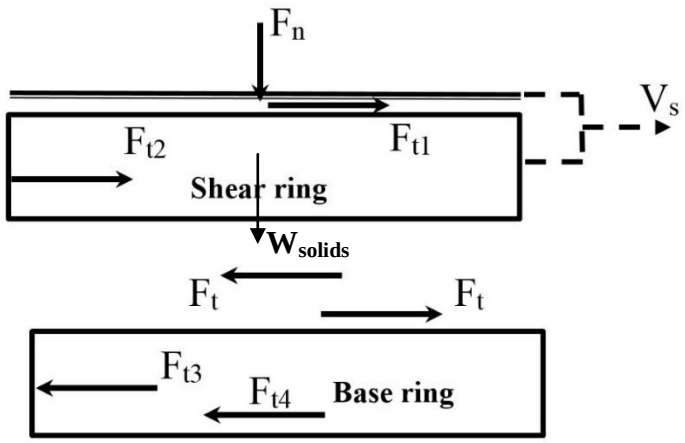

Figure 4.5 Free body diagram of the Jenike shear cell.

Figure 4.6 (a) shows the typical shear response of the particle assembly under a constant normal force. It was found that the fluctuations in the normal force were negligible thereby maintaining a constant value throughout the shearing. It can be seen that the shear force increases since the start of shearing and reaches a steady value. The force during the steady state was used for the calculation of bulk friction angle. Figure 4.6 (b) shows the shear force calculated from both forces on both the rings and it is evident that the force in the shear plane is same irrespective of which ring is used for the calculation.

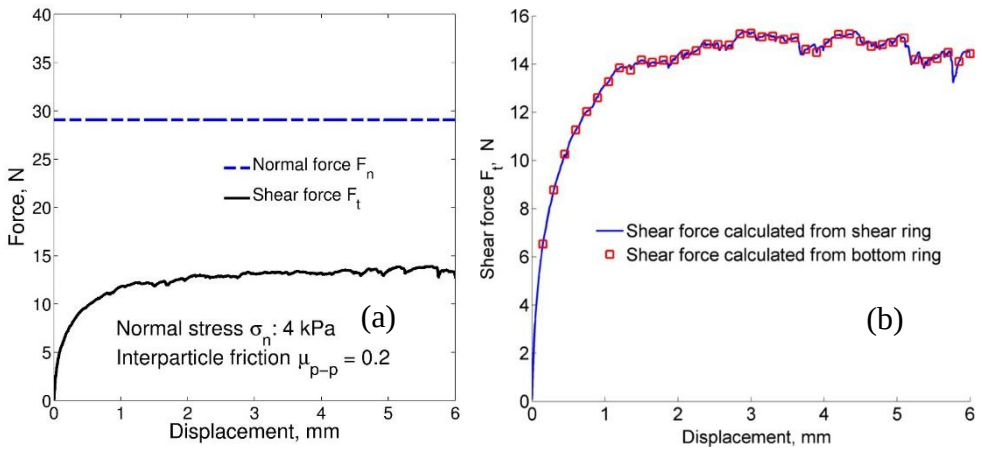

Figure 4.6 Force vs. displacement (a) Normal and shear force response during shearing (b) Shear force calculation from shear and bottom rings.

4.4 Particle scale vs. bulk scale friction: Zero rolling friction

The particle scale friction force is the resisting force due to the relative tangential velocity at the particle-particle contact or particle-wall contact, similarly the bulk scale friction force is the total resisting force in a plane due to the relative motion of bulk of particles against the particles or a wall. There are three possibilities in regard to the relationship between the bulk scale and particle scale friction as follows:

- The bulk scale friction is equal to the particle scale friction: This can arise, if each and every particle contact in the shear plane is fully mobilised. This situation could occur when the bulk of particles slide past a flat wall surface.
- The bulk scale friction is greater than the particle scale friction: This condition occurs only for the case of particle-particle contacts mainly because of additional resistance created due to the uneven particle surface in the shear plane (also called interlocking). In the case of particle-wall contacts there is no such possibility of interlocking in the shear plane because of the flat wall surface and therefore, the maximum bulk wall friction that can be achieved is equal to the particle-wall friction.

- The bulk scale friction is less than the particle scale friction: This can happen in both particle-particle contacts and particle-wall contacts. In some scenarios, the majority of the contacts in the shear plane are not fully mobilised leading to a bulk friction less than the particle friction.

In this section, the effect coefficient of restitution (CoR) and the shear lid rotation is discussed and then the relationship between the bulk friction and the particle scale friction for all the three particle shapes was explored.

4.4.1 Effect of coefficient of restitution

The CoR is known to have minimal influence on the flow in the silo because of lack of collisions. Anand et al. (2008) showed a negligible influence of CoR on the discharge rate in a hopper. Because of the difficulties in the measurement of CoR for non-spherical particles, four different values of CoR (1E-4, 0.1, 0.6 and 1) were considered in this work to study its influence on the bulk internal friction. The results are shown in Figure 4.7. It can be seen that at different values of CoR, the predicted shear response is insensitive to CoR which is obvious due to the fact that the collisions are absent during the shearing. A low CoR value of 1E-4 was chosen for further simulations so that the particle assembly can quickly reach to the steady state during the filling.

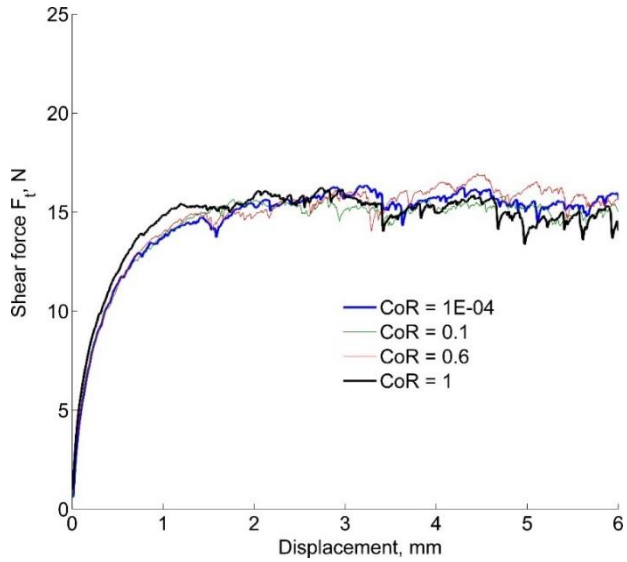

Figure 4.7 Effect of the coefficient of restitution on the shear response during direct shear.

4.4.2 **Effect of lid rotation**

The disadvantage of restricting the shear-lid rotation during the shearing was discussed in the section 4.4.1. Figure 4.8 shows the comparison of bulk friction at different inter-particle frictions for two clumped sphere against the results of Härtl and Ooi (2011). Härtl and Ooi (2011) used the servo control function to apply the force on the shear lid (in which case the shear-lid always remains horizontal irrespective of the unsymmetrical contact force distribution between the lid and particles). It is clear from this figure that the bulk friction at any given interparticle friction is higher when the servo control approach was used. It can also be seen that the difference in values of bulk friction is much higher at the higher interparticle friction.

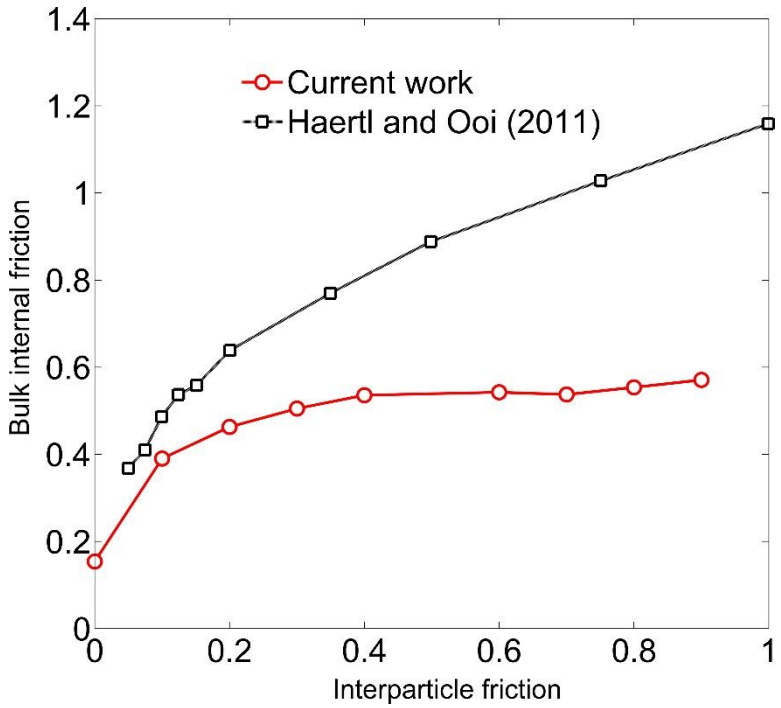

Figure 4.8 Variation of bulk friction with inter-particle friction and comparison with the results of Härtl and Ooi (2011).

4.4.3 **Effect of particle shape**

4.4.3.1 Internal friction

Figure 4.9 shows the variation of bulk internal friction with the increase of inter-particle friction at zero rolling friction for all the three particle shapes. It can be seen that the bulk internal friction is greater than the particle-particle friction until approximately 0.4 and reaches a plateau with any further increase in the particle friction. A saturated value of 0.42 for spherical particle shape and 0.54 for both the two and four clumped spheres was obtained.

It is also evident from this figure that although the inter-particle friction is zero, there exists a finite bulk friction due to interlocking of particles in the shear plane. Another worth noting point is that, although a two clumped sphere have a tendency to roll about an axis connecting both the spheres when compared to a four clumped sphere, a negligible difference can be seen in the bulk friction of both particle shapes at any inter-particle friction. The rolling behaviour of a two clumped sphere and a four clumped sphere can be different when subjected individually to sliding on a flat plane but their behaviour is shown to be identical in a bulk assembly. Further insights can be gained from the investigation of particle orientations of both the particle shapes (two and four spheres) in the shear plane during shearing of the assembly. Such particle scale analysis of orientations in the shear box is out of scope in this work.

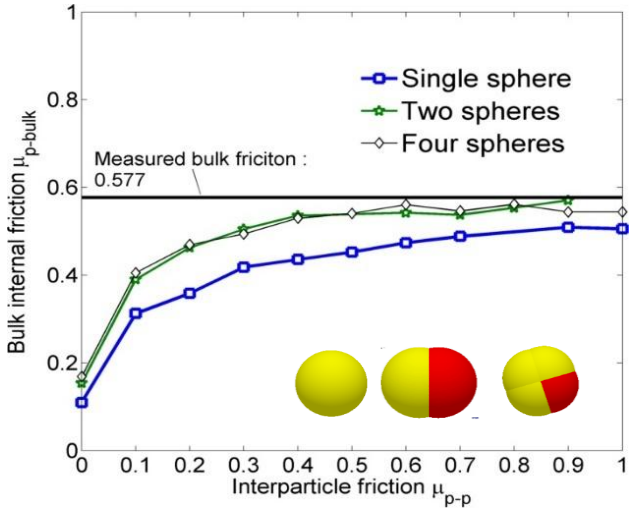

Figure 4.9 Variation of bulk internal friction with the increase of inter-particle friction at zero rolling friction (Particle shapes: Single sphere, two clumped sphere and four clumped sphere).

4.4.3.2 Wall friction

Figure 4.10 shows the variation of bulk wall friction with the increase of particle-wall friction at zero rolling friction. It should be noted that only a maximum bulk wall friction of 0.17 was achieved for spherical particles and 0.35 for two and four clumped spheres. It can be seen that the bulk wall friction is equal to the corresponding particle-wall friction at lower values i.e. all the particle-wall contacts in the shear plane are fully mobilised. As there is no interlocking (unlike in the case of internal friction) the bulk wall friction is not greater than the particle-wall friction. It is also evident that as the particle-wall friction is increased, a majority of the particle-wall contacts are not fully mobilised leading to a bulk wall friction smaller than the particle-wall friction.

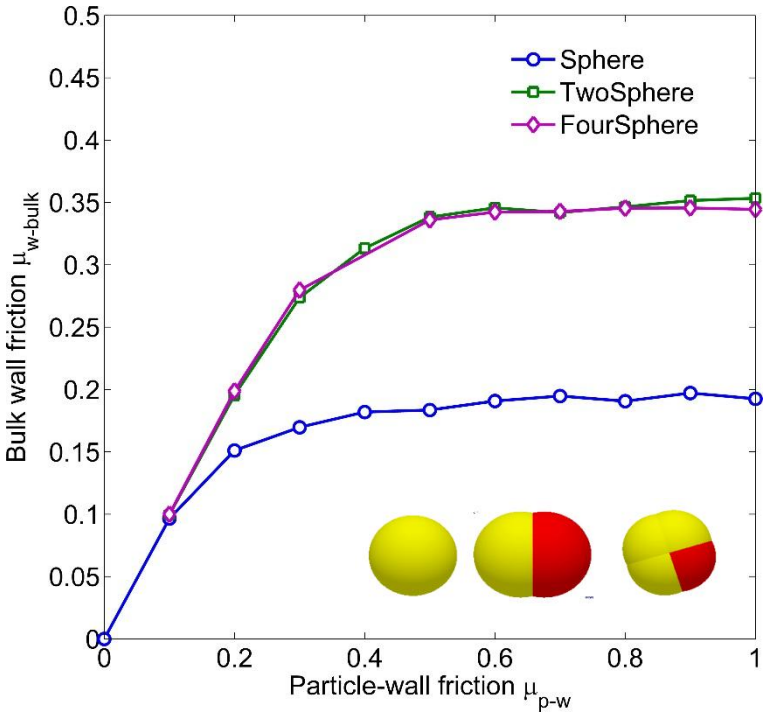

Figure 4.10 Variation of bulk wall friction with the increase of particle-wall friction (zero rolling friction).

4.4.4 Remarks

The plateau in the variation of bulk friction above a particle friction of 0.4 in both wall friction and internal friction simulations implies that the tendency of the interlocking decreases at higher particle friction. The same behaviour has also been observed in the simulations of Härtl and Ooi (2011) and Ketterhagen et al. (2009b).

Ketterhagen et al. (2009a) in his simulations of shear tester highlighted that the particle rotations during the shearing play a major role in limiting the bulk friction and they proved that by restricting the particle rotations, a higher bulk internal friction was achieved at higher inter-particle friction. They concluded that by allowing particle rotations, the maximum internal friction achieved was approximately close to 20^{o} whereas by restricting particle rotations, an internal friction as high as 70^{o} was achieved at an inter-particle friction of 0.8. The same effect has also been shown for particle-wall friction simulations.

To get further insights into the saturation of bulk friction, the particle rotations in the shear plane and the corresponding mobilisation of the particle-wall contacts are investigated. In the following section, the polar distribution of the particle rotations and the corresponding mobilisation of the friction at particle-wall contacts are shown followed by the discussion of results of bulk friction obtained by fully restricting the particle rotations in internal friction and wall friction simulations. Furthermore, instead of fully restricting the particle rotations, simulations were conducted with the addition of a rolling friction torque to limit the particle rotations based on the value of the coefficient of rolling friction. The variation of bulk internal friction with the inter-particle friction at different values of rolling friction is then presented and discussed.

4.5 Particle scale vs. bulk scale friction: Influence of rotations

4.5.1 Mobilised contact friction and particle rotations

From Figure 4.10, it can be concluded that at a particle-wall sliding friction of 0.5, only a bulk wall friction of 0.17 and 0.34 was achieved for single sphere and two clumped spheres respectively. This implies that 68 % of the total frictional force was mobilised for two spheres and merely 34 % for the single sphere. However, at a particle-wall friction of 0.1, friction was fully mobilised irrespective of the particle shape. In order to further study this behaviour, the mobilised friction of each contact in the shear plane was analysed. The time averaged polar distribution of mobilised contacts in the circular shear plane (between the particle assembly and the flat wall) during shearing with the particle-wall friction of $\mu_{p\text{-}w}$ = 0.1 and 0.5 are shown in Figure 4.11 (a) and (b) respectively. The data is time averaged during the steady state. The radial coordinate indicates the mobilised friction (ratio of the tangential contact force to the normal contact force). It can be seen that with $\mu_{p\text{-}w}$ = 0.1, a majority of the contacts fall on the line of 0.1 indicating a fully mobilised state and for $\mu_{p\text{-}w}$ = 0.5 the values of mobilised friction are highly dispersed within the circle of

0.5 and particularly for spheres all the points lie close to the zero value leading to a low value of bulk friction.

Figure 4.11 (c) and (d) shows the time averaged polar distribution of angular velocity in the shear plane with particle wall friction of $\mu_{p\text{-}w}$ = 0.1 and 0.5 respectively. The data shown here is the ensemble average of the angular velocities of all the particles in a 30^o segment. It is evident that with a particle-wall friction of $\mu_{p\text{-}w}$ = 0.1 and for all the simulated particle shapes, the angular velocity during the shearing is approximately equal to zero (pure sliding) and as the particle-wall friction is increased to 0.5, it increases to a finite value and in particular, it is higher for the sphere than for the other two particle shapes.

The increase in angular velocity can be explained by the fact that the torque acting on the particles in the shear plane is proportional to the sliding friction at the contact (either particle-particle contact or a particle-wall contact). The shearing of the particle assembly at higher contact friction generates a higher torque which leads to an increase in particle rotations in the shear plane. Therefore, the frictional resistance at the contact relieves by the increased particle rotations and hence majority of the contacts are not fully mobilised at higher particle friction.

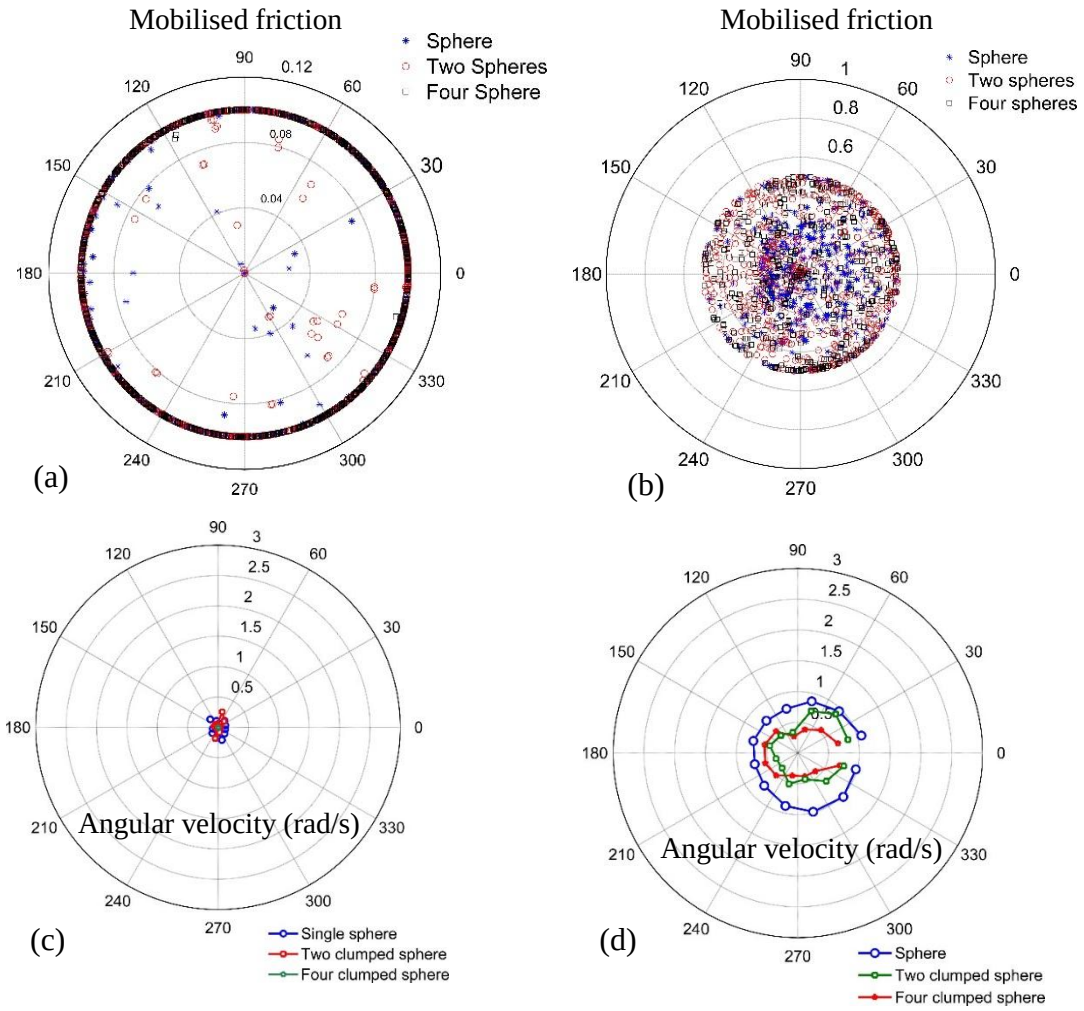

Figure 4.11 Polar distribution of particle-wall contact data in the shear plane (a) mobilised friction at particle wall friction of 0.1 (b) mobilised friction at particle wall friction of 0.5 (c) angular velocity at particle wall friction of 0.1 (d) angular velocity at particle wall friction of 0.5.

4.5.2 **Bulk friction: Rotations vs. No rotations**

Additional simulations were conducted to calculate the bulk friction by not allowing the particle rotations during shearing. Figure 4.12 (a) and (b) shows the comparison of bulk friction with and without particle rotations for internal friction and wall friction simulations respectively. It is clearly evident from Figure 4.12 (a), that at any inter-particle friction, the bulk internal friction is increased by restricting the particle

rotations and the increase becomes more dominant as the particle friction is increased. For example, at $\mu_{p\text{-}p}$ = 0.1 there is hardly any influence and at $\mu_{p\text{-}p}$ = 0.5 the bulk friction is approximately doubled by limiting the rotations. The similar effect can be seen in the case of wall friction simulations as shown in Figure 4.12 (b).

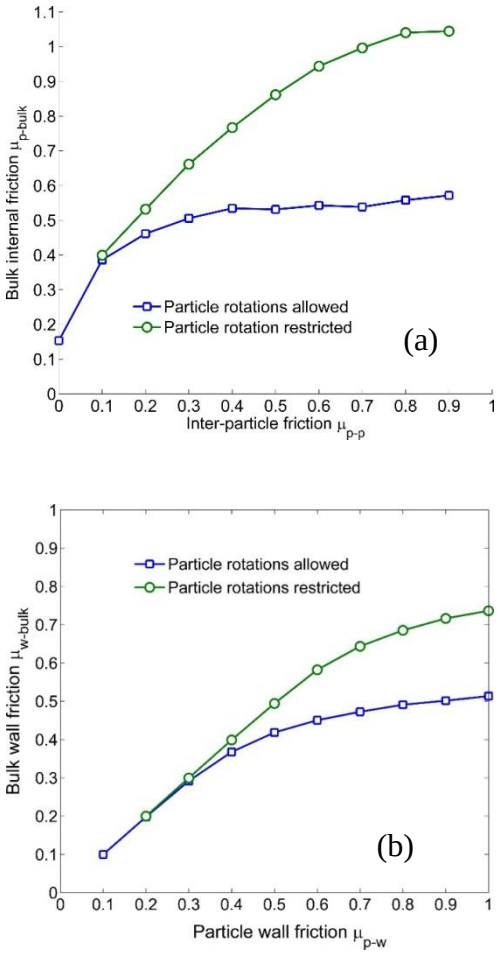

Figure 4.12 Effect of particle rotations on bulk friction (a) Internal friction (b) Wall friction.

4.5.3 Influence of rolling friction on bulk friction

Although fully restricting the particle rotations is an easy way of achieving the higher bulk friction, it is not realistic due to the fact that the degree of the particle's rotation is related to the magnitude of sphericity. An alternative way is to apply a rolling friction torque to partly limit the rotations based on the value of the coefficient of

rolling friction. In this section the effect of rolling friction on the bulk friction is reported and its influence on the silo flow predictions is reported in chapter 5.

The shape effects are often simulated with the use of a rolling friction model (Ai et al., 2011; Balevičius et al., 2012; Markauskas and Kačianauskas, 2010; Wensrich and Katterfeld, 2012; Zhou et al., 2002). Markauskas and Kačianauskas (2010) used multi- sphere model to approximate the shape of rice grains and they tested the model by simulating the discharge of rice grains in a hopper. They concluded that the multi sphere approach without the use of rolling friction does not give satisfactory results but when combined with rolling friction a good agreement was found. However, the choice of rolling friction coefficient is not clear yet in the literature. In this work the rolling friction was used as a calibration parameter which can take into account of any shape differences that exist between the test pellets and the modelled shape.

Figure 4.13 shows the variation of bulk internal friction with the increase of inter-particle friction at different rolling friction coefficients for a two-clumped sphere. The bulk frictions with zero rolling friction and with no particle rotations are used as a reference to study the effect of rolling friction at different inter-particle frictions. It was found that the effect of rolling friction on bulk internal friction depends on the value of inter-particle friction. The following conclusions can be drawn from this figure:

- Increasing the rolling friction coefficient (μ_r) from 0 to 0.1 at an inter-particle friction ($\mu_{p\text{-}p}$) of 0.1, there is a negligible change in the bulk internal friction whereas a nearly 20 % increase in the bulk friction is evident at $\mu_{p\text{-}p} = 0.5$.
- If the rolling friction is greater than the inter-particle friction, a decrease in bulk internal friction ($\mu_{p\text{-}bulk}$) is seen when compared to the one with zero rolling friction at the same inter-particle friction. For example, at $\mu_{p\text{-}p} = 0.4$ and $\mu_r = 0$ the $\mu_{p\text{-}bulk} = 0.52$ whereas at $\mu_{p\text{-}p} = 0.4$ and $\mu_r = 0.5$ the $\mu_{p\text{-}bulk} = 0.45$.
- At all inter-particle frictions, only a slight amount of rolling friction in the range of 0.05 - 0.1 is required to increase the bulk friction and any value higher than this does not lead to an increase in the bulk friction.

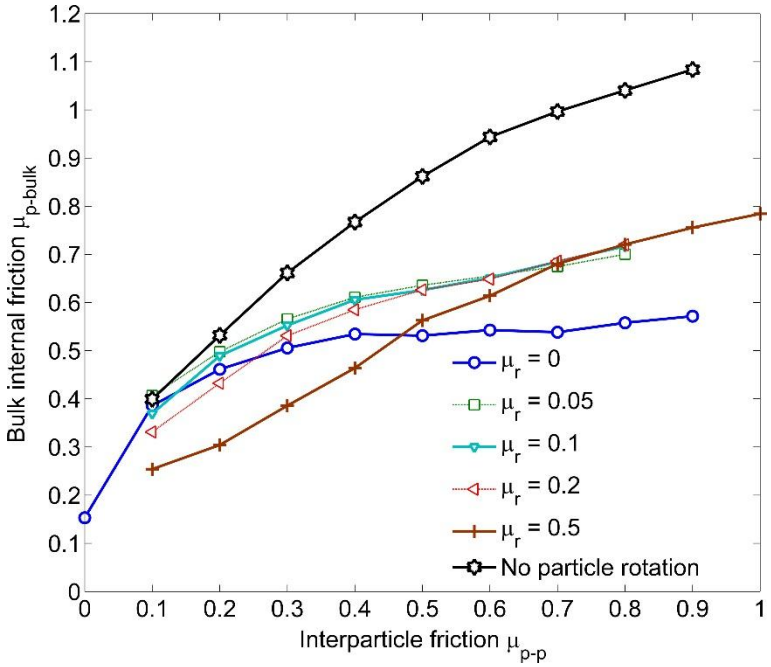

Figure 4.13 Bulk internal friction vs. inter-particle friction at different rolling friction for two clumped sphere.

As it was shown earlier that the particle rotations in the shear plane are negligible at lower particle friction and increases with the increase of particle friction, the amount of rolling resistance therefore required depends on the value of particle friction. However, the rolling friction torque implemented (refer to equation (4.1)) in this work neither depends on the particle friction nor on the magnitude of angular velocity instead it acts in a direction opposite to the unit angular velocity vector and it is directly proportional to the coefficient of rolling friction. As a result, the choice of rolling friction greater than the inter-particle friction is not desirable because of numerical stability and it could give unphysical bulk frictional behaviour.

4.6 Choice of frictional parameters from calibrated model

Of the three particle shapes (sphere, two clumped sphere and four clumped sphere) that were considered for the calibration simulations, a two clumped sphere was chosen to approximate the test pellets to save computational time. The particle-

particle friction, rolling friction and particle-wall friction correspond to the measured bulk properties were determined from the developed calibration chart. The calibration charts for the particle-particle friction and the particle-wall friction are shown in Figure 4.14 (a) and (b) respectively.

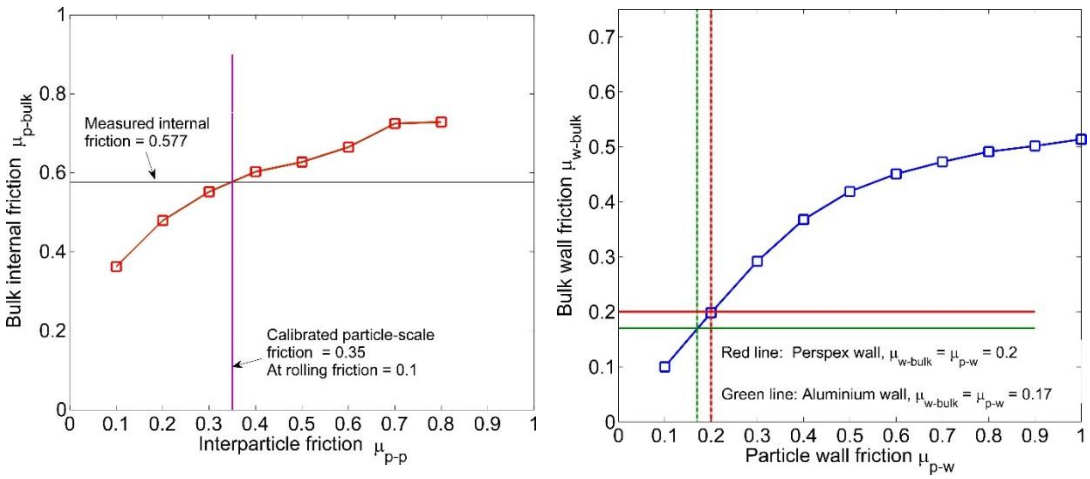

(a) Particle-particle friction **(b) Particle wall friction**

Figure 4.14 Calibration of particle scale friction against the bulk friction.

The rolling friction was used as a calibration parameter to achieve the required bulk friction of the test pellets. The rolling friction of 0.1 is found to reproduce the bulk friction values ranging from 18 – 38 deg. An inter-particle friction of 0.35 with a rolling friction of 0.1, a particle-wall friction of 0.17 and 0.2 for aluminium wall and perspex wall respectively has been used for the validation simulations as presented in chapter 5.

4.7 Summary

Jenike direct shear box simulations have been conducted to calibrate the frictional parameters of the model by obtaining the relationship between the bulk scale and particle scale friction. The multi-sphere method has been used to represent the cylindrical test pellets. A novel approach of replacing the flat shear lid geometry with a particle wall has been developed in order to apply a constant normal force and the details of its implementation in the EDEM software have been discussed. The effect

of lid-rotation, the coefficient of restitution and the particle shape on the bulk internal friction has been discussed. The relationship between the bulk friction and the particle scale friction has been explored for three scenarios: with and without rolling friction and the case when the particle rotations are fully restricted during the shearing. The following key conclusions can be drawn from this chapter:

- Without the application of rolling friction torque, the maximum bulk internal friction that can be obtained in the DEM model using the particles with two or four clumped spheres is 0.54 *i.e.* approximately 28^o of internal friction angle for the given set of parameters. The model is thus not able to simulate the flow behaviour of material with bulk friction values greater than 28^o. However, the majority of the pellets handled in industries have a bulk internal friction values in the range of 18^o to 45^o. For example, the HDPE test pellets used in this work have a bulk internal friction of 30^o.
- The particle scale data of angular velocity and the mobilised friction in the shear plane between the particles and the wall revealed that the particle rotations in the shear plane are dominant at higher inter-particle friction and the bulk friction resistance is relieved by the increases rotations. A huge increase in bulk internal and wall friction was found when the particle rotations are completely restricted during shearing.
- Increasing the rolling friction coefficient (μ_r) from 0 to 0.1 at an inter-particle friction $\mu_{p\text{-}p}$ = 0.1, a negligible change in bulk internal friction was found whereas there is a nearly 20 % increase in bulk friction at $\mu_{p\text{-}p}$ = 0.5.
- If the rolling friction is greater than the inter-particle friction, the bulk internal friction ($\mu_{p\text{-}bulk}$) decreases when compared to the one with zero rolling friction at the same inter-particle friction. For example, at $\mu_{p\text{-}p}$ = 0.4 and μ_r = 0 the $\mu_{p\text{-}bulk}$ = 0.52 whereas at $\mu_{p\text{-}p}$ = 0.4 and μ_r = 0.5 the $\mu_{p\text{-}bulk}$ = 0.45.

Chapter 5

5. Quantitative validation of DEM for silo flow and parametric study

5.1 Introduction

In this chapter, the accuracy of the DEM in simulating the flow patterns of cylindrical pellets in a flat bottom silo is assessed. The predicted flow rate, the velocity profiles and the flow channel boundary were compared with the corresponding measurements. Finally, a parametric study was conducted to investigate the effect of frontal wall friction, coefficient of restitution, inter-particle friction and rolling friction.

5.2 Validation experiment

A validation experiment involves the careful collection of appropriate, reliable and repeatable data in order to use it to assess the accuracy of corresponding predictions from a simulation. The flow behaviour of pellets during the discharge in a flat bottom (FB) silo was chosen as a validation experiment mainly because of the flow patterns produced in the FB silo represents the diverse characteristics of a granular material, such as co-existence of both stagnant and flowing zones during discharge. Assessing the capability of DEM in predicting the size and shape of these zones and the velocity profiles within the flow zone gives a first-hand idea about the accuracy of the model before using it to simulate the flow in a silo blender.

The computational time required to simulate a validation experiment should be manageable so that a large number of parametric studies can be conducted to identify the influential model parameters that can affect the flow. For this purpose, the scale of the model silo is chosen such that the number particles are approximately around 50,000 - 60,000. As the plastic pellets are cohesionless, the stress level within the material does not influence the frictional properties to a greater extent. Therefore, the model can be equally applicable to large scale silos without compromising on the

accuracy. The validated model is then used to simulate the flow in a relatively large scale model blending silo consisting of 606,000 particles (presented in chapter 7).

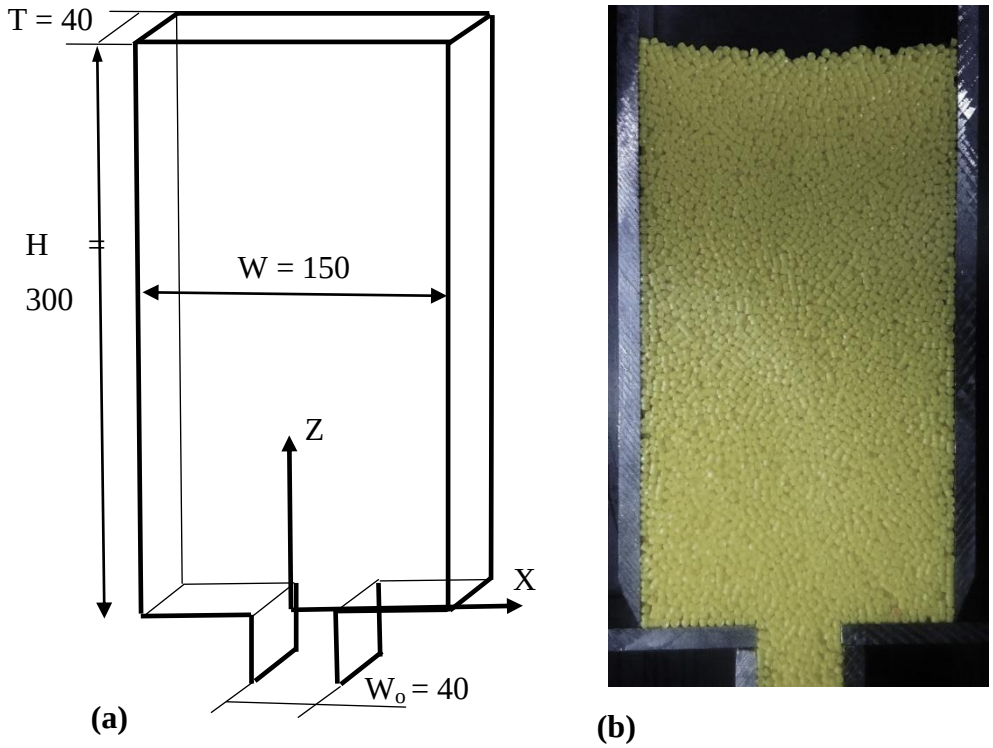

Figure 5.1 (a) Dimensions (in mm) of the test silo (b) Snapshot of particle assembly in the experiments.

A silo width of 150 mm with a thickness of 40 mm was used. The size of the outlet was set to 40 mm. The schematic of the silo with dimensions is shown in Figure 5.1 (a) and a photograph of the experimental set-up with test pellets is shown in Figure 5.1 (b). The silo was filled with pellets to a height of 280 - 300 mm. The discharge was then allowed by manually opening the thin plate attached to the outlet. A Photron FASTCAM SA6 camera was used to record the flow. The camera was mounted on a stand with its axis perpendicular to the central axis of the silo. Care was taken to ensure that the camera was aligned parallel to the ground. Images were then recorded at 500 fps with a spatial resolution of 1940 pixels x 1440 pixels. The maximum possible recording time at this frame rate was 3.8 sec. In addition to the

collection of images for velocity measurement, the filling bulk density and the mass flow rate were also measured.

5.3 DEM Model

A numerical silo same as the dimensions of the test silo was created as shown in Figure 5.2 (a). The silo is centrally filled using a dynamic particle factory in the commercial software EDEM 2.7. The number of particles at the end of filling was found to be 53,492. At the end of the particle generation, the assembly was considered to be static when the average kinetic energy of the system was found to be negligible ($< 10^{-12}$ J). The discharge was then allowed by simply deleting the outlet wall. The simulation time step was chosen as 10 % of the Rayleigh time. The data was saved at an interval of 0.005 s.

The discrete particle scale results were averaged using a coarse graining (CG) method in which Gaussian weighting function was used to get the continuum fields (Labra, Ooi and Sun, 2013). Several researchers have successfully applied CG to get the internal stress and velocity fields from discrete data (Zhu et al., 2007). A continuum field consisting of cartesian grid points with increments of dx = 6 mm, dy = 4 mm and dz = 6 mm was created and any quantity at each node were calculated from the particle data by applying a Gaussian weighting function of the width of 3 times the radius of the particle. A detailed investigation on selection of length and time scales for analysis of silo discharge was conducted by Weinhart et al. (2016).

Table 5.1 Values of DEM input parameters used for validation.

Property name	DEM Particles
Shape	Two clumped sphere
Diameter, d_p (mm)	3
Aspect ratio	1.25
Density, ρ_s (kg/m^3)	950
Poisson ratio, ν	0.4
Shear modulus, G (Pa)	$1x10^8$
Particle coefficient of restitution, e	$1x10^{-4}$
Particle-Particle sliding friction, $\mu_{s\text{-}pp}$	0.35
Particle-Particle rolling friction, $\mu_{r\text{-}pp}$	0.1
Particle-wall sliding friction, side and bottom walls, $\mu_{s\text{-}psbw}$	0.17
Particle-wall sliding friction, front and back walls, $\mu_{s\text{-}pfbw}$	0.2
Particle-wall rolling friction, $\mu_{r\text{-}pw}$	0.1

5.4 Assessment of DEM predictions

The important variables that characterise the behaviour of pellets in a silo are bulk density, mass flow rate, stress fields and the velocity fields. As the internal stress fields are difficult to measure, if not impossible, only a detailed assessment of the accuracy of flow patterns was conducted. In this section, first the internal stress state at the end of filling was evaluated and compared against the analytical solution of Janssen (1895). The predicted bulk density at the end of filling and the mass flow rate were then compared with the measurements. Finally, the velocity profiles and the flow channel boundary (FCB) at different instants were compared with measurements and kinematic model (Nedderman and Tüzün, 1979).

5.4.1 Vertical stress distribution at end of filling

It is well known that the static pressure in a liquid stored in a container increases linearly with the depth. In contrast, Janssen (1895) showed that the vertical stress

inside the granular material reaches a saturation point after a critical depth from the top surface. This classical behaviour exhibited by the granular material is often referred to as the Janssen effect, which is created due to the fact that the portion of the total weight of the solids is carried by the wall friction.

With the assumptions that the vertical and the horizontal stresses are principal stresses and the stress is uniform across the cross-section of the silo, Janssen (1895) derived an analytical equation to calculate the vertical stress which is given by (5.1).

$$\boldsymbol{\sigma_{zz} = \gamma z_c \left[1 - \exp\left(\frac{z - H_f}{z_c}\right)\right]} \quad \textbf{(5.1)}$$

where γ is the unit weight N/m^3, z_c is the characteristic depth m, H_f is the filling height m, z is the distance from the bottom of the silo m.

For circular silo of diameter D, $\boldsymbol{z_c = \frac{D}{4K\mu_w}}$ **(5.2)**

For rectangular silo of width W and thickness T, $\boldsymbol{z_c = \frac{WT}{2K\mu_w[T+W]}}$ **(5.3)**

For rectangular silo with different wall friction, $\boldsymbol{z_c = \frac{WT}{2K[\mu_{w-sw}T+\mu_{w-fw}W]}}$ **(5.4)**

$$\boldsymbol{K = \frac{1-\sin\emptyset}{1+\sin\emptyset}} \quad \textbf{(5.5)}$$

where K is the lateral pressure ratio in the active state, μ_w is the bulk wall friction on all walls, ϕ is the angle of internal friction, $\mu_{w\text{-}sw}$ is the bulk wall friction with the side walls and $\mu_{w\text{-}fw}$ is the bulk wall friction with the frontal walls.

The shape of the vertical stress distribution depends on the value of K and μ_w. It should be noted that the friction calculated at bulk scale should be used in the equation (5.1). The bulk friction values corresponding to the particle scale DEM values were taken from the developed calibration chart.

Figure 5.2 (b) shows the comparison of the DEM calculated averaged vertical stress distribution with the calculations using Janssen equation. It can be seen that in both cases, the stress increases linearly up to a certain depth and then begins to saturate towards a constant value. Although the two major assumptions of Janssen's theory are questionable, a good agreement with the DEM results can be seen. A detailed analysis conducted by Walters (1973) showed that the errors associated with the Janssen assumptions are often small.

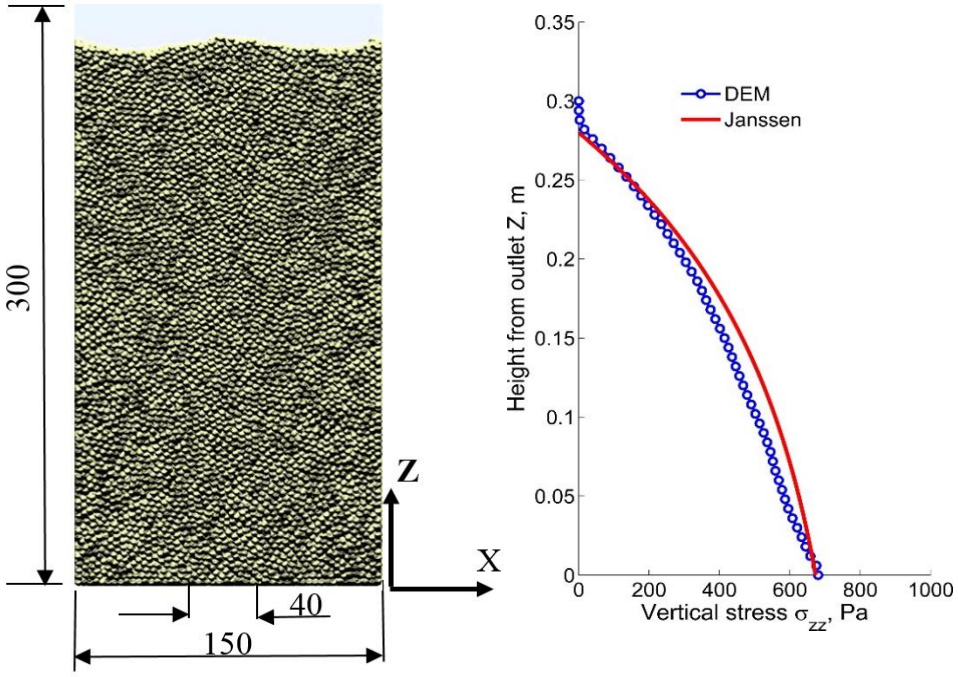

Figure 5.2 (a) Snapshot of the DEM particle assembly (b) Comparison of internal vertical stress distribution calculated from DEM and Janssen equation.

5.4.2 Bulk density and flow rate

Table 5.2 shows the comparison of filling bulk density, mass flow rate and volumetric flow rate against the measurements. The bulk density was calculated from the volume of the filling and the total mass of the particles. The obtained bulk density in the simulation is 6.6 % lower than the experiments although the packing was created with a low inter-particle friction of 0.15. The error could be due to the

fact that the cylindrical pellets give denser packing than with approximated multi-sphere particle of the same solid density.

Table 5.2 Comparison of bulk density and time averaged flow rate.

	Experiment	Simulation	% difference
Bulk density, kg/m^3	631 ± 6	590	-6.6
Overall Mass flow rate, kg/s	0.423 ± 0.012	0.408	-3.7
Overall Volumetric flow rate, L/s	0.670 ± 0.02	0.692	+ 3.2

Cleary (2002) showed that by increasing the angularity of a particle, the flow rate can reduce up to 28 % due to the increased flow resistance. This also implies that an increase in volumetric flow rate can be expected in simulations because of using a simplified particle shape (two clumped sphere) which has a 16 % higher sphericity than the test pellets. This problem was overcome with the inclusion of a rolling friction torque which takes into account the differences in the shape between the test and the numerical particles. As it can be seen in Table 5.2, only a slight discrepancy of 3.7 % and 3.2 % was found in mass flow rate and volumetric flow rate respectively.

5.4.3 **Flow patterns**

5.4.3.1 Qualitative comparison

Figure 5.3 shows the images of flow from the experiment and the simulation at different instants during the discharge. As expected, an internal flow is observed in experiments with a stable stagnant zones on either side of the flowing zone. It is also interesting to see a thin stagnant layer of 1 - 2 particle thick next to side wall (which is clearly visible in images at t = 0.6 sec and 0.7 sec). This particle layer is thought to be the result of interlocking between the cylindrically shaped pellets. The observed flow behaviour in the experiment is similar to that predicted by the DEM simulation. The stagnant layer of particles next to the side wall can also be seen in the

simulation. The quantitative comparison of predicted velocities against the measurements is discussed in the following subsections.

5.4.3.2 Centreline velocity

Figure 5.4 shows the comparison of predicted temporal variation of the centreline velocity with the corresponding measurements. It can be seen that in both the experiments and simulations, the centreline velocity at any height increases steadily to a maximum value and then decreases before reaching the steady state. Two noticeable discrepancies can be seen from this figure: the flow initiates more quickly during the simulations and velocities are under-predicted at the steady state.

5.4.3.3 Velocity profiles at different instants

The accuracy of the vertical velocity profiles at selected time instants at three different heights of Z = 20 mm, 40 mm and 80 mm is illustrated in Figure 5.5, Figure 5.6 and Figure 5.7 respectively. It can be seen from these figures that at t = 0.1 sec (during the flow initiation), the measured vertical velocities at any height are smaller in magnitude when compared to the simulation at the same instant. However, as the discharge progresses towards the steady state, the predicted velocities are in good agreement with the experiments at all the further times and at all heights. A reasonably good quantitative agreement was found when the flow is fully developed. The under prediction during the initiation of the flow is due to the slower upward propagation of the flow in the experiment when compared to the DEM simulation. This discrepancy could be attributed due to the particle shape approximation which further led to a lower bulk density at the end of filling thereby causing the upward propagation of the flow to be faster in the simulations.

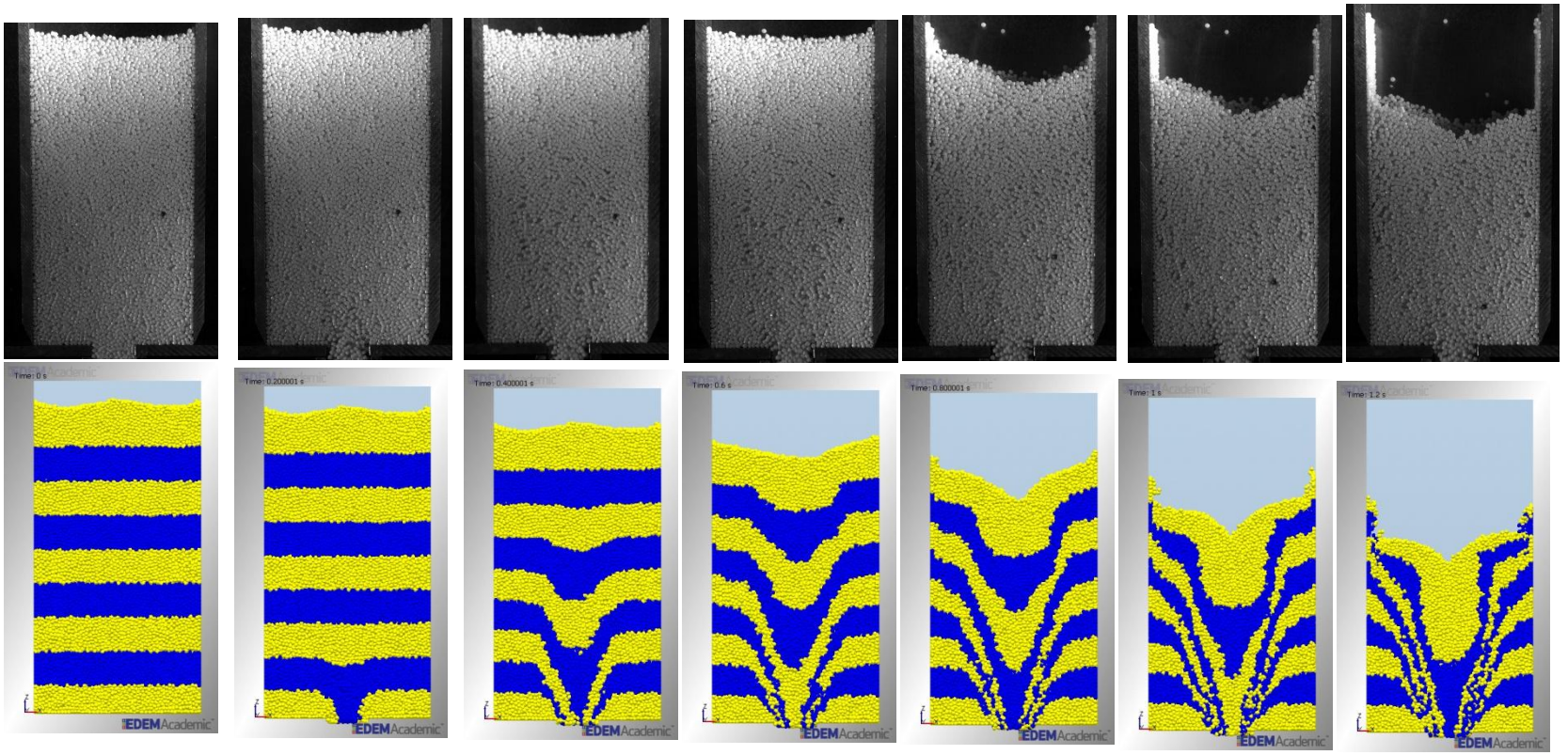

Figure 5.3 Snapshot of flow patterns at different instants from simulation and experiment.

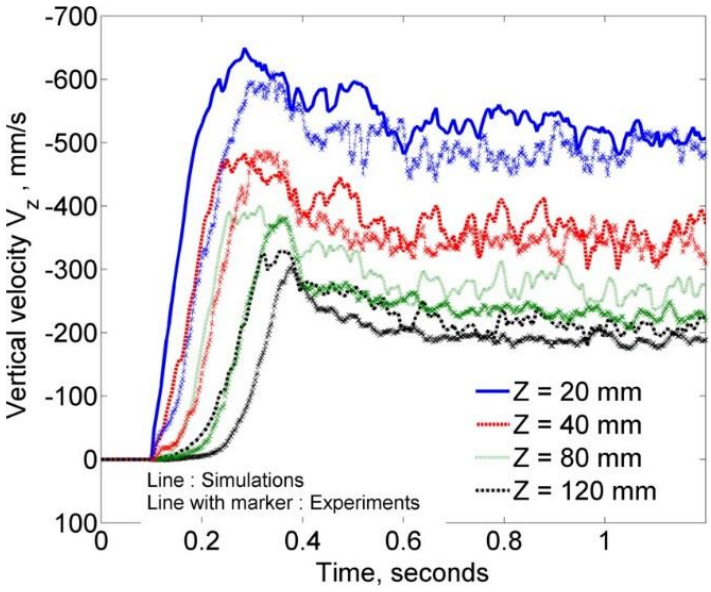

Figure 5.4 Temporal variation of centreline velocity at different heights.

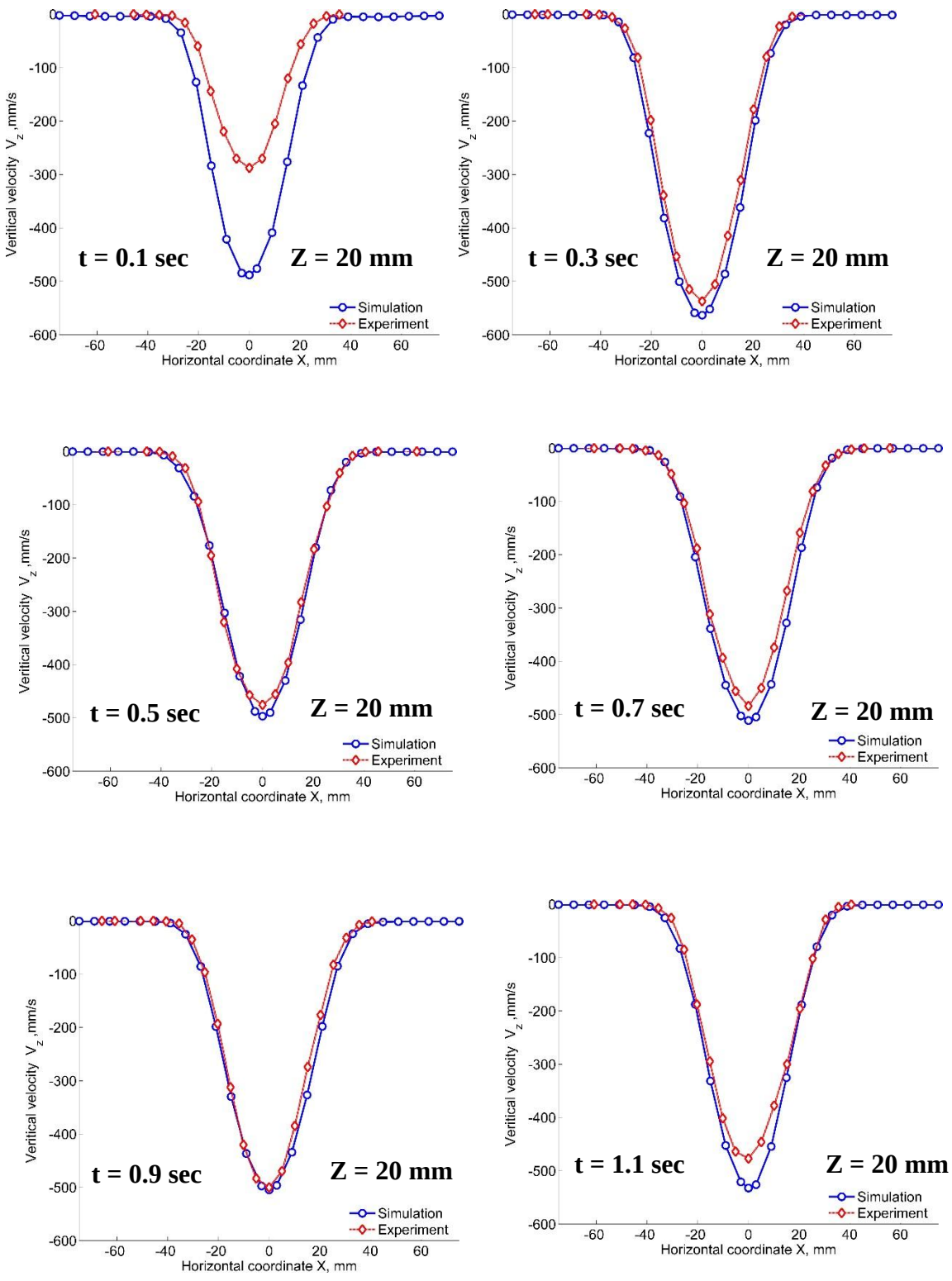

Figure 5.5 Comparison of DEM predicted vertical velocity profiles with PIV measurements at Z = 20 mm at different instants.

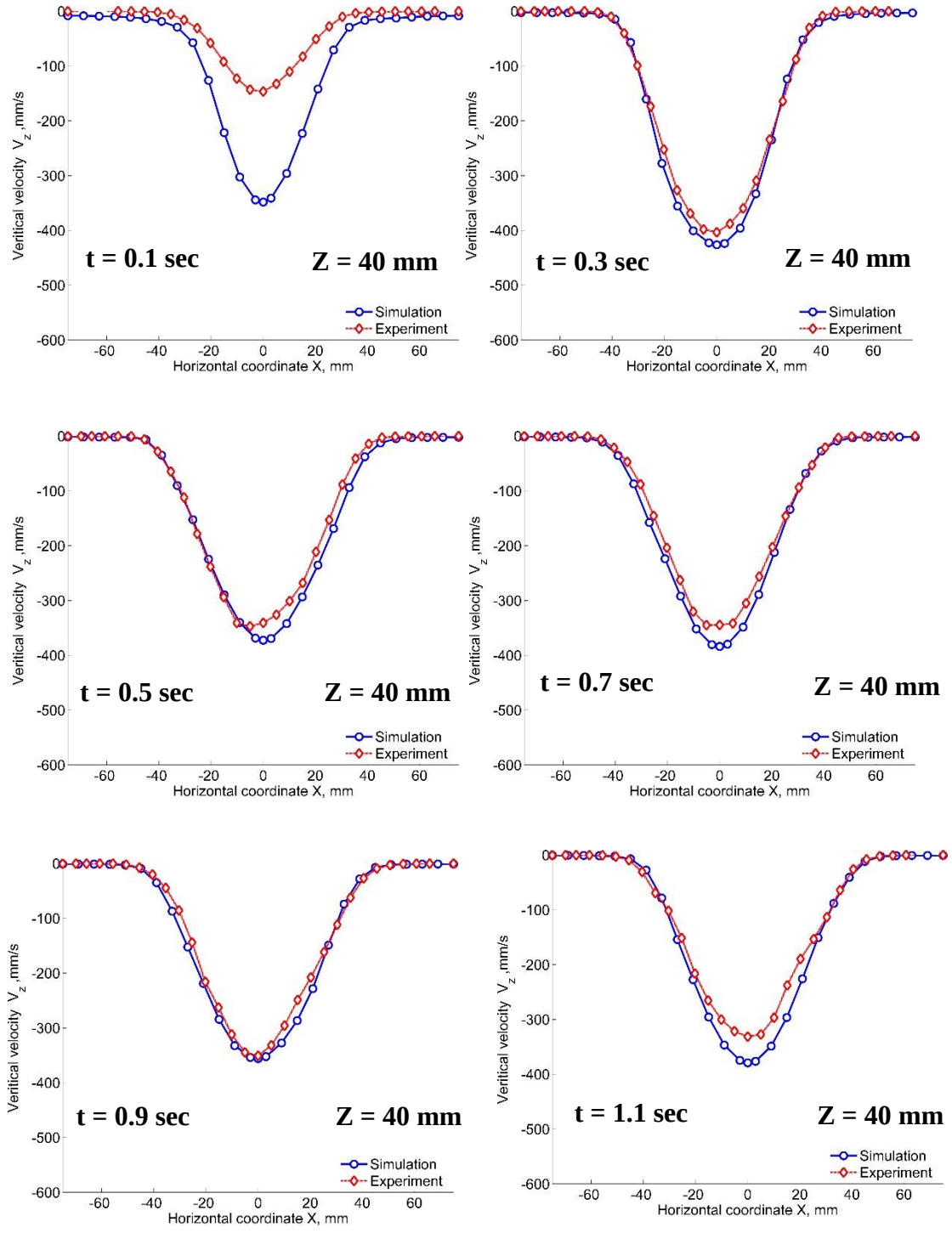

Figure 5.6 Comparison of DEM predicted vertical velocity profiles with PIV measurements at Z = 40 mm at different instants.

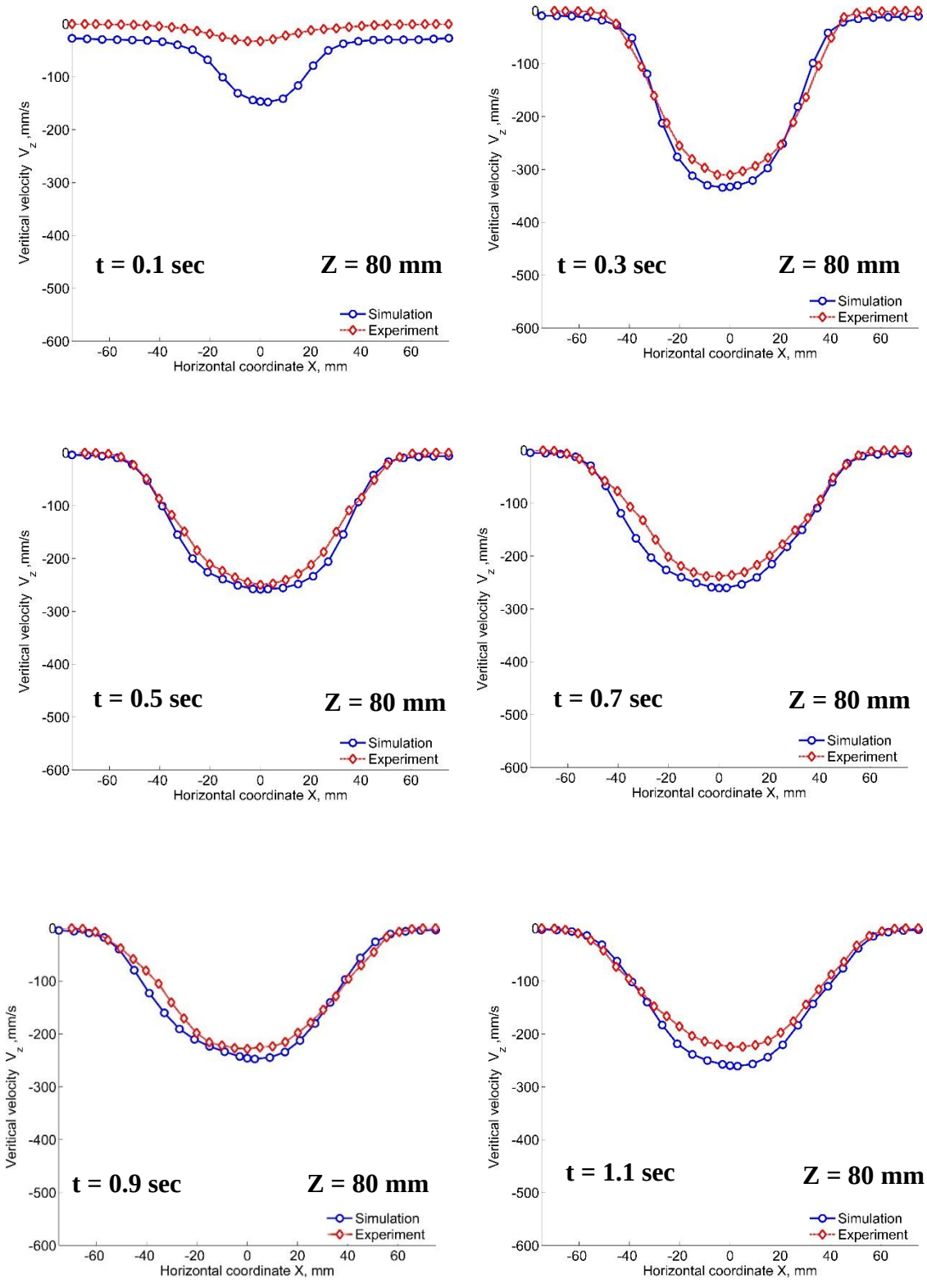

Figure 5.7 Comparison of DEM predicted vertical velocity profiles with PIV measurements at Z = 80 mm at different instants.

5.4.3.4 Time-averaged velocity profiles

The velocity profiles at each height are time averaged from t = 0.5 sec to 0.7 sec from the start of discharge. The predicted time averaged velocity profiles were compared with the corresponding PIV measurements as shown in Figure 5.8 (a) – (d). The DEM velocities at the front wall and those averaged along the depth are shown here. It is obvious that any deviation of velocities at the front wall surface from the average indicates the presence of velocity gradients along the depth. It can be seen that the predicted shape of the velocity profile at all heights is in a good match with the experiment except that the magnitude is slightly over predicted. Considering the simplifications made in the model, the DEM predictions of velocity profile can be considered to be in reasonably good agreement.

The DEM velocity predictions were also compared with the kinematic model. The kinematic constant *B* was calculated from the experimental vertical velocity data by fitting the equation (5.6).

$$\mathbf{V_z = a\ exp[-mx^2]} \tag{5.6}$$

$$\mathbf{B = \frac{1}{4mz}} \tag{5.7}$$

where *a* and *m* are fitting constants, *z* is the distance above the outlet.

As shown in Figure 5.8 (a) – (d) the kinematic model fits well with the experimental data at heights very close to the outlet (at Z = 20 mm and 40 mm) but a deviation is evident at Z = 120 mm where the velocity profile is flatter near the centre. The deviation of the kinematic model from the experiment in the regions far from the outlet exists mainly because it was assumed in the model that the frontal walls do not influence the velocity field. However, this assumption is valid only when the physical wall boundaries extend to ± ∞, but it is not true in the current test silo where the velocity fields could be highly affected by the frontal wall boundaries. As the DEM simulation involves no such assumptions, a close match in the shape of the

velocity profile can be seen. The evaluation of *B* from both the experimental and the DEM data proved that it decreases with the distance above the outlet as shown in Figure 5.9. A similar variation of B has been found in the experiments of Choi et al. (2005).

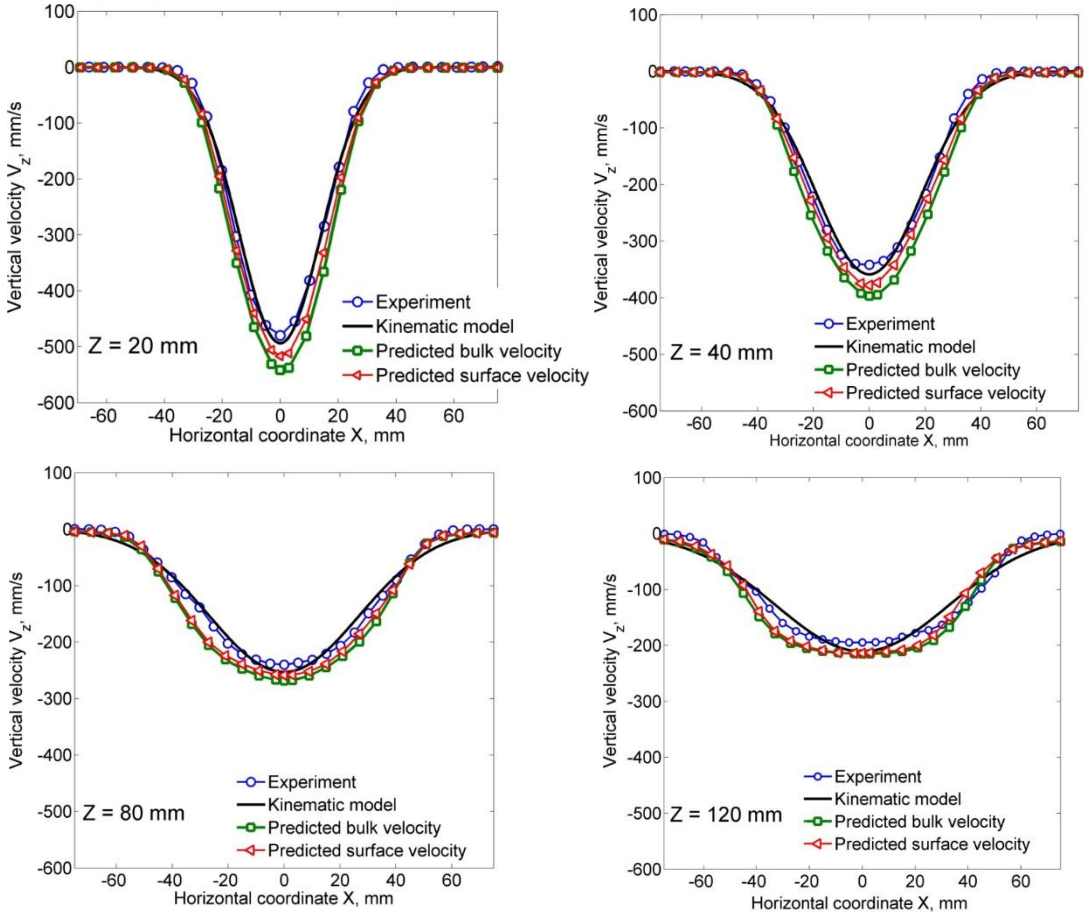

Figure 5.8 Comparison of steady-state vertical velocity profiles with experiment and kinematic model.

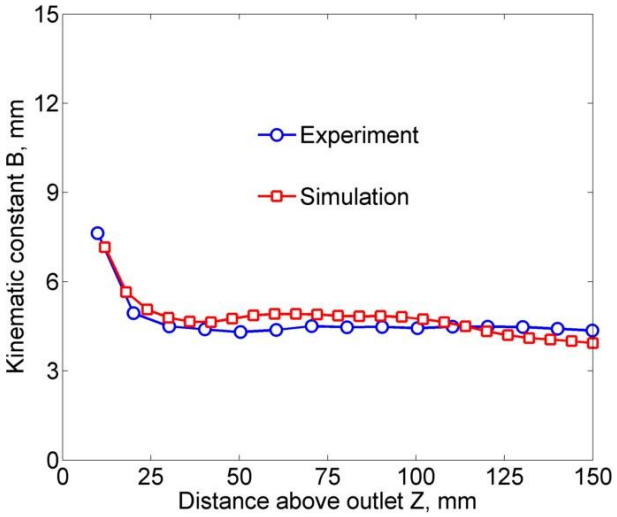

Figure 5.9 Comparison of kinematic constant from simulation and experiment.

The accurate prediction of horizontal velocity profiles is equally important as they describe the horizontal diffusion characteristics of the flow. Nedderman and Tüzün (1979) defined the horizontal velocity as a function of the gradient of vertical velocity in the horizontal direction and kinematic constant as given by (5.8).

$$\mathbf{u} = -\mathbf{B}\frac{\partial \mathbf{v_z}}{\partial \mathbf{x}} \qquad \textbf{(5.8)}$$

Figure 5.10 shows the comparison of time-averaged horizontal velocity profiles at heights of Z = 20, 40, 80 and 120 mm above the outlet. It can be seen that the predicted location of the maximum horizontal velocity at all heights is in close agreement with the experimental data. According to equation (5.8), the location of maximum horizontal velocity should correspond to that of the maximum horizontal gradient in the vertical velocity, which holds to be true as seen from both the experimental and simulation data.

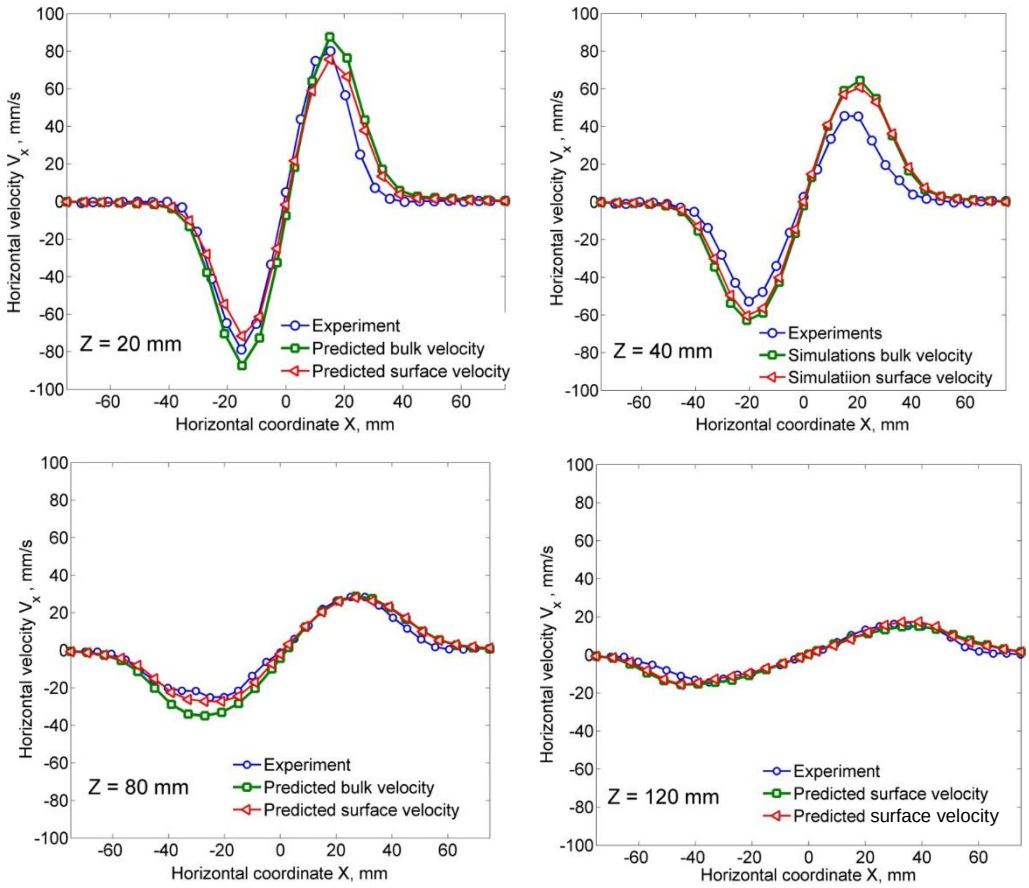

Figure 5.10 Comparison of steady-state horizontal velocity profiles with experiment.

5.4.3.5 Flow channel boundary (FCB)

Refer to section 3.8 for details on the definition of FCB. Figure 5.11 (a) – (c) shows the comparison of FCB evaluated from the time averaged vertical velocity profiles based on the three criteria. The minimum velocity limit based on the first criterion (1% of centreline velocity) can be within the uncertainties of experimental data particularly at heights far from the outlet. To avoid the errors while comparison, two other criteria based on 5 % and 10 % of centreline velocity were used in both the experiments and the simulations. As it can be seen from this figure that a good agreement was found close to the outlet whereas a discrepancy of approximately 2 - 3 particles far from the outlet and close to the side walls can be found. This discrepancy is due to the fact that the flat surface of the cylindrical test pellet is the

aligned with the side walls creating a more stable stagnant layer while in the simulations, although a rolling friction was used to represent the shape these localised effects were not reproduced.

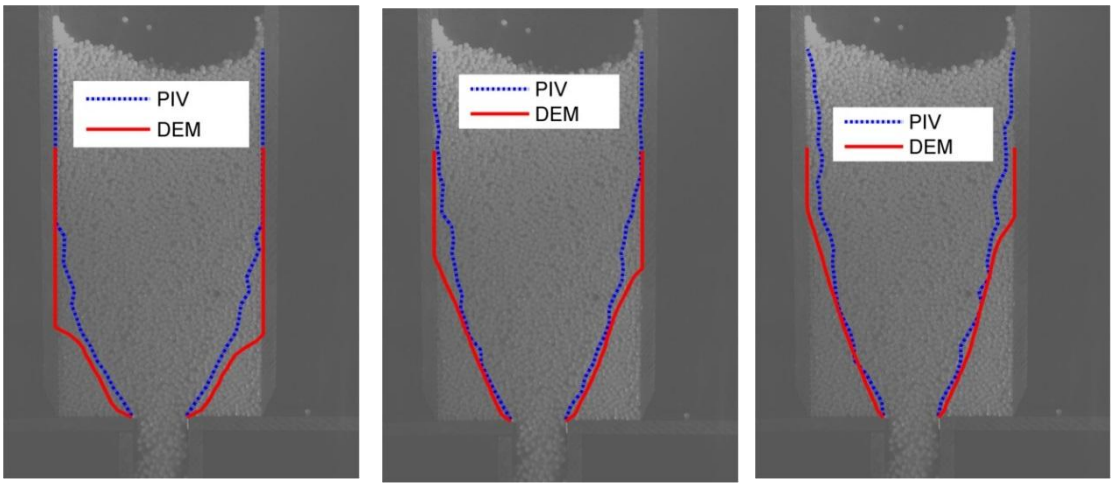

Figure 5.11 Comparison of flow channel boundary at different criteria (a) 1% (b) 5% (c) 10 % of centreline velocity

5.5 Effect of frontal wall friction

The granular material is highly confined by the walls of the planar 2D lab scale silo. It is known to be desirable to have a low friction on the front and back (frontal) walls to reduce the boundary effects on the flow. The effects of the frontal wall friction on the behaviour of flowing material includes:

- The condition of plane strain is violated and a 3D flow can be created,
- The decreased internal vertical stress due to increased frontal wall friction can lead to a different flow patterns.

The validated model presented in the above section is further used to explore the effect of the frontal wall friction. A transition of uniform to internal flow was found with the increase of frontal wall friction from zero to 1 and corresponding force

chain distributions were analysed qualitatively to get further insights into the flow transition.

5.5.1 Internal stress

Karim and Corwin (2014) presented the experiments and analysis on how to recover the Janssen effect in a 2D horizontal arrangement of circular coins which are compacted by friction using a conveyor. They showed a liquid-like or hydrostatic behaviour (all the weight of the coins transfers to the bottom) when the side walls are flat and the Janssen effect has been recovered with the placement of saw tooth on the side walls, which is obvious due to the generation of additional mechanical tangential force that supports the weight of the coins. This problem is similar to the vertical arrangement of granular material with frictionless frontal walls in a 2D rectangular silo. A similar liquid-like behaviour has been predicted in the current simulations when the frontal walls are frictionless and Janssen effect was recovered with the increase of frontal wall friction.

Figure 5.12 shows the internal vertical stress distribution averaged over the cross-section of the silo at the end of filling for different frontal wall frictions and also for periodic boundaries with no frontal walls. It is evident that in the case of the frictionless or the periodic boundaries, a liquid-like behaviour can be seen, whereas the Janssen effect was recovered with the increase of frontal wall friction. As the frontal wall friction is increased, the vertical stress begins to saturate at a depth approximately equal to the width of the silo. It can also be seen that by increasing the friction value to above 0.5, additional arching is not created, mainly due to the fact that the majority of the particle-wall contacts are not fully mobilised (which has also been found in the simulations of Jenike wall friction presented in chapter 4). Finally, it should be noted that the absence of friction on the frontal walls or considering a periodic boundaries can lead to a high internal stress and a hydrostatic behaviour. This increase in internal stress can have some implications on the flow patterns as discussed below. It can also be seen that the vertical stress in the assembly is increased with periodic boundary conditions when compared to the frictionless case. This might be due to an increase in bulk density of the assembly when the frontal walls are replaced by the periodic boundaries.

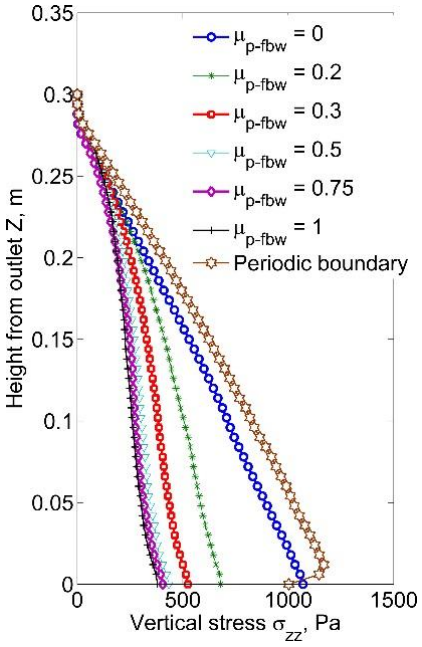

Figure 5.12 Internal stress distribution at the end of filling for the different frontal wall frictions.

5.5.2 Flow patterns

Figure 5.13 shows the time-averaged vertical velocity profile at Z = 120 mm above the outlet for different frontal wall frictions. The velocities were averaged from 0.5 sec to 0.7 sec from the start of discharge. It can be seen from this figure that the velocity profile is uniform at zero frontal wall friction, which is in contrast to the experiments where a non-uniform velocity profile was observed. This therefore indicates a major influence of frontal wall friction on the flow patterns in a 2D test silo. Furthermore, as the frontal wall friction is increased, the velocity profile changes from uniform to non-uniform and a minor difference can be noticed above a wall friction of 0.3 due to the partial mobilisation of wall friction at higher values.

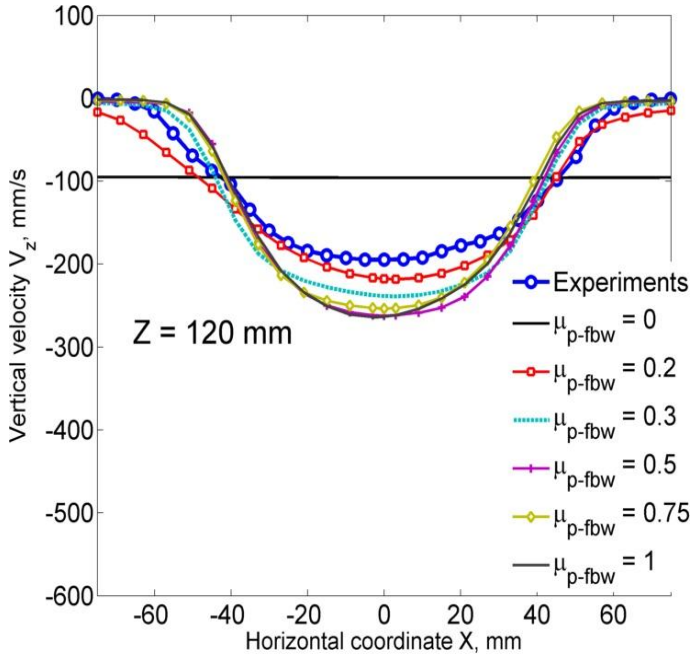

Figure 5.13 Time-averaged vertical velocity profile at Z = 120 mm for different front and back wall friction.

Figure 5.14 shows the images of the flow patterns during the discharge which are visualised with the aid of blue and yellow coloured particles arranged in horizontal layers of equal height at t = 0 sec. The flow channel boundary (FCB) is also depicted on the images. Three lines of FCB at each instant can be seen each with different criteria: solid line, dotted line and axis line were defined as 1%, 5% and 10% of centreline velocity respectively. A very narrow difference between three FCBs can be seen indicating a shear zone with the high-velocity gradients.

It can be seen from these images that the flow transits from the semi-mass flow to the internal flow with the increase of frontal wall friction. The size of the stagnant zones increases with the increase of frontal wall friction: the stagnant zone is the region between the side wall and the FCB.

	t = 0.3 s	t = 0.6 s	t = 0.9 s
$\mu_{\_p\text{-}fbw}$ = 0	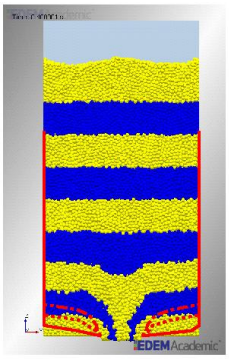	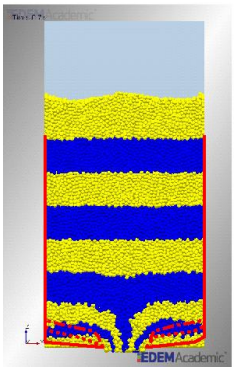	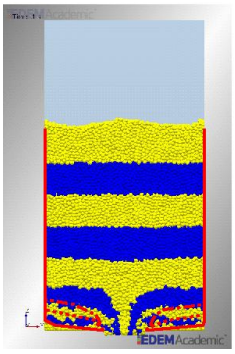
$\mu_{\_p\text{-}fbw}$ = 0 .2 *Validated case*	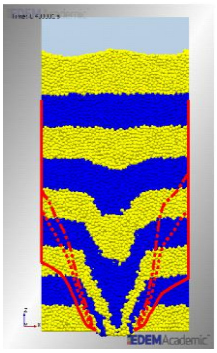	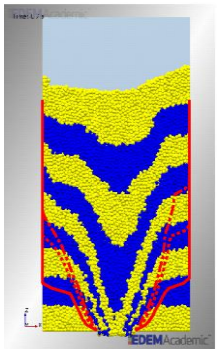	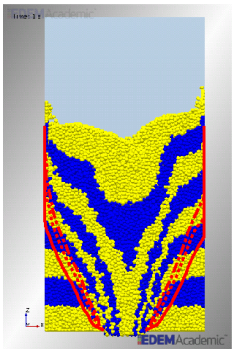
$\mu_{\_p\text{-}fbw}$ = 0.3	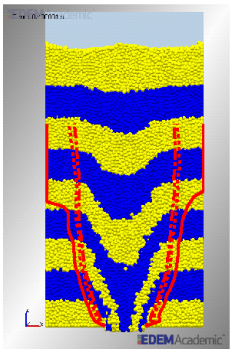	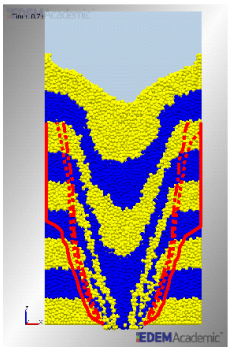	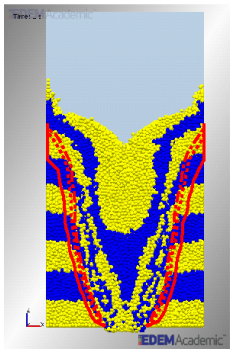
$\mu_{\_p\text{-}fbw}$ = 0.5	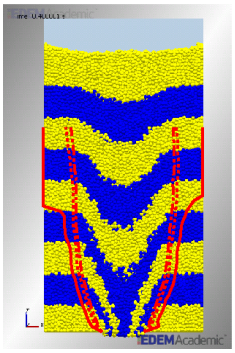	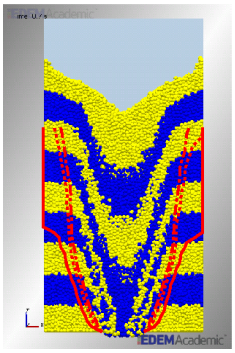	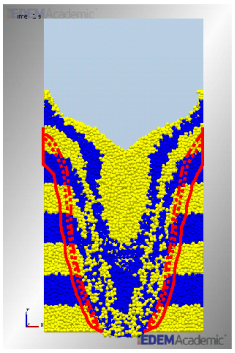

$\mu_{\_p\text{-}fbw}$ = 0.75	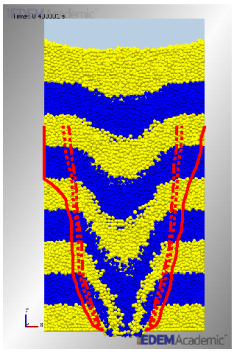	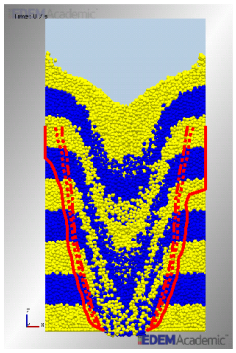	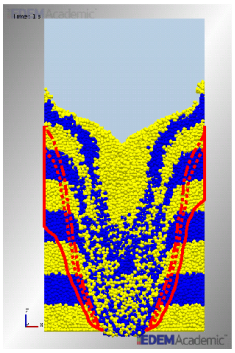
$\mu_{\_p\text{-}fbw}$ = 1	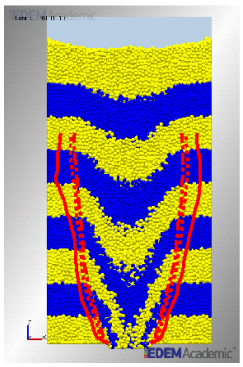	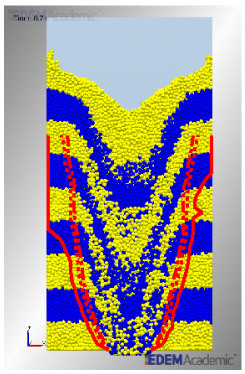	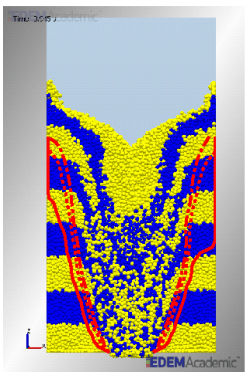

Figure 5.14 Comparison of flow patterns at different instants for different frontal wall frictions.

5.5.3 Force chain structure

The images of the branch vectors between the particles at selected instants during the discharge for different frontal wall frictions are shown in Figure 5.15. The vectors in a slice of thickness 6 mm and a height of 150 mm are shown here. The colour of each vector represents the contact normal force with a maximum value shown as red and zero as grey. The maximum value was chosen to be 50 times the weight of a particle as a reference value for all cases.

It can be seen that the branch vectors are randomly oriented and similar in magnitude for all values of frontal wall friction at the end of filling (at t = 0 sec) and upon opening the outlet, the intensity of the contact normal force decreases with the small increase of frontal wall friction. Upon opening the outlet wall, it is obvious that the particles immediately above the outlet exit the silo by free fall after experiencing an

unbalanced force in the vertical direction. This lead to the formation of an arch-like force chain network supported by the bottom wall, as shown at t = 0.1 sec, at all frontal wall frictions. As it can be seen that the strength of the force chains in this arch decreases with the slight increase of frontal wall friction and a stronger force chains (identified by colour of the branch vector) are evident for the frictionless front and back walls.

The strength of the force chain in the arch close to the bottom of the silo is believed to govern the development of flow. For example, the stronger the force chain network higher, the energy required to break the chains and vice versa. The presence of these strong force chains in the case of frictionless frontal walls enables the particles to move collectively leading to a semi-mass flow. In contrast, weaker force chains were formed with the increase of wall friction (weak enough to break with the shear caused by the gravity) thereby enabling an internal flow. The breakage of the force chains with the increase of frontal wall friction can be seen at t = 0.3 sec and 0.6 sec for the different values of frontal wall friction.

	t = 0 s	**t = 0.01 s**	**t = 0.3 s**	**t = 0.6 s**
$\mu_{\_p\text{-}fbw}$ =0	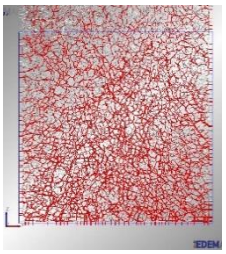	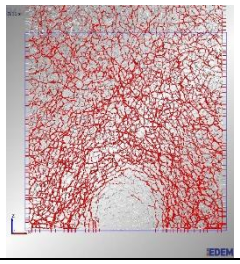	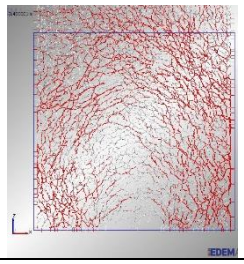	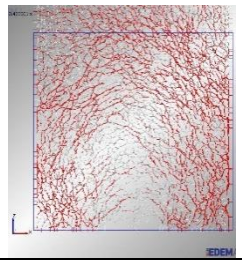
$\mu_{\_p\text{-}fbw}$ = 0 .2 **Validated case**	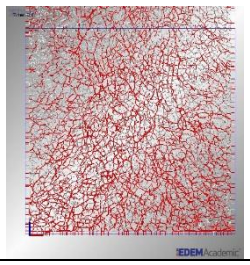	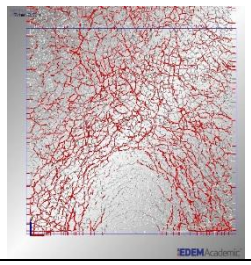	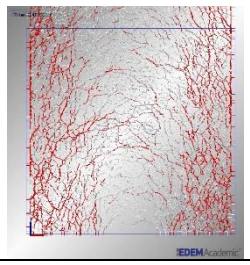	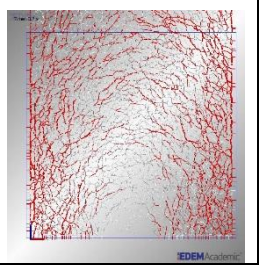

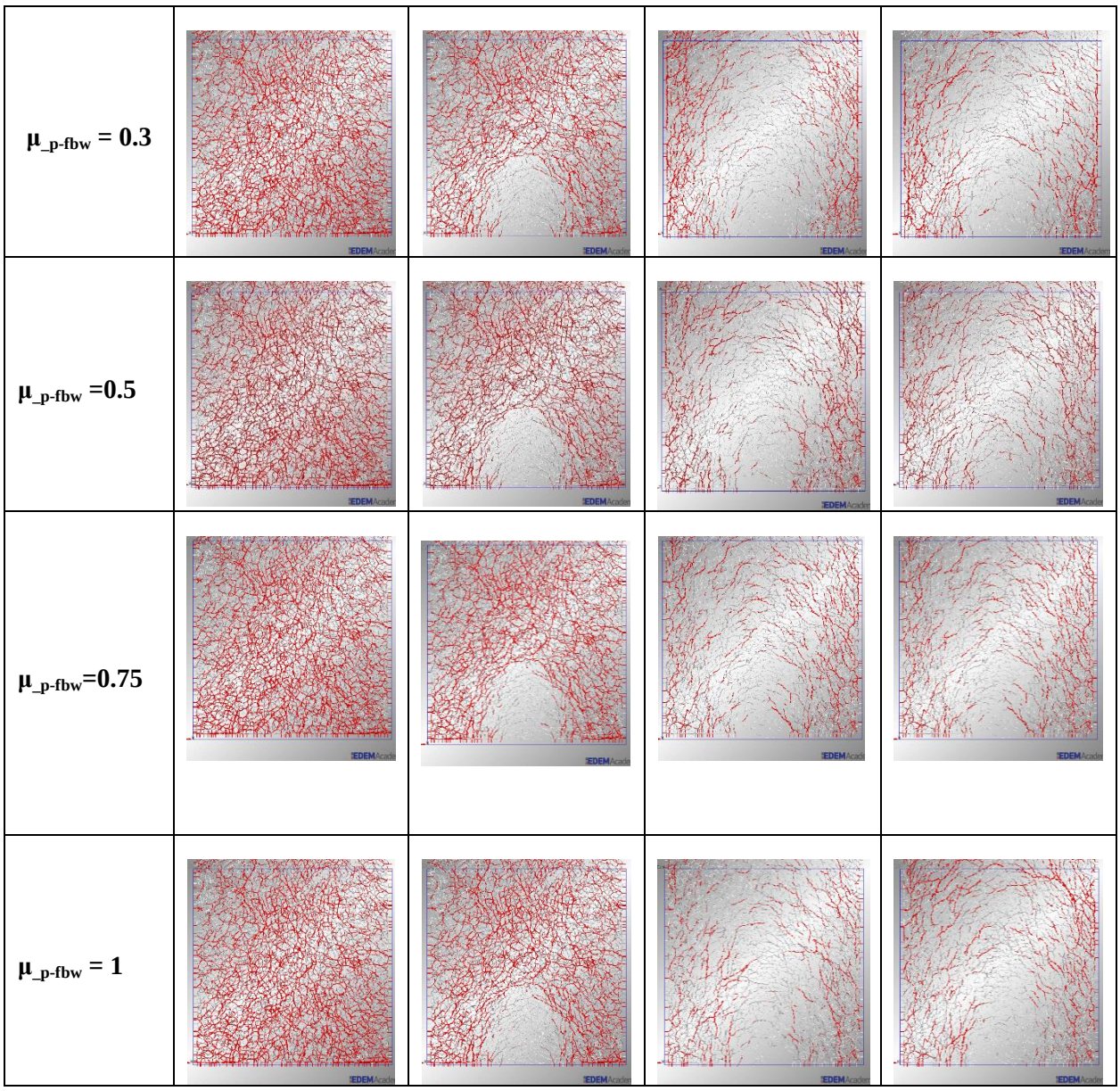

Figure 5.15 Comparison of force chain networks at different instants for different frontal wall frictions.

5.6 Effect of coefficient of restitution

It was already shown by Anand et al., (2008) that the coefficient of restitution (CoR) has no influence on the discharge rate in a hopper. It has also been confirmed in this work by conducting the simulations at various values of CoR = 1E-04, 0.6 and 1. The time-averaged velocity profiles at heights of Z = 20 mm and 120 mm are compared as shown in Figure 5.16 (a) – (b). It is evident from this figure that the CoR has a

negligible influence on the velocity profiles which is obvious due to the lack of collisions during the silo discharge.

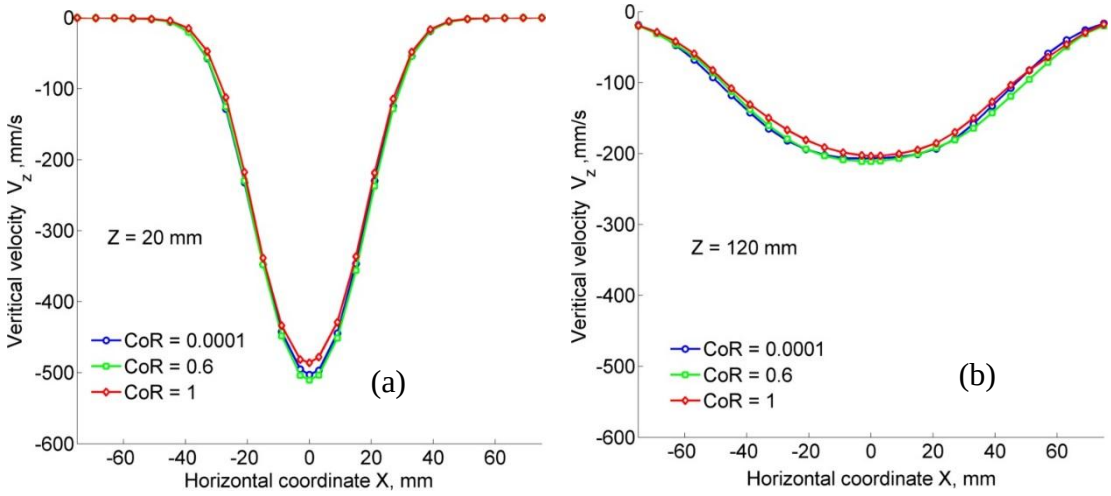

Figure 5.16 Effect of coefficient of restitution on velocity profiles (a) Z = 20 mm (b) Z = 120 mm.

5.7 Effect of inter-particle friction and rolling friction

The effect of inter-particle friction and rolling friction on bulk internal friction in the simulations of Jenike direct shear was presented in chapter 4. As already discussed in that chapter, it was found that the rolling friction has a negligible influence on the bulk friction at lower inter-particle friction and a significant influence at higher inter-particle friction. This has also been verified for the flow patterns during the silo discharge at two inter-particle frictions of 0.15 and 0.57 and at three rolling frictions of 0, 0.1 and 0.2.

Figure 5.17 shows the variation of time-averaged mass flow rate with the increase of inter-particle friction at different rolling frictions of 0, 0.1 and 0.2. At zero rolling friction, the mass flow rate decreases sharply with the increase of inter-particle friction from 0.15 to 0.57 and any further increase does not show a significant influence. Moreover, the mass flow rate was reduced with the increase of rolling friction to 0.1 and no further decrease was seen with $\mu_r = 0.2$.

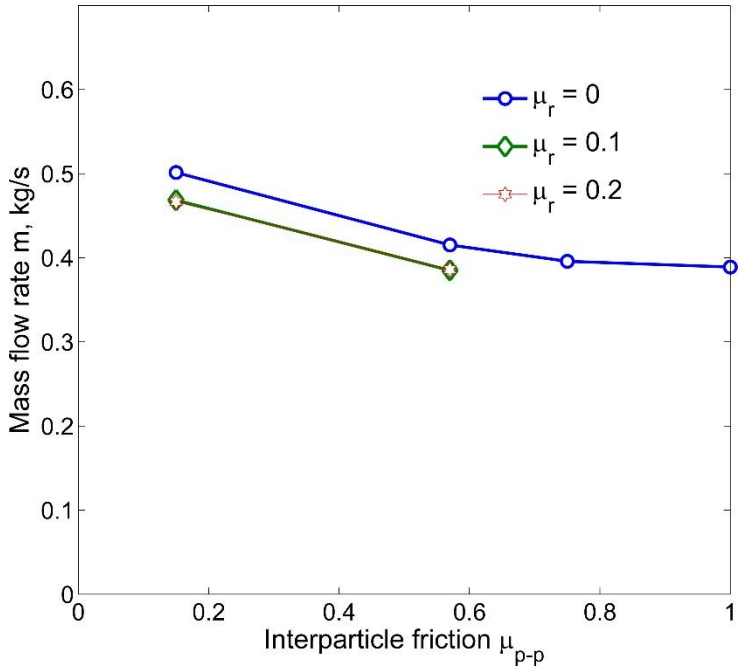

Figure 5.17 Effect of inter-particle friction and rolling friction on mass flow rate.

Figure 5.18 shows the time-averaged vertical velocity profiles at four selected heights (Z = 40, 80, 120 and 160 mm) for different inter-particle frictions at zero rolling friction. At distances close to the outlet (Z = 40 mm), the flow was found to be independent of inter-particle friction and as the distance increases the inter-particle friction comes into play. At greater distances from the outlet, a lower inter-particle friction (μ_{p-p} = 0.15) leads to a non-uniform velocity profile: maximum at the centre and decrease towards the side wall whereas a more uniform velocity profiles can be seen at particle friction of 0.57 and above. A minimal influence on the flow behaviour is evident for particle friction values above 0.57. This is due to the fact that the bulk internal friction saturates with the increase of inter-particle friction at zero rolling friction (as found in the simulations of Jenike internal friction).

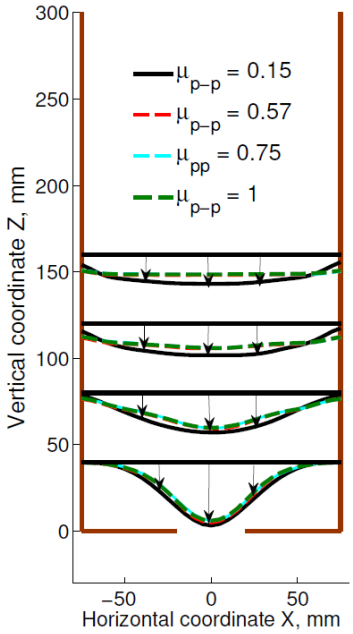

Figure 5.18 Effect of inter-particle friction on vertical velocity profiles at zero rolling friction.

The effect of rolling friction on vertical and horizontal velocity profiles at an inter-particle friction of 0.15 and 0.57 is shown in Figure 5.19 and Figure 5.20 respectively. As expected, the rolling friction barely has any influence on the velocity profiles at $\mu_{p\text{-}p}$ = 0.15 and a significant influence at $\mu_{p\text{-}p}$ = 0.57 is evident. With the increase of rolling friction from 0 to 0.1, it is evident that the flow patterns changes to internal flow: limiting the rotations at higher inter-particle friction lead to the formation of stable stagnant zones thereby creating an internal flow.

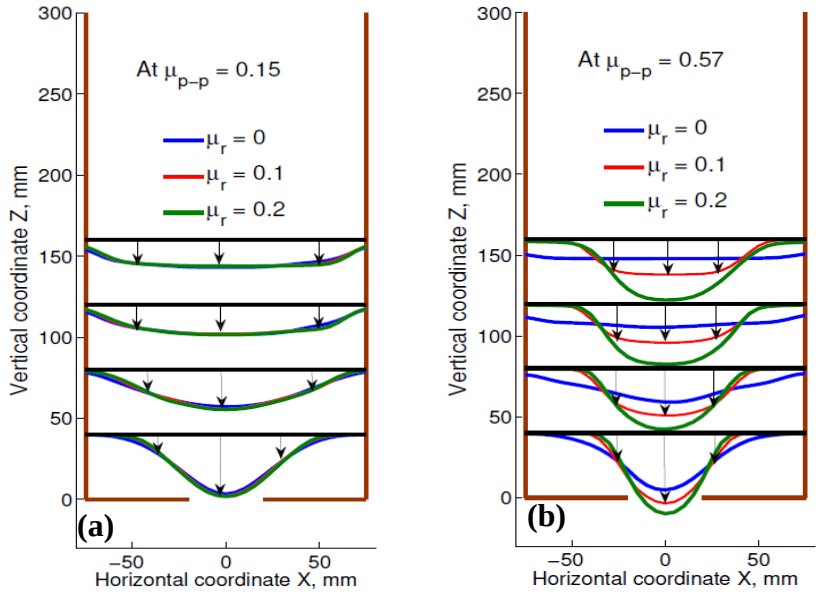

Figure 5.19 Effect of rolling friction on vertical velocity profiles (a) inter-particle friction = 0.15 (b) inter-particle friction = 0.57.

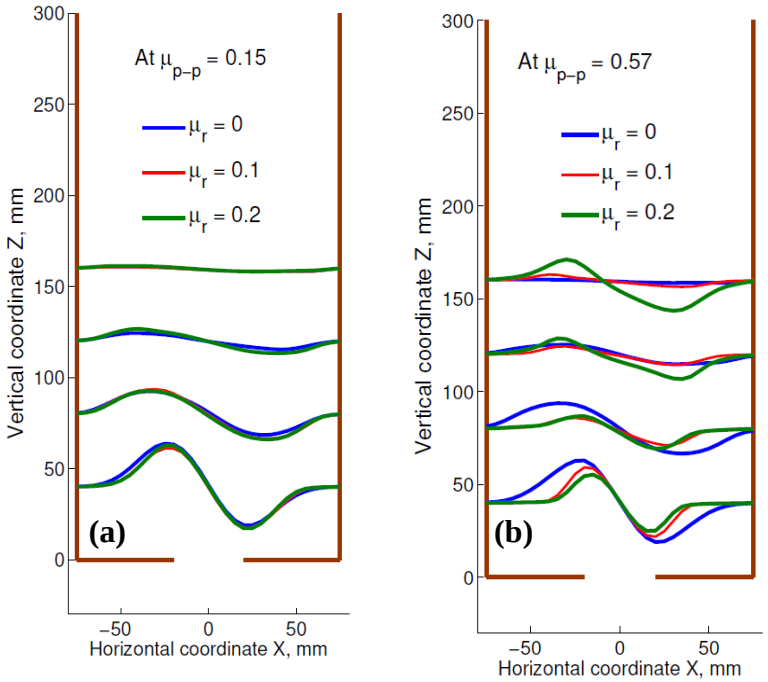

Figure 5.20 Effect of rolling friction on horizontal velocity profiles (a) inter-particle friction = 0.15 (b) inter-particle friction = 0.57.

5.8 **Summary**

To assess the accuracy of DEM, the flow behaviour of pellets during the discharge in a flat bottom silo has been chosen as a validation experiment. The development of a DEM model to simulate the flow of granules has been discussed. The DEM predicted internal stress at the end of filling was compared against the analytical solution of Janssen. The predicted filling bulk density and mass flow rate during discharge were compared with the measurements. Finally, the velocity profiles and flow channel boundary (FCB) at different instants were compared with measurements and kinematic model. The following main conclusions can be drawn from the assessment of DEM accuracy:

- The variation of the vertical stress with the depth of the silo at the end of filling was found be in good agreement with the Janssen equation.
- The inclusion of rolling friction torque (which takes into account the difference in shape between the test and numerical particle) gives a good prediction of flow rate within ± 5 % accuracy.
- It was found that a slightly lower filling bulk density was obtained in the simulations due to which the predicted upward propagation of flow is faster in comparison to the experiments. A reasonably good quantitative agreement was found when the flow is fully developed. Considering the simplifications made in the model, the DEM predictions of velocity profile can be considered to be in reasonably good agreement. The DEM velocity predictions were also compared with the kinematic model. It was found that kinematic constant decreases with the distance above the outlet in both the simulation and the experiment.
- The flow channel boundary was found to be in good agreement close to the outlet whereas a discrepancy of approximately 2-3 particles far from the outlet and close to the side walls was found.

The validated model was further used to study the effect of frontal wall friction, the coefficient of restitution (CoR), inter-particle and rolling friction. The following main conclusions can be drawn from the study:

- Liquid like behaviour was found when the frontal walls are frictionless and the Janssen effect was observed only when adequate frontal wall friction is applied.
- Flow transits from a semi-mass flow to an internal flow with the increase of frontal wall friction.
- The presence of strong force chains in case of frictionless frontal walls enables the particles to move collectively leading to a semi-mass flow. In contrast, weaker force chains were formed with the increase of wall friction (weak enough to break with the shear caused from gravity flow) thereby enabling internal flow.
- It was found that the CoR has a negligible influence on the velocity profiles due to the lack of collisions during the silo discharge. A low CoR is desirable in order to bring the system to equilibrium as quickly as possible.
- The rolling friction has negligible influence on flow patterns at lower inter-particle friction, however, an increase of rolling friction from 0 to 0.1 at higher inter-particle friction leads to changes in the flow patterns from semi-mass to internal flow; limiting the rotations at higher inter-particle friction lead to the formation of stable stagnant zones thereby creating an internal flow.

In the next chapter, the validated DEM model is used to study the mixing in a semi-mass and internal flow in a flat bottom silo and the various parameters that affects the mixing performance are discussed.

Chapter 6

6. DEM studies of blending process in a flat bottom silo and its dependency on flow patterns and process parameters

6.1 Introduction

The calibration and the validation of a DEM model to simulate the flow in a silo have been discussed in chapters 4 and 5 respectively. The DEM model has been validated by quantitatively comparing the velocity profiles during the batch discharge in a small scale flat bottom silo and also the influential parameters that affect the flow patterns have been discussed. The rest of the thesis is focussed on the investigation of blending from both the experiments and simulations using the developed PIV and DEM tools.

In this chapter, DEM model to understand the blending process in a flat bottom silo operating in both discontinuous and continuous modes is presented. Although the flat bottom silo is not used in practice as an industrial blender, the main focus is made on understanding the blending process in two contrasting flow patterns (semi-mass and internal flow) from the particle scale results and further to investigate the dependency of blending effectiveness on the process parameters such as volume of the batch, number of recirculations and number of sublayers of each batch in both mentioned flow patterns.

Furthermore, the blending effectiveness is also evaluated using the traditional approach of impulse-stimulus and linear system time-invariant (LTI) theory. The relatively small number of particles in the simulated small-scale flat bottom silo allows running the simulation for a longer time in order to extract data that is required to verify this traditional approach, before applying to a relatively large scale multi-flow blender (presented in the next chapter 7). This approach involves the

calculation of residence time distribution (RTD) function and convolution integral (Weiler et al., 2012).

The RTD function is calculated from the particle scale DEM results and also an algorithm is developed to determine the RTD function from the spatially averaged Eulerian velocity fields. The accuracy of the LTI theory is then assessed by comparing the calculation of time variation of outlet concentration of tracer particles against the corresponding particle scale DEM results. Finally, the blending effectiveness in continuous and discontinuous mode is evaluated using LTI theory particularly for those input conditions which are otherwise difficult to study using the DEM results.

6.2 DEM model of a silo blender

6.2.1 Modelling aspects of the blending process

The function of a blender is to reduce the fluctuations of a property of interest that exists within the batch and between the different batches of bulk solids. The property could be the melt index of pellets or simply a colour. The fluctuations are reduced either by operating the blender in the continuous mode or in the discontinuous mode as shown in Figure 6.1. In discontinuous mode of operation, the blender is filled with batches of particles in layer by layer. At the end of the filling, the contents are discharged through a feeder and constantly recycled to the inlet of the blender. After a certain number of passes or recirculation time, the recirculation is stopped and the homogenised contents are discharged. Whereas in the continuous mode of operation, the blender runs continuously with a constant stream of fresh input material with fluctuations that exist with time or in the other words the discharged contents are not recycled but passes through another silo of same or different configuration (Weiler et al., 2012).

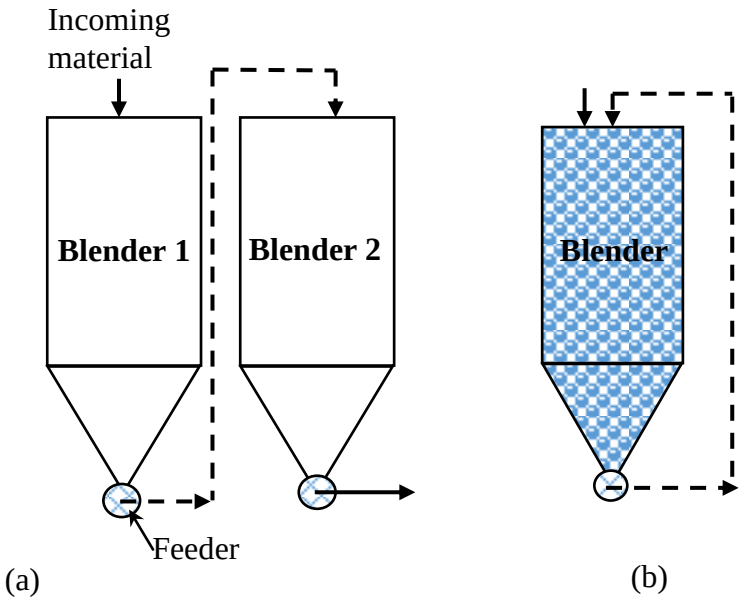

Figure 6.1 Modes of operation (a) Continuous mode (b) Dis-continuous mode.

The DEM modelling aspects of the blending process, therefore, includes the model representation of the property of interest and its fluctuation in continuous and discontinuous modes, the modelling of the feeder to control the outflow rate and the modelling of recirculation of the pellets. In this work, the property to be blended is chosen as the colour of the particles. The details of implementation of each these conditions are discussed below.

6.2.2 Simulation set-up

The geometric set-up and the particle assembly at the end of filling are the same as the one described in chapter 5. The flat bottom silo with a width and an outlet size of 150 mm and 40 mm respectively and an initially filling height of 270 mm was used. A rigid wall vertical channel of length 80 mm was created below the silo outlet for the purpose of controlling the outflow rate. The simulation set-up of the flat bottom silo blender is shown in Figure 6.2**.**

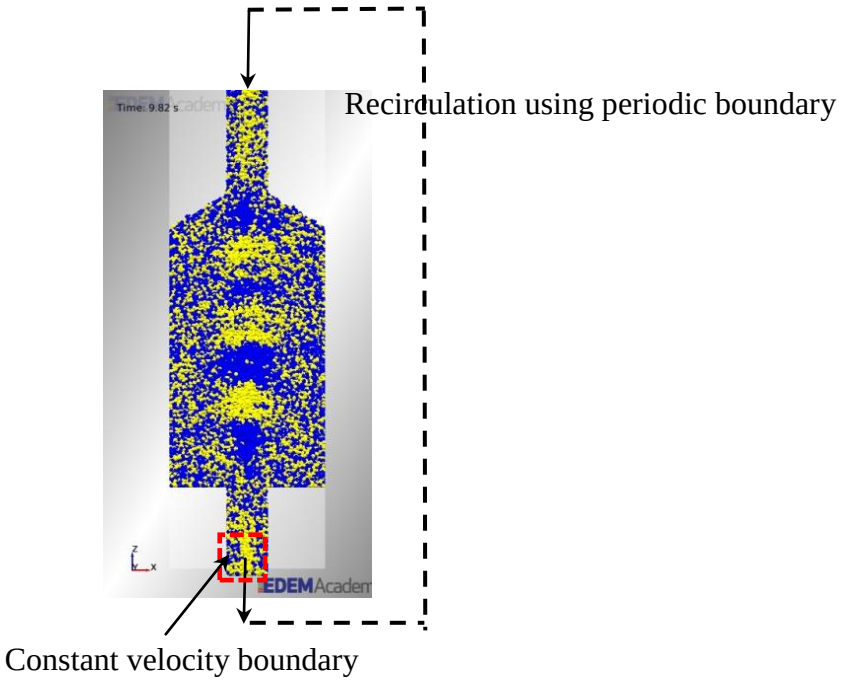

Figure 6.2 DEM model of flat bottom silo indicating boundary conditions.

Two different flow patterns were imposed by changing the frictional parameters of the model. As discussed in chapter 5, the most influential parameters of the model that affect the flow patterns are the front and back wall friction and the combination of inter-particle and rolling friction. It should be noted that the main focus here is to obtain the two different flow patterns that are possible in a flat bottom silo. Hence, they are chosen in such a way to simulate a semi-mass and internal flow in a flat bottom silo. The parameters implemented are listed in Table 6.1.

Table 6.1 DEM input parameters.

Property name	Internal flow	Semi-mass flow
Particle-Particle sliding friction $\mu_{s\text{-}pp}$	0.55	0.35
Particle-Particle rolling friction $\mu_{r\text{-}pp}$	0.2	0
Particle-wall sliding friction, side and bottom walls $\mu_{s\text{-}psbw}$	0.5	0.17
Particle-wall sliding friction, front and back walls $\mu_{s\text{-}pfbw}$	0.5	0
Particle-wall rolling friction $\mu_{r\text{-}pw}$	0.2	0

6.2.3 **Boundary conditions and runtime parameters**

6.2.3.1 Constant velocity at the outlet

The outflow rate was controlled by applying a constant vertical velocity condition in the bottom half of the vertical channel below the silo outlet as indicated in Figure 6.2. The zone indicated by the red box in this figure basically acts as a feeder. A body force given by (6.1) is implemented in EDEM software through its API functionality in order to set the velocity of the particles in the red box to a constant value.

$$\mathbf{F_{ext,z}} = \frac{\mathbf{m_p}}{\mathbf{dt}}(\mathbf{V_z} - \mathbf{V_{out}}) \qquad \textbf{(6.1)}$$

where $F_{ext,z}$ is the external body force in Z-direction, m_p is the mass of the particle, dt is the calculation time step, V_z is the velocity of the particles in the previous time step and V_{out} is the velocity at the outlet corresponding to the required flow rate.

Figure 6.3 shows the variation of the velocity of particles at outlet after the application of external body confirming the constant velocity boundary condition in both the simulated flows.

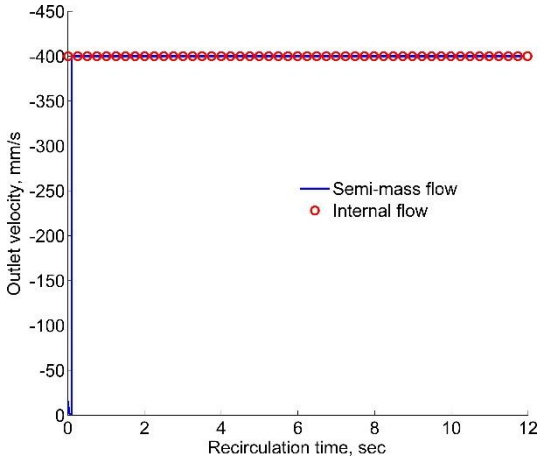

Figure 6.3 Time variation of vertical velocity at the outlet.

6.2.3.2 Periodic boundary condition at outlet

Periodic boundary conditions were used in the vertical direction in order to simulate the recirculation. With this boundary condition, the particles crossing the bottom of the simulation domain are simultaneously placed at the domain inlet. The outlet and inlet of the silo are therefore made to coincide with the domain boundaries so that the particles that leave the outlet are placed at the corresponding location at the inlet as shown in Figure 6.2. A sufficient empty space is required above the top pile of particles while using periodic boundary which would otherwise lead to a formation of a solid block with no flow.

6.2.3.3 Runtime parameters

A constant velocity of 0.4 m/s is applied at the outlet giving rise to a mean particle residence time of 2.75 sec (ratio of the volume of contents in the silo to the volumetric flow rate). A simulation time step of 10 % of Rayleigh time was used. The simulation was run for a total time of 12 sec which is approximately four

recirculations of silo contents. The simulation data was saved at an interval of 0.005 sec.

6.2.4 Methodology of blending analysis

The homogeneity of a blend from a silo is characterised by the data of temporal variation of concentration of a component of interest in the outflow, unlike from the spatial variation for example in the case of a mechanically agitated mixtures. The effectiveness of blending process is determined by the variance reduction ratio (VRR) which is given by the ratio of the variance of input fluctuations to the variance of output fluctuations of the property of interest, for example, the colour of granules (Beaudry, 1948; Johanson, 2006).

As presented in the section 2.2 of literature review chapter, the VRR can be calculated using the traditional impulse-stimulus approach which involves obtaining the residence time distribution (RTD) function of the blender from experiments or simulations and then applying a convolution integral (Johanson, 2006; Weiler et al., 2012). The RTD function basically represents the time variation of concentration of a tracer material in the outflow in response to a step impulse of a tracer in the inflow. Assuming blender as a linear time-invariant (LTI) system, the outlet concentration for any type of input variation is then determined from the convolution integral of RTD function and the input signal. It is obvious that this type of analysis is not needed in DEM because of availability of particle scale data (particle positions and Id's) at all times during the blending process. However, the main advantage of using the impulse-stimulus approach is that the DEM simulation is only needed to run for only a small duration of the order of mean residence time (in comparison to the time to complete the whole blending process) in order to determine the RTD function and consequently the blending effectiveness. This approach avoids the high computational time required to fully simulate the blending process and to minimise the post-processing of a large amount of particle scale data.

6.3 Evolution of flow patterns during recirculation

It is already known that for an effective blending in silos, two conditions have to be met: first, there should be no stagnant zones in the blender and second there should

be a wide difference between the residence times of the particles at different horizontal positions at the inlet (Johanson, 1970). These conditions imply that the flow in the silo should have the characteristics of both the mass flow (no stagnant zones) and internal flow (the presence of velocity gradients in the horizontal direction). This kind of flow can be only achieved by placing inserts and tubes in a mass flow silo such as Bi-insert blender and multi-flow blenders. Since in a flat bottom silo without the internals the presence of combined mass and funnel flow is not possible, the extreme scenarios (semi-mass flow and internal flow) were simulated to study the extent of blending in both cases and its dependence on the size of batch (in case of discontinuous mode of operation) and the frequency of fluctuations (in case of continuous mode).

In this section, the evolution of bulk density and velocity profiles during the recirculation of particles for two different set of material input parameters (refer to Table 6.1) are presented before analysing blending in the following sections.

6.3.1 Bulk density

Figure 6.4 shows the temporal variation of bulk density as the particles are recirculated to the inlet since the end of the filling. As expected, it can be seen that as the particles are recirculated the bulk density decreases until it reaches a steady state value, known as flowing bulk density which is lower than the stagnant bulk density (or bulk density at the end of filling) of the material. It is also evident that the particles with high internal and wall friction (referred as internal flow in the plot) attain a lower flowing bulk density when compared to its counterpart (referred as semi-mass flow). The presence of intense shearing in internal flow causes the dilation of the particles giving rise to a lower bulk density in the steady state. In addition to this, the time it takes to reach the steady state is also higher in the internal flow (or in other words the flow propagation is slower). The slower evolution of bulk density in the internal flow supports the theory of flow propagation proposed by the Nedderman (1995) which states that the velocity of flow propagation is inversely proportional to the difference between the bulk densities of stagnant and flowing zones. The percentage change in the bulk density is found to be 4.5 % and 13 % for the semi mass flow and the internal flow respectively.

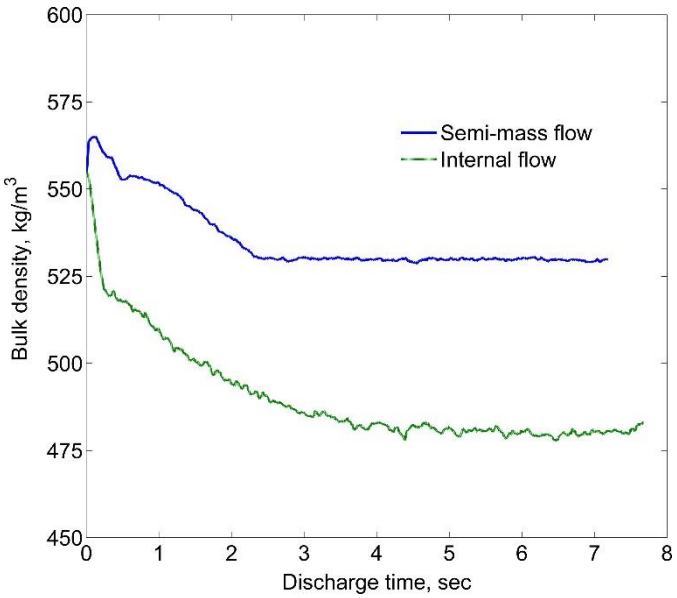

Figure 6.4 Variation of bulk density in semi-mass and internal flow during the recirculation.

6.3.2 Velocity profiles

The continuous recirculation of particles in the silo can drastically change the flow patterns or velocity profiles, particularly in the case of high internal and wall friction. Due to the presence of internal velocity gradients, the continuous shearing of flowing zone against the stagnant zone leads to the slow sideward expansion of the flow channel.

Figure 6.5 (a) shows the time and spatial evolution of vertical velocity profile at Z = 120 mm during the recirculation for internal flow scenario. It is evident from this figure that the velocity profile tends to change from a non-uniform profile towards a uniform profile because of continuous shearing. A steady state is reached nearly after 3 recirculations of silo volume. Conversely, for the case of semi-mass flow, the velocity profile is already uniform during the initial stages of the flow and it remains constant during the recirculation of material due to the lack of velocity gradients as shown in Figure 6.5 (b).

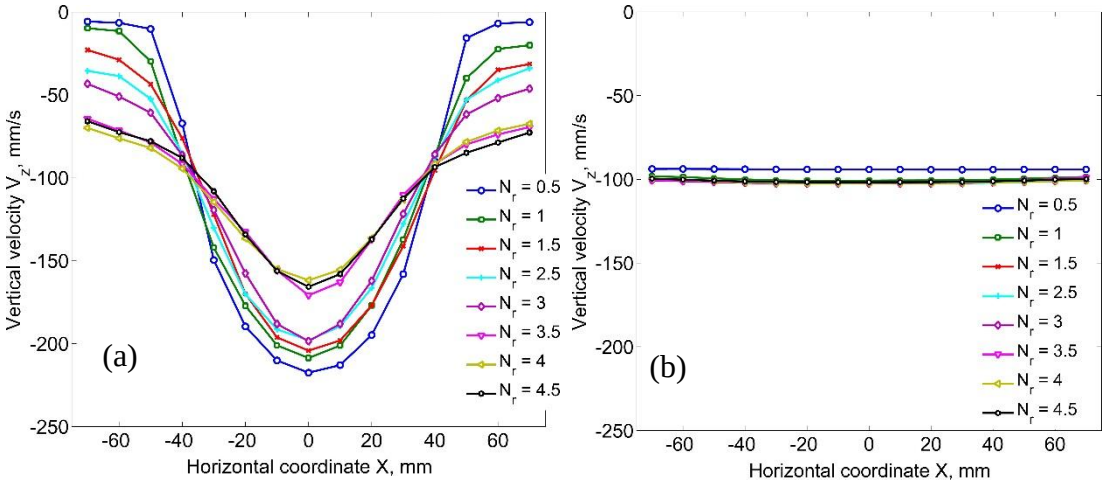

Figure 6.5 Vertical velocity profiles at different instants at Z = 120 mm (a) Internal flow case (b) Semi-mass flow case.

It was also observed that the vertical velocity profile at different heights changes drastically in such a way that an initially semi-mass flow is converted to a complete mass flow (material slides along the bottom wall of the flat bottom silo) after 3-4 recirculations and similarly the internal flow is converted to the semi-mass flow. Note that the two flow patterns simulated in this study are indicated as semi-mass and internal flow for reference, although they change their nature during recirculation. Because of these changes in the velocity profiles, the blending effectiveness of particles during the evolution could be different that during the steady state. However, the influence of this transitory evolution of the flow pattern on the blending could be neglected because of its short duration compared to the total blending times.

6.4 Blending effectiveness in discontinuous mode

The dependence of variance reduction ratio (VRR) on the batch size, the number of recirculations and the flow patterns is investigated in discontinuous mode. It is important to note that the definition of batch size in discontinuous and continuous mode is different. In the former, the batch size is defined in terms of ratio of volume

of a batch (V_b) to the volume of a silo (V_s) while in the latter it is defined as the ratio of time period of fluctuations of a property in the inflow (t_p) to the mean residence time of particles (t_r) (Pernenkil and Cooney, 2006). For example, if the fluctuations in the inflow are of sinusoidal form then the time period of the sine wave is taken as the batch size.

The batch sizes of V_b / V_s = 13 %, 25 % and 50 % having an inlet standard deviation of 34 %, 44 % and 50 % respectively were created as shown in Figure 6.6. Furthermore, two additional initial filling conditions were created for the latter case by arranging the blue and yellow particles into sub-layers of 3 and 5 as shown in Figure 6.6. The inlet standard deviation of blue colour concentration over the silo volume is also shown in this figure. It should be pointed out that all these different initial conditions are created from the same particle assembly by simply using the particle ids to assign them blue or yellow colour.

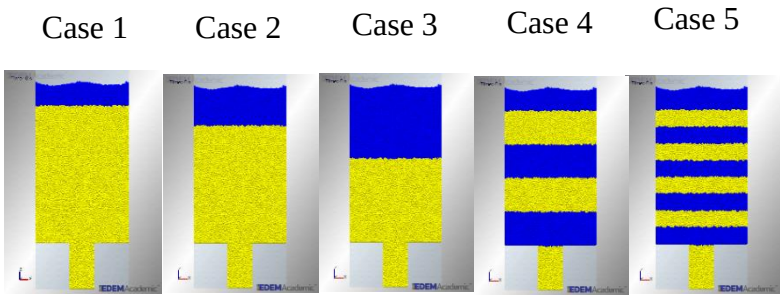

V_b / V_s	**%**	13	25	50	50	50
σ_{in}, %		34	44	50	50	50

Figure 6.6 Different initial conditions for blending in dis-continuous mode.

6.4.1 Blending process during recirculation and its mechanism

Figure 6.7 shows the sequence of images illustrating the blending process of blue and yellow particles in a semi-mass flow patterns during the recirculation. The recirculation time is defined in terms of a number of recirculations $N_{r,}$ where N_r is the ratio of time spent by the particles in the silo to their mean residence time, for

example N_r = 1, means all the contents of the silo are recycled once. As shown in this figure, as the number of recirculations is increased, the blending homogeneity of the blue and yellow particles increases especially near the side walls whereas they remain unmixed near the centre along the height of the silo. This is due to the fact that in a semi-mass flow, the vertical velocity gradients exists only close to the outlet while the motion of the particles is mostly uniform in the region far from the outlet. These gradients close to the outlet are responsible for the axial mixing (where the particles coming from the centre of the silo mix with the particles coming from the side walls), however this mixing is very limited to the edges of the outlet leaving the particles in the core of the outlet unmixed as shown in Figure 6.17. Since the size of the mixing region in comparison to the volume of the silo is small, the blending effectiveness is expected to be low.

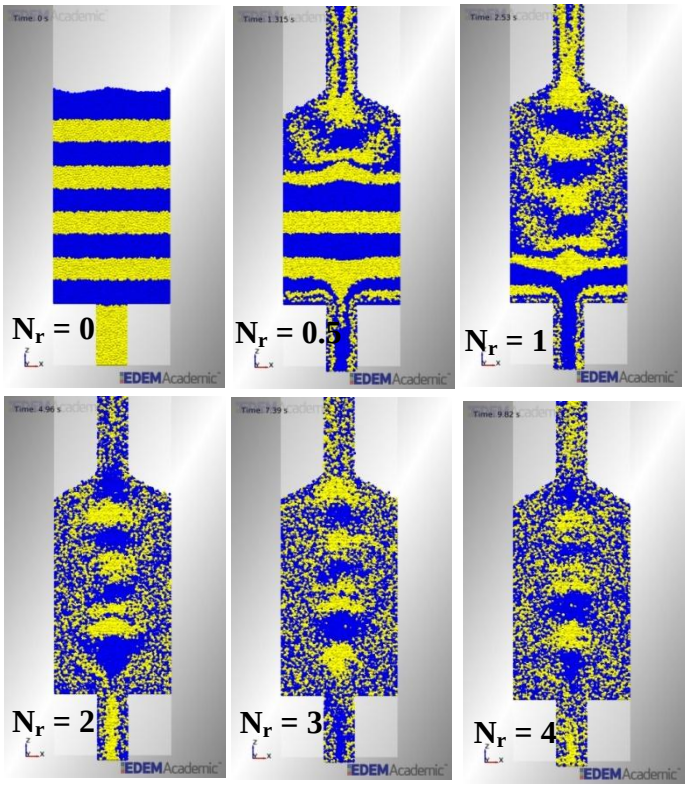

Figure 6.7 Evolution of blending of blue and yellow particles during recirculation in a semi-mass flow (Size of the batch: 50% of silo volume and 5 sub-layers).

Figure 6.8 shows the sequence of images illustrating the blending process of blue and yellow particles in internal flow patterns during the recirculation. As it can be seen, the presence of vertical velocity gradients in a large portion of the silo volume promotes the axial mixing of all horizontal layers at different heights unlike in the case of semi-mass flow where it was limited only close to the outlet. It is also evident that as the number of recirculations is increased, the blending homogeneity of the particles increases in the whole silo except for the stagnant zones located at the bottom corners of the container. In addition to the axial mixing created due to the bulk velocity gradients, there also exists a shear mixing within the shear band between the flowing and the stagnant material (refer to the image corresponding to N_r = 0.5). Because of the larger active volume of mixing regions, the blending effectiveness is higher in this case.

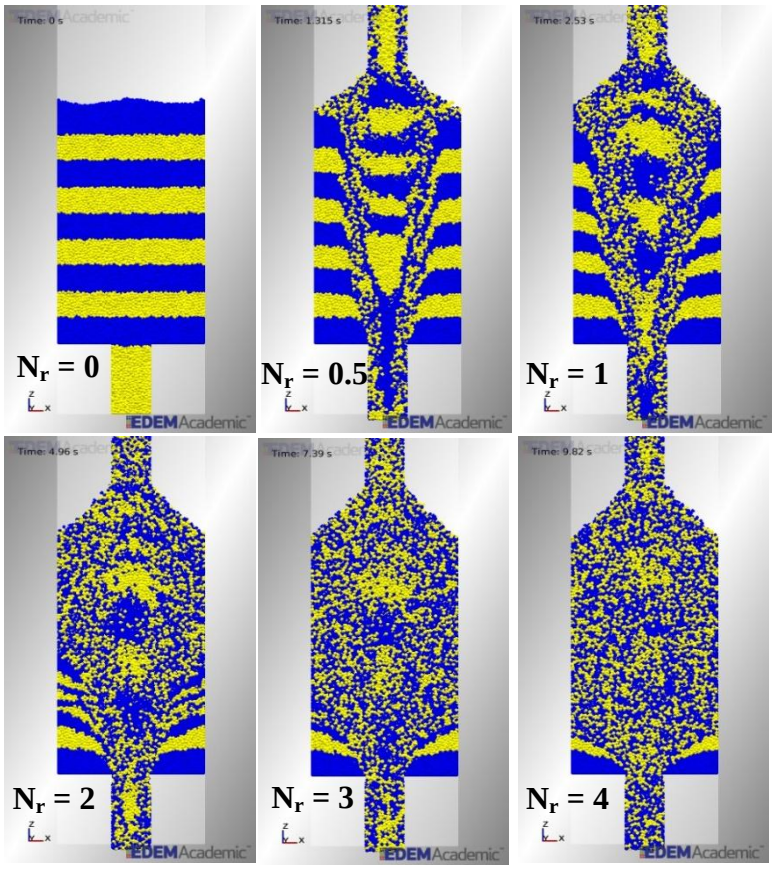

Figure 6.8 Evolution of blending of blue and yellow particles during recirculation in internal flow (Size of the batch: 50 % of silo volume and 5 sub - layers).

6.4.2 Outlet concentration and blending effectiveness

Figure 6.9 (a) and (b) shows the temporal variation of concentration of the blue particles in the outflow during the discharge after a different number of recirculations (N_r = 0, 2 and 4) for semi-mass and internal flow patterns. The concentration profile here is shown for the case 5 (blue particles of volume 50 % of silo contents are arranged in 5 sub-layers as shown in Figure 6.6). With no recirculation (N_r = 0), it is evident that for both the flows there is no mixing at the beginning of the discharge since only the first layer of yellow particles are discharged. Afterward, an intermittent discharge of blue particles in 5 cycles with a frequency proportional to the number of sublayers and the type of flow patterns is observed. As the number of recirculations is increased, the fluctuations in the concentration are reduced with a more prominent reduction in case of internal flow. In the case of internal flow, the presence of gradients of vertical velocity in horizontal direction draws the material from the regions far from the outlet and hence the frequency of concentration of blue particles in the outflow is higher than in the case of semi-mass flow. As the internal flow shows a higher frequency of the peaks on the concentration of blue particles which can be correlated with a high effectiveness of blending.

Figure 6.10 shows the variance reduction ratio (VRR) as a function of the number of recirculations for various batch sizes of blue particles (V_b/V_s = 13%, 25% and 50%) for semi-mass flow and internal flow. The thin line shows the data for semi-mass flow and thick line for internal flow. The following conclusions can be drawn from this figure:

- Irrespective of the batch size and the type of flow patterns, it is obvious that the VRR increases with an increase in the number of recirculations.
- The rate of increase of VRR decreases after 2 recirculations and seems to tend to an asymptotic value.
- In case of internal flow, the batch size significantly affects the VRR while a minor influence is evident in the case of semi-mass flow: lower the batch size higher the VRR.

- Depending on the batch size, the VRR at the end of 4 recirculations is found to be in the range of 4 - 6 and 8 - 13 for semi-mass and internal flow respectively.
- As expected, the recirculation effectiveness is higher in the case of internal flow when compared to its counterpart. However, the VRR is approximately the same irrespective of the flow patterns if the particles are discharged without recirculation.

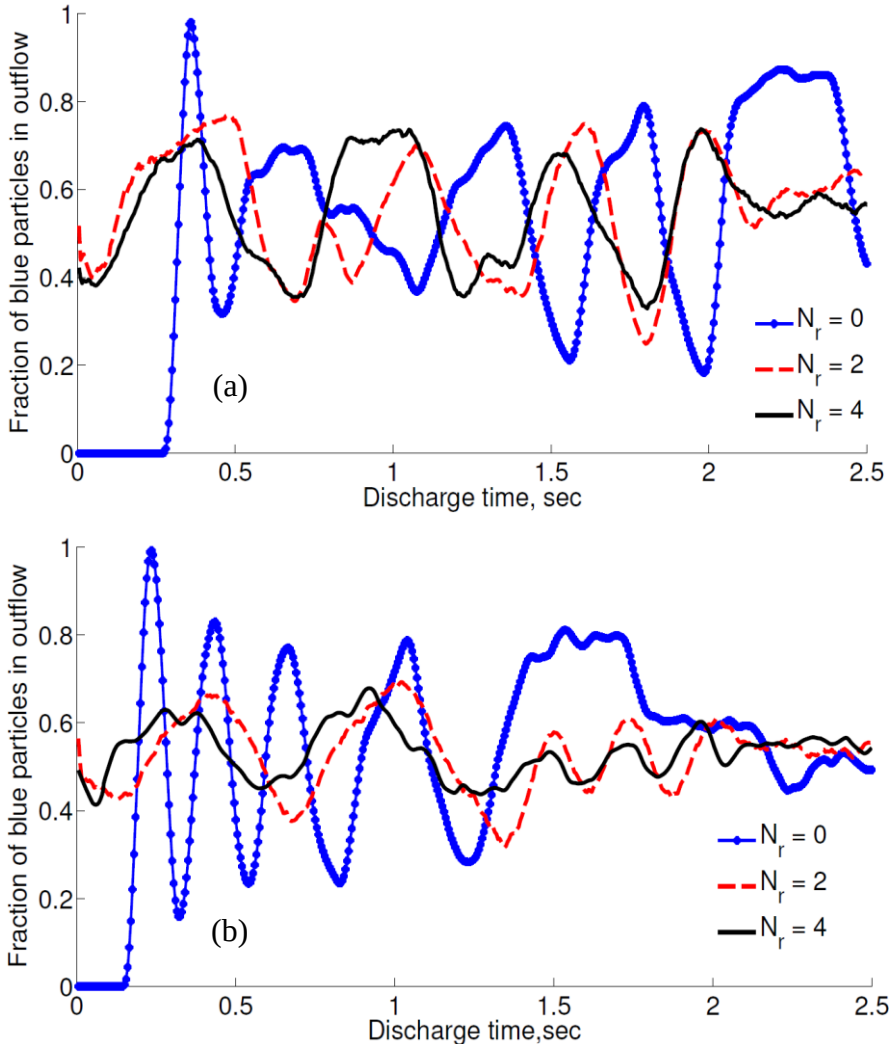

Figure 6.9 Concentration variation of blue particles in the outflow for a 50 % batch size with 5 sub-layers (a) Semi-mass flow (b) Internal flow.

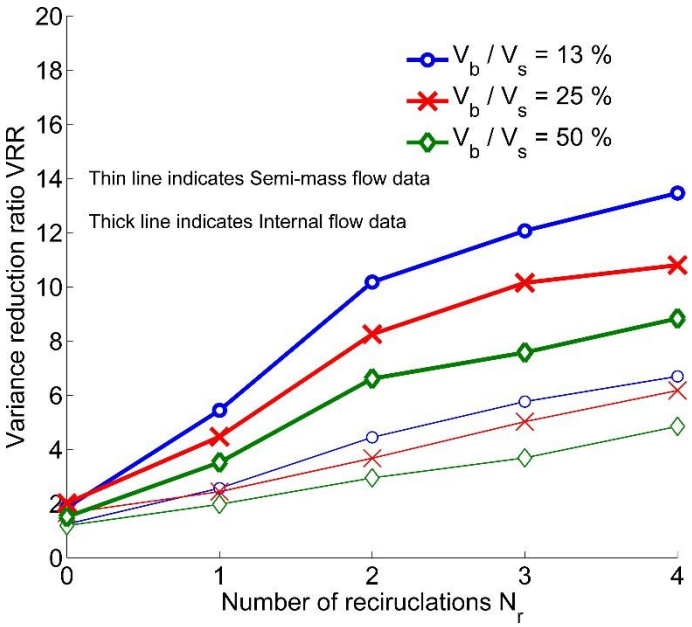

Figure 6.10 Effect of batch size on variance reduction ratio for semi-mass and internal flow patterns.

Figure 6.11 shows the variance reduction ratio as a function of a number of recirculations for different number of sub-layers of blue particles ($N_{sub\text{-}layers}$ = 1, 3 and 5) both for semi-mass and internal flow for a batch size of V_b / V_s = 50 %. The following conclusions can be drawn from this figure:

- In the case of internal flow, for $N_{sub\text{-}layers}$ = 3 and 5 the rate of increase of VRR is higher when compared to $N_{sub\text{-}layers}$ = 1. Whereas in the case of a semi-mass flow, although there seems to be an increase in VRR with the increase in $N_{sub\text{-}layer,}$ it reaches a saturation value after two recirculations irrespective of the value of $N_{sub\text{-}layers}$.
- The VRR increase in all cases with N_r (semi-mass and internal flow). However, the increase rate of VRR is increased with the N_r for internal flow while it keeps more or less the same for the mass flow (the curves are almost parallel, i.e., approximately same slope). For example, with the change in $N_{sub\text{-}layers}$ from 1 to 5: for internal flow, the VRR is found to be increased by 164 % at N_r = 0, but increased as high as 391 % at N_r = 4. For semi-mass

flow, the VRR is found to be increased by 200 % at $N_r = 0$ and 216 % at $N_r = 4$.

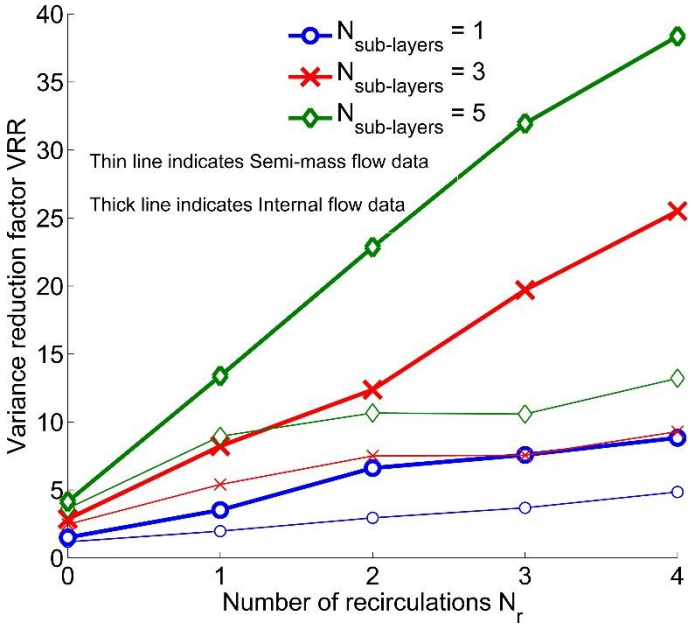

Figure 6.11 Effect of number of layers on variance reduction ratio

6.5 Residence time distribution (RTD) using impulse-stimulus approach

In this section, the evaluation of RTD function using two different methods is presented. The first method is to obtain it directly from the data of id's and positions of the tracer particles injected into a steady flow and the second method involves calculating it from a spatially averaged Eulerian velocity fields by virtually injecting tracers into a rectangular grid.

6.5.1 RTD from particle id's and positions

In a homogenous continuous flow of yellow particles, a small volume of blue coloured particles were instantaneously injected into the inlet stream. The number distribution of the injected tracer particles in the outflow was then obtained from the

DEM output of particle ids and the individual positions of the blue particles. The RTD function *E (t)* can then be calculated using (6.2).

$$\mathbf{E(t)} = \frac{\mathbf{1}}{\mathbf{N_0}} \frac{\mathbf{dN}_{trac}}{\mathbf{dt}} \quad \textbf{(6.2)}$$

where N_o is the total number of tracers injected into the inflow, dN_{trac} is the number of tracers left the silo during the time interval *dt*.

The *E (t)* can be made dimensionless by multiplying with the mean residence time t_{rm} as given by (6.3).

$$\mathbf{E(\theta)} = \mathbf{E(t)} * \mathbf{t_{rm}} \quad \textbf{(6.3)}$$

where θ is the dimensionless time obtained by normalising time with the mean residence time (t_{rm}).

The paths of injected blue tracer particles (of 10 % volume of the silo) are shown in Figure 6.12 and Figure 6.13 for semi-mass and internal flow respectively. As expected, in semi-mass flow, due to the lack of vertical velocity gradients, a major fraction of tracer particles is discharged in a small time interval, whereas in the internal flow they are discharged during a relatively larger time interval giving a wide spread in residence times. As it can also be seen that a small fraction of the tracer particles is trapped in the shear zones in case of internal flow and can take longer than the mean residence time to discharge. Figure 6.14 shows the dimensionless RTD function for semi-mass flow and internal flow. It can be seen that the peak concentration for semi-mass flow occurs nearly at $\theta = 1$ whereas for internal flow it occurs nearly at $\theta = 0.75$: earlier the peak occurs in relative to mean residence time higher the blender efficiency. For example, in the case of a plug or complete uniform flow, all the tracers appear at the outlet at $\theta = 1$ with no axial mixing. The ratio of the time duration of the first appearance of a tracer particle (t_s)

and the total time it takes for its complete discharge (t_d) is an important parameter in achieving a good blending (Johanson, 1970). It was found that the ratio of t_s/t_d is 0.39 and 0.46 for internal flow and semi-mass flow respectively. The lower this ratio, the higher the blending efficiency. The long tail of the RTD after the peak represents the discharge of tracer particles from the side wall and shear zones in semi-mass and internal flow respectively.

Figure 6.12 Images depicting the tracer profile in a semi-mass flow.

Figure 6.13 Images depicting the tracer profiles in an internal flow.

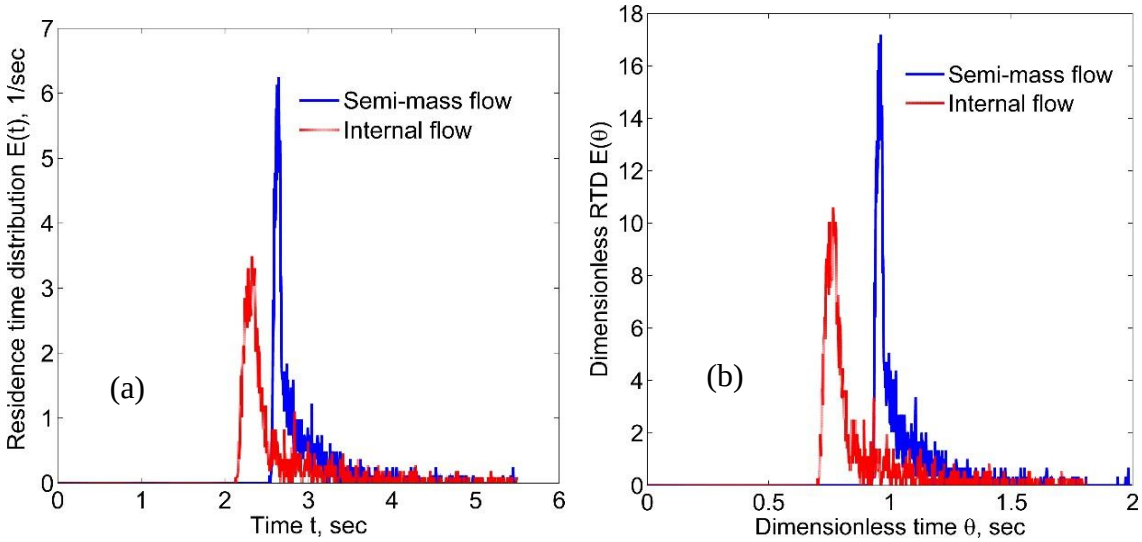

Figure 6.14 Residence time distribution for semi-mass and internal flow (a) Dimensional form (b) Dimensionless form.

6.5.2 RTD from Eulerian velocity fields

In this section, the algorithm to evaluate the RTD function using the bin-averaged velocities is first described followed by the verification of the algorithm by comparing the calculated virtual particle paths released from a selected bin with the actual particle tracks.

6.5.2.1 Algorithm

The schematic of the algorithm is shown in Figure 6.15. The flow domain is divided into square bins of volume *dxdydz* and the average velocity in each bin at each instant is then solely (without the need of individual particle positions and id's) used to calculate the RTD function described as follows.

The first step is to determine the total number of tracer particles (N_o) which can be obtained with the known bulk density and the mass of the particle for a known volume of the tracer. These virtual particles are then placed in a lattice arrangement in each bin at the inlet of the silo as shown in the Figure 6.15. The advantage of using the lattice arrangement is that the equal number of particles can be arranged in each bin without the knowledge of local packing structure. In practice, however, each bin contains a different number of particles because of their random arrangement and

also the particles exists on the intersection between the each bin. The residence time of each particle in each bin can then be obtained by calculating their path by solving the (6.5).

$$\frac{\mathbf{d}\vec{\mathbf{X}}_{ij}}{\mathbf{dt}} = \vec{\mathbf{V}}(\mathbf{x}, \mathbf{y}, \mathbf{z}, \mathbf{t}) \quad \textbf{(6.4)}$$

$$\overrightarrow{\mathbf{X}_\mathbf{i}}(\mathbf{t} + \mathbf{dt}) = \overrightarrow{\mathbf{X}_\mathbf{i}}(\mathbf{t}) + \vec{\mathbf{V}}(\mathbf{x}, \mathbf{y}, \mathbf{z}, \mathbf{t})\mathbf{dt} \quad \textbf{(6.5)}$$

where $\vec{X}_{ij}$ is the position vector of particle *j* of bin *i* at time *t*, $\vec{V}$ is the known velocity vector of that particle at location (x, y, z) at time *t* and *dt* is the time interval of the velocity data.

The time it takes for the vertical positon of the tracer particle to cross the outlet silo is taken as a residence time of that particle. The RTD function can be then be calculated using (6.2). It should be noted that as the velocities are only known at the centre of each bin, an interpolation technique was used to obtain the velocities at locations other than the bin centre.

6.5.2.2 Verification of algorithm

The algorithm was verified by comparing the particle paths calculated from the bin velocities against the paths of individual particles in DEM. For this purpose, a simulation was conducted in a silo of the thickness of one particle diameter as shown in Figure 6.16. Tracer particles were created at five different locations in EDEM post processing tool as indicated in this figure. The paths of these particles were used for the verification of the algorithm. Virtual tracers at the corresponding locations were created to calculate the paths using the algorithm. The silo flow domain was divided into bins of different sizes of 5 mm, 10 mm and 15 mm and the average velocities in each bin at all times were the extracted to a data file as an input to the algorithm.

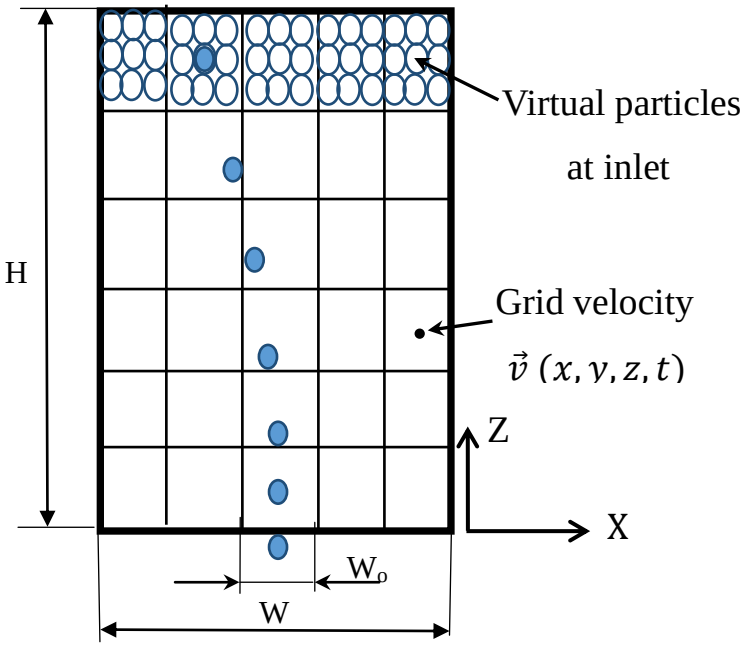

Figure 6.15 Schematic of calculation of particle path from grid velocities.

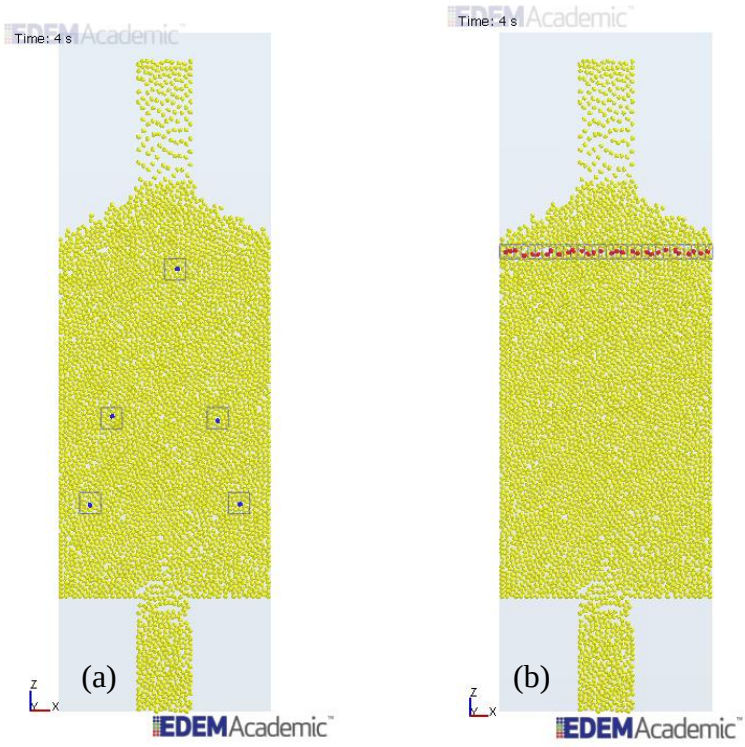

Figure 6.16 Particles chosen for verification of the calculation using bin velocities (a) Particle paths (b) Residence times.

Figure 6.17 (a) - (c) shows the comparison of the particle paths calculated from the bin velocities against the actual tracks. It can be seen that the particle paths calculated from the bin velocities are in close match with the actual path. A slight discrepancy can be seen for a grid size of 15 mm possibly because of errors in interpolation due to large spacing between the grid points. The residence times of virtual particles released at the centre of each bin across the width of the silo at the inlet was calculated (refer to Figure 6.16 (b)) and compared against the corresponding particle scale residence times. The comparison is shown in Figure 6.18 for three bin sizes of 5 mm, 10 mm and 15 mm. A good agreement between the two methods is evident.

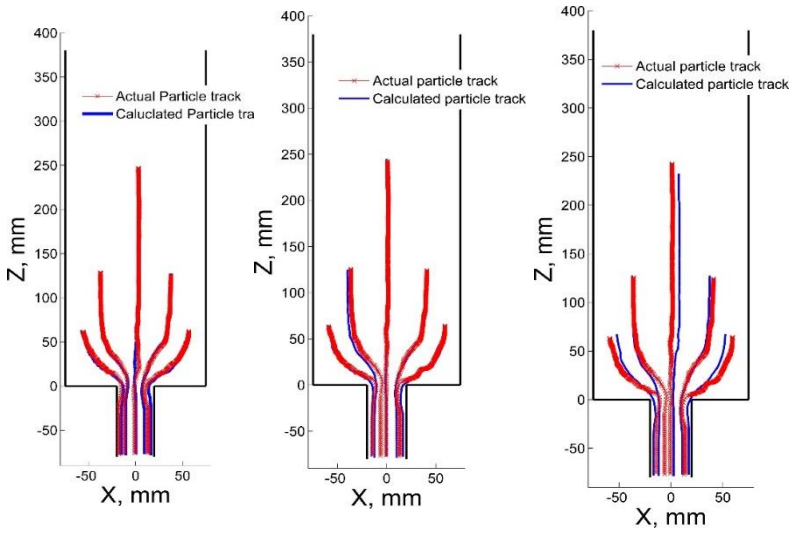

Figure 6.17 Comparison of particle paths calculated from spatially averaged velocities against particle scale DEM (a) Bin size = 5 mm (b) Bin size = 10 mm (c) Bin size = 15 mm.

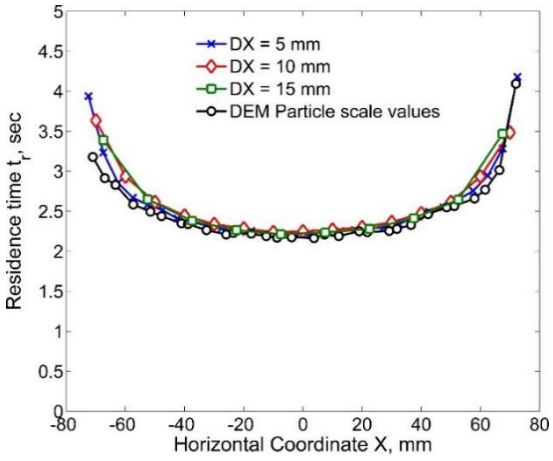

Figure 6.18 Comparison of residence times calculated from grid velocities against the DEM particle scale values.

Having verified the residence times and the particle paths in a single particle thick silo, the algorithm is further applied to the pseudo-2D simulations described in section 6.2 mainly to obtain the residence time spread of particles in each bin at the inlet and further to calculate the RTD function of the silo. For this purpose, the layer of blue colored tracers of height 15 mm and depth 40 mm was created as shown in Figure 6.19. The residence times of each of these tracers were calculated from bin velocities by virtually arranging them in the lattice structure of 10 equal sized bins. Figure 6.20 (a) shows the comparison of the calculated mean residence time of the particles in each bin against the actual value for the case of internal flow. The scattered values indicate the spread of the calculated residence times of particles in each bin. The corresponding the RTD function is shown in Figure 6.20 (b). A good match is evident between the two methods of RTD calculation. However, it should be noted that the RTD function calculated using the bin velocities assumes no velocity gradients within the heap and therefore, the tracer particles are virtually injected as a horizontal layer at the base of the heap. Because of this assumption, RTD shown for internal flow in the Figure 6.14 (b) is slightly different from the one shown here. The algorithm considering the velocity gradients within the heap can be developed in the future.

This algorithm has been further used in the PIV experiments to estimate the RTD function from the measured velocity profiles in a multi-flow blender, which therefore potentially avoids the expensive and time-consuming impulse response experiments with colored tracer particles in 2D planar silos.

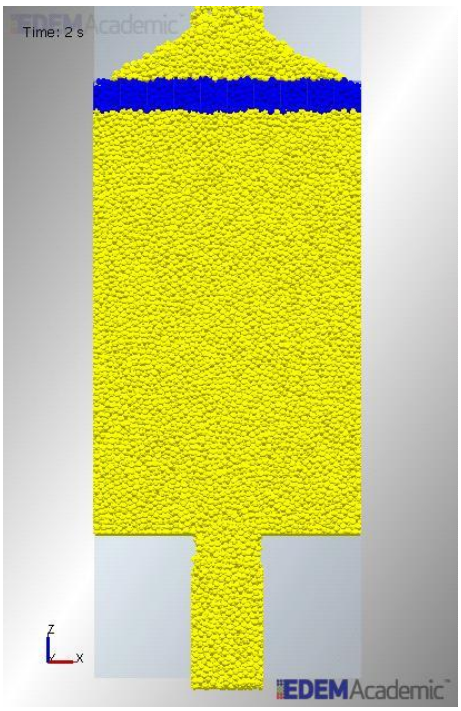

Figure 6.19 Blue colored tracers to calculate RTD function from bin velocities.

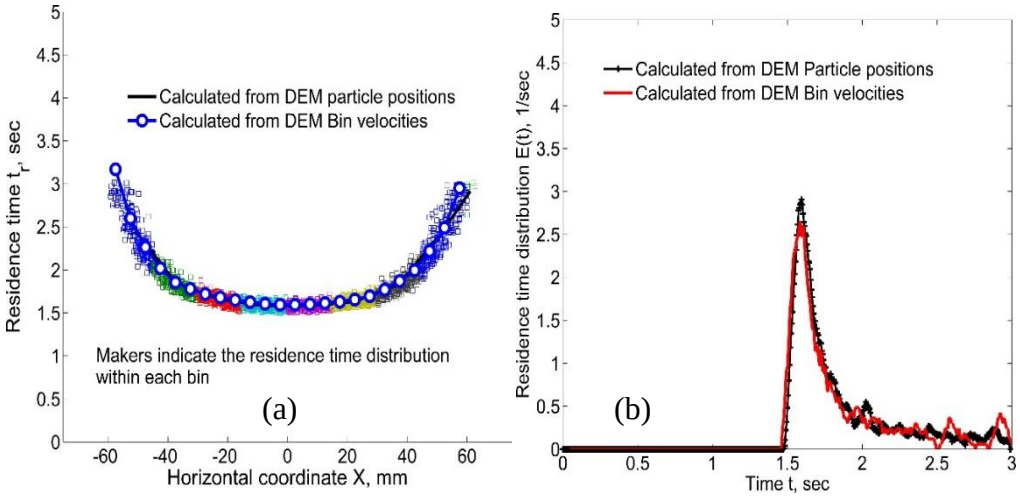

Figure 6.20 (a) Residence time spread of particles in each bin at the inlet (b) Comparison of RTD function from bin velocities against the particle scale.

6.6 Blending effectiveness using LTI theory

The computed RTD function is used to determine the blending effectiveness using the linear time-invariant (LTI) system theory. The LTI theory has been discussed in section 2.2 of literature review chapter. Figure 6.21 summarises the concept of convolution. In this section, first the accuracy of the convolution integral is verified against the particle scale DEM results followed by its application in the discontinuous mode in order to determine the total number of recirculations required to obtain a homogenous mixture and also in continuous mode to determine the VRR as a function of frequency of the input fluctuations.

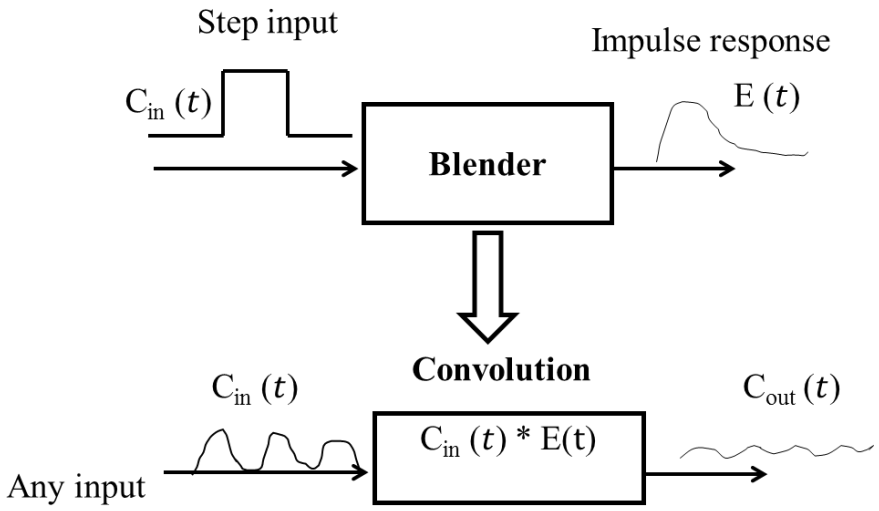

Figure 6.21 Schematic of the concept of impulse-stimulus response and linear system theory (reproduced from (Schneider et al., 2001)**).**

6.6.1 Accuracy of convolution integral

6.6.1.1 Discontinuous mode

Figure 6.22 shows the variation of outlet concentration of a tracer during recirculation obtained from direct particle scale DEM results and computed using LTI theory. It should be noted that in order to evaluate the convolution in

discontinuous mode, the output signal during the first pass is used as an input signal during the second pass and so on, in order to replicate the recirculation (Weiler et al., 2012). It can be seen from this figure that the variation of outlet concentration predicted by the convolution is smooth whereas in DEM a noise can be seen. While this noise in concentration is due to the particulate nature of the flow, the convolution integral is not able to calculate these fluctuations because of the continuous nature of the integral. However, it can be seen that the computation of time duration of the discharge cycles and the start time of the peak concentration are in good match with the DEM data. The noise in the concentration fluctuations is difficult to measure in experiments and also may be of no relevance in characterising the blending performance as a whole.

The decrease in peak concentration during the second pass and also in the subsequent passes indicates the spread of tracer inside the silo after each pass. Ideally after a large number of recirculations the concentration of tracer reaches the steady state. However, running the DEM simulations for large number of recirculations is time-consuming.

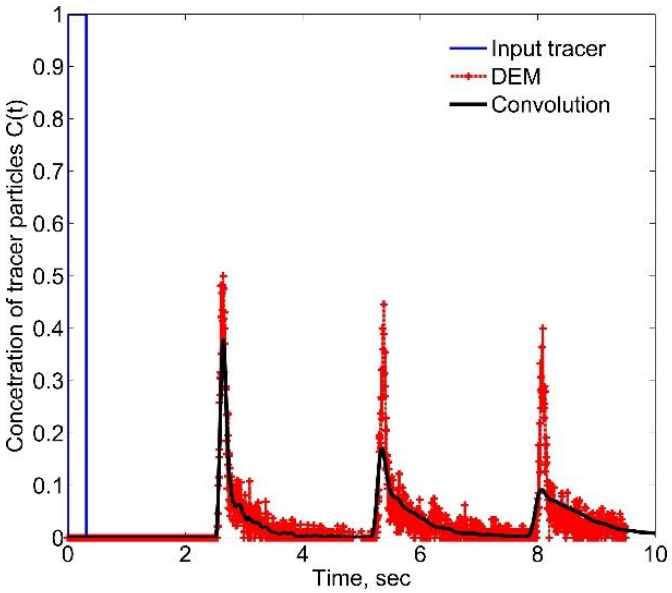

Figure 6.22 Concentration of tracers in outflow during recirculation in discontinuous mode operation. Comparison of convolution method against DEM.

6.6.1.2 Continuous mode

Figure 6.23 shows the variation of outlet concentration in response to a continuous square signal and its comparison with the corresponding calculation using a convolution integral. It should be remembered that in a continuous mode, the material is passed only once through the silo without recirculation and the fluctuations in the inflow are represented as the continuous time signal. In this particular case, square signals were used as an input because of ease their generation in DEM. Similar to the observations in discontinuous mode, it can be seen that the output signal obtained by the convolution integral is smooth and the large fluctuations are not observed. The frequency of the output signal is in good match and so it is obvious that if the output signal from the DEM is smoothed over a small time interval, a good match with the convolution can be found. The main advantage of using convolution in continuous mode is that any random input signal can be generated and the corresponding output variation can be obtained which is otherwise difficult if not impossible to obtain from the DEM data.

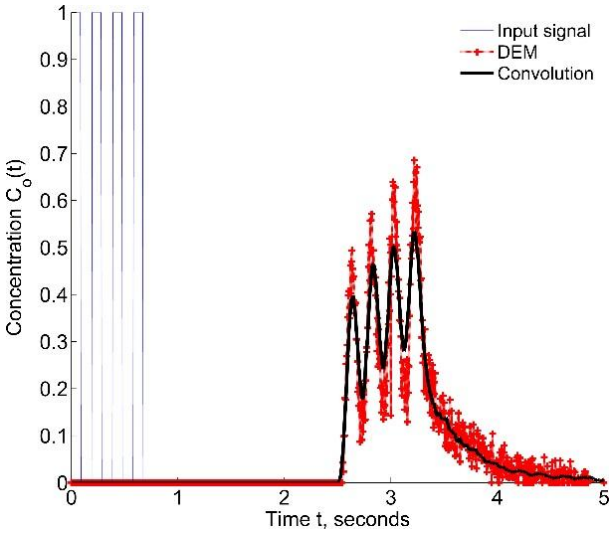

Figure 6.23 Variation of concentration of tracer at the outlet in response to a square signal at the inlet.

6.6.2 **Number of recirculations in discontinuous mode**

Figure 6.24 shows the time variation of concentration of tracers at the outlet computed using convolution for large number recirculations (up to 25) in semi-mass and internal flow. It can be seen that the concentration fluctuations in the outflow reduce faster for the internal flow when compared to the semi-mass flow which supports the discussion in section 6.4.2. Nearly 10 recirculations are required for homogenisation in internal flow and 15 recirculations are required for semi-mass flow for a tracer volume of approximately 20 % of silo volume (V_b / V_s = 20 %).

It should be noted that the convolution integral in discontinuous mode cannot calculate the outlet concentration of a tracer when the recirculation is stopped and the particles are subsequently allowed to discharge under decreasing head level. This is mainly because that the convolution is applicable only for a time-invariant system which holds true for a silo operating under a constant head level in a steady state flow. This also implies that the VRR cannot be calculated in dis-continuous mode using LTI theory. In addition to this, it also cannot calculate the concentration variations in the outflow during the evolution of flow from the end of filling to the steady state. However, its main strength lies in its ability to a give an estimate of the number of recirculations required in order to homogenise a given mixture ratio without having to run the DEM simulation for a long time.

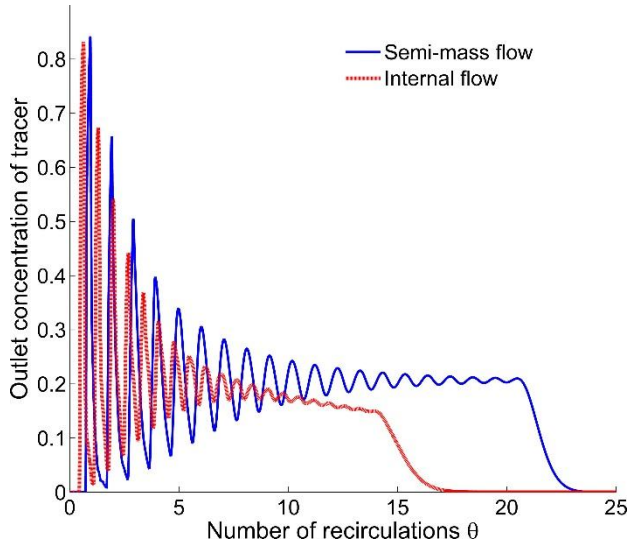

Figure 6.24 Variation of concentration of tracer in outflow for a large number of recirculations using the LTI theory.

6.6.3 **Variance reduction ratio in continuous mode**

The concentration variation at the outlet was computed in response to a continuous input signal represented by a sinusoidal wave and the effect of frequency of the input wave on the VRR was studied. Figure 6.25 (a) and (b) shows the input sinusoidal signal with a time period of 0.1 sec (*i.e.* 3.6 % of mean residence time) and the corresponding output response respectively, for semi-mass and internal flow. It was found that, in internal flow, the standard deviation of the fluctuations in output concentration is 0.042 and it is nearly doubled for the semi-mass flow. It was also found that in the case of internal flow, the mean concentration at the outlet is 0.47 while it is 0.5 at the inlet. This discrepancy arises mainly from the fact that a small fraction of the tracer particles that are trapped in the shear zone (refer to Figure 6.13) are not considered in the calculation of RTD.

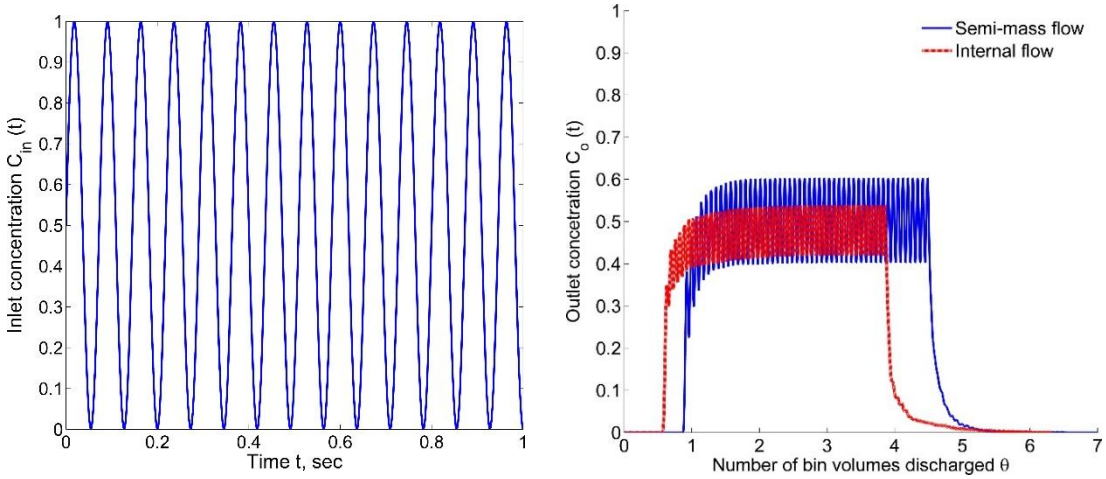

Figure 6.25 Time variation of concentration (a) Continuous input signal (b) Output signal.

Figure 6.26 shows the variance reduction factor for different frequencies of the input sinusoidal signal. It can be seen that the VRR is higher when the frequency of fluctuations is higher which is similar to the effect of batch size in a discontinuous mode (refer to section 6.4.2). However, VRR is much lower in comparison to the discontinuous mode due to the fact that the material is only passed once in the silo

and it can only be increased with the installation of internals to create a much a wider residence times of the particles and also by passing the material through the successive silos.

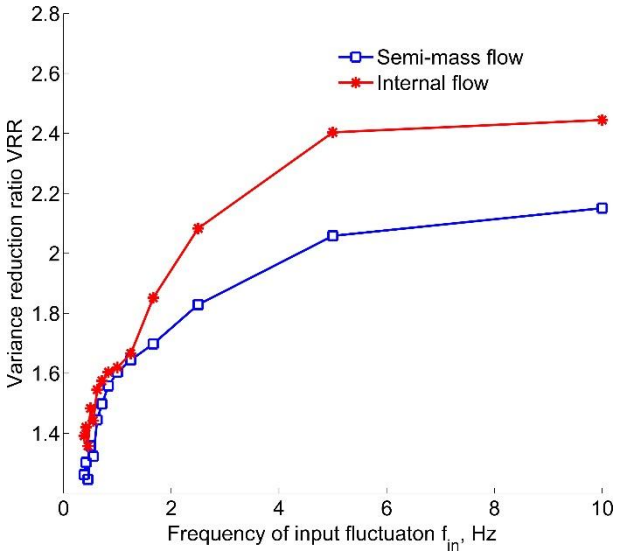

Figure 6.26 Variation of blending factor with the frequency of input fluctuation.

6.7 **Summary**

The DEM model to investigate the blending process in a flat bottom silo in continuous and discontinuous modes of operation has been presented. Two contrasting flow patterns (semi-mass and internal flow) have been simulated in a flat bottom silo by changing the material parameters of the model. The evolution of bulk density and the velocity profiles during recirculation from the end of filling to a fully developed steady have been analysed followed by the investigation of the corresponding blending process of alternative horizontal layers of blue and yellow particles. The blending effectiveness in discontinuous mode has been quantified using variance reduction ratio (VRR) and its variation with the size of batch, number of sub-layers of each batch, number of recirculations in both semi-mass and internal flow has been studied. The rest of the chapter has been focussed on calculating the VRR alternatively using the RTD function and convolution integral in discontinuous and continuous modes. In addition to calculating RTD function from DEM particle

scale results, an algorithm to evaluate RTD from spatially averaged velocity fields has been presented. The following main conclusions can be drawn from this chapter:

- The outflow rate is controlled by applying a constant velocity boundary condition in the outflow of the silo. This is implemented by means of a simple body force model written in the API interface of EDEM software.
- The bulk density and velocity profiles are found to change drastically during recirculation mainly due to the dilation of particle assembly caused by the shearing during the flow. The changes are more significant is case of high frictional internal flow.
- The blending process in the semi-mass flow is limited to very close to the outlet while in internal flow the blending is active in major portion of the silo leading to a higher blending efficiency when compared to the former.
- In case of the internal flow, the batch size significantly affects the VRR while a minor influence is evident in case of a semi-mass flow: lower the batch size higher the VRR.
- For the internal flow, the percentage increase in VRR with the increase in number of sub-layers was found be higher at higher number of recirculations (N_r) whereas it does not hold true for semi-mass flow (increase in VRR remains constant at all N_r).
- The RTD function calculated from spatially averaged Eulerian velocity fields is found to be accurate. This algorithm will be further used in the PIV experiments to estimate the RTD function from the measured velocity profiles in a multi-flow blender. This potentially avoids the expensive and time consuming impulse-response experiments with colored tracer particles in 2D planar silos.
- The variations of outlet concentrations calculated by convolution and from direct DEM output are found to follow the same trend. However, in the former case the variation is smooth whereas in DEM a noise in the concentration variation was found. While these fluctuations are due to the particulate nature of the flow, the convolution integral is not able to calculate these fluctuations because of the continuous nature of the integral.

- The blending effectiveness in continuous and discontinuous mode has been evaluated using LTI theory particularly for those input conditions which are otherwise difficult to study using the DEM results. In discontinuous mode, nearly 10 recirculations are required for homogenisation in internal flow and 15 recirculations are required for semi-mass flow for a tracer volume of approximately 20 % of silo volume. It was also found that in continuous mode, the VRR increases with the increase of the frequency of input fluctuations.

Building upon these studies, in the next chapter the blending and flow patterns are investigated in a multi-flow blender using PIV and DEM. Furthermore, the effect of angle of the cone-in-cone insert on the blending performance is studied.

Chapter 7

7. Development of flow around the internals in a multi-flow blender and the associated blending performance

7.1 Introduction

The multi-flow blender works on the principle of imposing a secondary velocity profile in the vertical section of a mass flow silo (refer to section 1.1 for details). It is similar to a Binsert blender which was originally developed by Johanson (1982). In addition to the placement of a Binsert in the hopper, a blending tube is also installed in a multi-flow blender as shown in Figure 7.1. The installation of the insert and the blending tube in a mass flow silo creates the differences in the velocities at different horizontal positions in both the hopper and the vertical sections of the silo, thus creating a spread in the residence times of the particles, which in turn promotes the blending of horizontal layers of particles at different heights. As illustrated in Figure 7.1, three different flow channels across the width of the silo can be created in the vertical section due to the presence of internals with each flow channel being separated by a thin shear zone. The presence of velocity gradients within these flow channels and between the flow channels creates the difference in residence times of the particles entering the silo. In this figure, the flow channel created due to the presence of the insert is labelled by FC_i while that of from blending tube is labelled by FC_b and the particles that flow through the exterior annulus between the insert and the hopper is indicated as FC_e. The shape and size of these flow channels can influence the extent of blending in this silo.

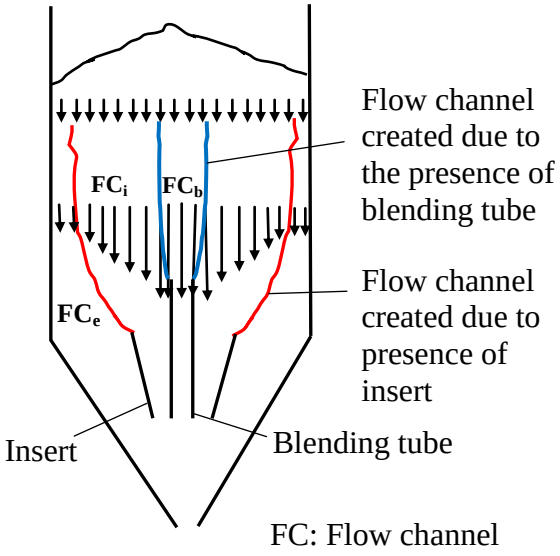

Figure 7.1 Schematic of flow patterns in a multi-flow blender.

The mechanism of development of these flow channels around the internals from the start of discharge and the flow conditions that govern the size and shape of the flow channel and the associated blending performance is of interest in this study. The primary aim of the work is, therefore, to understand the flow development around the different types of inserts and further to characterise the blending performance using the information of flow patterns. The secondary aim is to evaluate the accuracy of the flow predictions by DEM and further to study the effect of gravity on the local velocity profiles.

7.2 Description of the test set-up

A lab scale blender silo was designed according to the conditions proposed by Johanson (1970). The two essential conditions in order to have an efficient blending are: firstly, there should be no stagnant zones (or the bin should be a mass flow bin) and secondly a sufficient difference in residence times of the particles should exist at various horizontal positions across the width at the inlet of the bin. The Jenike design chart for a plane strain flow (Jenike, 1961) which gives the limiting half angle of the hopper (the angle below which a mass flow can be obtained) for a given wall friction and the internal friction of the bulk solids, was used to determine the appropriate

hopper angle for the test silo. It was found that the limiting angle corresponding to the measured properties of the test pellets is 43^o. The hopper angle of the test silo was therefore set to 30^o to create a mass flow condition.

As there are no strict guidelines to choose the size and placement of the insert, they have been chosen based on the experience in the industry. The parameter that controls the size and the placement of the insert in order to achieve a good blending was identified as the area ratio (A_r), which is defined as the ratio of the interior annulus area ratio (A_i) to the exterior annulus area ratio (A_e). All the relevant areas are indicated in Figure 7.2. The interior annulus area ratio (A_i) is defined as the ratio of the area of the interior annulus at the inlet of the insert (A_{ii}) to the corresponding area at the outlet of the insert (A_{io}). Similarly, the exterior annulus area ratio (A_e) is defined as the ratio of the area of the exterior annulus at the inlet of the insert (A_{ei}) to the exterior annulus at the outlet of the insert (A_{eo}).

Three different area ratios were created with the use of diverging insert, straight insert and converging insert as shown in Figure 7.3 (a) - (c) and the corresponding values of area ratio are listed in Table 7.1. For all the configurations, the cone-in-cone or Binsert was placed such that its inlet lies on the circle that passes through the hopper transition with the centre being at the apex of the hopper. The outlet of blending tube was placed at the same level as that of the insert. The inlet of the blending tube extends into the vertical section by an amount of 15 % of the width of the silo. The diameter of the blending tube was chosen to be 40 mm.

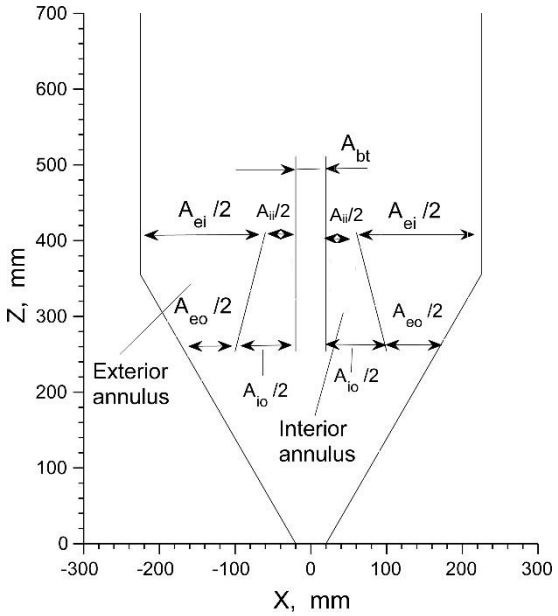

Figure 7.2 Schematic of silo labelled with various flow areas at the inlet and the outlet of the cone-in-cone insert.

Table 7.1 Area ratio for different configurations of the insert.

Configuration	**Interior area ratio (A_i)**	**Exterior area ratio (A_e)**	**Area ratio (A_r)**
Diverging insert	0.5	2.6	5.2
Straight insert	1	1.72	1.72
Converging insert	2	1.18	0.59

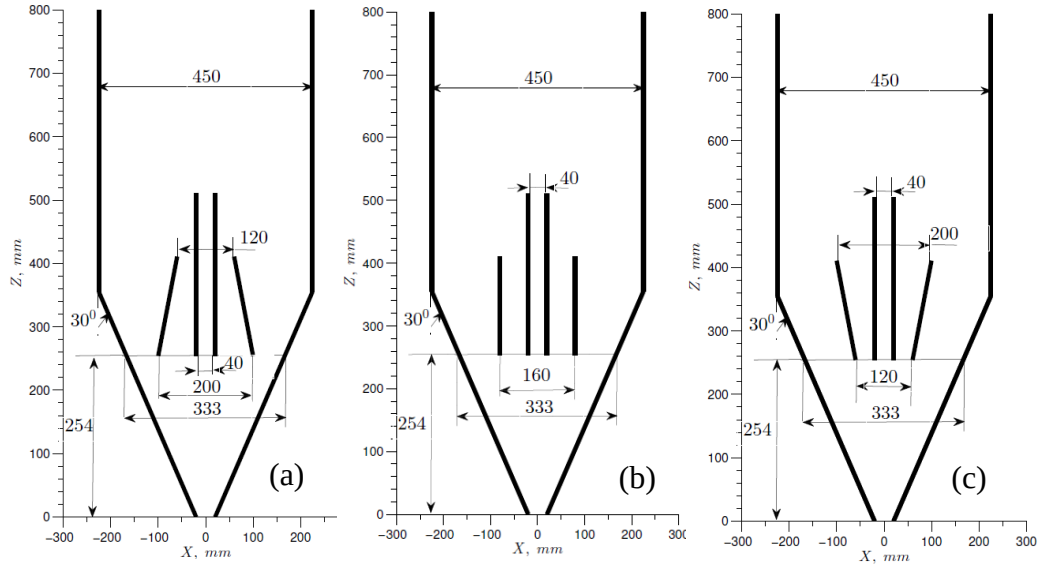

Figure 7.3 Schematic of the planar multi-flow blender indicating the dimensions and location of the insert and the blending tube (a) Diverging insert (b) Straight insert (c) Converging insert.

Figure 7.4 (a) shows the photograph of the test set-up. The set-up comprises of a planar silo, collecting bucket, pneumatic conveying system and a high-speed camera. The silo is of 450 mm wide, 40 mm deep and 1500 mm height above the hopper transition. The outlet size was set to a width of 40 mm. The pneumatic conveying system comprises of a high pressure air supply line, vacuum injector and a flexible hose pipe as shown in Figure 7.4 (b). The vacuum injector is the core component of this system which creates a suction force at its inlet when a high-pressure air (typically in the range 4-5 bar) is supplied to it. Therefore, the injector when placed in a container (in a discharge collecting bucket or in a storage container) conveys the pellets to the top of the silo through a flexible hose pipe that is connected to its other end as indicated in Figure 7.4 (b).

The silo can be discharged in one of the two modes: discontinuous/batch discharge and continuous discharge. During the continuous discharge, a constant head level is maintained by constantly refilling the silo with the discharged pellets while in the other mode the head level decreases with the discharge time. It should be noted that the outlet flow rate that is obtained in both these modes of discharge differ in an order of magnitude explained as follows. In the case of a batch discharge, the pellets

are discharged by free fall after manually opening the outlet wall thereby achieving a gravitational flow rate. Whereas in a continuous discharge, due to the limitations in the capacity of the installed pneumatic system, the maximum outflow rate that can be obtained is only a fraction of what could be achieved when pellets are discharged by free fall.

The silo was centrally filled to a height of 1125 ± 25 mm from the outlet, which is approximately 2.5 times the width of the silo. The total filling height was divided into four measuring windows. Each window is of size 450 mm x 250 mm with an overlap of 40 mm between each window. The selection of the size of the measuring window was discussed in section 3.7. The video was then recorded at a frame rate of 60 fps independently in each region for a maximum duration of 30 sec. The measured data in the overlap region was averaged and the measurements were then combined with each window in order to describe the flow in a full silo. The same test procedure was followed irrespective of the type of discharge mode.

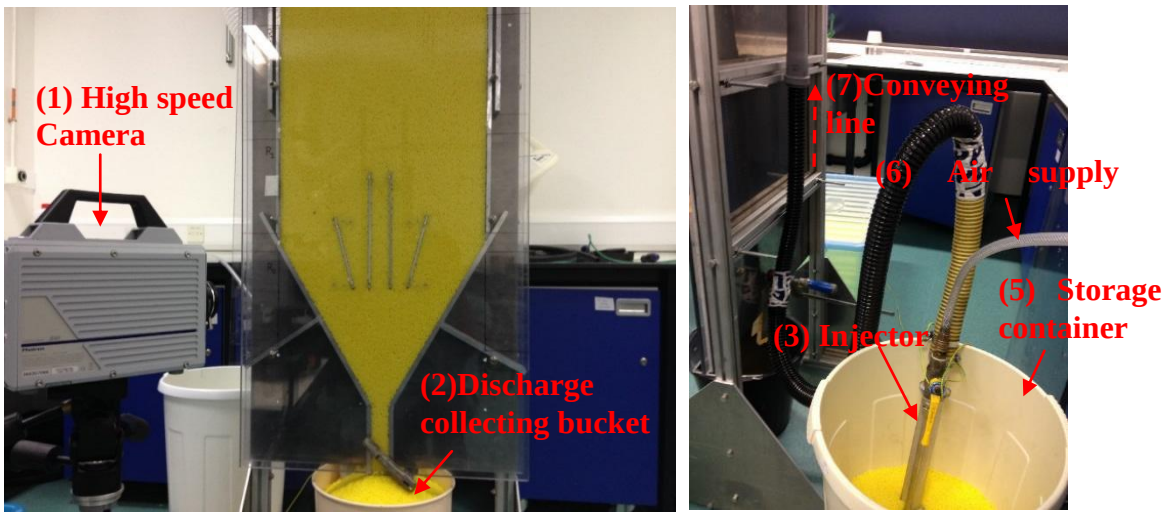

Figure 7.4 Planar multi-flow blender test set-up.

7.3 Details of flow measurement using PIV

Chapter 3 contains the methodology of PIV technique hence only the relevant details of the PIV analysis and the post processing are given in this section. In summary, the

displacement of the patch (a small square region in the image) is measured using the digital image correlation between the two consecutive images at t_1 and $t_1 + dt$. The velocity is then calculated from the displacement and the time interval between the images. A snapshot of the recorded image of each measuring window is shown in Figure 7.5 (a) and the locations of the patches for the measurement are shown in Figure 7.5 (b). A patch size of 40 pixels x 40 pixels (corresponds to approximately 3 particles x 3 particles) was used with an interval size of 20 pixels in horizontal and vertical directions thereby creating an overlap between the patches. It should be noted that the measurement of each patch is not affected by the overlap with its neighbouring patches. The effect of patch size on the measurements was also reported in chapter 3. The measured velocities at all times and at all locations can be written to a standard ASCII format in order to post-process them using commercial or open source post processing tools developed for CFD or FEM such as GiD and Para view. An In-house post processing tool using MATLAB software was developed which is customised particularly to visualise and quantify the flow in the planar silos.

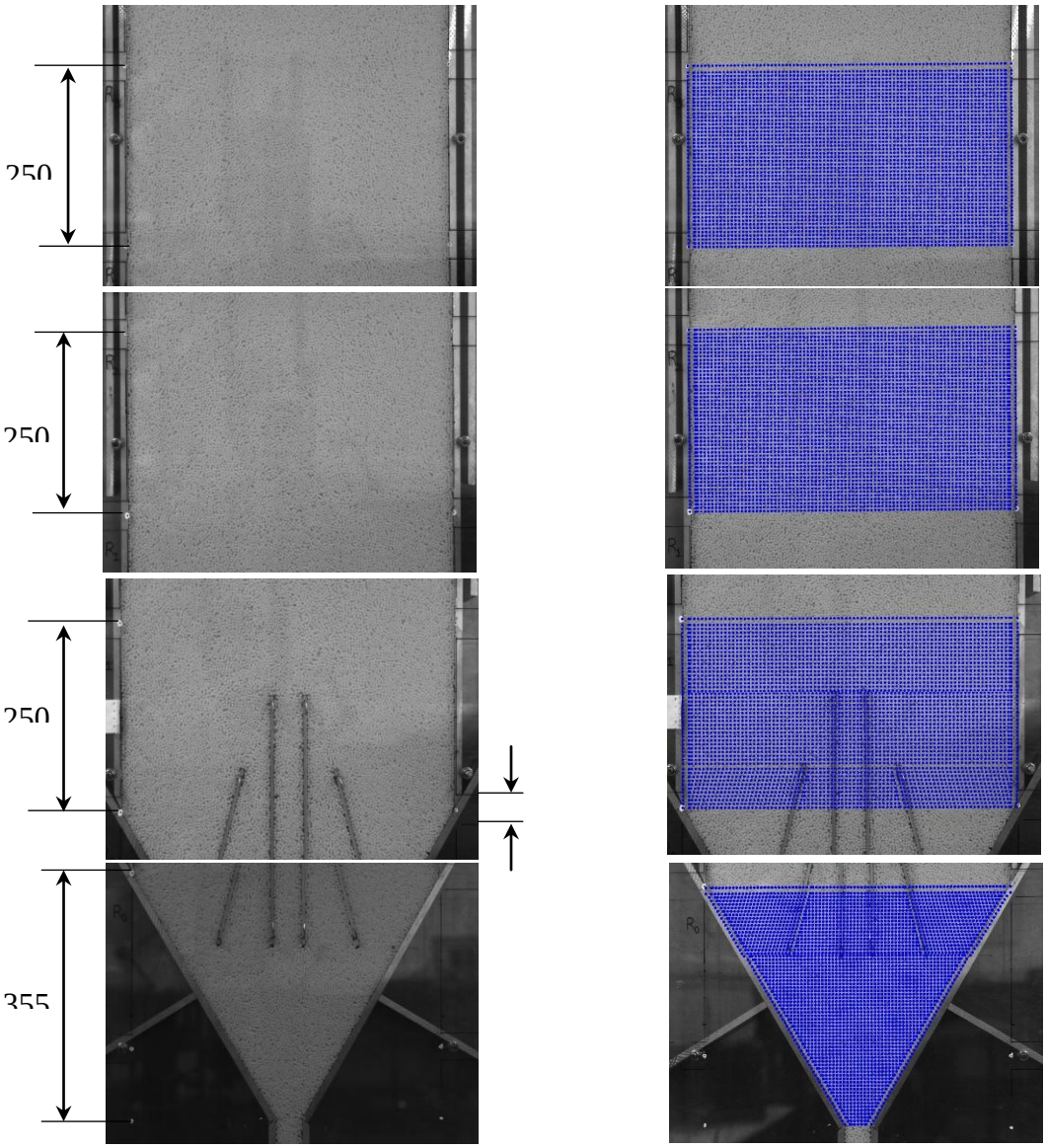

Figure 7.5 (a) Images from each measuring window (b) Patches created for velocity measurement.

7.4 **Evolution of flow in a silo with and without internals**

The temporal and spatial development of flow is investigated in order to understand the mechanism and origins of residence time spread of the discharged particles for different insert (diverging, straight and converging) configurations.

In this section, the state of flow patterns at different instants during the batch discharge are analysed to understand the process of evolution of flow to a steady state. First the evolution of flow without internals are described followed by the discussion of increased complexity resulted from the placement of a diverging insert and a blending tube. The flow patterns are described from the spatial and temporal changes of vertical velocity profiles at selected key locations as indicated in Figure 7.6 at different times (t = 0, 0.1, 0.2, 0.3, 0.4, 0.5, 1, 2, 4, 6 sec) from the start of discharge. The locations are defined in terms of positions of the insert (h_{ii} and h_{io}) and the blending tube (h_{bi} and h_{bo}), the width of the silo (W) as labelled in this figure.

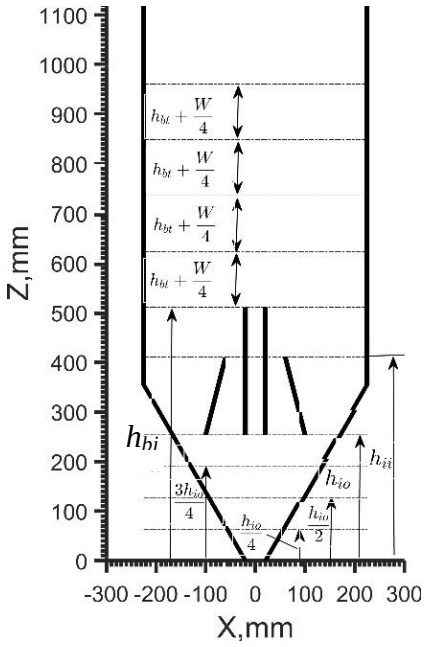

Figure 7.6 Schematic showing the selected key locations to investigate the development of flow.

7.4.1 **Silo without internals**

The velocity profiles within the hopper and the vertical section from the start of discharge until 6 sec are shown in Figure 7.7 illustrating the spatial and the temporal development of flow. The velocities at each time instant are averaged over a period of ± 0.05 sec. The velocities across the width of the silo at any height are normalised by the mean velocity over the cross-section at that height.

The coloured solid lines without the marker at any height indicates the velocity data for the silo without internals while the line with the markers indicates the data for the silo with internals. The value of the colour contour on each line at any height gives the ratio of the vertical velocity to the mean velocity at that height. The magnitude of the velocity in this figure can also be obtained by distance from the horizontal line at any height. The following observations and conclusions can be made from the Figure 7.7:

- Immediately after opening the outlet, the flow was found to propagate upwards from the outlet to the surface. This can be interpreted from the successive increase in the vertical velocity at different heights starting from the outlet in the upward direction. It is also evident from the shape of the vertical velocity profiles at t = 0.3 sec, which is only approximately 1 % of the total discharge time, the flow reaches the top surface indicating the upward propagation is very fast with a velocity of approximately 1.3 m/s.
- During the initial stages (at t = 0.1 sec and 0.2 sec) of flow, it can be seen that the flow in the vertical section is not symmetric about the axis (as highlighted in the figure at t= 0.1 sec). The possible existence of local differences in the bulk density at the end of filling is thought to be the cause of asymmetric upward propagation of flow. It can be imagined that as the flow propagates upwards, it homogenises the local differences in the bulk density consequently creating a symmetry in the flow which can be seen from the velocity profiles at t = 0.3 sec.
- The velocity profiles within the vertical section of the hopper were found to be completely uniform up to 1 sec from the start of discharge. However after 1 sec, it was found that the shape of the velocity profile at any height in the vertical section is successively changing to a non-uniform profile (as evident from the

changes in the velocity profiles from t = 1 sec to t = 6 sec) indicating the further development of the flow. This secondary development of flow channel in the vertical section is thought to be resulted from the flow propagation due to the bulk density differences within the hopper and the vertical sections: the vertical velocity gradients within the hopper causes the dilation of the pellets thereby creating a difference in the bulk density between the vertical section and the hopper.

- Regardless of local velocity gradients at any height, a mass flow across the full silo is evident which is in accordance with the predictions from the Jenike chart.

7.4.2 Silo with internals

The flow evolution with an insert and a blending tube was found to be a complicated phenomenon particularly in the regions above the insert and the blending tube because of the coupled interaction of flow channels that are resulted from the presence of this two internals. The development of flow above the internals can be divided into three processes: firstly the development above the blending tube, secondly the development above the insert and finally the interaction of flow channels resulted from these two. In the following, step by step changes in the flow from the start of discharge (below the insert, above the blending tube and the insert) are described with the aid of normalised vertical velocity profiles shown in Figure 7.7 at different times:

- The developed flow patterns below the insert were found to be similar to the profiles in hopper without internals, except in the region close to the outlet of the insert. Up to a certain distance below the insert, the velocities at the hopper wall were reduced due to the presence of insert.

It can be seen that during the initial stages (until t = 0.5 sec) of flow evolution, the velocity profiles above the blending tube resembles the flow in a flat bottom silo (refer to t = 0.5 sec in Figure 7.7). However, in the latter stages, the flow that propagates upwards from the opening of insert was found to interact with the funnel flow developed above the blending tube resulting in the flattening of velocity profile above the tube as evident in the Figure 7.7 at t = 1, 2, 4 and 6 sec.

- It can also be seen from the shape of the velocity profiles at any height above the blending tube at t = 1, 2, 4 and 6 sec, the flow channel expands side wards until it reaches a steady state and during this process the centreline velocity at a given height found to decrease because of the increased flow area.
- It was found that the flow at all heights reaches steady state between 4 sec to 6 sec from the start of discharge. Figure 7.8 shows the comparison of steady velocity profiles during the batch discharge and continuous discharge. It can be seen that the steady state flow profiles developed during a batch discharge are similar to that in continuous discharge thereby suggesting that the flow profiles in the downstream are independent of falling head. It should be noted that as the outflow rate achieved in batch and continuous discharge are different, the velocity at each height in both cases are normalised by the cross-sectional mean velocity in order to make a sensible comparison.

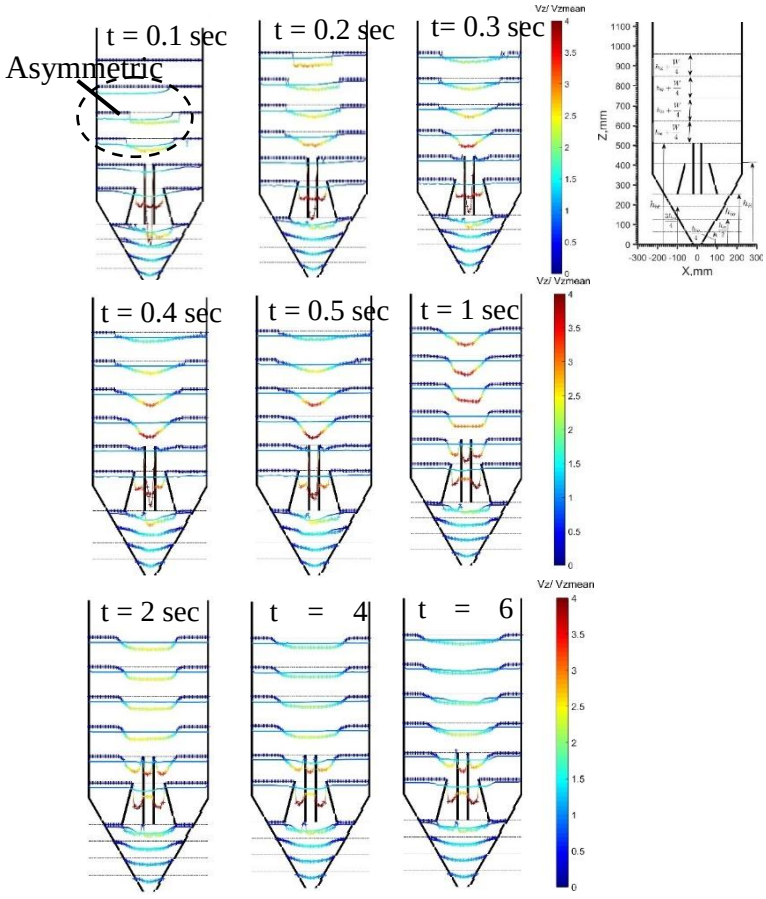

Figure 7.7 Normalised vertical velocity profiles illustrating the spatial and temporal changes of flow in the silo with and without internals. (Solid line

indicates the data for the silo without the internals and solid line with markers indicate the data for the silo with the internals).

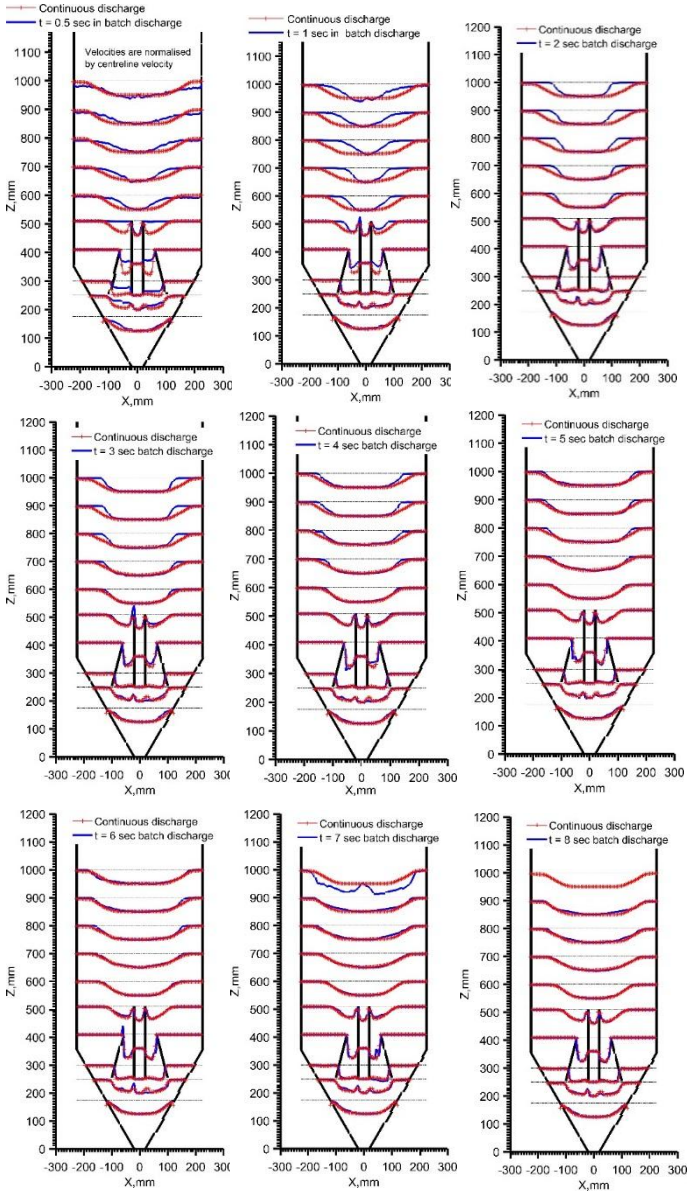

Figure 7.8 Comparison of steady state velocity profiles in continuous discharge with the evolution of velocities in a batch discharge.

7.5 Characterisation of steady flow patterns

Having investigated the evolution of flow from the start of discharge to a steady state during a batch discharge, the steady state flow characteristics during the continuous discharge including the velocity distribution around the insert and the blending tube,

the flow channel boundary in the vertical section of the silo for three different types of inserts (each giving rise to different area ratios) are investigated. In the next section, the blending performance is evaluated from the flow patterns developed in each of these configurations.

The velocities were averaged over a steady state period of 2 sec containing 120 data points. The velocities across the cross-section of the silo at any height are normalised by the mean velocity at that height. The mean cross-sectional velocity at the inlet of the silo for all the configurations is found to be 3.5 ± 0.42 mm/s.

7.5.1 **Diverging insert and blending tube**

7.5.1.1 Velocity distribution at the outlet and the inlet of the insert

Figure 7.9 shows the steady state normalised vertical velocity distribution at the outlet of the insert for a diverging insert configuration in comparison to the distribution without the internals. It can be seen from this figure that due the placement of the insert and the blending tube, a velocity differential exists between the exterior and the interior annulus at the outlet of the insert. Various distinct features of the velocity differential can be noticed from this figure: the velocity is very low and uniform across the exterior annulus and, within the interior annulus it gradually increases towards the centre followed by a high velocity within the blending tube. Furthermore, a sharp decrease in the velocity can also be seen at the boundary between the insert and the blending tube. This dip in velocity occurs due to the formation of the empty space directly below the walls of the blending tube.

It was found that at the outlet of the insert, the mean velocity in the exterior annulus is only 0.16 times of the cross-sectional mean velocity while it is 1.49 and 1.79 in the interior annulus and the blending tube respectively. The velocity in the exterior annulus is low due to the fact that at the outlet of the insert, the diverging insert occupies 63 % of the cross-section of the hopper leading to a high included angle of 44^{o} between the outer hopper and the insert which potentially retards the flow in the exterior annulus.

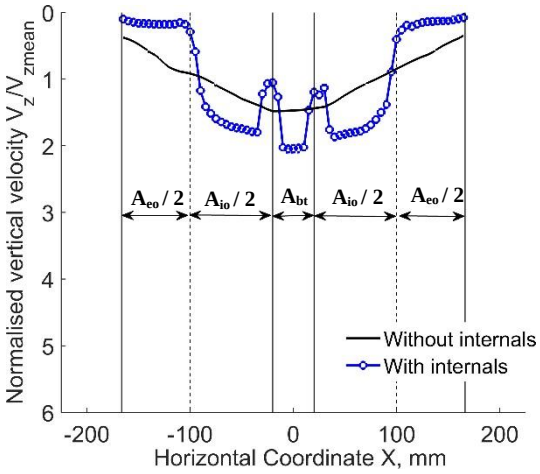

Figure 7.9 Steady state vertical velocity distribution for diverging insert at the outlet of the insert.

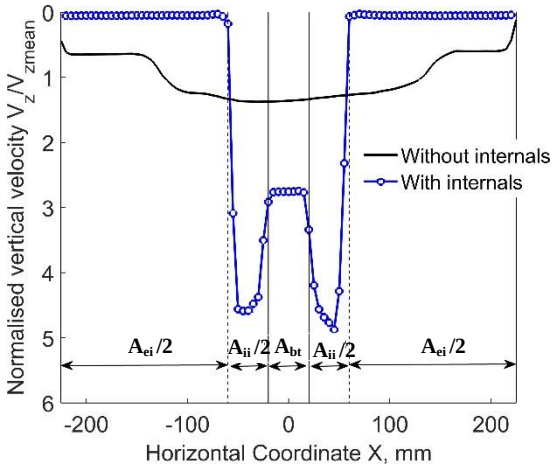

Figure 7.10 Steady state vertical velocity distribution for diverging insert at the inlet of the insert.

The velocity distribution at the inlet of the insert as shown in the Figure 7.10 is mainly governed by the interior and the exterior area ratio. According to the continuity equation, if the area decreases, the product of the density and velocity increases in order to maintain a constant mass flow rate. As it can be seen in this

figure, that because of increase in the area of the exterior annulus (from the outlet to the inlet of the insert) the velocity in this region further decreases, conversely the velocity in the interior annulus increases. The expansion and contraction of the area in the exterior and the interior annulus lead to the development of a strong velocity differential between both the annulus at the inlet of the inlet.

Due to the large difference in the residence times between both the annuli, the slow moving pellets from this exterior zone do not actively participate in the blending process. Therefore, the mixing/blending with this configuration relies mainly on the presence of velocity gradients within the interior annulus and also between the interior annulus and the blending tube.

7.5.1.2 Flow above the diverging insert and the blending tube

Figure 7.11 shows the vertical velocity distribution at different heights in the silo and the computed flow channel boundary (FCB) in the vertical section of the silo. The FCB at any height was defined as 10 % of the centreline vertical velocity at that height. It was found that there is a slight movement of pellets near the side walls at any height in the vertical section and at the same time there exist shear zones at some distance from the side wall at that height. Therefore, in order to accurately compute the FCB, the velocities across the width of the silo at any height in the vertical section were deducted by the velocities near the side wall at that height. It should also be noted that the FCB is not characterised by a single point at any height but can be defined by two points between which the strong velocity gradients can exist (Zhang and Ooi, 1998). In this figure, the FCBs correspond to the points that are close to the side wall on either side of the axis of the silo are shown. There can two more FCBs slightly closer towards the centre. It can be seen that the FCB extends deep into the vertical section indicating a larger influence of the insert. It is also evident that the flow channel created by the insert widens with the distance from the insert.

It was found that with the diverging insert configuration, the presence of blending tube does not create the vertical velocity gradients above it. This is mainly because of the interaction of flow profiles that are caused by the diverging insert with those caused by the blending tube consequently leading to a uniform vertical velocity above the tube (as also discussed in the section 7.4.2). Furthermore, due to the finite wall thickness of the blending tube, a localised effect on the flow can be seen in Figure 7.12 which shows the normalised vertical velocity distribution above the tube up to a height of one diameter of the tube. It can be seen that at the inlet of the tube (at $Z_{bt} = 0$), the flow is faster in the tube and a very low velocity exists on the walls of the tube due to the intermittent resting of the particles. This wall effect was found to extend up to a small height of one diameter of the tube as shown in this figure.

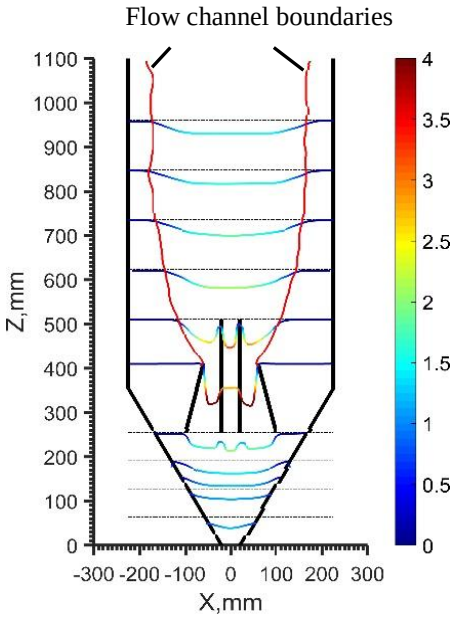

Figure 7.11 Steady state vertical velocity profiles and flow channel boundary in a silo with diverging insert and blending tube.

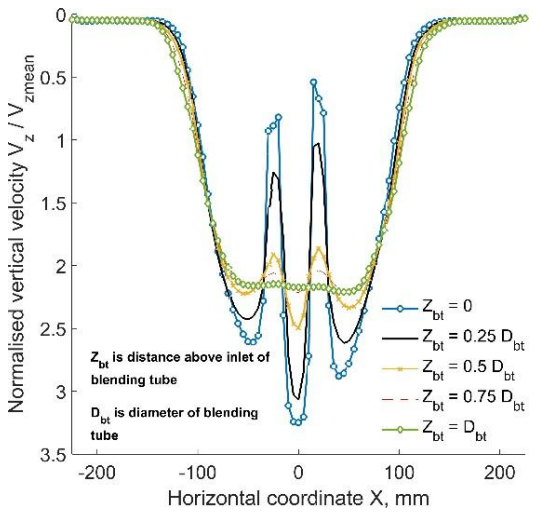

Figure 7.12 Steady state vertical velocity profiles above the opening of the tube in a silo with diverging insert and blending tube.

7.5.2 Straight insert and blending tube

The area ratio was decreased by changing the configuration of the insert to straight (refer to Figure 7.3). Figure 7.13 shows the steady state normalised vertical velocity distribution at the outlet of the insert for a straight insert configuration. With this configuration, at the outlet of the insert, the area of the interior annulus is lower and that of exterior annulus is higher in comparison to the diverging insert. This led to an increase of velocity in the exterior annulus as shown in this figure. Unlike in the case of diverging insert configuration, the velocity distribution within the interior annulus was found to be uniform. Furthermore, it can be seen that the average velocity within the interior annulus and the blending tube is nearly same. Similar velocity distribution can be seen at the inlet of the insert as shown in Figure 7.14: the velocity is high and uniform across the interior annulus and the blending tube, when compared to the velocity in the exterior annulus. But due to the expansion of area in the exterior annulus (from the outlet to the inlet the insert), the magnitude of velocities within each annulus at the inlet of insert redistributes according to the

continuity equation. Therefore, an increase in velocity within the interior annulus and the blending tube is evident.

It is important to note that the magnitude of velocity differential (difference in mean velocity between the interior and exterior annulus) across both the annuli at the inlet of the insert is lower than the velocity differential developed in the case of the diverging insert. Consequently, it will have an implication on the size and shape of the flow channel boundary discussed as follows.

Figure 7.15 shows the vertical velocity distribution at different heights in the silo and the computed flow channel boundary (FCB) in the vertical section of the silo. It can be seen that the flow profiles changes when compared to those developed in case of a diverging insert: an increased movement along the side walls can be seen and the velocity distribution at different heights in the vertical section is slightly uniform. Due to the presence of low-velocity differential across both the annuli at the insert, the angle of approach of the pellets into the insert (or in the other words the angle of FCB with the horizontal at the inlet of the insert) is found to be steeper. Furthermore, the flow profiles developed above the blending tube are similar to those developed in the diverging insert as shown in the Figure 7.16. Due to the increased movement in the exterior annulus with straight insert configuration, the pellets may effectively mix/blend with those coming from the insert and the tube due to the differences in the residence times.

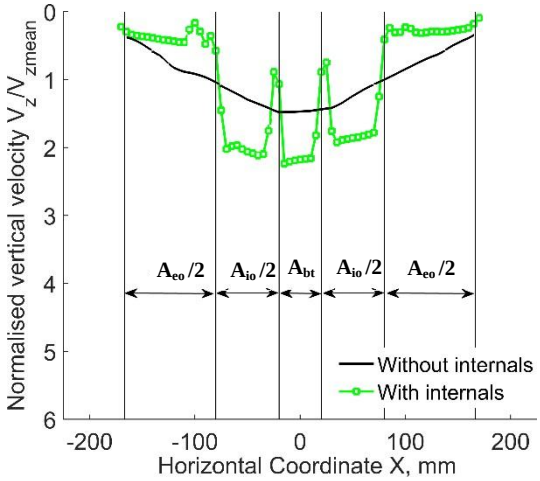

Figure 7.13 Steady state vertical velocity profile for straight insert at the outlet of the insert.

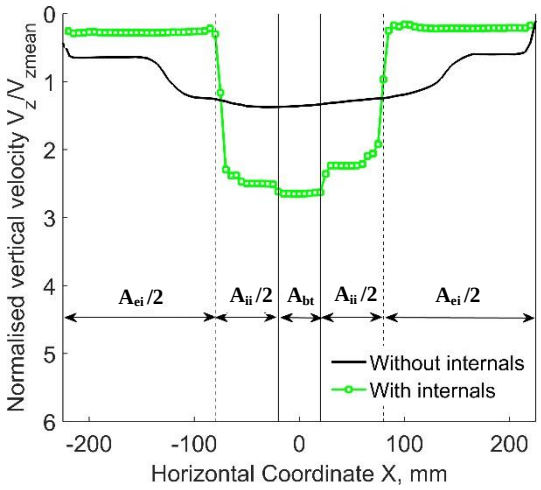

Figure 7.14 Steady state vertical velocity profile for straight insert at the inlet of the insert.

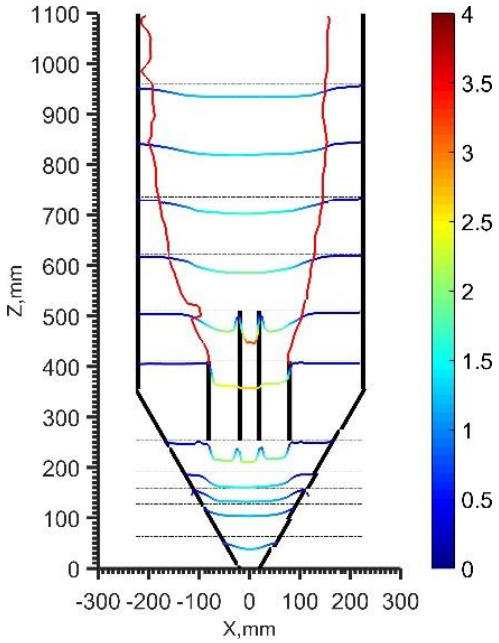

Figure 7.15 Steady state vertical velocity profiles and flow channel boundary in a silo with the straight insert and the blending tube.

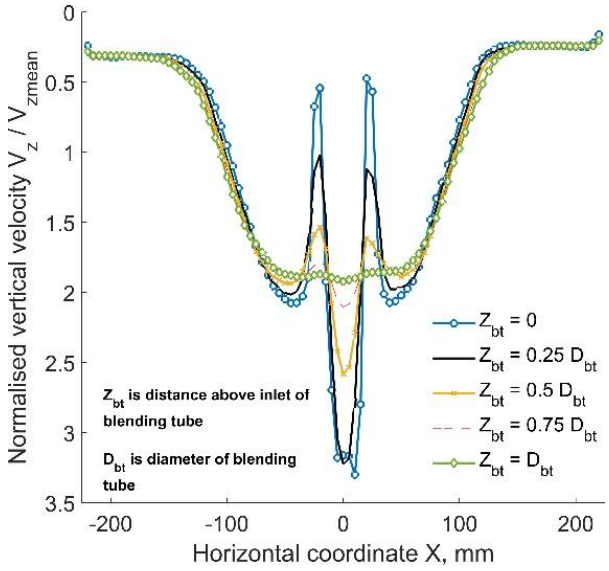

Figure 7.16 Steady state vertical velocity profiles above the opening of the tube in a silo with the straight insert and the blending tube.

7.5.3 Converging insert and blending tube

With a further decrease in the area ratio, the area of the exterior annulus at the outlet is increased whereas that of the interior annulus is decreased in comparison to both straight and diverging insert configurations. Figure 7.17 shows the steady state normalised vertical velocity distribution at the outlet of the insert for a converging insert configuration. It can be seen that with this configuration, three distinct velocities in each zone are evident: the flow is faster in the tube followed by within the interior annulus and then in the exterior annulus. Figure 7.18 shows the corresponding velocity distribution at the inlet of the insert. Although there exists a velocity differential between both the annuli at the outlet of the insert, it can be seen that the velocity is uniform across both annuli at the inlet of the insert. This due to the expansion and contraction of the area in each of the annulus leading the reduction of velocity differential.

Figure 7.19 shows the vertical velocity distribution at different heights in the silo and the computed flow channel boundary (FCB) in the vertical section of the silo. It can be seen that due to the lack of velocity differential between both the annuli at the

inlet of the insert, no distinct flow channel boundary is evident in the vertical section. Therefore, the velocity is completely uniform across the width of the silo at all height in the vertical section except close to the blending tube. At the opening of the blending tube, as shown in the Figure 7.20, a funnel type flow was developed above the blending tube (similar to those develops during the discharge in a flat bottom silo). This is due to the fact that at the inlet of the blending tube, a velocity differential exists between the flow through the tube and the rest of the silo cross-section at that height unlike in the case of both diverging and straight insert configuration.

Due to the lack of vertical velocity gradients in the major portion of the vertical section of the silo, there will be no significant mixing in this region. However, the existence of vertical velocity gradients at the outlet of the insert, inlet of the blending tube and within the hopper enhances the blending of pellets in this silo.

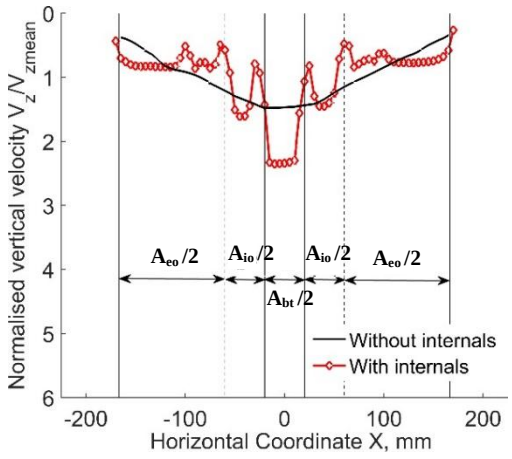

Figure 7.17 Steady state vertical velocity distribution for converging insert at the outlet of the insert.

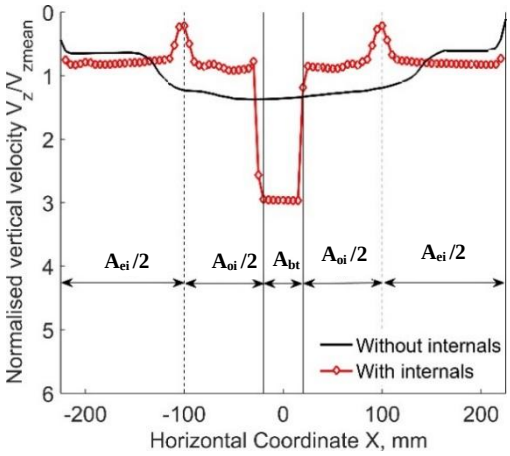

Figure 7.18 Steady state vertical velocity distribution for converging insert at the inlet of the insert.

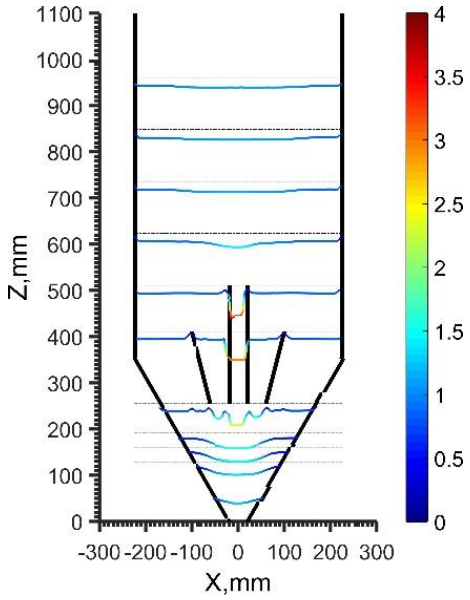

Figure 7.19 Steady state vertical velocity profiles in a silo with converging insert and blending tube.

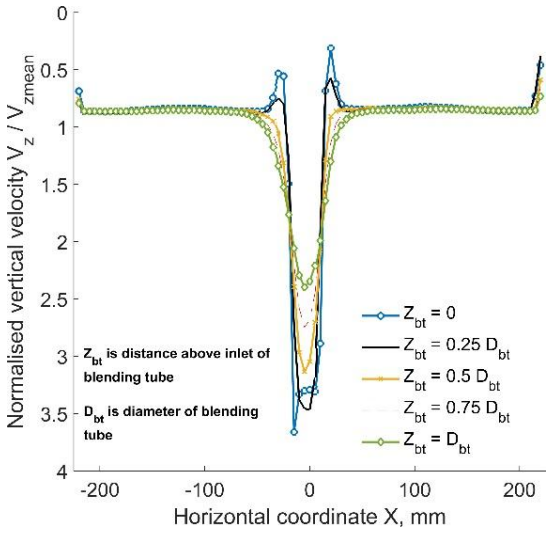

Figure 7.20 Steady state vertical velocity profiles above the opening of the tube in a silo with converging insert and blending tube.

7.6 Predicting blending performance using linear system theory

In the previous chapter 6, an algorithm to evaluate the residence time distribution (RTD) function from the Eulerian velocity fields and the computations of blending performance using the linear system theory have been presented. In this section, the results of computations of RTD function and the blending performance for each configuration which is evaluated using the same concepts are presented.

7.6.1.1 Path lines, residence times and residence time distribution function

The residence time is the time taken by a particle (placed at any location at the inlet of the silo) to reach the outlet of the silo. It can be calculated by computing the path line (locus of points of x and z position at each instant) of a particle for a given starting position from the data of velocity fields. Virtual tracers/particles were considered at different horizontal positions at a spacing of 15 mm and at a distance of 1200 mm above the silo outlet. The computed path line of each tracer particle is

shown in the Figure 7.21 (a), (b) and (c) for diverging, straight and converging insert configurations respectively. It can be seen that the particle paths are smooth and continuous due to the fact that they are calculated from the time averaged state velocity fields ignoring the minor local fluctuations with time. The resulting error in the calculation of path line after ignoring the local velocity fluctuations was found to be negligible as shown in section 6.5 of chapter 6.

In a mass flow silo without internals, it is known the path of the particles in the vertical section is vertical while in the hopper they are in the radial direction towards the apex of the hopper. It is obvious that due to the change in the velocity fields with the placement of the insert and the blending tube, the path lines changes in both these sections. It can also be imagined that the role of the insert and the blending tube is to divert these path lines thereby influencing the residence times. Figure 7.21 (a) – (c) shows the computed path lines in each silo configuration. The thick path lines shown in these figures indicate the boundary between the flow channels of the exterior annulus, the interior annulus and the blending tube. It can also be seen in the Figure 7.21 (a) that, for the diverging insert configuration, the path lines in the vertical section starts to deviate from the vertical path approximately at a height of 400 mm above the location of the inlet of the insert. With the decrease of area ratio or in the other words changing the configurations to straight insert and converging insert, the following changes in the path lines can be noticed:

- The curvature of the path lines caused by the insert in the vertical section decreases with the decrease of area ratio while the curvature above the blending tube slightly increases.
- For a converging insert configuration, the path lines in the vertical section remain vertical (except in the region very close to the opening of the tube) and they change to radial direction at a point on the circle that passes through the transition points of the hopper with its centre at the apex of the hopper: it should be noted that this location also corresponds to the location of the inlet of the insert.

- The path of the particles is vertical directly below the insert for all configurations up to a certain distance below the insert before changing to the radial direction towards the outlet.

Figure 7.22 (a), (b) and (c) shows the residence times of the particles released at different horizontal positions at the inlet of the silo for diverging, straight and converging insert configuration respectively. It can be seen that for the diverging and the straight insert configurations, the residence times are uniform across the major central portion of the silo and differ by a large amount when compared to residence times close to the side walls, whereas there exist three different residence times (each corresponding to the exterior annulus, interior annulus and within the blending tube) for converging insert configuration.

In order to calculate the RTD function from individual particle residence times, tracers of 10 % of the volume of the silo were virtually created at the inlet. The number of tracer particles corresponds this volume were calculated from the known bulk density. These particles were then arranged in a lattice arrangement as opposed to a random arrangement in a real scenario. The procedure presented in section 6.5 of chapter 6 was repeated to calculate the RTD function. The computed non-dimensional RTD ($E(\theta)$) is shown in Figure 7.23 (a) - (c) for each configuration. The time axis is normalised by the mean residence time giving rise to a dimensionless time θ. For $\theta = 1$, means that one volume of silo contents are recycled once. It can be seen that for a diverging insert configuration, approximately at $\theta = 0.15$, a peak in $E(\theta)$ appears which indicates the time at which the discharge rate of the tracer particles is maximum and then drops zero at nearly $\theta = 0.3$. In addition to this, it can also be seen that a small amount of tracer particles starts to discharge from nearly $\theta = 1$ which continues to discharge intermittently up to $\theta = 3.5$. The initial triangular distribution of discharge of tracer particles for $\theta < 1$ represents the fast discharge from within the interior annulus and the blending tube, while the discharge for $\theta > 1$ represents the slow discharge from the exterior annulus. The long tail of discharge for $\theta > 1$ can be considered as a stagnant zone of particles as they don't effectively participate in the mixing process. The percentage of tracer particles discharged between θ and $\theta + d\theta$ can be computed from the area of the RTD function between θ

and $\theta + d\theta$. It was found that the long tail of discharge constitutes 56 % of the tracer particles. Similar shape of the RTD function can be seen for the straight insert configuration as shown in Figure 7.23 (b).

Figure 7.23 (c) shows the computed RTD function for the converging insert configuration. It can be seen that there exist three tracer profiles each discharging approximately in a triangular fashion. The three peaks of each triangle represent the discharge from the three annuli: blending tube, interior annulus and exterior annulus. This type of variation clearly indicates the wide residence time distribution which occurs due to the differences in residence time in each triangle and also the differences between each triangle.

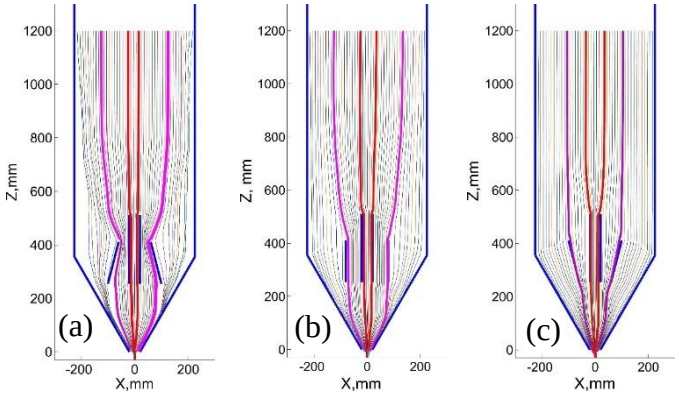

Figure 7.21 Path lines of tracer particles (a) Without internals (a) Diverging insert and blending tube (b) Straight insert and blending tube (c) Converging insert and blending tube.

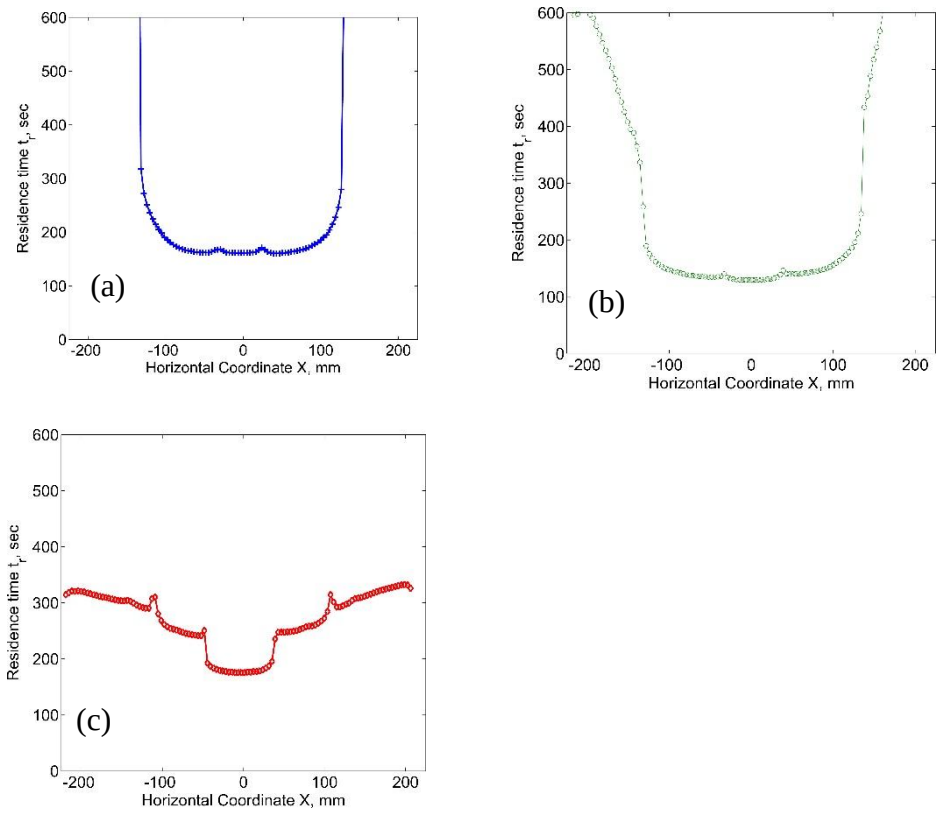

Figure 7.22 Residence times of tracer particles (a) Diverging insert (b) Straight insert (c) Converging insert.

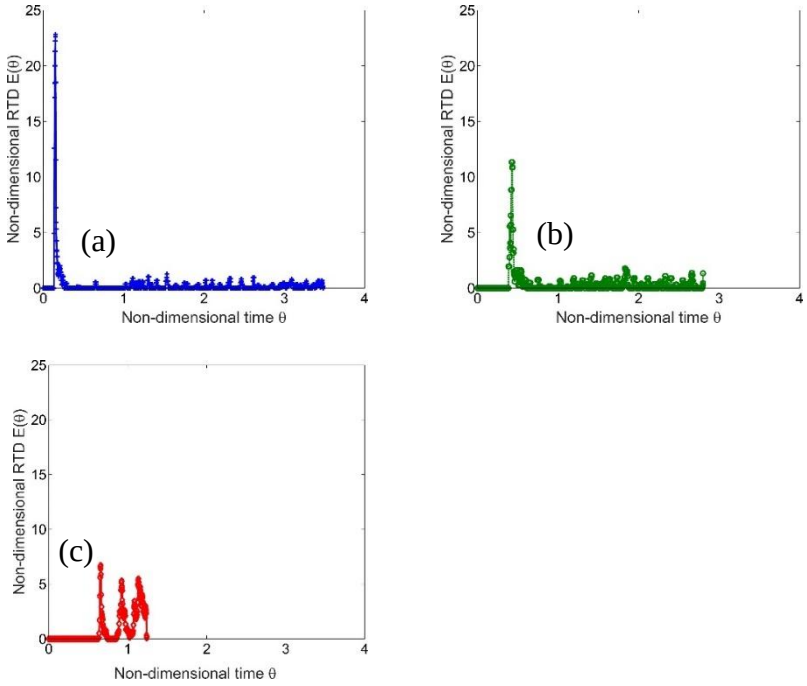

Figure 7.23 Dimensionless residence time distribution function (a) Diverging insert (b) Straight insert (c) Converging insert.

7.6.1.2 Outlet concentration in discontinuous and continuous mode

In discontinuous mode, the number of recirculations required to homogenise the variations in a given property is of interest in this study. For this purpose, the blending of 20 % tracer material and 80 % base material initially arranged in two layers as shown in Figure 7.24 (a) was considered.

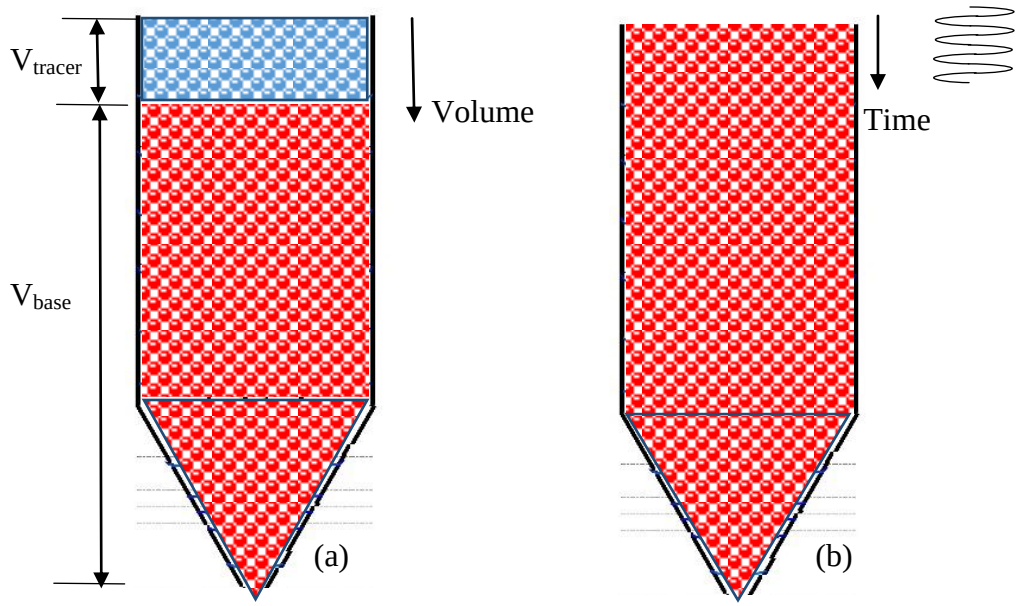

Figure 7.24 Input condition to evaluate the blending performance (a) Discontinuous mode (b) Continuous mode.

Figure 7.25 (a), (b) and (c) shows the temporal variation of concentration of tracer particles in the outflow for diverging, straight and converging insert configurations. It should be noted that in discontinuous mode, the computed concentration at the outlet during the first pass is taken as the input concentration for the computation during the second pass and so on. The summation of the concentrations from each pass then gives the total concentration of the tracer as shown by the red line.

It can be seen in Figure 7.25 (a) that for a diverging insert configuration, as expected, the concentration variation of tracer in the outflow is highly erratic: with the concentration at any time lies outside the limits of the mean concentration of 0.2,

indicating poor blending in the silo. The initial peaks in the concentration are due to repeated fast recirculation of material coming from the interior annulus whereas concentration below the mean is coming the exterior annulus which appears nearly after one recirculation. Whereas the concentration of the tracer in the outflow reaches within ± 10 % after nearly 3 and 4 recirculations for straight and converging insert configurations respectively as shown in Figure 7.25 (b) and (c).

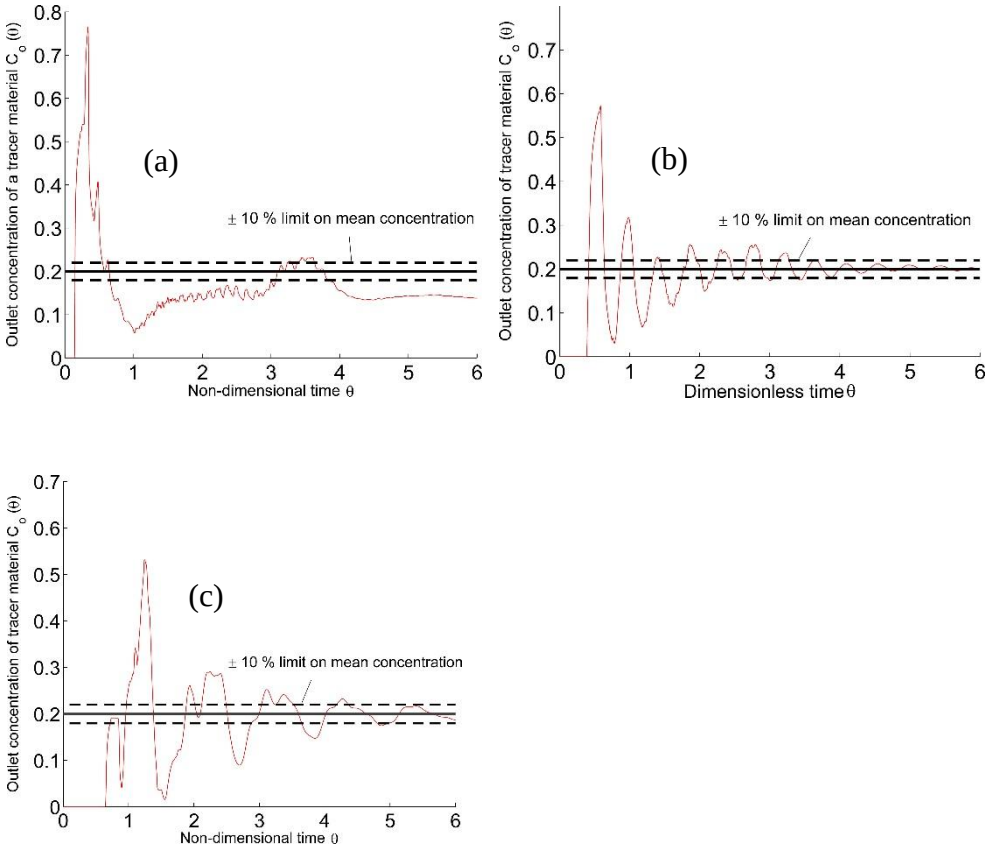

Figure 7.25 Variation of the concentration of tracer particles in the outlet (a) diverging insert (b) straight insert (c) converging insert.

In continuous mode, the variation reduction ratio (VRR) of the blender for any given input signal is of interest. An input signal of sinusoidal form was assumed and the VRR of different frequencies of the input signal was evaluated. The schematic of the input condition for continuous mode is shown in Figure 7.24 (b). It should be noted that the batch size in discontinuous mode is defined in terms of the volume of the silo

while in continuous mode it can be defined in terms of time period of the fluctuations. For example, a time period of 0.1 of the mean residence time represents the batch size of 10 % of the silo volume. Figure 7.26 shows the input concentration variation of sinusoidal form over a period of one mean residence time. Figure 7.27 shows the corresponding computed output concentration variation for all the insert configurations. It can be seen that the fluctuations in the concentration for converging insert configuration are within the ± 10 % of the mean concentration while for the other two configurations the fluctuations are outside this range. Figure 7.28 (a) and (b) shows the coefficient of variance (CoV) of output concentration fluctuations and the VRR respectively for all the configurations. It can be seen that the CoV of output concentration decreases with the increase of the frequency of fluctuations for straight and diverging insert configurations. This is due to the fact that the higher frequency in fluctuation implies lower batch size which in turn effectively participate in mixing with the other batches. It is interesting to see that for a converging insert configuration, there exist high and low peaks in CoV and VRR at certain frequencies. For example, at f = 2.84 Hz and 3.98 Hz, the CoV was found to be 5 % and 40 % respectively.

It was found that the frequency of the peaks in the RTD function (for converging insert concentration) in relation to the frequency of input signal is responsible for the huge jumps in the performance. If the concentration peaks of the input signal are in phase with the concentration peaks in RTD function, the CoV was found to be higher (in the other words VRR is lower as shown in Figure 7.28 (b)), leading to a poor blending. On the other hand, if the concentration peaks of the input signal are out of phase with the peaks in the RTD, the CoV was found to be lower. This behaviour is shown in Figure 7.29 (a) and (b) which illustrates the computation of convolution integral at $\theta = 5.5$ at which a large difference exists in the calculated outlet concentration at f = 2.84 Hz and 3.98 Hz. It can be seen in Figure 7.29 (b), that the overlap area between the RTD function and the input signal corresponding to f = 3.98 Hz is higher leading to a higher value in outlet concentration whereas a low overlap can be seen at f = 2.84 Hz.

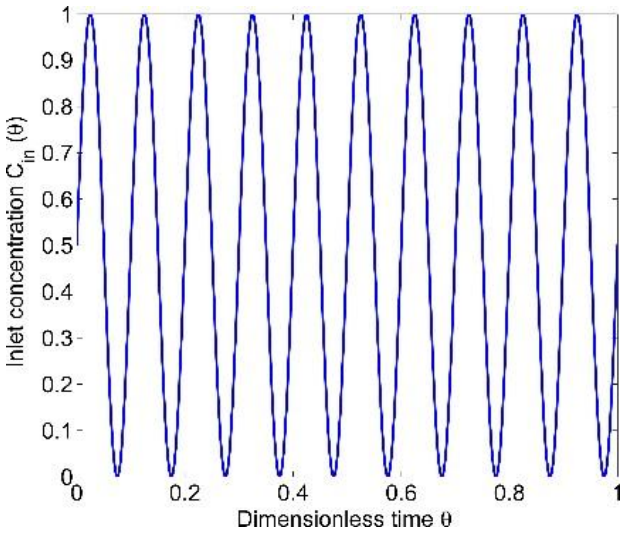

Figure 7.26 Input concentration signal of sinusoidal form with a time period of 0.1 of mean residence time.

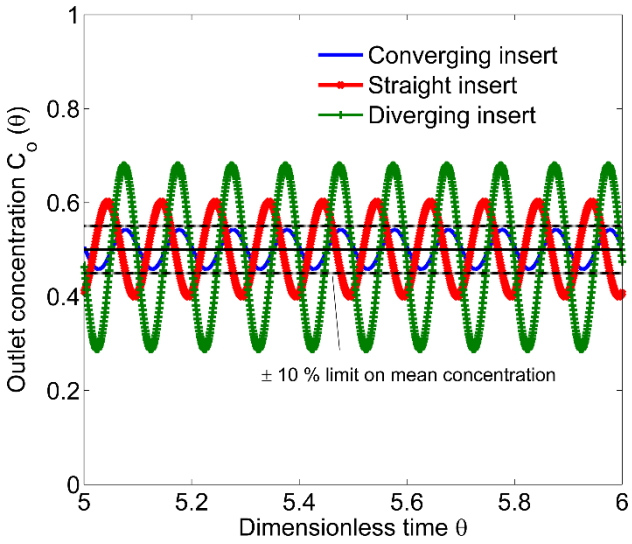

Figure 7.27 Computed temporal variation of output concentration corresponds to a sinusoidal input signal with a time period of 0.1 of mean residence time.

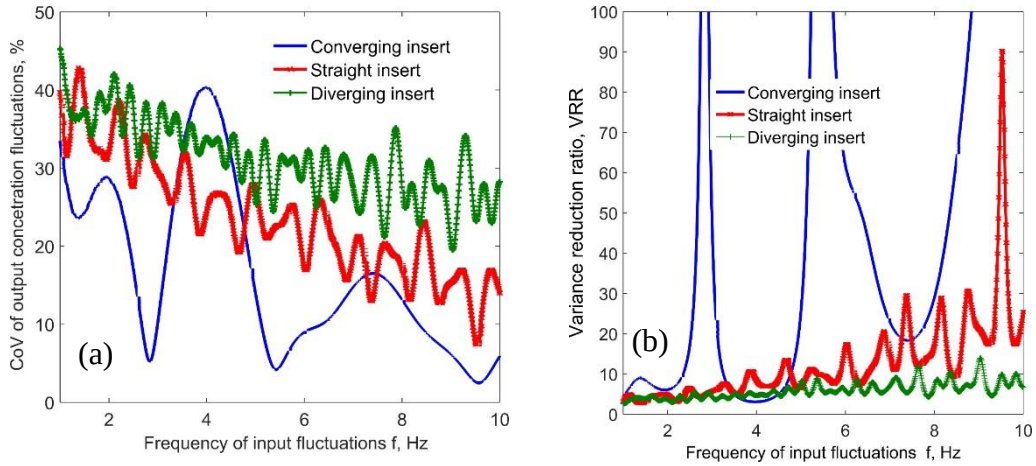

Figure 7.28 (a) Coefficient of the variance of the output signal for different frequencies of the input signal. (b) Variance reduction ratio of the blender for different frequencies of the input signal.

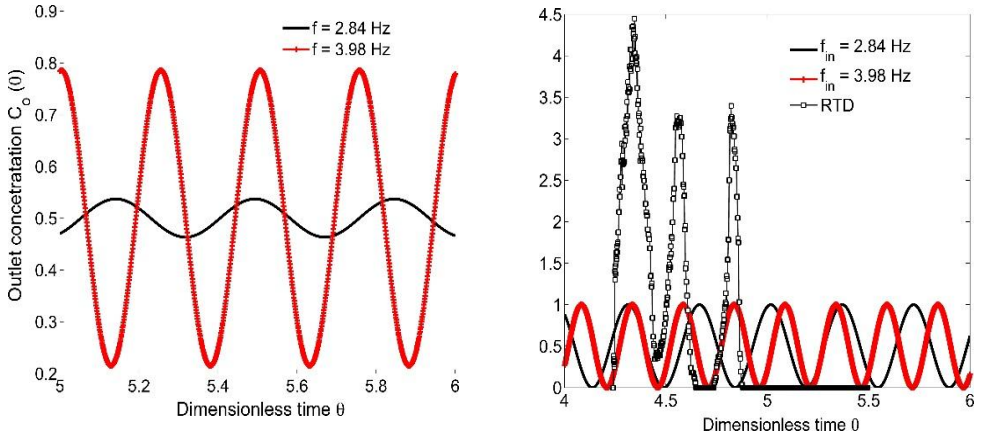

Figure 7.29 (a) Outlet concentration variation at frequencies f = 2.84 Hz and 3.98 Hz (b) Overlap of RTD funtion with input concentration at θ = 5.5 at frequencies f = 2.84 Hz and f = 3.98 Hz.

7.7 DEM implementation of model silo

The developed flow patterns in each configuration of the blender were simulated using the DEM model in order to mainly to assess the accuracy of the flow patterns and further to study the effect of gravity on flow patterns.

The theory, calibration, and validation of the DEM model were reported in the chapters 4 and 5. Here only the specific details of the simulation set-up are given. The particle size and shape, mechanical and interaction properties that were used for the validation of flow in a flat bottom silo (presented in Chapter 5) were deployed. No further modifications to the parameters were made.

The total number of the particles needed to replicate the test blender was found to be 606652 and the time required to empty the blender was found to be approximately 32 sec. With reference to this, the following computational challenges were identified:

- With the available computational resources, it was found that it takes 32-37 hours of computational time to simulate one second duration of flow i.e. on an average it will take 42 days to simulate the flow for one residence time.
- The common practice of downscaling the dimensions of the test silo or upscaling the particle size is not feasible because of the possibility of mechanical arching around the small size openings around the internals in the hopper.
- To simulate the test blender in continuous mode or, in a discontinuous mode with recirculation, a constant head level should be maintained. This requires a huge amount of computational time due to the longer simulation time. To address this challenge, the possibility of increasing the discharge rate by increasing the gravity was explored.

The numerical model same as the size of the test set-up was created. The filling was considered to be complete when the average kinetic energy of the system was found to be negligible (<1E-12 J). The particle assembly at the end of filling is shown in Figure 7.30. At the end of filling, the particles were allowed to discharge under normal gravity by simply deleting the outlet wall. The total number of simulations conducted are listed in Table 7.2.

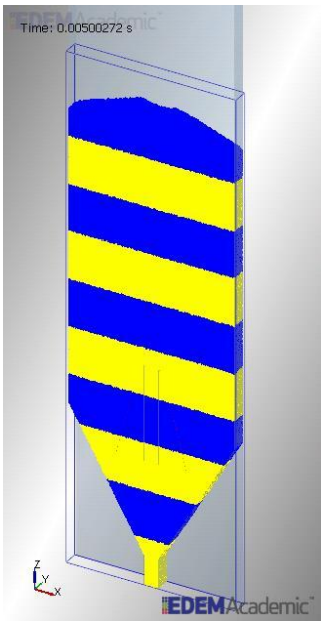

Figure 7.30 Numerical set-up of the lab-scale multi-flow blender.

A simulation time step of 10 % of Rayleigh time was used and the data was saved at a time interval of 0.005 sec. Each simulation was conducted for only 10 sec under normal gravity by which the flow in the silo already reaches steady state. The total run time for each studied case is also shown in Table 7.2 with the corresponding total file size. It can be seen that for most of the simulations the total size is as large as 350 - 400 Gb and it was found the chances that the data gets corrupted are high at this large file size and cannot be opened in the software once corrupted. One way to avoid this is that instead of saving full run time in one simulation deck, multiple decks can be created to reduce the total size of each deck. This way each deck can be accessed quickly and the chances of data corruption are low.

The velocity data from the DEM results is extracted by creating bins of size 15 mm x 15 mm across the full length of the silo, similar to patches used for measurement using PIV.

Table 7.2 List of simulations conducted in the multi-flow blender.

Case No.	Gravity	Blender configuration	Total simulation time, sec	File size, Gb
1	g	Inward Bi-insert	10	482
2	g	Straight Bi-insert	10	482
3	g	Outward Bi-insert	10	482
4	5g	Inward Bi-insert	5	270
5	50g	Inward Bi-insert	2	345

7.8 DEM predictions of flow and comparison with measurements

It should be noted that the accuracy of DEM model has been assessed for the flow in a small scale flat bottom silo which is presented in chapter 5. The purpose of the comparison in this section is to confirm whether the accuracy of DEM predictions holds true in a different and relatively larger scale silo configuration without any further modification of the parameters.

The DEM flow predictions in a silo with the diverging insert and the blending tube during a batch discharge were compared with the experiments. The following spatial and temporal variation of flow quantities were considered for the comparison:

a. Temporal variation of centreline velocity at different heights;
b. Spatial variation of cross-sectional mean velocity along the height;
c. Vertical velocity distribution at the outlet and the inlet of the insert at different instants during discharge;
d. Steady-state vertical velocity distribution across the full silo.

7.8.1 **Qualitative description of predicted flow**

The flow during the discharge was visualised with the aid of relative movement of alternative layers of blue and yellow particles at selected time instants (t = 0, 2, 3, 4 and 6 sec) as shown in Figure 7.31 (a) – (c) for all the insert configurations. The change in position of these coloured particles with reference to the positions at t = 0 sec demonstrates the major developments of flow in the blender. It can be noticed from Figure 7.31 (a) that upon opening the outlet wall, the blue and yellow colored particles below the insert and the tube were discharged by mass flow after which the feed to the silo outlet is primarily being coming from the area covered by the insert and the blending tube, while the particles in the exterior annulus remain stagnant (refer image at t = 2 sec). Consequently, the flow, which is initiated within the insert and the blending tube, draws the particles across the width in the vertical section of the silo by producing a funnel type flow channel in which the size of the stagnant zones decreases with the distance from the insert. It is, therefore, evident that these developed flow patterns in the hopper and the vertical section are in good qualitative agreement with the experimental results presented in section 7.4. Furthermore, the relative proportion of the particles in the silo outlet, that are coming from the interior annulus and the exterior annulus can also be seen from the image at t = 3 sec in Figure 7.31 (a): the flow from the former dominates the major cross-section of the silo outlet while as thin as 1-2 particle thick is coming from the latter. This very slow discharge of 1-2 particles from the exterior annulus causes the slow motion of the particles along the side walls. It can also be seen that with the increase in area ratio (refer to flow patterns developed in straight and converging insert in Figure 7.31 (b) and (c)), the motion on the side walls increases and the flow tend to become uniform in the vertical portion of the silo which is similar to the observations made in the experiments.

(a) 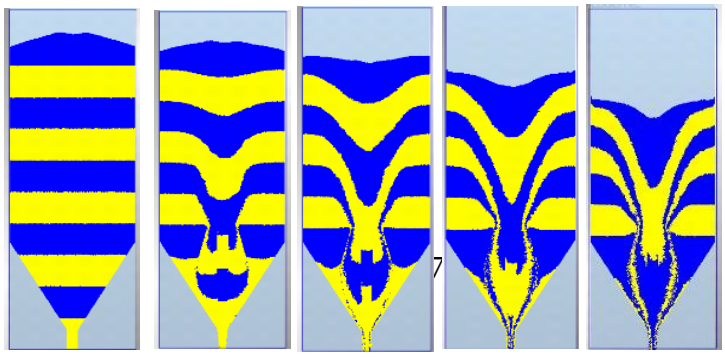

Figure 7.31 Visualisation of DEM predicted flow patterns at different time instants (a) Diverging insert (b) Straight insert (c) Converging insert.

7.8.2 Quantitative comparison of DEM predictions of flow

7.8.2.1 Comparison of centreline velocity

Assessing the accuracy of temporal variation of velocity at a smaller time interval of order of 0.005 sec is not realistic due to the fact that the particle contacts in DEM are modelled as springs and therefore one can expect high velocity fluctuations due to the numerical calculations which could be different to physical fluctuations that arises due to the discrete nature of flow. It should also be noted that the velocity measurements were made at a time interval of 0.0167 sec. Therefore, in order to be

consistent and to avoid any misinterpretation during the comparison, the centreline velocity data at each instant shown here is averaged over a relatively larger time interval of 0.5 sec in both the experiments and the simulations thereby nullifying the fluctuations in the flow. Figure 7.32 (a) - (c) shows the comparison of temporal variation of centreline vertical velocity with the experiments at three key locations: below the internals (at Z = 100 mm), within the blending tube (at Z = 400 mm) and above the internals (at Z = 700 mm) for a diverging insert configuration. It should be noted that both the predicted velocities behind the front wall and that depth averaged are compared against the measurements in this figure.

It can be seen that the centreline velocity increases to a maximum value during the initial phase of discharge before reaching a steady state value. The predicted velocity follows the similar trend as in experiment with an error in the magnitude of steady state velocity found to be 10 mm/s, - 8 mm/s and 9 mm/s at Z = 100 mm, Z = 400 mm and 700 mm respectively. It should be noted that the centreline velocity in the blending tube (Z = 400 mm) was under predicted while it was over predicted in the region below and above the blending tube.

The experimental results showed that there is a decrease in velocity magnitude directly above the walls of the blending tube (due to the intermittent resting of the particles) which could lead to an increased velocity in the tube due to the decrease in available flow area across the width of the silo. This behaviour was not predicted in the simulations because of ignoring the thickness of the internals, which possibly led to an under prediction of velocity in the tube.

7.8.2.2 Comparison of mean velocity and velocity distribution

Figure 7.33 shows the comparison of mean velocity across the cross-section of the silo. The velocities shown here were averaged during 3 sec to 4 sec from the start of the discharge. The mean velocity multiplied by the silo cross-section gives the volumetric flow rate. It was found that there is a difference in mean velocity of 5 mm/s between the experiment and the simulation which corresponds to a 14 % discrepancy in the volumetric flow rate. This error possibly arises due to the high retardation of flow behind the frontal wall when compared to the simulation and also

due to the increased motion of particles along the side walls in simulation due to the infinitesimal thickness of internals.

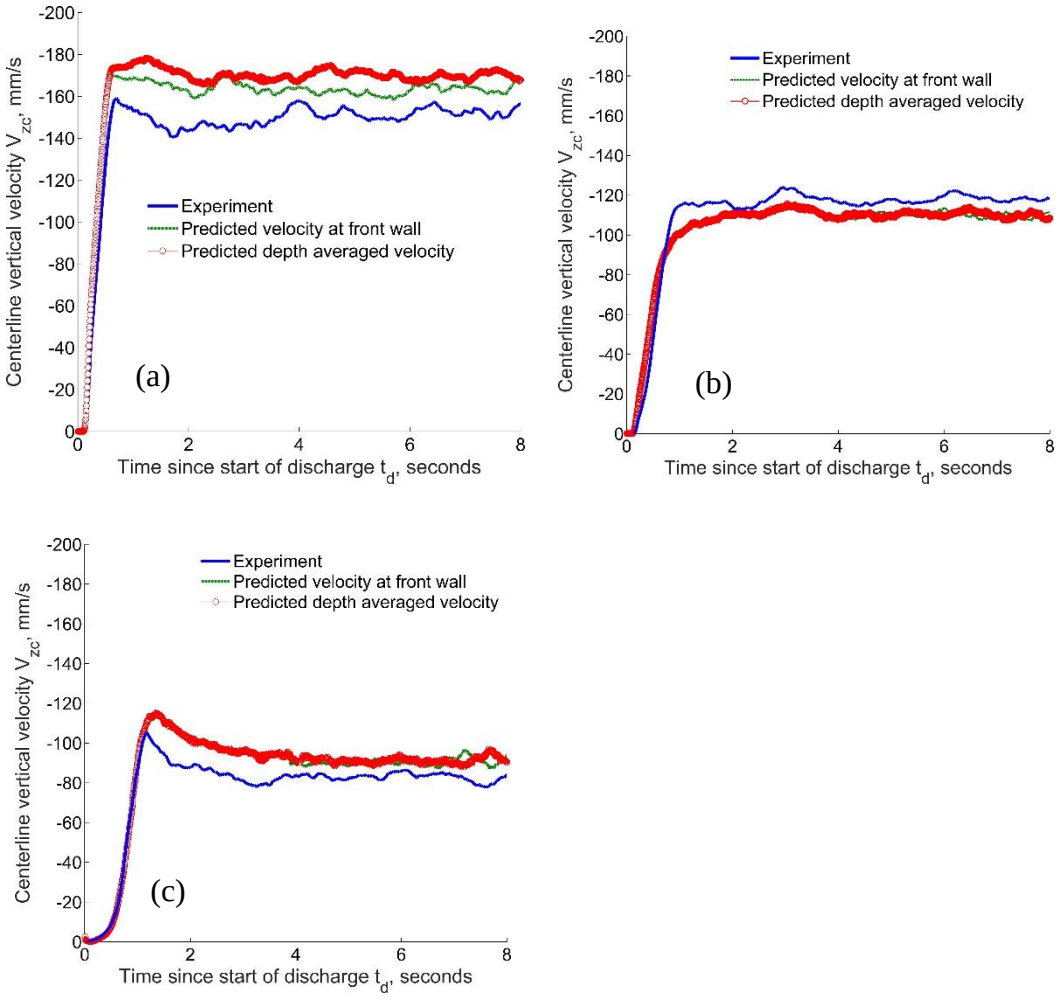

Figure 7.32 Comparison of centreline velocity variation with height against the PIV measurements (a) Z = 100 mm (b) Z = 400 mm (c) Z = 700 mm.

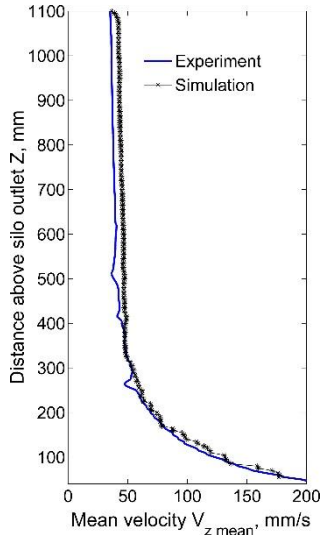

Figure 7.33 Comparison of mean vertical velocity across the cross-section of the silo.

It was shown earlier that the velocity distribution at the inlet and the outlet of the insert govern the velocity distribution in the vertical section of the silo and any discrepancy in the prediction of either of these distributions would lead to a further discrepancy in the velocity profiles in the vertical section of the silo. Figure 7.34 and Figure 7.35 shows the comparison of normalised velocity distribution at the outlet and the inlet of the insert respectively at different time instants. The velocity at each time was averaged over a time period of ± 0.05 sec. It can be seen that at all instants the predicted velocity in the exterior annulus at the outlet is higher when compared to the experiment and there is a relatively good quantitative agreement within the interior annulus and blending tube. The over prediction of velocity in the exterior annulus at the outlet also results in the over prediction at the inlet of the insert as shown in Figure 7.35 at all the time instants. Due to the increased mobilisation of particles near the side walls in the simulations, it can be noticed that the centre-line velocity is highly under predicted.

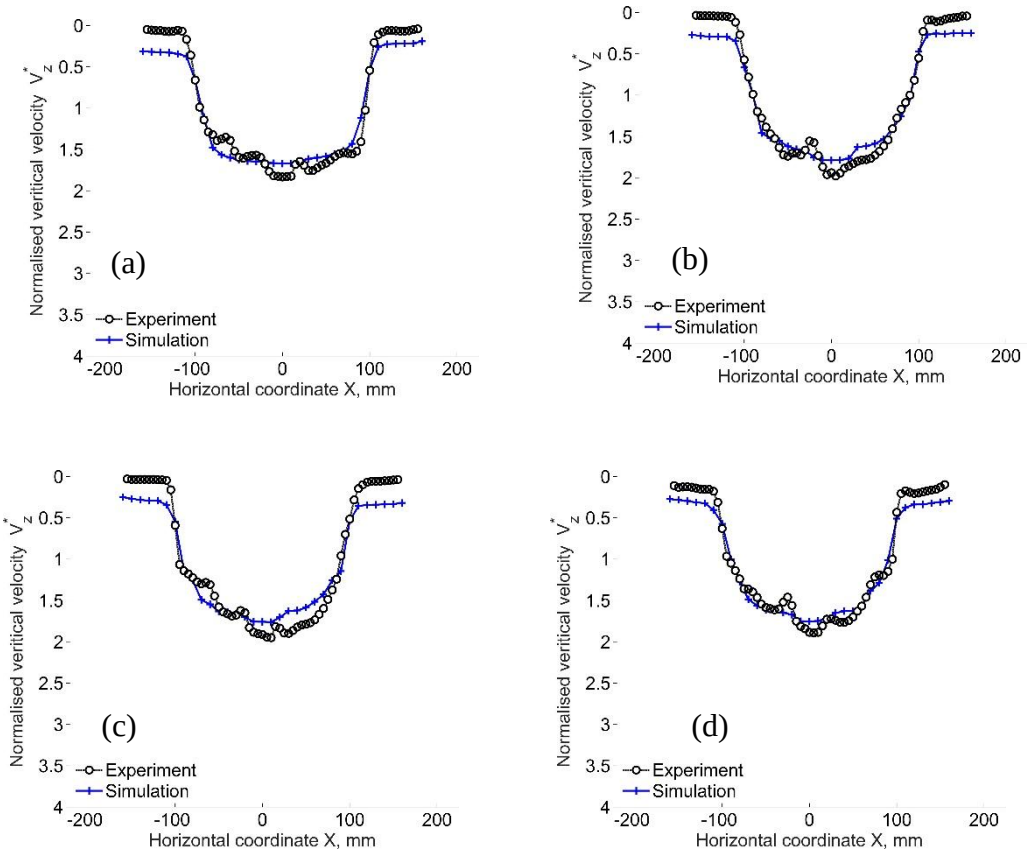

Figure 7.34 Comparison of velocity distribution at the outlet of insert (a) t = 1 sec (b) 2 sec (c) 3 sec (d) 6 sec.

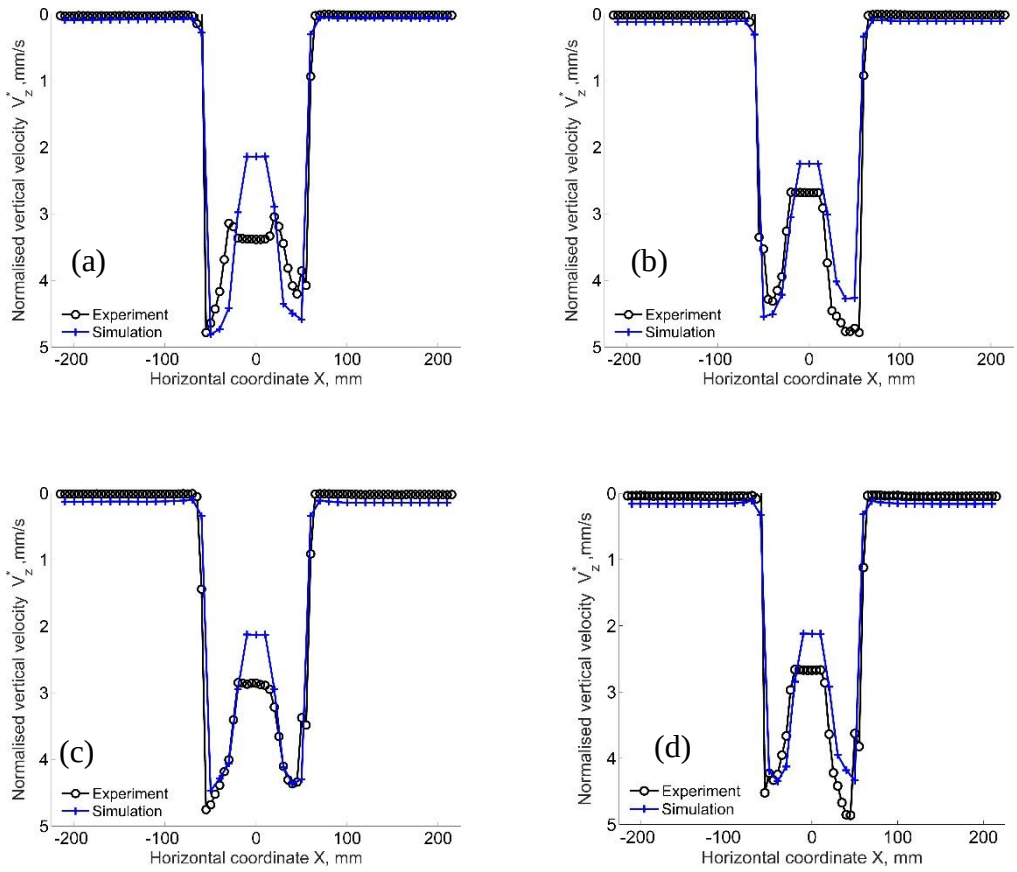

Figure 7.35 Comparison of velocity distribution at the inlet of insert (a) t = 1 sec (b) 2 sec (c) 3 sec (d) 6 sec.

The comparison of vertical velocity averaged during 3 sec - 4 sec at different heights of the silo is shown in Figure 7.36. Because of over prediction of velocity in the exterior annulus, the velocity differential between the exterior and the interior annulus is lower in simulation when compared to the experiments consequently leading to a slight more uniform velocity distribution in the vertical section of the silo. In addition to this, at Z = 510 mm (the location corresponding to the inlet of blending tube), the vertical velocity profile predicted by the DEM is smooth unlike in the experiments. This is due to the fact that the pellets found to rest intermittently on the blending tube in the experiments. As the thickness of the internals was ignored in the modelling, this type of variation cannot be seen.

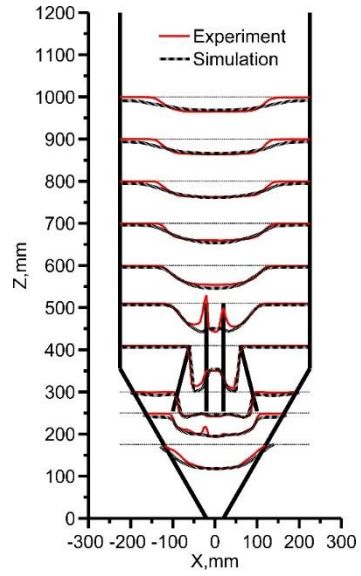

Figure 7.36 Comparison of prediction of vertical velocity profiles averaged during 3 sec to 4 sec from the start of discharge.

7.9 Scaling discharge rate by gravity

For a constant silo volume and particle size, it is known that the volumetric flow rate from a silo is directly proportional to the square root of gravity (Beverloo and Leniger, 1961). This also implies that the total discharge time is inversely proportional to the square root of gravity as shown in (7.2).

$$\mathbf{Q_{silo}} \propto \sqrt{\mathbf{g}} \tag{7.1}$$

$$\frac{\mathbf{V_{silo}}}{\mathbf{t_d}} \propto \sqrt{\mathbf{g}} \tag{7.2}$$

$$\frac{\mathbf{t_{d2}}}{\mathbf{t_{d1}}} = \sqrt{\frac{\mathbf{g_1}}{\mathbf{g_2}}} \tag{7.3}$$

It has been also confirmed in the experiments of silo discharge conducted by Mathews, (2013) that the mass flow rate scales with square root of the gravity. Chung and Ooi (2008) in their simulations of DEM also showed that mass flow scales with sqrt (g). It is of interest in this study whether the local velocity profiles at different heights scales similarly with gravity in which case the computational time

required for the silo discharge and blending simulations can be effectively reduced by square root of gravity ratio as shown in (7.3). For example, the total discharge time under normal gravity g is 32 sec and if discharged under increased gravity of 5g and 50 g the discharge time will be 14.3 sec and 4.5 sec respectively. To this extent simulations of discharge in the silo with the diverging insert and the blending tube were conducted at different gravities (g, 5g and 50g). For comparison of results, the time and the velocities are normalised with the square root of gravity ratio.

Figure 7.37 (a) shows the predicted mass flow rate from a silo discharged under gravities of g, 5g and 50g. It is evident from this figure that the mass flow is proportional to the square root of gravity. The mean velocity variation with height during the steady period is shown in Figure 7.37 (b). It is evident from this figure that not only the outlet mass flow rate scales with the square root of gravity, the cross-sectional mean velocity at any height also scales similarly.

Figure 7.38 shows the vertical velocity profiles (normalised with the gravity ratio) across the width of the silo at gravities of g, 5g and 50g at different heights during the steady state. It can be seen that although the mean velocity scales with the gravity ratio, there is a deviation in local velocity within the exterior and the interior annulus at the outlet of the insert with the increase of gravity. The velocity differential across both the annulus at the inlet of insert found to decrease with the increase of gravity mainly because of increased velocities of particles along the hopper wall, which further lead to more uniform velocity profiles in the vertical section as shown in this figure.

The deviation of local velocity profiles with the increase of gravity needs to be studied further by investigating the force chains and stress state of the system and also by conducting the calibration simulations at higher gravity in order to determine its effect on particle scale properties of the model.

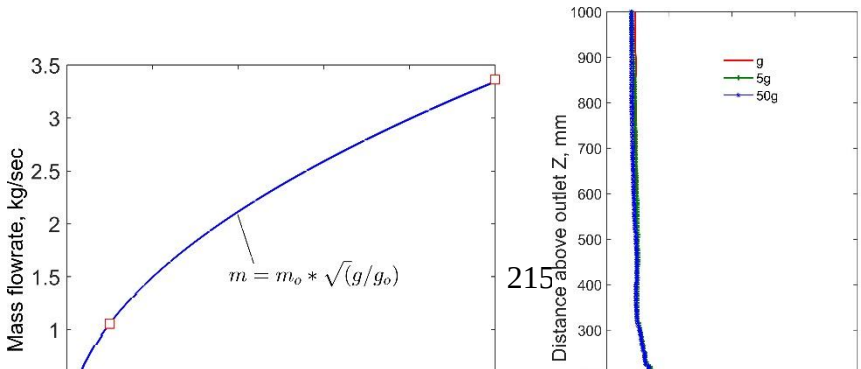

Figure 7.37 Effect of gravity on (a) mass flow rate (b) mean velocity with height.

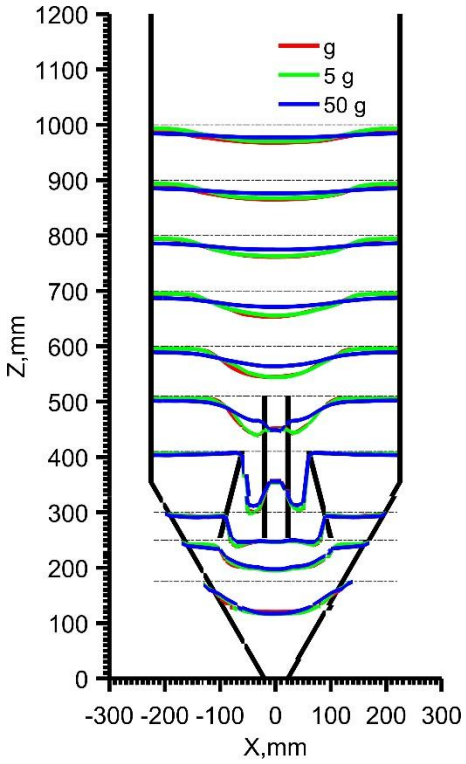

Figure 7.38 Effect of gravity on vertical velocity profiles across the silo.

7.10 **Summary**

The flow patterns in a multi-flow blender during the evolution and the steady state have been experimentally investigated using the developed PIV tool. The blending performance has been evaluated from the velocity fields using the linear system

theory. It was shown that the evolution of flow in the silo with the internals is a complicated process that involves the coupled interaction of flow channels that are resulted from the presence of the insert and the blending tube. It was further shown that the shape of the velocity distribution at the inlet and the outlet of the insert govern the shape of the velocity profiles in the vertical section of the silo. The angle of the insert was found to have a significant influence on the flow patterns. The placement of the converging insert imposed a uniform velocity across the interior and the exterior annulus at the inlet of the insert thereby leading to a complete mass flow in the vertical section of the silo except in the region above the blending tube. Conversely, a non-uniform velocity profiles were developed in the vertical section for the case of diverging and straight insert mainly due to the presence of the velocity differential across the exterior and the interior annulus at the inlet of the insert. The silo with the converging insert and the blending tube was found to be an efficient blender in both continuous and discontinuous modes of operation. The variance reduction ratio (VRR) for each configuration was evaluated. It was found that for the converging insert configuration, there exist certain resonant frequencies between the frequency of input fluctuation and the frequency of residence time distribution function at which the VRR was found be very low.

The flow during the batch discharge for all the insert configurations was simulated using the calibrated DEM model. The flow predictions in the silo with the diverging insert and the blending tube were compared with the measurements. The flow patterns were found be in good qualitative agreement. However, due to neglecting the thickness of the internals in the model, an over prediction of velocity in the exterior annulus at the outlet of the insert was observed, which further lead an over prediction of volumetric flow rate.

The effect of gravity on the flow patterns has also been investigated in order to check the possibility of scaling up the discharge rate using a high gravity. It was found that the discharge rate and the cross-sectional mean velocity at any height are proportional to the square root of the gravity. However, the local velocities that are normalised with the gravity ratio does not scale with the increasing gravity

particularly in the regions next to the side walls of the hopper and the vertical section.

Chapter 8

8. Conclusions and suggestions for future research

In this thesis, Discrete Element Method (DEM) and Particle Image Velocimetry (PIV) technique are deployed to understand the flow characteristics and blending of cylindrical plastic pellets in a planar flat bottom silo and a multi-flow blender. The DEM predictions are also validated against high-resolution velocity measurements analysed using Particle Image Velocimetry (PIV) technique. This chapter presents the conclusions from the all the studies conducted in this work.

8.1 General conclusions

Accuracy of PIV technique and evolution of flow of granules in a flat bottom silo

The accuracy of the PIV has been assessed using the computer generated images of the silo flow followed by the application of PIV to the experiments in a flat bottom silo in order to understand the evolution of flow of pellets from the start of discharge to a steady state and further to analyse the depth of the silo on the steady state flow patterns. The following are the key conclusions:

I. It was found that the number of pixels representing the voids within a patch is an important factor that affects the accuracy of the measurement. It was also found that a moderate image resolution of 1000 pixels x 1400 pixels is adequate to make an accurate measurement of mean velocity within ± 0.5 %.
II. It was shown that the flow propagates upwards very quickly to the surface during the initial stages of the discharge followed by the sideward expansion of the flow.
III. It was found that with the increase in the depth of the silo, the size of the steady state flow channel increases and the angle of discharge decreases.
IV. The analysis of the mass flow rate from the velocity profiles revealed that there exists a significant retardation of flow at the frontal wall of the silo for a 100 mm depth and a negligible retardation for 40 mm and 20 mm deep silo.

Relationship between the bulk scale and particle scale friction from simulations of Jenike direct shear box

Jenike direct shear box simulations have been conducted to calibrate the frictional parameters of the model by obtaining the relationship between the bulk scale and particle scale friction. The multi-sphere method has been used to represent the cylindrical test pellets. A novel approach of replacing the flat shear lid geometry with a particle wall has been developed in order to apply a constant normal force. The relationship between the bulk friction and the particle scale friction has been explored for three scenarios: with and without rolling friction and the case when the particle rotations are fully restricted during the shearing. The following key conclusions can be drawn from this study:

I. Without the application of rolling friction torque, the maximum bulk internal friction that can be obtained in the DEM model using the particles with two or four clumped spheres is 0.54 i.e. approximately 28^o of internal friction angle for the given set of parameters. The model is thus not able to simulate the flow behaviour of material with bulk friction values greater than 28^o. However, the majority of the pellets handled in industries have a bulk internal friction values in the range of 18^o to 45^o. For example, the HDPE test pellets used in this work have a bulk internal friction of 30^o.

II. The particle scale data of angular velocity and the mobilised friction in the shear plane between the particles and the wall revealed that the particle rotations in the shear plane are dominant at higher inter-particle friction and the bulk friction resistance is relieved by the increased rotations. A huge increase in bulk internal and wall friction was found when the particle rotations are completely restricted during shearing.

III. Increasing the rolling friction coefficient (μ_r) from 0 to 0.1 at an inter-particle friction $\mu_{p\text{-}p} = 0.1$, a negligible change in bulk internal friction was found whereas there is a nearly 20 % increase in bulk friction at $\mu_{p\text{-}p} = 0.5$.

IV. If the rolling friction is greater than the inter-particle friction, the bulk internal friction ($\mu_{p\text{-}bulk}$) decreases when compared to the one with zero rolling friction at the same inter-particle friction. For example, at $\mu_{p\text{-}p} = 0.4$ and $\mu_r = 0$, the $\mu_{p\text{-}bulk} = 0.52$ whereas at $\mu_{p\text{-}p} = 0.4$ and $\mu_r = 0.5$ the $\mu_{p\text{-}bulk} = 0.45$.

Quantitative validation of DEM model and parametric study

To assess the accuracy of DEM, the flow behaviour of pellets during the discharge in a flat bottom silo has been chosen as a validation experiment. The DEM predicted internal stress at the end of filling was compared against the analytical solution of Janssen. The predicted filling bulk density and mass flow rate during discharge were compared with the measurements. Finally, the velocity profiles and flow channel boundary (FCB) at different instants were compared with the measurements and the kinematic model. The following main conclusions can be drawn from the assessment of DEM accuracy:

I. The variation of vertical stress with the depth of the silo at the end of filling was found be in good agreement with the Janssen equation.
II. The inclusion of rolling friction torque (which takes into account the difference in shape between the test and numerical particle) gives a good prediction of flow rate within ± 5 % accuracy.
III. It was found that a slightly lower filling bulk density was obtained in the simulations due to which the predicted upward propagation of flow is faster in comparison to the experiments. A reasonably good quantitative agreement was found when the flow is fully developed. Considering the simplifications made in the model, the DEM predictions of velocity profile can be considered to be in reasonably good agreement. The DEM velocity predictions were also compared with the kinematic model. It was found that the kinematic constant decreases with the distance above the outlet in both the simulation and the experiment.
IV. The flow channel boundary was found to be in good agreement close to the outlet whereas a discrepancy of approximately 2-3 particles far from the outlet and close to the side walls was found.

The validated model was further used to study the effect of frontal wall friction, the coefficient of restitution (CoR), inter-particle friction and rolling friction. The following main conclusions can be drawn from the study:

I. Liquid-like behaviour was found when the frontal walls are frictionless and the Janssen effect was observed only when adequate frontal wall friction is applied.

II. Flow transits from a semi-mass flow to an internal flow with the increase of frontal wall friction.

III. The presence of strong force chains in case of frictionless frontal walls enables the particles to move collectively leading to a semi-mass flow. In contrast, weaker force chains were formed with the increase of wall friction (weak enough to break with the shear caused from gravity flow) thereby enabling internal flow.

IV. It was found that the CoR has a negligible influence on the velocity profiles due to the lack of collisions during the silo discharge. A low CoR is desirable in order to bring the system to equilibrium as quickly as possible.

V. The rolling friction has a negligible influence on the flow patterns at lower inter-particle friction, however, an increase of rolling friction from 0 to 0.1 at higher inter-particle friction leads to changes in the flow patterns from semi-mass to internal flow; limiting the rotations at higher inter-particle friction lead to the formation of stable stagnant zones thereby creating an internal flow.

DEM studies of blending in a flat bottom silo

The DEM model to investigate the blending process in a flat bottom silo in continuous and discontinuous modes of operation has been presented. Two contrasting flow patterns (semi-mass and internal flow) have been simulated in a flat bottom silo by changing the material parameters of the model. The evolution of bulk density and the velocity profiles during recirculation from the end of filling to a fully developed steady have been analysed followed by the investigation of the corresponding blending process of alternative horizontal layers of blue and yellow particles. The blending effectiveness in discontinuous mode has been quantified using variance reduction ratio (VRR) and its variation with the size of the batch, number of sub-layers of each batch, number of recirculations in both semi-mass and internal flow has been studied. The following main conclusions can be drawn from this study:

I. The outflow rate is controlled by applying a constant velocity boundary condition in the outflow of the silo. This is implemented by means of a simple body force model written in the API interface of EDEM software.

II. The bulk density and velocity profiles are found to change drastically during recirculation mainly due to the dilation of particle assembly caused by the shearing during the flow. The changes are more significant is the case of high frictional internal flow.

III. The blending process in the semi-mass flow is limited to very close to the outlet while in internal flow the blending is active in the major portion of the silo leading to a higher blending efficiency when compared to the former.

IV. In case of the internal flow, the batch size significantly affects the VRR while a minor influence is evident in the case of semi-mass flow: lower the batch size higher the VRR.

V. For the internal flow, the percentage increase in VRR with the increase in number of sub-layers was found be higher at a higher number of recirculations (N_r) whereas it does not hold true for semi-mass flow (increase in VRR remains constant at all N_r).

VI. The RTD function calculated from spatially averaged Eulerian velocity fields is found to be accurate and this potentially avoids the expensive and time consuming impulse-response experiments with coloured tracer particles in 2D planar silos.

VII. The variation of outlet concentration calculated by convolution and from the direct DEM output are found to follow the same trend. However, in the former case, the variation is smooth whereas in DEM a noise in the concentration variation was found. While these fluctuations are due to the particulate nature of the flow, the convolution integral is not able to calculate these fluctuations because of the continuous nature of the integral.

VIII. The blending effectiveness in continuous and discontinuous mode has been evaluated using LTI theory particularly for those input conditions which are otherwise difficult to study using the DEM results. In discontinuous mode, nearly 10 recirculations are required for homogenisation in internal flow and 15 recirculations are required for semi-mass flow for a tracer volume of

approximately 20 % of silo volume. It was also found that in continuous mode, the VRR increases with the increase of the frequency of input fluctuations.

Development of flow in a multi-flow blender and the associated blending performance

The flow patterns in a multi-flow blender during the evolution and the steady state have been experimentally investigated using the developed PIV tool. The blending performance has been evaluated from the velocity fields using the linear system theory. It was shown that the evolution of flow in the silo with the internals is a complicated process that involves coupled interaction of flow channels that are resulted from the presence of the insert and the blending tube. It was further shown that the shape of the velocity distribution at the inlet and the outlet of the insert govern the shape of the velocity profiles in the vertical section of the silo. The angle of the insert was found to have a significant influence on the flow patterns. The placement of the converging insert imposed a uniform velocity across the interior and the exterior annulus at the inlet of the insert thereby leading to a complete mass flow in the vertical section of the silo except in the region above the blending tube. Conversely, a non-uniform velocity profiles were developed in the vertical section for the case of diverging and straight insert mainly due to the presence of the velocity differential across the exterior and the interior annulus at the inlet of the insert. The silo with the converging insert and the blending tube was found to be an efficient blender in both continuous and discontinuous modes of operation. The variance reduction ratio (VRR) for each configuration was evaluated. It was found that for the converging insert configuration, there exist certain resonant frequencies between the frequency of input fluctuation and the frequency of residence time distribution function at which the VRR was found be very low.

The flow during the batch discharge for all the insert configurations was simulated using the calibrated DEM model. The flow predictions in the silo with the diverging insert and the blending tube were compared with the measurements. The flow patterns were found be in good qualitative agreement. However, due to neglecting

the thickness of the internals in the model, an over prediction of velocity in the exterior annulus at the outlet of the insert was observed, which further lead an over prediction of volumetric flow rate.

The effect of gravity on the flow patterns has also been investigated in order to check the possibility of scaling up the discharge rate using a high gravity. It was found that the discharge rate and the cross-sectional mean velocity at any height are proportional to the square root of the gravity. However, the local velocities that are normalised with the gravity ratio does not scale with the increasing gravity particularly in the regions next to the side walls of the hopper and the vertical section of the silo.

8.2 Suggestions for future work

The planar model test silo fabricated for this research work has a great potential to conduct further investigations of flow in the silo with and without internals using the developed in-house PIV pre and post processing tool. Several areas of work towards the DEM modelling of flow in the silo have also been identified. The experimental and the DEM investigations that are recommended for the future research are:

I. In this work, the evolution of flow of high-density polyethylene granules (having an internal friction of 30^{o}) in a flat bottom silo has been investigated. A further experimental study with a range of cohesionless bulk solids with different internal frictions can be conducted in order to gain a deeper understanding of flow propagation and to develop empirical models that can fully describe the evolution of flow in a flat bottom silo. In addition to this, the development of an algorithm to evaluate the void ratio during the discharge of granules would also be useful for this study.

II. The multi-sphere approach along with the rolling friction has been used in this work to model the shape of the pellets. However, there are alternative approaches for representing the shape such as the use of the polyhedral technique. The comparative studies of predictions of flow patterns in a flat bottom silo using these two techniques can be conducted.

III. Jenike direct shear box simulations can be conducted to determine the bulk wall friction for a wall sample that is modelled with a number of glued rigid spheres instead of a flat wall geometry (similar to the one used in this work to model the shear lid geometry). Different diameters of spheres can be created to achieve a different roughness of the wall and the corresponding amount of interlocking can be investigated.

IV. Wall boundary effects in relation particle size and the shear cell height in the current simulations needs to be assessed.

V. The drastic influence of rolling friction at the higher inter-particle friction on the flow patterns in a flat bottom silo can be further investigated from the micro-scale analysis of force chains structures.

VI. The ways to reduce the computational time in DEM simulations of a large scale silo discharge without the compromising the physics of the flow need to be addressed. Some of the approaches would be to replace a zone of smaller size particles in the mass flow region of the silo with the larger particles and to increase the discharge rate by using high gravity.

VII. DEM simulations of blending in a multi-flow blender with the different angles of internal friction can be conducted to study its influence on the flow patterns and blending.

References

Ai, J. et al. (2011) 'Assessment of rolling resistance models in discrete element simulations', *Powder Technology*, 206(3), pp. 269–282.

Albaraki, S. and Antony, S.J. (2014) 'How does internal angle of hoppers affect granular flow? Experimental studies using digital particle image velocimetry',

Powder Technology, 268, pp. 253–260.

Anand, A. et al. (2008) 'Predicting discharge dynamics from a rectangular hopper using the discrete element method (DEM)', *Chemical Engineering Science*, 63, pp. 5821–5830.

Aoki, K.M. and Akiyama, T. (1995) 'Simulation studies of pressure and density wave propagations in vertically vibrated beds of granules', *Physical Review E*, 52(3), pp. 3288–3291.

Babic, M. (1997) 'Average balance equations for granular materials', *International Journal of Engineering Science*, 35(5), pp. 523–548.

Babout, L. et al. (2013a) 'Influence of wall roughness and packing density on stagnant zone formation during funnel flow discharge from a silo: An X-ray imaging study', *Chemical Engineering Science*, , pp. 210–224.

Babout, L. et al. (2013b) 'Influence of wall roughness and packing density on stagnant zone formation during funnel flow discharge from a silo: An X-ray imaging study', *Chemical Engineering Science*, 97, pp. 210–224.

Bagster, D.F. (1973) 'A Geometric Study of In-Bin Blending', *Journal of Engineering for Industry*, 95(1), p. 86.

Balevičius, R. et al. (2011) 'Investigation of wall stress and outflow rate in a flat-bottomed bin: A comparison of the DEM model results with the experimental measurements', *Powder Technology*, 214(3), pp. 322–336.

Balevičius, R. et al. (2012) 'Effect of rolling friction on wall pressure, discharge velocity and outflow of granular material from a flat-bottomed bin', *Particuology*, 10(6), pp. 672–682.

Bartholomew, L.. (1992) 'Mixing related to gravity- Material from pellets to powders', *Powder handling & Processing*, 4(4), pp. 309–311.

Beaudry, J. (1948) 'Blender efficiency', *Chemical Engineering*, 55(7), pp. 112–114.

Beverloo, W. et al. (1961) 'The flow of granular solids through orifices', *Chemical*

engineering science, 15, pp. 260–269.

Beverloo, W. and Leniger, H.A. (1961) 'The flow of granular solids through orifices', *Chemical Engineering Science*, 15(3-4), pp. 260–269.

Boss, J. (1986) 'Evaluation of the homegeneity degree of a mixture', *Bulk Solids Handling*, 6(6), pp. 1207–1215.

Boss, J. and Dabrowska, D. (1985) 'Stochastic model of mixing during discharging of granular materials from a bin. I: Two-component system', *Journal of powder and bulk solids technology*, 9(4), pp. 1–11.

Brown, C.J. and Nielsen, J. (1998) *Silos : Fundamentals of Theory, Behavior and Design*. Taylor & Francis.

Buick, J.M. et al. (2004) 'Motion of granular particles on the wall of a model silo and the associated wall vibrations', *Journal of Physics D: Applied Physics*, 37(19), pp. 2751–2760.

Butterfield, R. and Andrawes, K.Z. (1973) 'The measurement of planar displacements of sand grains', *Géotechnique*, 23(4), pp. 571–576.

Carson, J.W. and Royal, T.A. (1992) 'In-bin blending improves process control', *Powder Handling and Processing*, 4(3), pp. 301–307.

Carson, J.W. and Royal, T.A. (1991) 'Techniques of In-bin blending', *Bulk Materials Handling Towards 2000*. I.Mech.E.

Cassidy, D.J. et al. (1992) 'An experimental study of the blending of granular materials', *Powder Technology*, 72(2), pp. 177–182.

Choi, J. et al. (2005a) 'Velocity profile of granular flows inside silos and hoppers', *Journal of Physics: Condensed Matter*, 17(24), pp. S2533–S2548.

Choi, J. et al. (2005b) 'Velocity profile of granular flows inside silos and hoppers', *Journal of Physics: Condensed Matter*, 17(24) IOP Publishing, pp. S2533–S2548.

Chung, Y. and Ooi, J. (2006) 'Confined Compression and Rod Penetration of a

Dense Granular Medium: Discrete Element Modelling and Validation', in Wu, W. and Yu, H.-S. (eds.) *Modern Trends in Geomechanics SE - Springer Proceedings Physics*. Springer Berlin Heidelberg, pp. 223–239.

Chung, Y. et al. (2004) 'Measurement of mechanical properties of agricultural grains for DE models', *17th ASCE Engineering Mechanics Conference*

Chung, Y.C. (2006) 'Discrete element modelling and experimental validation of a granular solid subject to different loading conditions', *PhD Thesis, The University of Edinburgh*

Chung, Y.-C. and Ooi, J. (2008) 'A study of influence of gravity on bulk behaviour of particulate solid', *Particuology*, 6(6), pp. 467–474.

Chung, Y.C. and Ooi, J.Y. (2011) 'Benchmark tests for verifying discrete element modelling codes at particle impact level', *Granular Matter*, 13(5), pp. 643–656.

Cleary, P. (2002) 'DEM modelling of industrial granular flows: 3D case studies and the effect of particle shape on hopper discharge', *Applied Mathematical Modelling*, 26(2), pp. 89–111.

Coetzee, C.J. and Els, D.N.J. (2009) 'Calibration of discrete element parameters and the modelling of silo discharge and bucket filling', *Computers and Electronics in Agriculture*, 65(2), pp. 198–212.

Craig, D. (1996) 'An investigation of blending and mixing in bulk materials handling and process systems', *PhD Thesis, The University of New Castle*, , p. 378.

Craig, D.A. et al. (1994) 'Utilising the impulse response concept to predict blending capabilites of silos', *Powder handling & Processing*, 6(4), pp. 373–378.

Cui, L. and O'Sullivan, C. (2006) 'Exploring the macro- and micro-scale response of an idealised granular material in the direct shear apparatus', *Géotechnique*, 56(7), pp. 455–468.

Cundall, P.A. and Strack, O.D.L. (1979) 'A discrete numerical model for granular assemblies', *Géotechnique*, 29(1), pp. 47–65.

Danckwerts, P.V. (1953) ‘Continuous flow systems’, *Chemical Engineering Science*, 2(1), pp. 1–13.

Dau, G. and Ebert, F. (1996) ‘Measurement of residence time distributions in bulk solids handling devices’, *CHISA’96, 12th International Congress of Chemical and Process Engineering*. Prague.

Dau, G. et al. (1994) ‘On-line Analyse der Austrittskonzentration von Feststoffmischern (On-line Analysis of Discharge Concentration in Solids Mixers)’, *Aufbereitungstechnik*, 35(6), pp. 281–289.

Eichler, P. et al. (1997a) ‘Geometry and Mixing Performance of Gravity Discharge Silo Mixers’, *Engineering, Proceedings of the First European Congress on Chemical*. Florence, Italy, May 4-7, 1997, pp. 983–987.

Eichler, P. et al. (1996) ‘Videobased Measuring Technique to Determine the Blending Quality of Gravity Mixers’, *CHISA’96, 12th International Congress of Chemical and Process Engineering*. Prague.

Eichler, P. et al. (1997b) ‘Methoden zur Vorhersage der Mischgüte von Schwerkraftmischern’, *Chemie Ingenieur Technik*, 69(9) WILEY-VCH Verlag, p. 1260.

Favier, J.F. et al. (2001) ‘Modeling nonspherical particles using multisphere discrete elements’, *Journal of Engineering Mechanics*, 127(October), pp. 971–977.

Fore, L.B. et al. (2005) ‘Nonlinear temporal filtering of time-resolved digital particle image velocimetry data’, *Experiments in Fluids*, 39(1), pp. 22–31.

Forterre, Y. and Pouliquen, O. (2008) ‘Flows of Dense Granular Media’, *Annual Review of Fluid Mechanics*, 40(1), pp. 1–24.

Fowler, R.T. and Glastonrury, J.R. (1959) ‘The flow of granular solids through orifices’, *Chemical Engineering Science*, 10, pp. 150–156.

Gericke, H.R. (1993) ‘Different methods of batch and continuous mixing of bulk solids’, *Bulk Solids Handling*, 13(1), pp. 77–85.

Goins, R.R. (1984) ‘Method and apparatus for blending of solids or the like’, *Patent: U.S Patent 4472064*

Goldhirsch, I. (2010) ‘Stress, stress asymmetry and couple stress: from discrete particles to continuous fields’, *Granular Matter*, 12(3), pp. 239–252.

González-Montellano, C. et al. (2011) ‘Validation and experimental calibration of 3D discrete element models for the simulation of the discharge flow in silos’, *Chemical Engineering Science*, 66(21), pp. 5116–5126.

Harmens, A. (1963) ‘Flow of granular materials through horizontal apertures’, *Chemical Engineering Sci*, 18, pp. 297–306.

Hartl, J. (2008) ‘A study of granular solids in silos with and without an insert’, *PhD Thesis, The University of Edinburgh*

Härtl, J. (2008) ‘A study of granular solids in silos with and without inserts, University of Edinburgh’, *PhD Thesis, The University of Edinburgh*

Härtl, J. and Ooi, J.Y. (2011) ‘Numerical investigation of particle shape and particle friction on limiting bulk friction in direct shear tests and comparison with experiments’, *Powder Technology*, 212(1), pp. 231–239.

Härtl, J. and Ooi, J.Y. (2008) ‘Experiments and simulations of direct shear tests: porosity, contact friction and bulk friction’, *Granular Matter*, 10(4), pp. 263–271.

Haung, H.T. et al. (1993) ‘Limitation and improvement of PIV Part I : Limitation of conventional techniques due to deformation of particle image patterns’, *Experiments in Fluids*, 15, pp. 168–174.

Hertz, H. (1882) ‘Über die Berührung fester elastischer Körper’, *J. reine und angewandte Mathematik*, 92, pp. 156–171.

Höhner, D. et al. (2013) ‘Experimental and numerical investigation on the influence of particle shape and shape approximation on hopper discharge using the discrete element method’, *Powder Technology*, 235, pp. 614–627.

Itasca Consulting Group Inc (2006) *PFC 3D - Particle Flow Code in 3 Dimensions,*

Version 3.1 Minneapolis, USA

Janssen, H.A. (1895) 'Versuche über Getreidedruck in Silozellen', *Zeitschr. d. Vereines deutscher Ingenieure*, 39(35), pp. 1045–1049.

Jenike, A. and Shield, R.T. (1959) 'On the plastic flow of coulomb solids beyond original failure', *Journal of Applied Mechanics*, (Dec), pp. 599–602.

Jenike, A.W. (1961) 'Gravity flow of bulk solids', *Utah engineering experimental station, Bulletin*, 108

Jenike, A.W. (1964) 'Storage and flow of bulk solids', *University of Utah, Utah Engineering Experimental Station Bulletin*

Jiang, M. et al. (2015) 'A novel three-dimensional contact model for granulates incorporating rolling and twisting resistances', *Computers and Geotechnics*, 65, pp. 147–163.

Johanson, J. (1982a) 'Controlling flow patterns in bins by use of an insert', *Bulk Solids Handling*, 2(3), pp. 495–498.

Johanson, J. (1964) 'Stress and velocity fields in the gravity flow of bulk solids', *Journal of Applied Mechanics*, 31(3), pp. 499–506.

Johanson, J.R. (1970) 'In bin blending', *Chemical Engineering Progress*, 66(6), p. 50.

Johanson, J.R. (1982b) 'BinsertTM', *Patent: U.S Patent 4286883*

Johanson, J.R. (1965) 'Method of calculating rate of discharge from hoppers and bins', *Transactions of the Society of mining engineers*, (March), pp. 69–80.

Johanson, K. (2006) 'Predicting cone-in-cone blender efficiencies from key material properties', *Powder Technology*, 170(3), pp. 109–124.

Karim, M.Y. and Corwin, E.I. (2014) 'Eliminating friction with friction: 2D Janssen effect in a friction-driven system', *Physical Review Letters*, 112(May), pp. 1–4.

Ketterhagen, W.R. et al. (2005) 'Stress results from two-dimensional granular shear

flow simulations using various collision models', *Physical Review E*, 71(6), p. 061307.

Ketterhagen, W.R. et al. (2009a) 'Predicting the flow mode from hoppers using the discrete element method', *Powder Technology*, 195(1), pp. 1–10.

Ketterhagen, W.R. et al. (2009b) 'Predicting the flow mode from hoppers using the discrete element method', *Powder Technology*, 195(1), pp. 1–10.

Kiesgen, M. and Wilms, H. (1991) 'Zentralrohr-Mischsilo verbessert die Homogenitat von Kunststoffen', *Kunststoffen*, 81(12), pp. 1100–1104.

Kruggel-Emden, H. et al. (2007) 'Review and extension of normal force models for the Discrete Element Method', *Powder Technology*, 171(3), pp. 157–173.

Labra, C. et al. (2013) 'Spatial and Temporal Coarse-Graining for DEM Analysis', *Powders & Grains 2013*. Sydney, Australia, pp. 3–6.

Langston, P. (1995) 'Discrete element simulation of internal stress and flow fields in funnel flow hoppers', *Powder Technology*, 85(2), pp. 153–169.

Langston, P.A. et al. (1993) 'Continous Potential Discrete Particle Simulations of Stress and Velocity Fields in Hoppers: Transition from Fluid to Granular Flow', *The first Nisshin Engineering Particle Technology International Seminar: Discrete Particle Simulations in Powder Technology*. Osaka, Japan, p. 43.

Langston, P.A. et al. (1995) 'Discrete element simulation of granular flow in 2D and 3D hoppers: Dependence of discharge rate and wall stress on particle interactions', *Chemical Engineering Science*, 50(6), pp. 967–987.

Liu, S. et al. (2014) 'Flow characteristics and discharge rate of ellipsoidal particles in a flat bottom hopper', *Powder Technology*

Lommen, S. et al. (2014) 'DEM speedup: Stiffness effects on behavior of bulk material', *Particuology*, 12, pp. 107–112.

Luding, S. (2008) 'Introduction to discrete element methods', *European Journal of Environmental and Civil Engineering*, 12(7-8) Taylor & Francis Group, pp. 785–

826.

Lueptow, R.M. et al. (2000) ‘PIV for granular flows’, *Experiments in Fluids*, 28(2), pp. 183–186.

Mack, S. et al. (2011) ‘Experimental validation of polyhedral discrete element model’, *Powder Technology*, 214(3), pp. 431–442.

Manjunath, K.S. et al. (1992) ‘Homogenisation of bulk poweders in plane symmetric silos’, *Powder handling & Processing*, 4(3), pp. 283–292.

Markauskas, D. and Kačianauskas, R. (2010) ‘Investigation of rice grain flow by multi-sphere particle model with rolling resistance’, *Granular Matter*, 13(2), pp. 143–148.

Mathews, J. (2013) ‘Investigation of granular flow using silo centrifuge models’, *PhD Thesis, University of Natural Resources and Life sciences*

Medina, A. et al. (2000) ‘Gravity induced granular flow measurements in a 2D silo with a lateral bottom exit’, *Physics Letters A*, (August), pp. 109–116.

Medina, A. et al. (1998) ‘Velocity field measurements in granular gravity flow in a near 2D silo’, *Physics Letters A*, 250, pp. 111–116.

Michalowski, R.L. (1984) ‘Flow of granular material through a plane hopper’, *Powder Technology*, 39, pp. 29–40.

Mindlin, R. and Deresiewica, H. (1953) ‘Elastic spheres in contact under varying oblique forces’, *Journal of applied mechanics*, 20, pp. 327–344.

Morrissey, J.P. (2013) ‘Discrete Element Modelling of Iron Ore Pellets to Include the Effects of Moisture and Fines’, *PhD Thesis, The University of Edinburgh*

Nedderman, R. (1992) *Statics and kinematics of granular materials*. Cambridge: Cambridge University Press.

Nedderman, R.M. (1995) ‘The use of the kinematic model to predict the development of the stagnant zone boundary in the batch discharge of a bunker’,

Chemical Engineering Science, 50(6), pp. 959–965.

Nedderman, R.M. and Tüzün, U. (1979a) 'A kinematic model for the flow of granular materials', *Powder Technology*, 22(2), pp. 243–253.

Nedderman, R.M. and Tüzün, U. (1979b) 'A kinematic model for the flow of granular materials', *Powder Technology*, 22(2), pp. 243–253.

Nedderman, R.M. et al. (1982) 'The flow of granular materials- I', *Chemical Engineering Science*, 37(11), pp. 1597–1609.

Negi, S.C. et al. (1997) 'A Numerical Model for Flow of Granular Materials in Silos. Part 2: Model Validation', *Journal of Agricultural Engineering Research*, 68, pp. 231–236.

Ooi, J.Y. (2013) 'Establishing predictive capabilities of DEM – Verification and validation for complex granular processes', *POWDERS AND GRAINS 2013: Proceedings of the 7th International Conference on Micromechanics of Granular Media*. AIP Publishing, Vol.1542, pp. 20–24.

Ooi, J.Y. et al. (1996) 'Prediction of static wall pressures in coal silos', *Construction and Building Materials*, 10(2), pp. 109–116.

Ooi, J.Y. and She, K.M. (1997) 'Finite element analysis of wall pressure in imperfect silos', *International Journal of Solids and Structures*, 34(16), pp. 2061–2072.

Ostendorf, M. and Schwedes, J. (2005) 'Application of Particle Image Velocimetry for velocity measurements during silo discharge', *Powder Technology*, 158(1-3), pp. 69–75.

Pearson, R.K. (2005) *Mining Imperfect Data: Dealing with Contamination and Incomplete*. Society for Industrial and Applied Mathematics.

Pernenkil, L. and Cooney, C.L. (2006) 'A review on the continuous blending of powders', *Chemical Engineering Science*, 61(2), pp. 720–742.

Peshcl, I.A.S.. (1986) 'Universal Blender - A blending and mixing system for cohesive and free-flowing powders', *Bulk Solids Handling*, 6(3), pp. 575–578.

Di Renzo, A. and Di Maio, F.P. (2004) 'Comparison of contact-force models for the simulation of collisions in DEM-based granular flow codes', *Chemical Engineering Science*, 59(3), pp. 525–541.

Roberts, A.W. (1991a) 'Bin and feeder design criteria for anti-seggregation and blending', *MECH 91 Congress*. Sydney, Australia: College of Mechanical Engineers, Institution of Engineers.

Roberts, A.W. (1991b) '*Bin and Feeder Design Criteria for Anti-segregation and Blending*', Institution of Engineers, Australia, p. 7.

Roth, C.E. (1982) 'Blending system for Dry solids', *U.S. Patent*, 4(358), p. 207.

Rotter, J.M. et al. (1998) 'Silo pressure predictions using discrete–element and finite–element analyses', *Philosophical Transactions: Mathematical, Physical and Engineering Sciences*, 356(1747), pp. 2685–2712.

Sakaguchi, H. and Ozaki, E. (1993) 'Analysis of the Formation of Arches Plugging the Flow of Granular Materials', Thornton, C. (ed.)*Powders & Grains 93*. Rotterdam OR - Conference on micromechanics of granular media: Balkema, p. 351.

Schneider, H. et al. (2001) 'Blending of Stochastic Fluctuating Bulk Materials in Gravity Mixers.', *Proceedings of international Congress for Particle Technology*. Nürnberg, Germany, 27-29 March 2001.

Schulze, D. (1995) 'Theoretische Betrachtungen von Mischsilos, 1 : Grundlagen', *Schüttgut*, 3(1), pp. 483–486.

Scrivens, B.G. et al. (1991) 'Study of a Port Design for Silo Blenders', *Journal of Engineering for Industry*, 113(3), p. 343.

Sielamowicz, I. et al. (2005) 'Optical technique DPIV in measurements of granular material flows, Part 1 of 3-plane hoppers', *Chemical Engineering Science*, 60(2), pp. 589–598.

Sielamowicz, I. et al. (2011a) 'Empirical analysis of eccentric flow registered by the DPIV technique inside a silo model', *Powder Technology*, 212(1), pp. 38–56.

Sielamowicz, I. et al. (2010) ‘Empirical description of flow parameters in eccentric flow inside a silo model’, *Powder Technology*, 198(3), pp. 381–394.

Sielamowicz, I. et al. (2011b) ‘Empirical description of granular flow inside a model silo with vertical walls’, *Biosystems Engineering*, 108(4), pp. 334–344.

Slominski, C. et al. (2007) ‘Application of particle image velocimetry (PIV) for deformation measurement during granular silo flow’, *Powder Technology*, 173(1), pp. 1–18.

Standard, A. (2000) ‘*D6128: Standard test method for shear testing of bulk solids using the Jenike shear cell. ASTM International*’

Standish, N. et al. (1988) ‘Quantification of the degree of mixing in bins’, *Powder technology*, 54, pp. 197–208.

Stein, M.R. (1990) ‘Gravity blending: Storage and blending in one-step’, *Powder & Bulk Engineering*, (January), pp. 32–36.

Steingart, D.A. and Evans, J.W. (2005) ‘Measurements of granular flows in two-dimensional hoppers by particle image velocimetry. Part I: experimental method and results’, *Chemical Engineering Science*, 60(4), pp. 1043–1051.

Thornton, C. et al. (2011) ‘An investigation of the comparative behaviour of alternative contact force models during elastic collisions’, *Powder Technology*, 210(3), pp. 189–197.

Tsuji, Y. et al. (1992) ‘Lagrangian numerical simulation of plug flow of cohesionless particles in a horizontal pipe’, *Powder Technology*, 71(3), pp. 239–250.

Tuzun, U. et al. (1982) ‘The flow of granular materials- II’, *Chemical Engineering Science*, 37(12), pp. 1691–1709.

Tüzun, U. and Nedderman, R.M. (1982) ‘Investigation of the Flow Boundary a Funnel-Flow Bunker’, *Powder Technology*, 31(1), pp. 27–43.

Tüzün, U. and Nedderman, R.M. (1979) ‘Experimental evidence supporting kinematic modelling of the flow of granular media in the absence of air drag’,

Powder Technology, 24(2), pp. 257–266.

Ulissi, F. et al. (2009) 'PIV Technique applied to granular flows in hoppers', *Journal of Physics: Conference Series*, 166, p. 012004.

Vidyapati, V. and Subramaniam, S. (2013) 'Granular Flow in Silo Discharge: Discrete Element Method Simulations and Model Assessment', *Industrial & Engineering Chemistry Research*, 52, pp. 13171–13182.

Walters, J.K. (1973) 'A theoretical analysis of stresses in axially-symmetric bunkers hoppers and', *Chemical Engineering Science*, 28, pp. 779–789.

Waters, A.. and Drescher, A. (2000) 'Modeling plug flow in bins/hoppers', *Powder Technology*, 113(1-2), pp. 168–175.

Watson, G.R. and Rotter, J.M. (1996) 'A finite element kinematic analysis of planar granular solids flow', *Chemical Engineering Science*, 51(16), pp. 3967–3978.

Weiler, R. et al. (2012) 'Using the Discrete Element Method for Predicting the Mixing Behavior of Gravity Blenders in Different Operation Modes', *Chemical Engineering & Technology*, 35(8), pp. 1465–1472.

Weinhart, T. et al. (2016) 'Influence of coarse-graining parameters on the analysis of DEM simulations of silo flow', *Powder Technology*, 293, pp. 138–148.

Weinhart, T. et al. (2012) 'From discrete particles to continuum fields near a boundary', *Granular Matter*, 14(2) Springer Berlin / Heidelberg, pp. 289–294.

Wensrich, C.M. and Katterfeld, A. (2012) 'Rolling friction as a technique for modelling particle shape in DEM', *Powder Technology*, 217, pp. 409–417.

White, D. et al. (2003) 'Soil deformation measurement using particle image velocimetry (PIV) and photogrammetry', *Geotechnique*, 53(7), pp. 619–631.

Williams, K.C. et al. (2014) 'Particle shape characterisation and its application to discrete element modelling', *Particuology*, 12, pp. 80–89.

Wilms, H. (1986) 'Homogenization of Bulk Solids in Blending Silos', *Chem. Ing.*

Tech., 58(11), pp. 867–875.

Wilms, H. (1992) 'Blending Silos : An overview', *Powder handling & Processing*, 4(3), pp. 293–299.

Wilms, H. (1988) 'Blending and homogenisation of bulk solids with Zeppelin Multi-pipe gravity flow blender', *Bulk Solids Handling*, 8(6), pp. 733–736.

Yang, S. (2001) 'The simulation and experimental study of granular materials discharged from a silo with the placement of inserts', *Powder Technology*, 120(3), pp. 244–255.

Young, H.T. (1982) 'Apparatus for gravity blending of Particulate solids', *U.S. Patent*, 4(353) U.S, p. 652.

Zhang, K.F. and Ooi, J.Y. (1998) 'A kinematic model for solids flow in flat-bottomed silos', *Geotechnique*, 48(4), pp. 545–553.

Zhao, X.-L. et al. (2008) 'Flow patterns of solids in a two-dimensional spouted bed with draft plates: PIV measurement and DEM simulations', *Powder Technology*, 183(1), pp. 79–87.

Zhou, Y. et al. (2002) 'An experimental and numerical study of the angle of repose of coarse spheres', *Powder technology*, 125, pp. 45–54.

Zhou, Y.C. et al. (1999) 'Rolling friction in the dynamic simulation of sandpile formation', *Physica A: Statistical Mechanics and its Applications*, 269(2-4), pp. 536–553.

Zhu, H.P. and Yu, A.B. (2002) 'Averaging method of granular materials', *Physical Review E*, 66(2), p. 021302.

Zhu, H.P. et al. (2007) 'Discrete particle simulation of particulate systems: Theoretical developments', *Chemical Engineering Science*, 62(13), pp. 3378–3396.

Appendix A Details of model silo

A.1 Introduction

The focus of this appendix is to give the details about the experimental set-up such as the design requirements of the model silo, main components of the set-up and the video recording system.

A.2 Description of the set-up

A planar rectangular silo of 2.5 m height and 0.45 m wide was built by Zeppelin Systems Gmbh, Germany. The set-up is designed to quantitatively measure the flow patterns of granules using Particle Image Velocimetry (PIV).

A.3 Design requirements

To meet the objectives of the research, the following design requirements were set:

a. A rectangular wedge silo that produces 2D flow;
b. The model silo should be simulated using DEM within a manageable computational time without scaling down;
c. The front wall of the model silo should be transparent so that flow can be digitally recorded using a camera;
d. The walls of the silo should be strong enough to prevent bulging outwards after loading with the bulk solid;
e. The configuration of the model silo including the width, depth, outlet size and hopper angle should be easily varied;
f. The model silo should be filled using a pneumatic conveying system;
g. The model should accommodate the placement of internals such as inserts and blending tubes;

A.4 Components of model silo

The main components of the set-up consist of aluminium plates, perspex sheets, pneumatic conveying system, high pressure air supply line, storage and discharge containers. The vertical side walls, hopper and internals (inserts and blending plates) are made of aluminium whereas front and back walls are made of perspex sheets. All the outer side walls have the wall thickness of 10 mm and the internal walls have the wall thickness of 5 mm. The front and back perspex walls have wall thickness of 12 mm. The silo was initially constructed with perspex sheets of the wall thickness of 8 mm but when loaded with the material it walls bulged outward. Hence, the perspex sheets were replaced 12 mm wall thick which was found to be strong enough to prevent bulging. The photograph of assembled model with insert and blending tube is

shown in Figure A.1 (a). The same model is dismantled and assembled to a flat bottom silo configuration as shown in Figure A.1 (b). The aluminium plates are held in place between the front and back perspex sheets by friction which in turn makes it easy to dismantle and assemble the set-up to any required configuration. The silo can be configured with either of three depths of 20 mm, 40 mm and 100 mm. The depth is measured perpendicular to the plane of the paper.

The pneumatic conveying system comprises of high pressure air supply line, vacuum injector and a flexible hose pipe. The photograph of the system is shown in Figure A.2. An air pressure ranging from at 4-5 bar is supplied to the system. The vacuum injector is the core component and its main function is to create a suction force when high pressure air is supplied to it. Therefore, the injector when placed in a container of bulk solids it sucks the material. The flexible hose pipe that is connected to its other end then conveys the material to the top of the silo.

The dimensions of the model used and the configurations that were studied, test procedure are described in chapter 4, where the experiments in the flat bottom configuration are presented and in chapter 7 where the experiments in the silo with insert and blending tube are presented.

(a)

(b)

Figure A.1 (a) Silo configured with hopper and internals (b) Silo configuration with flat bottom without internals.

Figure A.2 Pneumatic conveying system.

The video recording set-up is the critical part of the set-up comprising high speed camera, tripod and two headlamps with supporting stands. The typical set-up of the system is shown in Figure A.3. This figure is just a representative of the camera set-up and does not truly depicts the current experimental set-up. The main function of this set-up is to record the high quality images of flow behind the transparent front wall of the model silo. Photron FASTCAM SA6 camera was used to record the flow (shown in Figure A.4). It can record at frame speeds ranging from 50 to 75000 fps at varying resolutions. For example, at a frame rate of 1500 fps a maximum resolution

of 1920 x 1080 can be obtained. The components and operating instructions of the camera can be found in the manual guide. The camera has to be mounted on a tripod with its axis perpendicular to the central axis of the silo. The spirit level available on the tripod and camera can be used to adjust the levelling of the camera with respect to the floor and silo. The front wall of the silo can be illuminated with two lamps placed on either side of the silo. The intensity and focus of the lights can be changed by adjusting the distance from the front surface of the silo.

Figure A.3 Typical set-up of video recording system.

Figure A.4 FASTCAM SA6 from Photron.

A.5 Summary

A planar rectangular silo of 2.5 m height and 0.45 m wide was built by Zeppelin Systems Gmbh, Germany. The set-up is designed to quantitatively measure the flow patterns of granules using Particle Image Velocimetry (PIV). The design features and the components of the model silo were discussed. The various configuration of the model silo can be easily achieved because of its robust design. The width (range: 100 -450 mm), outlet size (range: 0 to 450 mm), hopper angle (range: 0 to 90 deg) can be changed to any desired value within the limits of the dimensions. The model can be configured to 20, 40 and 100 mm depths. Photron FASTCAM SA6 camera is deployed to record the flow. It can record frame rates ranging from 50 to 75000 fps.